# In-Depth Kinetic Understanding and Design of [4+4] Anthracene Photocycloadditions

**Anastasia Kislyak**

**Supervisors**

Prof. Dagmar D'hooge, PhD* - Prof. Christopher Barner-Kowollik, PhD** -
Prof. Paul Van Steenberge, PhD* - Prof. Leonie Barner, PhD**

\* Department of Materials, Textiles and Chemical Engineering
Faculty of Engineering and Architecture, Ghent University

\*\* School of Chemistry & Physics
Faculty of Science, Queensland University of Technology, Australia

GHENT
UNIVERSITY

QUT

**In-Depth Kinetic Understanding and Design of [4+4] Anthracene Photocycloadditions**

**Anastasia Kislyak**

Doctoral dissertation submitted to obtain the academic degrees of
Doctor of Chemical Engineering (UGent) and Doctor of Philosophy (QUT)

**Supervisors**
Prof. Dagmar D'hooge, PhD* - Prof. Christopher Barner-Kowollik, PhD** -
Prof. Paul Van Steenberge, PhD* - Prof. Leonie Barner, PhD**

\*   Department of Materials, Textiles and Chemical Engineering
    Faculty of Engineering and Architecture, Ghent University

\** School of Chemistry & Physics
    Faculty of Science, Queensland University of Technology, Australia

November 2021

**GHENT UNIVERSITY**

**QUT**

# Members of the Examination Board

## Chair

Prof. Em. Luc Taerwe, PhD, Ghent University

## Other members entitled to vote

Prof. Ludwig Cardon, PhD, Ghent University

Prof. Richard Hoogenboom, PhD, Ghent University

Prof. Anthony O'Mullane, PhD, Queensland University of Technology, Australia

Prof. Kei Saito, PhD, Kyoto University, Japan

Prof. Yin-Ning Zhou, PhD, Shanghai Jiao Tong University, China

## Supervisors

Prof. Dagmar D'hooge, PhD, Ghent University

Prof. Christopher Barner-Kowollik, PhD, Queensland University of Technology, Australia

Prof. Paul Van Steenberge, PhD, Ghent University

Prof. Leonie Barner, PhD, Queensland University of Technology, Australia

# STATEMENT OF ORIGINAL AUTHORSHIP

The work contained in this jointly by QUT and UGent supervised doctoral thesis has not been previously submitted to meet requirements for an award at these or any other higher education institutions. To the best of my knowledge and belief, the thesis contains no material previously published or written by another person except where due reference is made.

Date     26/07/2021

Signature

# Table of Contents

# ACKNOWLEDGEMENTS

# DUTCH SUMMARY

Sinds de vorming van onze planeet hebben fotochemische reacties, d.w.z. reacties waarbij licht nodig is om door te gaan, een cruciale rol gespeeld bij het in stand houden van het leven op aarde. Mensen hebben sindsdien bewust en onbewust gebruik gemaakt van de kracht van fotochemische reacties. Enkele van de grootste voordelen van fotochemische reacties zijn het op afstand besturen van chemische processen met ruimtelijke en tijdsafhankelijk precisie. Bij het nastreven van steeds fijnere controle hebben scheikundigen veel verschillende fotochemische reacties ontdekt, waaronder omkeerbare fotocycloaddities, die een overvloed aan mogelijkheden voor dynamisch en adaptief materiaalontwerp ontgrendelde. Eén van dergelijke toepassingen is in lichtgevoelige dynamische materialen van zachte materie, waar omkeerbare fotocycloaddities kunnen worden gebruikt om de polymeernetwerkstructuur en de resulterende mechanische eigenschappen te veranderen. Gedetailleerde controle over die mechanische eigenschappen is zeer wenselijk voor toepassingen van dynamische polymeermaterialen, bijvoorbeeld bij het ontwerpen van aanpasbare scaffolds voor celbiologie. Om de kracht van fotochemisch omkeerbare cycloaddities volledig te benutten, moet een uitgebreid wiskundig model worden ontwikkeld om de dynamische polymeernetwerkstructuur en veranderingen daarvan onder lichte bestraling te verbinden met de weergegeven mechanische eigenschappen. Het huidige proefschrift heeft tot doel de basis te leggen voor zo een uitgebreid model voor een goed gekozen referentiesysteem. De basis is gelegd door de complexiteit van het model stapsgewijs te vergroten.

Eerst wordt in **Hoofdstuk 2** een model ontwikkeld om de kinetiek van een antraceen fotocycloadditiereactie in oplossing te voorspellen. De afgeleide kinetische uitdrukking modelleert exclusieve antraceen fotocycloadditie met behulp van een vereenvoudigd reactieschema. Een eenvoudig modelkader werd bereikt door een schijnbare snelheidscoëfficiënt in te voeren. De schijnbare snelheidscoëfficiënt bestaat uit snelheidscoëfficiëntverhoudingen, waardoor het niet nodig is om de individuele snelheidscoëfficiënten te bepalen. Er werd een eenvoudige methode voorgesteld om de snelheidscoëfficiëntverhoudingen van de fotoreactie te bepalen door een reeks korte tijd (i.e. tot slechts een lage conversie) experimenten te gebruiken. Het geïntroduceerde modelraamwerk zou mogelijk verder kunnen worden uitgebreid tot andere fotocycloadditiereacties. Bovendien biedt het model een uitgebreide hoeveelheid informatie aan op gemakkelijke wijze, bijvoorbeeld integrale en differentiële kwantumopbrengsten of een fractie van het door het

antraceen geabsorbeerde licht. De golflengte-afhankelijkheid van antraceen fotocycloadditie werd onderzocht in het golflengtebereik van 375 nm tot 430 nm via een zogenaamde "actieplot". De "actieplot" onthulde dat de omzetting van de antraceen-fotocycloadditiereactie zelfs bij 430 nm, d.w.z. in een zichtbaar lichtbereik, detecteerbaar is. De reactiviteit van antraceen in het zichtbare lichtbereik is gunstig omdat het helpt om schade door UV-licht te voorkomen.

Vervolgens breidt **Hoofdstuk 3** het model uit om competitieve antraceen fotocycloadditie en antraceen fotocycloreversie te voorspellen, door de aanwezigheid van antraceendimeer op te nemen in het model en fotocycloreversie van dit dimeer in het reactieschema op te nemen. De kinetische uitdrukkingen werden afgeleid om antraceendimeersplitsing te modelleren met behulp van een vereenvoudigd reactieschema, gevolgd door het afleiden van een model voor competitieve antraceen-fotocycloadditie en antraceendimeersplitsing. Een eenvoudig modelkader werd opnieuw bereikt door de schijnbare snelheidscoëfficiënten te introduceren, één schijnbare snelheidscoëfficiënt voor fotocycloadditie en één voor fotocycloreversie. Beide schijnbare snelheidscoëfficiënten bestaan opnieuw uit verhoudingen van snelheidscoëfficiënten. De methodologie schetste de experimentele procedure die nodig is om stapsgewijs (in twee stappen) de snelheidscoëfficiëntverhoudingen te bepalen voor competitieve antraceenfotocycloadditie en antraceendimeersplitsing. Ten eerste werden de snelheidscoëfficiëntverhoudingen voor antraceenfotocyclo-additie bepaald met behulp van korte tijd (lage conversie) experimenten en uitgaande van exclusieve antraceen fotocycloadditie zoals in **Hoofdstuk 2**. Ten tweede werd de snelheidscoëfficiëntverhouding voor antraceen fotocycloreversie bepaald, tevens met behulp van korte tijd (lage conversie) experimenten. De golflengte-afhankelijkheid van beide reacties werd onderzocht in het golflengtebereik van 260 nm tot 330 nm via actieplots. De schijnbare antraceenreactiviteit bleek af te nemen naar een kortere golflengte, terwijl de schijnbare antraceendimeerreactiviteit optimaal bleek te zijn bij een golflengte van 280 nm.

Vervolgens stelt **Hoofdstuk 4** een uitbreiding van het model in **Hoofdstuk 2** voor, die kan worden toegepast voor het vouwen van nanodeeltjes met één enkele keten (*single-chain nanoparticle*, SCNP). Dit zijnmisschien wel de eenvoudigste soort polymeernetwerken, waarbij antraceengroepen aan een polymeerketen zijn verankerd, wiens volume vervolgens instort door crosslinking. Het model voor SCNP's gebruikt de snelheidscoëfficiëntverhoudingen uit **Hoofdstuk 2** en een correctiefactor, die rekening houdt met de beperkingen die worden opgelegd door de verankering op en de architectuur van de polymeerketens. Het model kan de voortgang van de intramoleculaire fotocycloadditie reactie berekenen op een gemiddelde wijze

8

voor een gemiddelde keten. Net als in de **Hoofdstukken 2** en **3** levert het model informatie over een groot aantal parameters op, b.v. integrale en differentiële kwantumopbrengsten. Bovendien konden exacte gegevens over antraceenposities binnen elke afzonderlijke keten worden verkregen door de RAFT-polymerisatie te modelleren via een in-house ontwikkeld kinetische Monte Carlo (kMC) model. Bovendien kan het kMC model de intramoleculaire fotocycloadditiereactie van antracenen, die aan een polymeerketen zijn verankerd, voorspellen. De polymeerketens konden vervolgens in elk stadium van het vouwproces in 3D worden gevisualiseerd. Er werd een experimentele methodologie voorgesteld om aanvullende parameters te bepalen die de macromoleculaire opsluiting van de fotoreactie weerspiegelen.

Ten slotte vat **Hoofdstuk 5** de in de literatuur gerapporteerde snelheidscoëfficiënten samen voor het modelleren van dynamische polymeernetwerken verkregen via direct laserschrijven (DLS). Helaas zijn de meeste coëfficiënten van de polymerisatiesnelheid niet gekend in de wetenschappelijke literatuur, daarom werden ook enkele afschattingen voorgesteld en hoe zij kunnen geimplementeerd worden. Het potentiële modelraamwerk om het DLS-proces te modelleren met behulp van een in house kinetische Monte Carlo (kMC) model werd besproken, waarbij een stapsgewijze toename van de complexiteit werd voorgesteld. Ten eerste, het modelleren van alleen de kinetiek van de polymerisatiereactie op een gemiddelde wijze. Vervolgens werd de methodologie besproken om een ruimte - en tijdsafhankelijkheid van de reactieve species tijdens de DLS in het model te modelleren met behulp van een in-house kinetisch Monte Carlo model. Geïnspireerd door de parallelle kMC-benadering, kon een één-dimensionale ruimtelijke resolutie van de reactieve species tijdens de DLS worden bereikt. Analoog zou de 2D- en ten slotte de 3D-resolutie geïmplementeerd kunnen worden. Een implementatie voor antraceen fotocycloreversiereactie tijdens DLS werd voorgesteld. Verdere uitbreiding van het anthraceen fotocycloadditiereactiemodel uit **Hoofdstuk 4** om fotocycloadditie van antraceen verankerd aan een polymeernetwerk te voorspellen, werd ook onderzocht.

Samenvattend, dit proefschrift legt de basis voor de ontwikkeling van een model dat de fotoresponsieve structuur van dynamische polymeermaterialen, geproduceerd via DLS, en de resulterende mechanische eigenschappen verbindt. Er wordt een modelraamwerk geïntroduceerd om op antraceen gebaseerde omkeerbare fotocycloadditties in eerste instantie in oplossing te voorspellen, gevolgd door een methodologie voor de uitbreiding van het model die de voorspelling mogelijk maakt van de eigenschappen van omkeerbare fotocycloadditties van antraceen verankerd aan een polymeerketen of ingebed in een polymeernetwerk. Ten slotte onderzoekt het proefschrift beschikbare snelheidscoëfficiënten en mogelijke modelleringsstrategieën om de productie van DLS-gebaseerde dynamische polymeermaterialen te modelleren via kMC.

# ENGLISH SUMMARY

Since the formation of our planet, photochemical reactions, i.e. reactions that require light to proceed, have played a vital role in sustaining life on Earth. Humans have since consciously and subconsciously harnessed the power of photochemical reactions. Some of the greatest benefits of photochemical reactions include enabling remote control of chemical processes with spatial and temporal precision. In pursuit of ever-finer control, chemists have discovered many different photochemical reactions including reversible photocycloadditions, which unlocked a plethora of possibilities for dynamic and adaptive material design. One such application is in light-responsive dynamic soft matter materials, where reversible photocycloadditions can be used to change the polymer network structure and the resulting mechanical properties. Intricate control over those mechanical properties is highly desirable for applications of dynamic polymeric materials, e.g., in designing adaptable scaffolds for cell biology. To fully harness the power of photochemically reversible cycloadditions, a comprehensive mathematical model needs to be developed to connect the dynamic polymer network structure and changes thereof under light irradiation with the displayed mechanical properties. The current thesis aims at constructing the basis for such a comprehensive model for a well-chosen reference system. The basis was constructed by increasing the model complexity incrementally step-by-step.

First, **Chapter 2** develops a model to predict the kinetics of an anthracene photocycloaddition reaction in solution. The derived kinetic expression models exclusive anthracene photocycloaddition using a simplified reaction scheme. A simple model framework was achieved by introducing an apparent rate coefficient. The apparent rate coefficient consists of rate coefficient ratios, thus eliminating the need for determining the individual rate coefficients. A simple methodology was proposed to determine the photoreaction rate coefficient ratios by using a series of short time (i.e. low conversion) experiments. The introduced model framework can be further adapted to other photocycloaddition reactions. Additionally, an extensive amount of information is easily retrievable from the model, for example, integral and differential quantum yields or a fraction of light absorbed by the anthracene. The wavelength-dependency of anthracene photocycloaddition was probed in the 375 nm to 430 nm wavelength range via an action plot. The action plot revealed that conversion of anthracene photocycloaddition reaction is detectable even at 430 nm, i.e. in a visible light range. The visible light range reactivity of anthracene is advantageous because it helps to avoid UV light related damage.

Next, **Chapter 3** expands the model to predict competitive anthracene photocycloaddition and anthracene photocycloreversion, by including anthracene dimer photocycloreversion into the reaction scheme. The kinetic expressions were first derived to model anthracene dimer cleavage using the simplified reaction scheme, followed by deriving a model for competitive anthracene photocycloaddition and anthracene photocycloreversion. A simple model framework was once again achieved by introducing the apparent rate coefficients, one apparent rate coefficient for photocycloaddition and one for photocycloreversion. Both apparent rate coefficients consist of rate coefficient ratios. The methodology outlined the experimental procedure requires the determination of the rate coefficient ratios for competitive anthracene photocycloaddition and anthracene dimer cleavage in two steps. First, rate coefficient ratios for anthracene photocycloaddition were determined using short time (low conversion) experiments and assuming exclusive anthracene photocycloaddition like in **Chapter 2**. Second, the rate coefficient ratio for anthracene photocycloreversion was determined using short time (low conversion) experiments. The wavelength-dependency of both reactions was probed in the 260 nm to 330 nm wavelength range via action plots. The apparent anthracene reactivity was found to be decreasing towards a shorter wavelength, while the apparent anthracene dimer reactivity was found to be optimal at a wavelength of 280 nm.

Subsequently, **Chapter 4** proposes an extension of the model in **Chapter 2**, which can be applied for single-chain nanoparticle (SCNP) folding – perhaps the simplest form of polymer networks – where anthracene moieties are attached to a polymer chain, which subsequently collapses in volume by crosslinking. The model for SCNPs uses rate coefficient ratios from **Chapter 2** and a correction factor, which accounts for the restrictions enforced by the attachment to and the architecture of the polymer chains. The model allows to calculate the reaction progress of the intramolecular photocycloadditions on average for an average chain. Just as in **Chapters 2** and **3**, information regarding an extensive amount of parameters is retrievable, e.g. integral and differential quantum yields. Furthermore, exact data on anthracene positions within every single chain could be accessed by modelling the RAFT polymerisation via an in-house kinetic Monte Carlo (kMC) model. Additionally, the kMC model predicted the intramolecular photocycloaddition reaction of anthracenes attached to a polymer chain. The polymer chains were subsequently visualised in 3D at any stage of the folding process. An experimental methodology was proposed to determine additional parameters that reflect the macromolecular confinement of the photoreaction.

Finally, **Chapter 5** summarizes the rate coefficients known in the literature for modelling dynamic polymer networks obtained via direct laser writing (DLW). Unfortunately, the majority of the polymerisation rate

coefficients are not known, therefore, some approximations and their implementation were also suggested. The potential framework to model the DLW process using an in-house kinetic Monte Carlo (kMC) model was discussed, proposing a stepwise increase in complexity. First, modelling only the kinetics of the polymerization reaction on average. Subsequently, the methodology to achieve a spatial and temporal variation of the reactive species during the DLW in the model was discussed. Inspired by the parallel kMC approach, a 1D spatial resolution of the reactive species during the DLW was proposed to be achieved in future work. Analogously, the 2D and, finally, the 3D resolution may be implemented. An implementation for anthracene photocycloreversion reaction during DLW was suggested. Further extension of the anthracene photocycloaddition reaction model from **Chapter 4** to predict photocycloaddition of anthracenes attached to a polymer network was also explored.

In conclusion, the current thesis prepares the basis for the development of a model connecting the photoresponsive structure of dynamic polymeric materials generated via DLW and the resulting mechanical properties. A model framework is introduced to predict reversible anthracene-based photocycloadditions initially in solution, followed by a methodology for the extension of the model enabling the prediction of the reversible photocycloaddition properties of anthracenes attached to a polymer chain or embedded into a polymer network. Finally, the thesis explores available rate coefficients and potential strategies to model the production of DLW dynamic polymeric materials via kMC.

# LIST OF SYMBOLS

| Symbol | Units | Definition |
|---|---|---|
| **A** | - | anthracene |
| **A$_2$** | - | anthracene dimer |
| **$^1$A** | - | anthracene in a singlet excited state |
| **$^3$A** | - | anthracene in a triplet excited state |
| **AA$^1$** | - | anthracene excimer |
| **$^1$A$_2$** | - | anthracene dimer in a non-relaxed singlet excited state |
| $c$ | mol L$^{-1}$ | molar concentration |
| $E_{pp}$ | J pulse$^{-1}$ | energy per pulse |
| $E_\lambda$ | J photon$^{-1}$ | the energy of a single photon of wavelength $\lambda$ |
| $f$ | pulses s$^{-1}$ | frequency of laser pulses |
| $g$ | - | Zimm and Stockmayer contraction factor |
| $g_A$ and $g_{A2}$ | - | auxiliary functions |
| $i$ | - | chain length |
| $I$ | mol s$^{-1}$ | the overall rate of photon absorption |
| $J$ | mol L$^{-1}$ s$^{-1}$ | photon volumetric absorption rate |
| $k_{+app}$ | s$^{-1}$ | **A** dimerization apparent rate coefficient |
| $k_{-app}$ | mol L$^{-1}$ s$^{-1}$ | **A$_2$** cleavage apparent rate coefficient |
| $k_{-1}$ | s$^{-1}$ | **A** de-excitation rate coefficient |
| $k_{-4}$ | s$^{-1}$ | **A$_2$** de-excitation rate coefficient |
| $k_2$ | L mol$^{-1}$ s$^{-1}$ | dimerization rate coefficient |
| $k_3$ | L mol$^{-1}$ s$^{-1}$ | concentration quenching rate coefficient |
| $k_5$ | s$^{-1}$ | dimer cleavage rate coefficient |
| $L$ | cm | light path length |
| $M_i$ | g mol$^{-1}$ | the molar mass of a polymer chain of length $i$ |
| $\bar{M}_n$ | g mol$^{-1}$ | number average molecular weight |

| | | |
|---|---|---|
| $\bar{M}_w$ | g mol$^{-1}$ | weight average molecular weight |
| $n$ | mol | number of moles |
| $N_A$ | mol$^{-1}$ | Avogadro number |
| $N$ | - | number of molecules/units |
| $N_i$ | mol | moles of the polymer chain of length $i$ |
| $R$ | dm | radius |
| $r$ | mol s$^{-1}$ | rate of reaction |
| $t$ | s | time |
| $T_\lambda$ | - | glass transmittance |
| $V$ | L | volume |
| $w$ | g | total weight of a polymer sample |
| $w_i$ | - | mass fraction of molecules with chain length $i$ |
| $w$ | - | SCNP fitting parameter for chain flexibility |
| $X$ | - | fractional conversion |
| $z$ | - | confinement factor |
| | | |
| Đ | - | dispersity of a polymer |
| $\varepsilon$ | L mol$^{-1}$ cm$^{-1}$ | molar attenuation coefficient |
| $\lambda$ | nm | wavelength |
| $\rho$ | - | crosslinking density, i.e. mol crosslinks per mol monomer units |
| $\Phi_{diff}$ | - | differential or instantaneous quantum yield |
| $\Phi_{int}$ | - | integral or cumulative quantum yield |

Abbreviations

| | |
|---|---|
| DLW | direct laser writing |
| *k*MC | kinetic Monte Carlo |
| NMR | nuclear magnetic resonance |
| QSSA | quasi-steady-state approximation |
| SCNP | single-chain nanoparticle |
| TTA | triplet-triplet annihilation |

# LIST OF PUBLICATIONS

## Full-length peer-reviewed research articles

1. A. Kislyak, H. Frisch, M. Gernhardt, P.H.M. Van Steenberge, D.R. D'hooge, C. Barner-Kowollik 'Time dependent differential and integral quantum yields for wavelength dependent [4+4] photocycloadditions' *Chem. Eur. J.* **2020** 26, 478 (SCI-IF 2018: 5.16)

2. A. Kislyak, D. Kodura, H. Frisch, F. Feist, P.H.M. Van Steenberge, C. Barner-Kowollik, D.R. D'hooge 'A holistic approach for anthracene photochemistry kinetics' *Chem. Eng. J.* **2020**, 402, 126259 (SCI-IF 2019: 10.652)

## Conference Abstracts

1. D.R. D'hooge, L. De Keer, E. Loccufier , K. Karsu, P.H.M. Van Steenberge, A. Kislyak, H. Frisch, L. Daelemans, K. De Buysser, M.F. Reyniers, C. Barner-Kowollik, R. Dauskardt, K. De Clerck
   The amazing world of network polymers and their applications
   Virtual Milan Polymer Days (MIPOL2020)
   Milan, Italy, 15-17 July **2020**, oral presentation

2. A. Kislyak, F. J. Arraez; H. Frisch, M. Gernhardt; D. Kodura; F. Feist; P. Van Steenberge; C. Barner Kowollik; D.R. D'hooge
   Unravelling the wavelength dependency of anthracene photoinitiated reactions
   69th Canadian Chemical Engineering Conference (CCEC)
   Ottawa, Canada (virtual), October 25-28, **2020**, oral presentation

3. A. Kislyak, F.J. Arraez , D. Kodura, F. Blöβer, H. Frisch, P. H. M. Van Steenberge, D. R. D'hooge, C. Barner-Kowollik
   [4+4] anthracene photodimerization for controlled folding of single chain polymer nanoparticles
   The First International Conference on "Green" Polymer Materials 2020
   Virtual MDPI, 5-25 November **2020**, poster presentation

# CHAPTER 1. INTRODUCTION

## 1.1    Introductory statement

Photochemical reactions are chemical reactions that are enabled by the absorption of light.[1] Photochemical reactions are an integral part of nature, where many processes are driven by light. Examples of these processes include photosynthesis in plants,[2] the synthesis of vitamin D in humans[3] as well as the rhodopsin photoisomerization reaction enabling vision.[4-5] On the other hand, photochemical reactions are also known to be the cause of phytophotodermatitis, where skin contact with furocoumarin present in specific plants in combination with UV light exposure leads to skin burns.[6] Exposure to UV light may also cause significant DNA disruption.[7]

Humans have employed photochemistry for their own benefit for centuries. For example, hundreds of years ago Egyptians used to treat leukodermia (a skin depigmentation) by using the *Ammi majus L.* plant in combination with sun exposure.[8-10] Photochemistry has also enabled the development of photography when Louis Daguerre discovered silver-based photography in 1835.[11] Ciamician envisioned a grand future for photochemistry in his 1912 publication, proposing vast applications in industry to conduct a wide range of reactions from polymerizations to isomerizations as well as substituting coal with light as a source of energy for the future.[12] Today, there is a large number of photochemical reactions available, one of which, reversible photocycloadditions, will be considered in the current thesis.[13-14]

Reversible photocycloadditions have particularly interesting applications in dynamic polymeric materials, where they can function as dynamic covalent bonds. Under exposure to external stimuli, e.g. light, dynamic bonds and interactions can be initiated or disturbed, enabling dynamic changes of mechanical properties in polymer materials. Dynamic polymer materials have high application potential in a variety of fields including cell biology.[15-16] Using light as an external stimulus has a major advantage, as light allows intricate control over the reaction, both spatially and temporally.[17] In addition, using light-gated triggers in dynamic polymer materials for cell biology research is beneficial since light, especially long-wavelength, has a minimum impact on cells.[18-19]

The mechanical properties of the synthesised polymer structures define their application scope. The mechanical properties of the polymer structures are dependent on the polymer network structure. Therefore, it is important to correlate the polymer network structure and its changes under a specific stimulus with the displayed mechanical properties. The challenge here lies in the development of a simple, but a comprehensive

model for kinetic modelling of reversible photocycloadditions in complex environments, i.e. polymer networks. Such a model would allow obtaining the highly desirable intricate control over the outcome of the photochemical reaction and thus, the changes in the mechanical properties of the dynamic polymeric materials. The current thesis aims to lay the groundwork for the generation of such a comprehensive model that will ultimately correlate the polymer network structure and its changes under a specific stimulus with the displayed mechanical properties. The thesis explores the model development in a step-wise approach of increasing complexity. As the physical systems are highly complex, we isolate physical phenomena by designing dedicated reaction conditions, e.g. small-molecule systems, free of any interference of polymer matrix effects. Initially, a model is presented for predicting experimental data during the reversible photocycloaddition in solution using the example of anthracene photocycloaddition, starting with exclusive photodimerization (**Fig 1-1 Step 1** and **Chapter 2**) and subsequently adding the photocleavage reaction (**Fig 1-1 Step 2** and **Chapter 3**). Next, the complexity of the model is increased by incorporating the adaptation of the anthracene photocycloaddition model to the intramolecular crosslinking of single polymer chains (**Fig 1-1 Step 3** and **Chapter 4**). The model adapts to the polymer chain environment by correcting the rate coefficients for the confinement effects. The last chapter (**Fig 1-1 Step 4** and **Chapter 5**) discusses the approach that could be taken to build the model for generating dynamic polymer networks formed via direct laser writing (DLW). DLW is considered here as it is a powerful additive manufacturing technique, for example, able to generate micro-scaffolds studying the behaviour of single cells.[15] **Chapter 5** further discusses the available kinetic data and how the kinetic model for reversible anthracene photocycloaddition developed in the current thesis could be adapted for use in dynamic polymer networks.

In the next subsections of this thesis chapter, an introduction is provided to photochemistry (**§1.2**) with a focus on the reversible photocycloaddition of anthracene. An introduction into polymerization reactions (**§1.3**) follows. The application of reversible cycloadditions lies in dynamic polymer materials, which are introduced in **§1.4**. Finally, insight into kinetic modelling techniques is presented in **§1.4**. The contents of the following chapters are outlined in **§1.6**.
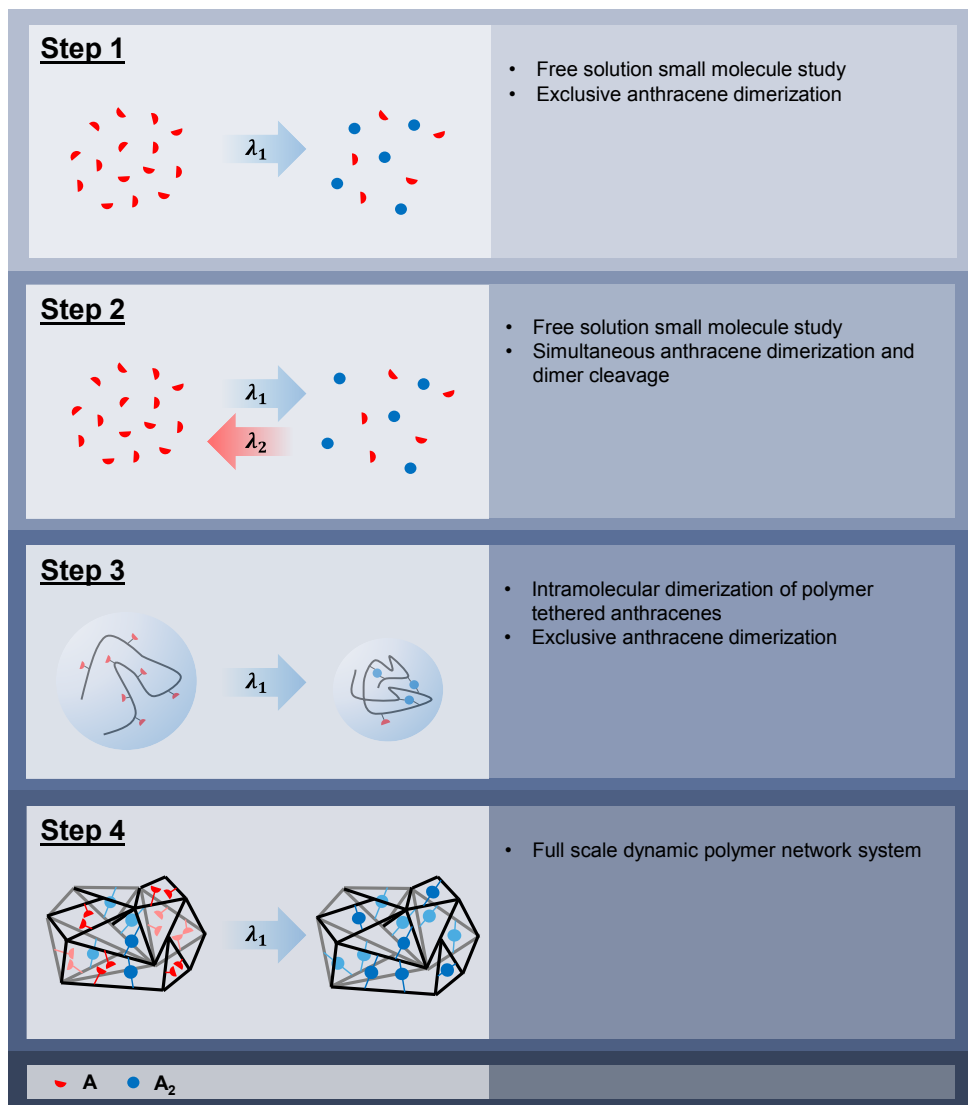
**Fig 1-1 Schematic overview of the research methodology governing the current thesis. The thesis aims to lay the groundwork for the generation of a comprehensive model that will ultimately correlate the polymer network structure and its dynamic molecular changes under a specific light stimulus with the displayed mechanical properties. The following steps were taken to construct the groundwork. Step 1: a model for exclusive anthracene photocycloaddition in solution. Step 2: a model for competitive anthracene photocycloaddition and cleavage in solution. Step 3: model proposal for the exclusive intramolecular photocycloaddition of anthracenes attached to a polymer chain. Step 4: discussion of the approach that could be taken to build the model for generating dynamic polymer networks and subsequent adaptation of the kinetic model for anthracene photocycloaddition for use in dynamic polymer networks.**

## 1.2    Photochemistry

Photochemical reactions are processes that proceed after the absorption of light.[1] These reactions play a significant role in everyone's life – in fact enabling life itself – and are instrumental in a range of processes, starting from the synthesis of vitamin D,[3] enabling vision via photoreceptors,[4-5] to being responsible for DNA disruption.[7] The use of light for conducting a reaction offers exceptional advantages, such as the ability to precisely and remotely control the reaction without the involvement of heat, thus enabling very mild reaction conditions. The wide range of different photochemical reactions that are available (in terms of wavelength and light intensity) increases the potential of photochemical reactions for application in various fields. Some of the examples of the many implemented photochemical reactions include photo-isomerization, cleavage and hydrogen abstraction as well as reversible cycloaddition.[20] Isomerization of rhodopsin, responsible for colour vision, is a vivid example of a photo-isomerization reaction.[4] Cleavage and hydrogen abstraction reactions are integral in photoinitiated polymerisations,[21] while reversible cycloaddition reactions are employed for use in light-responsive materials.[13] Photochemical reactions take are central to the current thesis, as the kinetics of the reversible photocycloaddition reaction of anthracene is explored in-depth, with the view to providing the basis for modelling the time-dependent behaviour of dynamic soft matter materials (**§1.4**), particularly in the context of photo-initiated polymerisation reactions that are used for the construction of intricately controlled 3D polymer structures on sub-micron levels via direct laser writing (**§1.3.3**). To introduce the foundations of the photochemical reactions, first, basic concepts such as Beer-Lambert's law and quantum yields are introduced (**§1.2.1**). Next, an example of a photochemical reaction – a reversible cycloaddition reaction - is showcased (**§1.2.2**) with an emphasis on the anthracene reversible dimerization (**§1.2.3**), as this entities form the basis of the current thesis.

### 1.2.1 General photochemistry

Light plays a fundamental role in a photochemical reaction as photons need to be absorbed for the reaction to proceed. Absorption of light by molecules occurs in a nonlinear fashion following the famous Beer-Lambert law:

$$I_l = I_0(1 - 10^{-\varepsilon cl})$$    eq 1-1

with $I_l$ being the intensity of light at wavelength $\lambda$ absorbed by the species at pathlength $l$, $\varepsilon$ - molar attenuation coefficient of the absorbing species at wavelength $\lambda$, L mol$^{-1}$ cm$^{-1}$, $c$ - concentration of the absorbing species, mol L$^{-1}$, $l$ - path length, cm. The molar attenuation coefficient, $\varepsilon$, varies with wavelength, giving rise to the

absorbance spectrum specific to each molecule (for example **Fig 1-4**). A higher $\varepsilon$ indicates that more light will be absorbed.

According to the well known Stark-Einstein Law, a single photon, once absorbed, leads to excitation of one molecule only.[2, 22] However, multi-photon absorption is also possible, i.e. one molecule is excited by two or more photons simultaneously.[2] Depending on the employed wavelength, $\lambda$, the energy contained in one photon, $E_\gamma$, varies and is described by:

$$E_\gamma = \frac{hc}{\lambda}$$
eq 1-2

with Planck constant $h$ (6.63 × 10$^{-34}$ J s), $c$ - speed of light (3 × 10$^8$ m s$^{-1}$) and $\lambda$ - wavelength, m.

Once an electron has been excited within the molecule by the photon energy and reached a higher electronic state, molecules can undergo a variety of transformations. These transformations are often illustrated using a Jablonski diagram (**Fig 1-2**).[23] Upon excitation, a molecule enters a singlet excited state (an excited state where the electron spin quantum number is 0, i.e. paired electrons have opposite spins).[1, 22] Molecules can transition from a singlet excited state to a triplet excited state (an excited state where the electron spin quantum number becomes 1, i.e. paired electrons have parallel spins) via the radiationless (no photon emitted) process of intersystem crossing (ISC).[1, 22] Molecules in either singlet or triplet excited states can de-excite back to the ground state radiationlessly or by emitting a photon. For the de-excitation with emission of a photon, two cases can be distinguished: in the case of a singlet excited state, the process is termed fluorescence and, in the case of triplet excited state, de-excitation is known as phosphorescence.[1] In addition to radiative de-excitation, two types of radiationless de-excitation, known as internal conversion and vibrational relaxation, can also occur. Vibrational relaxation is the de-excitation of molecules due to collisions with other molecules.[1] Internal conversion, i.e. radiationless de-excitation, on the other hand, occurs by molecules moving to a different electronic state of the same multiplicity (i.e. spin angular momentum has the same number of possible orientations).[23] Finally, and most importantly for this thesis, molecules in the excited states can also participate in a reaction.
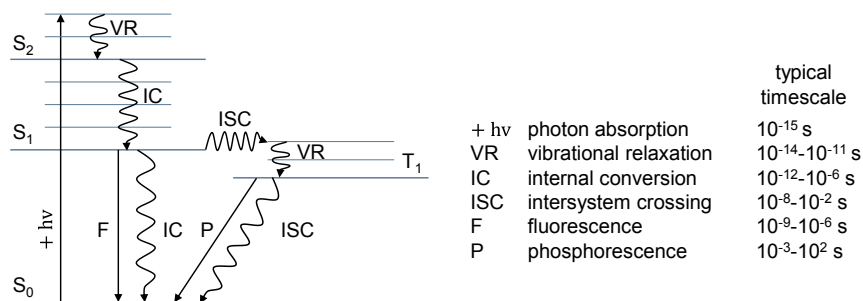
**Fig 1-2 Illustration of Jablonski diagram depicting a variety of transformations that the excited molecule could undergo. Adapted with permission from Springer Nature and Copyright Clearance Center: Springer Nature. Calculation of Excited States: Molecular Photophysics and Photochemistry on Display by Luis Serrano-Andrés, Juan José Serrano-Pérez [COPYRIGHT] 2017**

The rate of a chemical reaction is given by a rate law. First, a non-photochemical reaction will be introduced as an example. Here, reaction rate laws are defined depending on the order of the reaction. A $0^{th}$ order reaction rate, $r$, is concentration-independent - $r = k$, in which $k$ is the rate coefficient of the chemical reaction. The rate of a $1^{st}$ order reaction is given by $r = kc_B$ and, hence, is dependent on the concentration of species B ($c_B$). Analogously, the rate of a $2^{nd}$ order reaction is often expressed as $r = kc_B c_C$ in case of an asymmetric reaction or $kc_B^2$ in case of a symmetric one, and, therefore, also depends on the concentration of the reaction partners, species B ($c_B$) and species C ($c_C$). According to the law of Arrhenius, the reaction rate coefficient $k$ critically depends on temperature. The definitions above are typical for thermally induced chemical reactions. However, in the case of a photochemical reaction, light also controls the reaction rate, thus the usual rate coefficient, $k$, is not sufficient to describe the reaction kinetics. Thus, to incorporate light absorption into the description, the quantum yield, $\Phi$, is introduced for the description of the effectiveness of photochemical reactions. In the current thesis, the term quantum yield will exclusively be used to refer to the quantum yield of the photochemical reaction, i.e. it does not denote the quantum yields for ICS, fluorescence, etc. The definition of the quantum yield for a photochemical reaction depends on the reaction in question and typically exhibits values between 0 and 1.[24-27] However, examples of quantum yield values above 1 are possible in the case of chain reactions.[24-27] The International Union of Pure and Applied Chemistry (IUPAC) defines two types of quantum yield, i.e. integral and differential quantum yields.[1] Therefore, in the case of a photochemical reaction, the integral quantum yield can be defined as:

$$\Phi_{int} = \frac{moles\ of\ molecules\ decomposed}{moles\ of\ photons\ absorbed} \qquad \text{eq 1-3}$$

or

$$\Phi_{\text{int}} = \frac{moles\ of\ product\ formed}{moles\ of\ photons\ absorbed}$$  eq 1-4

The integral quantum yield represents an averaged quantum yield of the reaction over a period of irradiation, *t*. The difference between **eq 1-3** and **eq 1-4** is that in the case of fragmentation reaction (e.g. $A \rightarrow B + C$), **eq 1-3** is used and, in case of an addition reaction (e.g. $A + B \rightarrow C$), **eq 1-4** is required. On the other hand, the differential quantum yield, $\Phi_{\text{diff}}$, represents the rate of change in the number of moles of molecules over the rate of photon absorbtion, i.e. $\Delta t \rightarrow 0$, and would, therefore, be defined as:

$$\Phi_{\text{diff}} = \frac{d(moles\ of\ molecules\ decomposed\ or\ product\ formed)/dt}{d(moles\ of\ photons\ absorbed)/dt}$$  eq 1-5

$\Phi_{diff}$ may also be estimated experimentally by measuring conversion at short irradiation times, $\Delta t$, such that the conversion is small. The differential quantum yield is important in the evaluation of the kinetics of photochemical reactions, as it provides a more accurate picture of the reaction rate at any given moment in time as opposed to the integral quantum yield, which reflects the averaged reaction rate over the entire time period. Such knowledge is of key importance when one wishes to explore the potential of photochemical reactions for remote-control materials, where the ability to control reactions will directly influence the prospects of the material. **Chapter 2** of the current thesis will explore the differential and integral quantum yields in more detail.

### 1.2.2 Reversible cycloadditions

One of the interesting examples of photochemical processes is reversible cycloaddition reactions.[28] These reactions have shown potential in a variety of dynamic polymeric materials e.g. photoresponsive hydrogels, self-healing materials and nanocarriers.[13, 17, 19, 28-33] Most prominent examples of reversible photocycloadditions, also shown in **Fig 1-3**, include cycloadditions of coumarin,[34-38] thymine,[39-41] stilbene,[42-43] cinnamic acid[30-31, 44-45], styrylpyrene,[46-47] and anthracene,[13, 32, 47] as well as their derivatives.

Cycloadditions can proceed symmetrically, i.e. reacting with the same species,[48-49] as well as in an asymmetric way, i.e. by reacting with other species.[50-52] Different cycloaddition reactions can proceed at different wavelengths, thus two different reactions could be triggered mostly independently of each other.[47-48] Therefore, two such cycloaddition reactions could be used in combination with each other with minimal interference, constituting a $\lambda$-orthogonal system.[48, 53] Ideally for $\lambda$-orthogonal reactions, the different reactions should be triggered completely independently, i.e. in any sequence, and without any interference. However, often only one of the reactions can be triggered independently, as the wavelength region for the second reaction overlaps with the first one.[17] Light intensity could also be employed to favour different reactions, i.e. an asymmetric

reaction over a symmetric one, based on their respective quantum yields at a given wavelength.[50] In these systems, when high light intensities are applied, the number of molecules in the ground state is reduced, and thus the reaction between two molecules both in excited states is not allowed, so the excited molecules have no option but to react asymmetrically with another species in the ground state.[50] Furthermore, the shift of the window in which the cycloaddition reaction can be triggered is possible using different substitutes on the molecule. A shift towards longer wavelengths is referred to as red- or bathochromic shift and a shift towards shorter wavelengths – blue- or hypsochromic shift. A red-shift of the reaction is especially desirable, as harsh UV light is often not ideal due to UV light damaging effects.[54] A red-shift for the peak wavelength of the anthracene absorption spectra was observed by introducing substituents with increasing electron-donating power.[7] Such flexibility and versatility of reaction control makes these cycloadditions strong candidates for remotely controlled dynamic materials and a subject of intense research interest.[28, 31, 55]
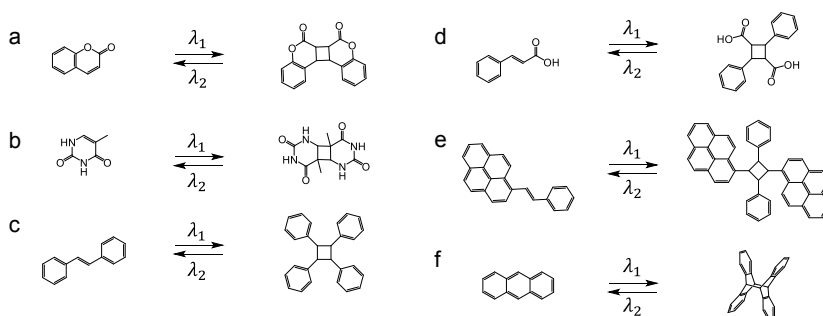


**Fig 1-3 Examples of molecules capable of reversible photocycloaddition reactions. a: coumarin; b: thymine; c: stilbene; d: cinnamic acid; e: styrylpyrene; f: anthracene.**

During a cycloaddition, a molecule absorbs a photon and reaches an excited state. The excited molecule subsequently reacts with another molecule in the ground state forming covalent bonds.[56] The use of the optimum wavelength for irradiation is desirable to ensure, for example, that the highest quantum yield is observed (**§1.2.1**). One may instinctively look at the UV-VIS spectrum of the absorbing molecule, however, the quantum yield of the reaction does not necessarily mimic the shape of the UV-VIS spectrum of the absorbing molecule.[3] UV-VIS spectrum corresponds only to the photon absorption by the molecule (labelled "+ hv" in **Fig 1-2**), while the transitions that follow (e.g. ISC) may not necessarily be most efficient at the same wavelength as the maximum absorption wavelength.[4] An experimental assessment of the reactivity of a specific molecule at a range of wavelengths is necessary for obtaining a complete picture of the reaction potential of said molecule. For this purpose, so-called "action plots" were devised.[46, 53, 57-59] Action plots are obtained using the

following method: a solution with a photoreactive molecule is irradiated with the same number of photons at different (monochromatic) wavelengths and the conversion is measured, thus establishing wavelength dependency of the conversion or product yield.[46, 53, 57-59]

Action plots, however, do not use kinetic expressions derived from the reaction schemes and do not yield reaction rate coefficients, hence, they are not able to fully describe the kinetics of the concentration-dependent reactions. Therefore, action plots are not sufficient for obtaining a complete picture of the reaction kinetics when considering concentration-dependent reactions, in particular anthracene photocycloaddition. Knowledge of reaction kinetics, however, is important for establishing control over the reaction. The best way to approach this challenge is to develop a model capable of predicting reaction kinetics. Once the developed model has been benchmarked against the experiment, the number of experiments required to deduce the ideal conditions and irradiation time for achieving the desired reaction conversion can be reduced, thus saving tedious experimental work and resources. However, the knowledge of the reaction mechanism is required to implement the rate laws of the sub-reactions and, ultimately, to model the reaction kinetics of the reversible photocycloadditions. In addition, the ability to determine the rate coefficients of these rate laws under the conditions of interest is required to estimate the influence of the reaction environment (e.g. different solvents, molecules are attached to a chain or network).

Accounting for the environment in which the reaction proceeds, as mentioned above, is important, since it affects the kinetics of the reaction.[36] For instance, as was illustrated by Kehrloesser et al., the photostationary state of the coumarin photocycloaddition was affected due to spatial confinement on the nanoparticle, as opposed to the coumarin reaction in free solution.[36] Importantly, some of the coumarin dimers were shielded from irradiation by the nanoparticles themselves.[36] These considerations may have a large impact on the values of the rate coefficients.

Therefore, the main challenges (**§1.1**) of the current thesis are accessing the orthogonality of the reversible photochemical cycloaddition reaction of choice (i.e. anthracene, *vide infra*) and the development of a model capable of describing the kinetics of the reversible photocycloaddition. The kinetic model will account for the reaction environment, starting with reactions in solution for simplicity. In the next stage, the model will be translated to the compaction, i.e. intramolecular crosslinking, of single polymer chains as a simplistic model and, perspectively, to a full network environment. For the current work, the reversible cycloaddition of anthracene was selected, the mechanism of which will now be discussed in more detail.

### 1.2.3 Anthracene driven photochemistry

One of the most prominent molecules capable of reversible [4+4] photocycloadditions is anthracene. Anthracene reversible photocycloaddition is a powerful tool for remote control of materials where repeated cycloaddition and cleavage is desired.[55] Anthracene photodimerization occurs predominantly at irradiation above 300 nm (**Fig 1-4**) and its quantum yield depends on the concentration of anthracene in the solution.[49, 60-61] Anthracene dimer photocleavage occurs at wavelengths below 300 nm, where the dimer starts to absorb (e.g. refer to **Fig 1-4**).[49, 60] The mechanisms of photodimerization and cleavage are complex and involve multiple competing side routes.[49, 61-63] The progress was carefully reviewed by Bouas-Laurent et al.[49] and a simplified summary of dimerization and dimer cleavage mechanisms is provided below (**Fig 1-5**).
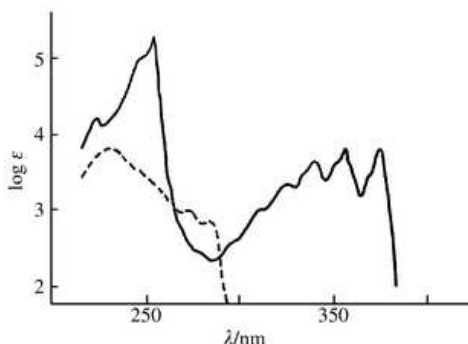


**Fig 1-4 An example of UV-VIS spectra of anthracene and its dimer. Republished with permission of Royal Society of Chemistry, from "Photodimerization of anthracenes in fluid solutions: (part 2) mechanistic aspects of the photocycloaddition and of the photochemical and thermal cleavage" Bouas-Laurent, H. et al. 30, 4, 2001; permission conveyed through Copyright Clearance Center, Inc.[49]**

The anthracene photodimerization reaction mechanism has been examined in a plethora of studies and will be initially considered. Dimerization reactions normally proceed via two possible routes: a singlet excited state ($^1A$) forming an excimer ($^1AA$), or via triplet-triplet annihilation (TTA) (**Fig 1-5a**). For the singlet excited state route, upon absorption of a photon, an anthracene molecule (A) is excited into a singlet excited state ($^1A$). $^1A$ can subsequently either de-excite via a variety of routes or form an excimer ($^1AA$) with another anthracene in the ground state.[61, 64-69] The excimer in turn can dissociate to recover two anthracene units in the ground state via different routes or form an anthracene dimer ($A_2$). [61, 64-69]

The triplet-triplet annihilation (TTA) route can proceed when sensitized.[63, 73] In the TTA route, first, anthracene in a singlet excited state undergoes intersystem crossing forming anthracene in the triplet excited state ($^3A$).[63] Next, two anthracenes in a triplet excited state form a two triplet encounter pair ($^3A^3A$). The two triplet encounter pair then, in turn, either forms an excimer or dissociates back into two anthracenes via various routes.[63] The

resulting excimer can subsequently form a dimer or dissociate back into two anthracenes.[63] The triplet-triplet

annihilation route is eliminated by the presence of oxygen and at anthracene concentrations above 0.005 mol

$L^{-1}$ due to self-quenching (i.e. quenching of the anthracene in the triplet state due to interaction with another

anthracene in the ground state).[1, 49, 63] Light intensity influences the rate of the TTA route, i.e. higher-intensity

– faster TTA.[63] When the TTA route is sensitised and oxygen is present in the reaction mixture, endoperoxide

can be formed as a side product.[49]



| A | anthracene monomer | $^1AA$ | excimer |
| $A_2$ | anthracene dimer | $^3A$ | anthracene monomer in |
| $^1A$ | anthracene monomer in a | | a triplet excited state |
| | singlet excited state | $^3A^3A$ | two triplet encounter pair |
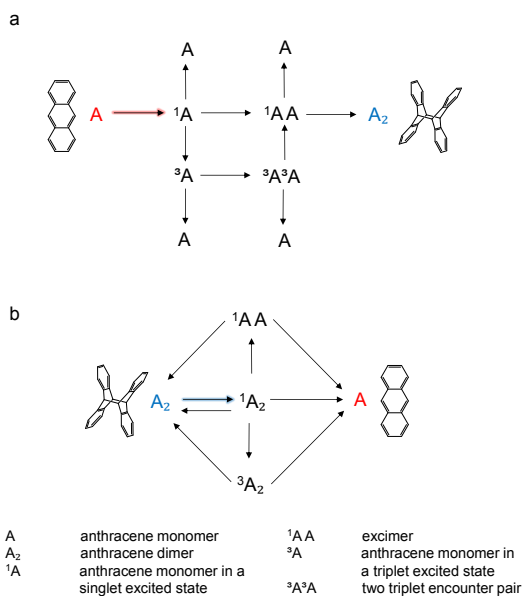
**Fig 1-5 Simplified mechanisms of a: anthracene dimerization[61, 64-69] and b: anthracene dimer cleavage.[62, 70-72]**

The mechanism of anthracene dimer ($A_2$) cleavage is less clear than the mechanism of anthracene

dimerization (**Fig 1-5b**).[49] The anthracene dimer is capable of dissociating thermally and photochemically.

Photochemical dissociation of the anthracene dimer depends on the wavelength and takes place in the

wavelength range where dimerization is also possible. Irradiation, therefore, leads to a photostationary state,

where the rates of dimerization and dimer cleavage are equal.[49] Menter and Forster have stated in their work

that the majority of dimer photocleavage proceeds via a diabatic route (i.e. via radiationless transition to

another potential surface), where excited dimer ($^1A_2$) is cleaved directly into two anthracenes.[62] The minority

of cleavages proceeds via two adiabatic routes (those of which the resulting products are on the same potential

surface as the reactants), either through direct cleavage of excited dimers or via excimers.[62]

Aside from a dependency on the wavelength, the mechanism of dimer photocleavage is also known to be temperature-dependent.[70-71] Yamamoto et al. differentiated three temperature regimes of anthracene cleavage: high (300-220 K), intermediate (190-120 K) and low (110-77 K).[71] In their work, these authors noted that cleavage in the low-temperature regime proceeds via a triplet state, in the intermediate temperature regime via an excimer, and in the high-temperature regime via a hypothetical intermediate (the nature of which was not exactly determined).[70-72] In their later work, they proposed the existence of an electronically tight complex as an intermediate through which the majority of the reaction proceeds at 293 K.[70] Iannone et al. noted that the low-temperature triplet state route also showed higher yield under two different wavelength absorptions as opposed to when the single wavelength was used.[72]

In the current thesis, the kinetics of the anthracene photochemical reaction will be explored using a pulsed laser. A laser can provide monochromatic irradiation with minimal divergence, which is ideally suited for detailed kinetic studies over a range of wavelengths. In addition to wavelength specificity, the low divergence means that the laser also enables good control over the amount of irradiation received by a sample.

When it comes to tracking the reaction conversion, the two most straightforward experimental techniques available are UV-Visible spectroscopy (UV-VIS) and nuclear magnetic resonance (NMR). Quantifying conversion via UV-VIS measurements requires different absorbance spectra of the product and reactant. UV-VIS has the benefit of being a sensitive and quick technique. In the case of anthracene, the absorption spectrum of the anthracene dimer is distinct from the anthracene absorption spectrum, particularly for wavelengths above 300 nm, where dimer absorption is minimal, providing an ideal window to track the conversion. On the other hand, UV-VIS measurements are extremely sensitive to changes in concentration. Therefore, care must be taken during the transfer and dilution of the sample in preparation for measurement, as the possibility of additional error is high. Nuclear magnetic resonance (NMR) spectroscopy, in contrast, does not pose this challenge of concentration dependency, however, the required concentrations for measurement are much higher. $^1$H-NMR resonance shifts for anthracene and its dimer are clearly distinguishable in the NMR spectrum, allowing the conversion to be readily traced using a well-pronounced shift from close to 8.6 ppm to around 5.6 ppm (**Fig 1-6** (a to a')).[74] Furthermore, NMR spectroscopy provides more information on the molecular structure than UV-VIS, i.e. indicating clearly whether contamination or side reactions are present. For these reasons, $^1$H NMR spectroscopy was used in the current work, whenever possible, to determine anthracene monomer to dimer conversions.
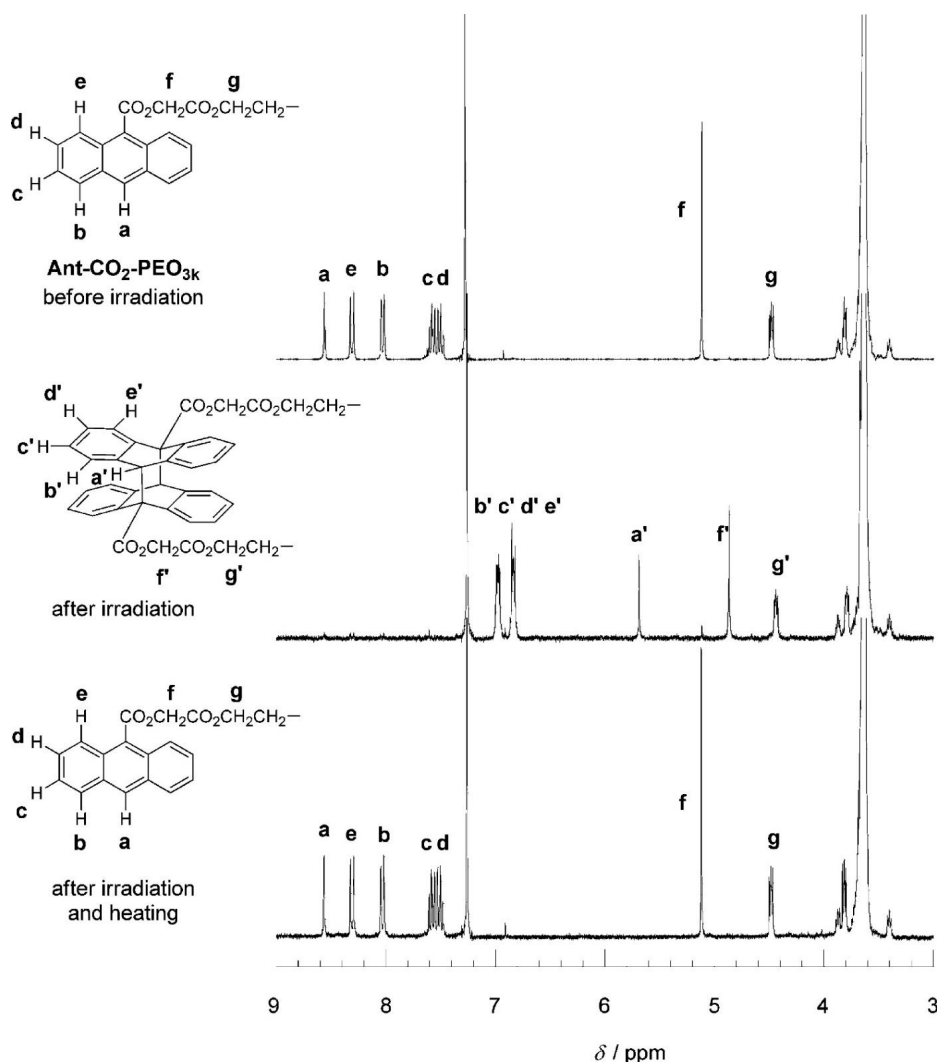
**Fig 1-6 A well-pronounced shift in the $^1$H-NMR spectra during anthracene photocycloaddition (a to a'). Reprinted with permission from Yamamoto et al.[74] Copyright 2021 American Chemical Society.**

## 1.3 Polymerisation

In the current thesis, the anthracene reversible photodimerization is modelled with an application for dynamic polymer materials in mind. Dynamic or reprogrammable materials (**§1.1** and **§1.4**) are materials capable of changing their mechanical properties upon an external stimulus, e.g. light, using reversible bonds.[13, 31] This ability is of key interest for a range of applications, such as self-healing materials.[31, 75] The presence of the

reversible bonds in dynamic materials can be realised with the help of anthracene reversible photodimerization. To model reversible photodimerization of anthracene in dynamic materials, representation of the influence of the reaction environment is important, i.e. attachment to the polymer chain backbone which constitutes the dynamic materials. Consideration of how these single polymer chains, or networks, are generated is vital to model the kinetics of the reversible photodimerization of anthracenes attached to these chains or networks.

Polymerisation reactions can be divided into two groups depending on the mechanism involved - step growth and chain growth polymerisations. Step growth polymerizations occur by reaction between the functional groups of the reacting species.[5] Chain growth polymerisations reaction involves a reactive centre where the polymer chain growth occurs by the addition of the monomers to the reactive centre.[5] Depending on the type of the reactive centre, chain growth polymerisation reactions are divided into ionic and radical polymerisations.[5] In ionic polymerisations reactive centre is either a positively or negatively charged ion/radical ion hence dividing ionic polymerizations into cationic and anionic polymerizations respectively.[5] In radical polymerization the reactive centre is radical.[5] Radical polymerisations can be free radical polymerisations (FRP) and controlled (also known as living) radical polymerisations.[6] Controlled radical polymerisations, as could be deduced from the name, allow better control over the polymerisation reaction in comparison to FRP resulting in the synthesis of more defined polymers.[6] Different types of controlled radical polymerizations include atom-transfer radical polymerization (ATRP), stable free-radical polymerization (SFRP) and finally reversible addition-fragmentation transfer (RAFT).[5] ATRP introduces reversible chain termination reaction by creating dormant chains through the use of organic halide and catalyst containing a transition metal.[5] In SFRP, stable radicals are used to replace active propagating radicals instead.[5] Finally, RAFT is employing chain transfer agents which take part in reversible chain transfer.[5]

The dynamic materials, the model for which is discussed in the current work (**Chapter 5**) can be synthesized via radical polymerisation reactions. Radical polymerisation is particularly suited for the synthesis of functional polymers, as it allows the use of a wide range of monomers that otherwise would need to be chemically protected for polymerisation (i.e. in ionic polymerisation more polar functional groups can react with the propagating reactive centre and terminate the polymerisation reaction).[5] Therefore, in this section, a brief introduction to polymerisation reactions relevant for the synthesis of polymer chains or networks in this work is presented. First, free radical polymerisation (FRP) (**§1.3.1**) is introduced, then reversible addition−fragmentation chain-transfer polymerisation (RAFT) polymerisation (**§1.3.2**) (suggested for the synthesis of polymer chains for single-chain nanoparticles in **Chapter 4** and **§1.4.2**). Finally, in **§1.3.3** direct

laser writing (DLW) method for generating dynamic polymer network structures in **Chapter 5** & **§1.4.1** is discussed.

### 1.3.1 Free radical polymerisation

Polymers are macromolecules formed through a chemical reaction where many molecules, termed monomers are combined.[76] Such chemical reactions are called polymerisations. Free radical polymerisation is an important polymerisation mechanism in which the reactive species are radicals, i.e. species containing unpaired electrons.[77]

The mechanism of free radical polymerisation consists of (at least) four steps (**Fig 1-7**): initiation, propagation, termination and chain transfer. During the initiation step, an initiator molecule is cleaved to form, usually, a pair of potentially initiating radicals. Several types of initiators exist. Thermal initiators dissociate with heat, while photoinitiators are cleaved with the use of light.[77] Other initiators rely on redox reactions, ionising radiation or persulfate decomposition in an aqueous solution.[77] The resulting initiator radical fragments consequently react with a monomer to form oligomeric radicals. The formed radicals participate in propagation reactions, where the radicals keep reacting with new monomers, increasing the length of the polymer chain. The polymer chain continues to grow until two radicals meet and react in a so-called termination reaction, in which the growth of the chains stop. Termination reaction can occur in two ways: combination or disproportionation. During the combination termination reaction, two radical chains are combined into one dead polymer chain, while, during disproportionation, two dead polymer chains are formed. A chain transfer can also occur, where the radical centre is transferred to either a small molecule (another monomer, a solvent molecule, a chain transfer agent) or a polymer chain.[76]

The synthesised polymer chains are not identical but contain a distribution of lengths.[76] Characterising a distribution of polymer chains mathematically is non-trivial and several different methods exist to describe the distribution of lengths of polymer chains. Some of the frequently used methods include number average molecular weight and weight average molecular weight. These average molecular weights differ in the way they are calculated.

Initiation
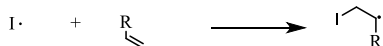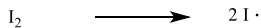


Propagation



Termination
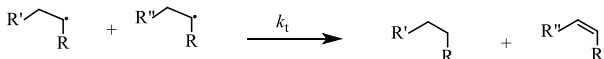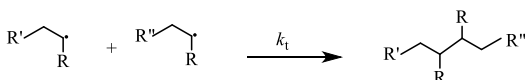




Chain transfer to monomer



**Fig 1-7 Illustration of the main reaction steps of the free radical polymerisation mechanism.**

Number average molecular weight, $\bar{M}_\text{n}$, is defined as:[76]

$$\bar{M}_\text{n} = \frac{w}{\sum N_i} \qquad \text{eq 1-6}$$

where $w$ is the total weight of polymers in grammes and $\sum N_i$ - moles of polymer chains in total in moles.

Weight average molecular weight, $\bar{M}_\text{w}$, in turn, is defined as:[76]

$$\bar{M}_\text{w} = \sum w_i M_i \qquad \text{eq 1-7}$$

where $M_i$ - molar mass of molecules with chain length $i$, g mol$^{-1}$ and $w_i$ represents mass fraction of molecules with chain length $i$, which can be calculated as:

$$w_i = \frac{i N_i}{\sum i N_i} \qquad \text{eq 1-8}$$

The ratio of the weight average molecular weight and the number average molecular weight is defined as the dispersity of the polymer, Đ, (**eq 1-9**). If all the polymer chains are identical in chain length, then Đ=1, otherwise - Đ>1. [76]

$$Đ = \bar{M}_\text{w}/\bar{M}_\text{n} \qquad \text{eq 1-9}$$

Typical dispersities for FRP polymers range from Đ=1.5, with exclusively recombination occurring, to Đ=2 for purely disproportionation modes in ideal cases (e.g. perfect mixing, isothermic, no side-reaction, no gel effect etc.), whereas any non-idealities (e.g. non-ideal mixing, non-isothermic, side-reactions, gel effect, etc.) will increase the dispersity to higher values than 1.5-2. The FRP mechanism forms the basis of the RAFT polymerisation mechanism, which is introduced in the next section (**§1.3.2**). FRP is commonly employed in direct laser writing to generate crosslinked networks (**§1.3.3**).

## 1.3.2 RAFT polymerisation

The reaction mechanism of reversible addition−fragmentation chain-transfer polymerisation (RAFT) features thermal initiators and vinyl monomers, similar to free radical polymerisation. However, for a RAFT polymerisation, a RAFT agent is also added to the mixture. The addition of the RAFT agent (also termed a chain transfer agent) allows control over the polymer chain growth, thus producing polymers with narrow molecular weight distributions.[76] The mechanism of the RAFT polymerisation includes initiation, propagation and termination steps, identical to a conventional FRP, but with the addition of 2 equilibrium steps involving the RAFT agent. These equilibrium steps are illustrated in **Fig 1-8** below. The main RAFT equilibrium occurs between the dormant chain, which has a RAFT agent attached to one of its terminal groups and a radical chain.[78] The RAFT pre-equilibrium step occurs between the initial RAFT agent and a radical chain.[78] Most polymer chains are dormant during RAFT and only a few polymer chains are radicals at any given time, the polymer chains "take turns" in adding ca. 1-10 monomer units at a time, leading to rather uniform growth of all chains and (ideally) to a dispersity close to 1.
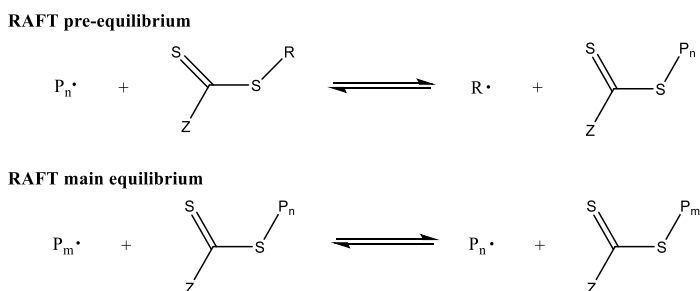


**Fig 1-8 Steps of RAFT polymerisation mechanism associated with the RAFT agent.[76]**

The ability to prepare well-defined versatile polymers makes RAFT polymerisation an ideal candidate for synthesizing stimuli-responsive polymers.[79] RAFT is actively used for the synthesis of polymer chains containing moieties capable of undergoing photochemical reactions. The photoreactive moieties then form

crosslinks under irradiation, hence, folding these polymer chains into single-chain nanoparticles (SCNPs).[35, 47-48, 80] In **Chapter 4** of the current thesis, RAFT polymerisation is used to synthesise polymer chains as precursors for SCNPs.

### 1.3.3 Direct laser writing (DLW)

Direct laser writing (DLW) is an important technique for fabricating 3D polymeric structures on the sub-micron range, including dynamic materials.[13] The current thesis aims to explore dynamic materials (**§1.4**) fabricated via DLW. Therefore, in this section, the basics of the DLW techniques are explored.

DLW relies on the use of a femtosecond pulsed laser to generate sub-micron scale 3D polymeric structures.[81-82] A simple illustration of the DLW set-up is shown in **Fig 1-9a**. The basic principle of DLW involves a high-intensity pulsed laser beam that is tightly focused forming a narrow focal point.[81, 83] At the focal point, the photon flux is sufficiently high that two low energy photons produced by the laser can simultaneously be absorbed providing sufficient energy to decompose a photoinitiator (see **§1.3.1**) and hence start a polymerisation reaction.[81, 83] Since this phenomenon is only contained to the focal point of the laser beam, the localised polymerisation reaction leads to the formation of a so-called 3D voxel (smallest volume element) (**Fig 1-9a-b**).[21, 81, 83] As the liquid, a so-called 'photoresist', is translated relative to the focus of the laser beam, the desired 3D polymer structure is realised (**Fig 1-9b**).[83]

In DLW, the polymerisation reaction usually occurs via a conventional free radical polymerisation (FRP) mechanism (**§1.3.1**) or cationic polymerisation.[21] For purposes of the current thesis, only free radical polymerisation is considered. Photoresists for DLW (**Fig 1-9a**) consist primarily of a photoinitiator and a monomer.[83] The initiation reaction during DLW proceeds via a two-photon absorption process, which implies a simultaneous absorption of two photons by the photoinitiator.[84] The energy transferred via absorption of two photons with wavelength $\lambda$ and energy E is equivalent to the energy contained in the absorption of one photon with wavelength $\lambda/2$ and energy 2E.[85] However, the probability of the simultaneous absorption of two photons exhibits a quadratic dependence to the laser beam intensity, and thus is only viable in the high intensities located at the focal point. **Fig 1-9c** presents an illustration of the difference between single and two-photon absorption. The number of molecules excited through two-photon absorption per pulse, $n^{(2)}$, can be calculated using the following expression:

$$n^{(2)} = \frac{1}{2}\sigma_{2PA,\lambda}N_g\left(\frac{I}{h\nu}\right)^2$$

eq 1-10[85-86]

where $I$ – light intensity (W cm$^{-2}$), $N_g$ - number of molecules in the ground state, $h\nu$ - photon energy, J, and, finally, $\sigma_{2PA,\lambda}$ - two-photon absorption cross-section at wavelength $\lambda$, GM ($1GM = 10^{-50}\mathrm{cm}^4\,\mathrm{s\,photon}^{-1}$). A two-

photon absorption cross-section represents the probability of the two-photon absorption event for a given molecule at a wavelength $\lambda$.[87] $\sigma_{2PA,\lambda}$ can be measured experimentally using, for example, a Z-scan technique, where transmittance through the sample is measured.[88]

**a**



**b**



**c**



**Fig 1-9 DLW. a: A direct laser writing (DLW) setup. A drop of the resist is placed on the substrate and the laser beam is then focused inside the resist forming a focal point, where polymerisation reaction forms a voxel;[83] b: the steps involved in the DLW process; c: the difference in resolution of single and two-photon absorption. SPA – single-photon absorption, TPA – two-photon absorption.[21]**

This quadratic absorption dependence in two-photon absorption reduces the area where the polymerisation threshold is reached, below which there is insufficient polymerisation to form a polymer network.[21, 81, 83-84, 89] Therefore, two-photon absorption enables 3D resolved structures.[21, 81, 83-84, 89] In addition, two-photon absorption minimises the unwanted absorption, thus widening the depth range accessible for writing.[85] The drawback of two-photon absorption, however, is the need for high laser intensity. High intensities are required because photoinitiators typically have low two-photon absorption cross-sections, which is correlated with the absorption coefficient of the photoinitiator.[90-91]
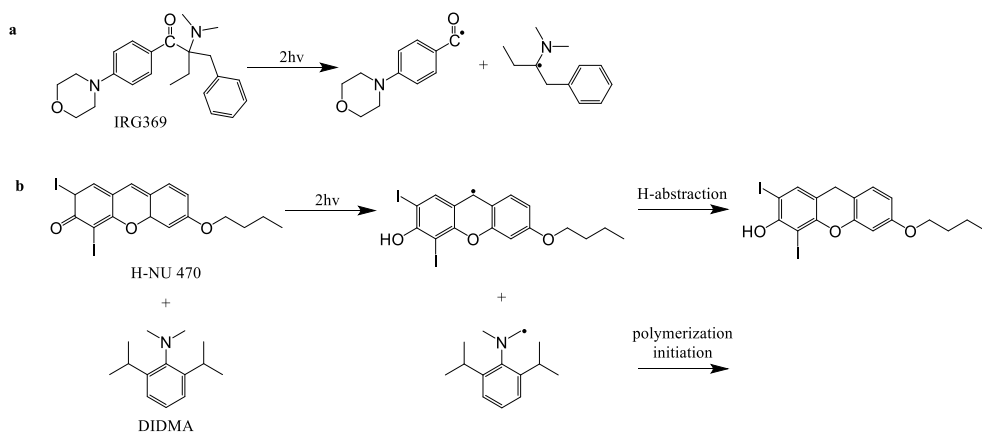
**Fig 1-10 Examples of two-photon adsorption initiators. a: Norrish I cleavage mechanism of IRG 369;[92-93] b: Norrish II initiation mechanism of H-NU 470 and DIDMA.[94]**

Photoinitiators used in two-photon absorption can be divided into two types: Norrish I and II.[21] Norrish I photoinitiator molecules dissociate directly from the excitation via α-cleavage and forms two radicals.[1, 92] An example of such an initiator, considered in this work, is Irgacure 369 (IRG369) (**Fig 1-10a**). In contrast to Norrish I initiators, Norrish type II initiators are used in tandem with a co-initiator.[95] The reaction, in this case, proceeds via hydrogen abstraction from the co-initiator (an example is illustrated in **Fig 1-10b**).[1, 92, 95]

After the generation of the initiator radicals, polymerisation is initiated by the addition of the monomer (**Fig 1-7**), here multi-functional acrylates such as pentaerythritol tetraacrylate (PETA) are often used.[83, 96] As the polymerisation proceeds, a voxel starts to form. The resulting voxel dimensions depend on the key writing parameters of the DLW process including the laser power, the exposure time,[82] the numerical aperture, molecular diffusion and the reaction kinetics.[97-99] An increase in the laser power increases the size and aspect ratio of the focal point, which in turn leads to a change in voxel sizes and dimensions.[100] This phenomenon is named focal spot duplication (**Fig 1-11a**).[100] Numerical aperture (NA), which defines how tightly the laser beam is focussed, also contributes to the dimensions of the voxel.[99] An increase in the exposure time results in an increase of the voxel size due to the molecular diffusion of the radical out of the focal point (voxel growth **Fig 1-11b**).[100] Aside from the outward molecular diffusion of the radical, oxygen diffusion into the focal point is also an important phenomenon to consider.[101] Oxygen terminates radicals in FRP thus impacting polymerisation progress during long exposure times (**Fig 1-11b**).[101] If the selected laser power is too low, no polymer network structures will be formed regardless of the exposure time.[101] Consequently, mechanical properties of the written polymer network structures, e.g. hardness, also depend on key writing parameters, such as laser

intensity and writing speed, as they will influence the reaction kinetics.[32] Therefore, obtaining a very detailed kinetic description of polymerisation in DLW is imperative for the prediction of the structure and the mechanical properties of the DLW 3D structures. The kinetics of polymerisation in DLW will be explored in **Chapter 5** of the current thesis.
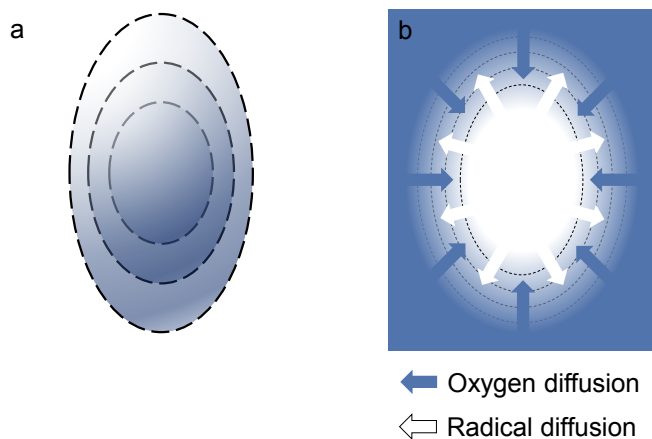


**Fig 1-11 Illustration of a: focal spot duplication and b: voxel growth and oxygen diffusion into the focal point. As adapted from Ref[100].**

## 1.4    Application in dynamic polymeric materials

The reversible photocycloaddition of anthracene has applications in dynamic polymeric materials as it provides dynamic covalent bonds. Dynamic polymeric materials, i.e. materials capable of changing their properties in response to an external trigger, have a wide range of potential applications, from self-healing materials to catalysis. Examples of dynamic polymeric materials are discussed in the following section, starting from polymer networks (**§1.4.1**) and followed by nanoparticles or, more specifically, single-chain nanoparticles (SCNP) (**§1.4.2**).

### 1.4.1 Dynamic networks

Dynamic networks are polymer networks capable of breaking and reforming their bonds upon external stimuli, which enables desirable abilities such as self-healing,[31, 102-105] shape memory,[31, 102, 104] degradability,[106-109] malleability[110] as well as mechanically adaptable properties.[13, 32] Common external stimuli for dynamic networks include changes in pH,[75, 111] temperature[104, 110, 112-113] and light.[13, 31] Specific requirements of a particular target application, e.g. stability under ambient conditions, dictate the choice of reaction, and thus the

associated trigger controlling the dynamic response of the material. For example, light-triggered dynamic materials are of critical interest when remote control is desired and temperature changes are not suitable as a trigger.[31] For biomedical applications, biocompatibility is key and mild triggers are preferable,[106] along with additional functional features, such as biodegradability.[75]

**Dissociative network**
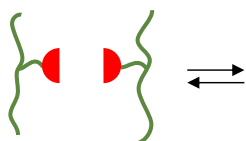
**Supramolecular network**
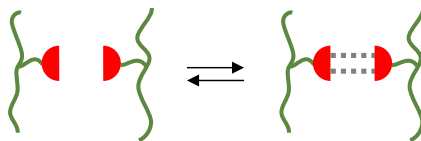
**Associative network**
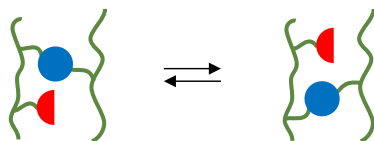
**Fig 1-12 Schematic illustrations of the three different types of dynamic polymer networks: dissociative, supramolecular and associative. [114-115]**

Dynamic polymer networks can be divided into dissociative, associative, and supramolecular polymer networks depending on the type of chemical bonds that are susceptible to the external stimulus, and whether the overall number of crosslinks in the polymer network remains constant (**Fig 1-12**).[115] First, we will discuss dissociative networks, then the supramolecular networks, and finally associative networks.

The first type of network polymers, i.e. dissociative polymer networks (**Fig 1-12**), break and reform their bonds upon an external stimulus, changing the number of crosslinks present.[115] Examples of the reactions used for dissociative polymer networks are Diels-Alder reactions,[104, 116-117] transalkylations,[113] [4+4] photocycloadditions[13, 32, 118] and [2+2] photocycloadditions.[31, 102] Dissociative polymer networks possess self-healing abilities allowing the ability to extend the lifetime of the polymeric material,[117] as well as enabling shape-memory abilities.[31] Dissociative polymer networks can widen the functionality of polymer actuators, which find applications in emerging areas such as artificial muscles.[119-120] For instance, light-induced reconfiguration of a polymer actuator was possible with the help of reversible anthracene photocycloaddition.[121] Anthracene dimers embedded into a uniaxially aligned liquid crystal polymer network (LCN) were selectively photocleaved using UV irradiation leading to decrosslinked areas of the polymer film (i.e. non-actuation domains). Through spatially resolved UV irradiation of these polymer films, from either the top or the bottom, it was possible to control the distribution of actuation and non-actuation domains, which induced bending of the film upon order-disorder

phase (**Fig 1-13**).[121] Furthermore, anthracene fluorescence could be used for crack detection in the polymer networks under stress as demonstrated in **Fig 1-14**.[10] Incorporation of anthracene moieties into micrometre scale structures *via* DLW (**§1.3.3**) permitted post-writing adjustments of the mechanical properties of the written polymer network structures, e.g. **Fig 1-15**.[13, 32] In this case, the DLW writing process opened anthracene crosslinks, which led to a softening of the material. Subsequent LED irradiation ($\lambda$ = 415 nm) induced the re-formation of anthracene crosslinks, enabling an on-demand hardening of the material through an increased number of crosslinks in the underlying polymer network. 3D polymer structures written via DLW are envisioned for use in medical research in the construction of micro-scaffolds for studying the behaviour of single cells.[15, 122-126] **Fig 1-16** illustrates one of such examples where the written DLW structures allowed to measure the force exerted by the cells using the visible deflection of the beam.[8] Design of the tailored cell niches is of critical importance as they form the cell's microenvironment, which has a strong effect on cell behaviour. A number of studies suggest that cells can be sensitive to the elasticity and stiffness of the environment they are in.[15, 122, 127-130] Light in the visible range is deemed to be a highly suitable external trigger, as light - especially low energy, long-wavelength light - has a minimal impact on cells.[18-19] Finally, due to the ability to change the number of crosslinking points, dissociative polymer networks could be capable of dissociating the entire polymer network and reforming it,[131] which is an attractive feature e.g. for recyclability of polymeric materials.

The second type of network polymers, i.e. supramolecular polymer networks (**Fig 1-12** change the number of crosslinking points upon an external stimulus), is similar to dissociative polymer networks. The only difference compared to dissociative polymer networks is that supramolecular polymer networks use non-covalent interactions, e.g. hydrogen bonding and π-π interactions.[115, 132] Incorporating supramolecular polymer networks into hydrogels have already shown promise in the fields of tissue engineering, drug delivery and 3D cell scaffolds, due to (i) their superior ability to mimic cell environments, (ii) shear-thinning and (iii) self-healing ability under mild/no external stimulus.[132-133] Shear-thinning is an especially attractive feature of supramolecular hydrogels resulting from the rapid dynamic exchange of the underlying bonds. Shear-thinning makes the hydrogel injectable, therefore, enabling injection at the target location with a needle, after which the hydrogel hardens. This approach avoids the need for more invasive methods of delivering the material (e.g. drugs, proteins or cells).[132-133] Self-integration properties of hydrogels, where two hydrogels carrying different materials form one polymer network (as illustrated in **Fig 1-17**), show promise for 3D printing composite scaffolds for the reconstruction of complex tissues.[133-134]
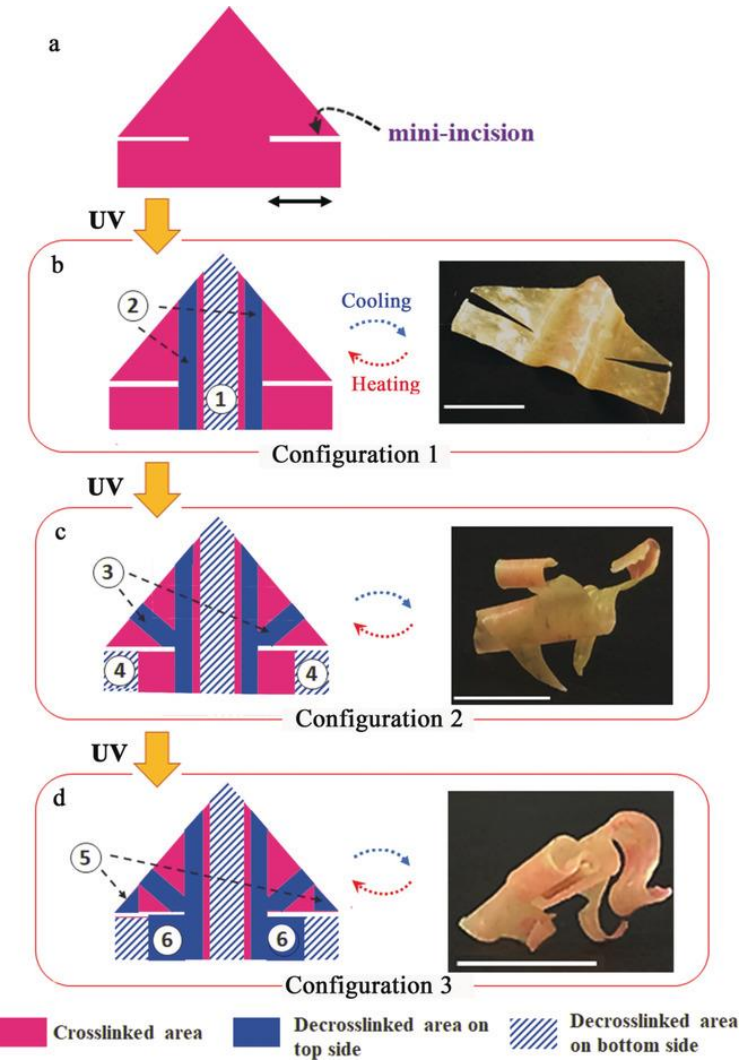
**Fig 1-13 Illustration of the reprogrammable self-folding 3D origami by sequentially making a plane (b), a bull (c) and a frog (d). Crosslinked and decrosslinked areas display different contraction/extension behaviours enabling the folding of the actuator. Reprinted with permission from Ref.[121]**
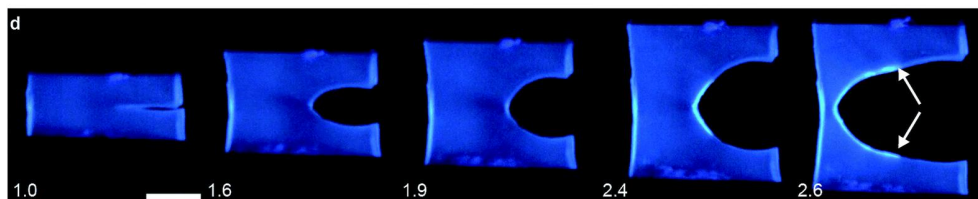
**Fig 1-14 Anthracene fluorescence was used for crack detection and partial self-healing when incorporated into multi-network elastomers. Anthracene fluorescence is visible along the edges where the applied stress resulted in cleaving anthracene dimers. Reproduced from Ref. 10 with permission from the Royal Society of Chemistry.**
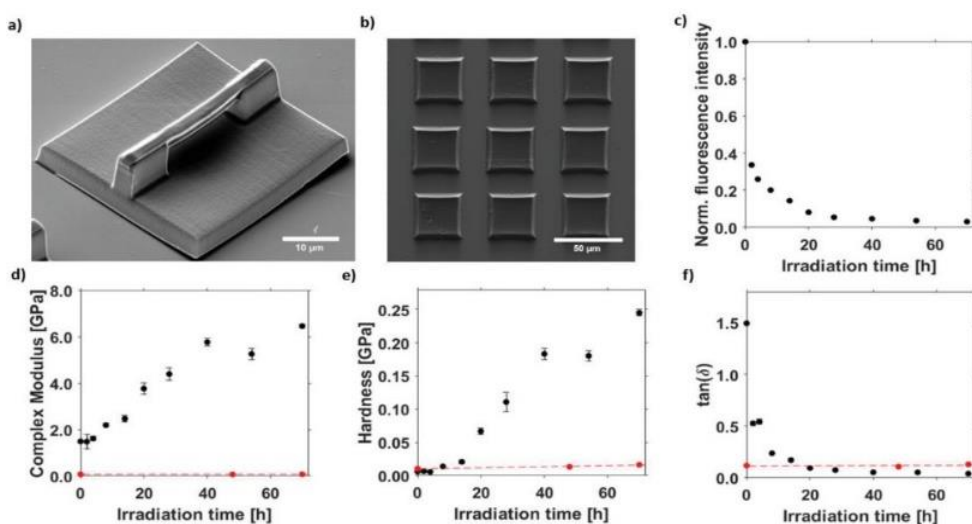


**Fig 1-15 a: DLW written structure containing 60% anthracene dimer as a bifunctional monomer and 40% pentaerythritol triacrylate (PETA) as a trifunctional monomer; b: DLW written structure made up entirely of anthracene dimer as a bifunctional monomer; c: decrease in fluorescence of the DLW structures as they are irradiated with 415 nm LED indicating anthracene dimerization reaction; d-f: change various measured mechanical properties for anthracene containing structures after irradiation with 415 nm LED (in black) and reference blank samples (in red) written with poly(ethylene glycol) diacrylate (PEG-DA). Mechanical properties were measured using nano-DMA (nanoscale Dynamic Mechanical Analysis). Reprinted with permission from Ref. 9.**
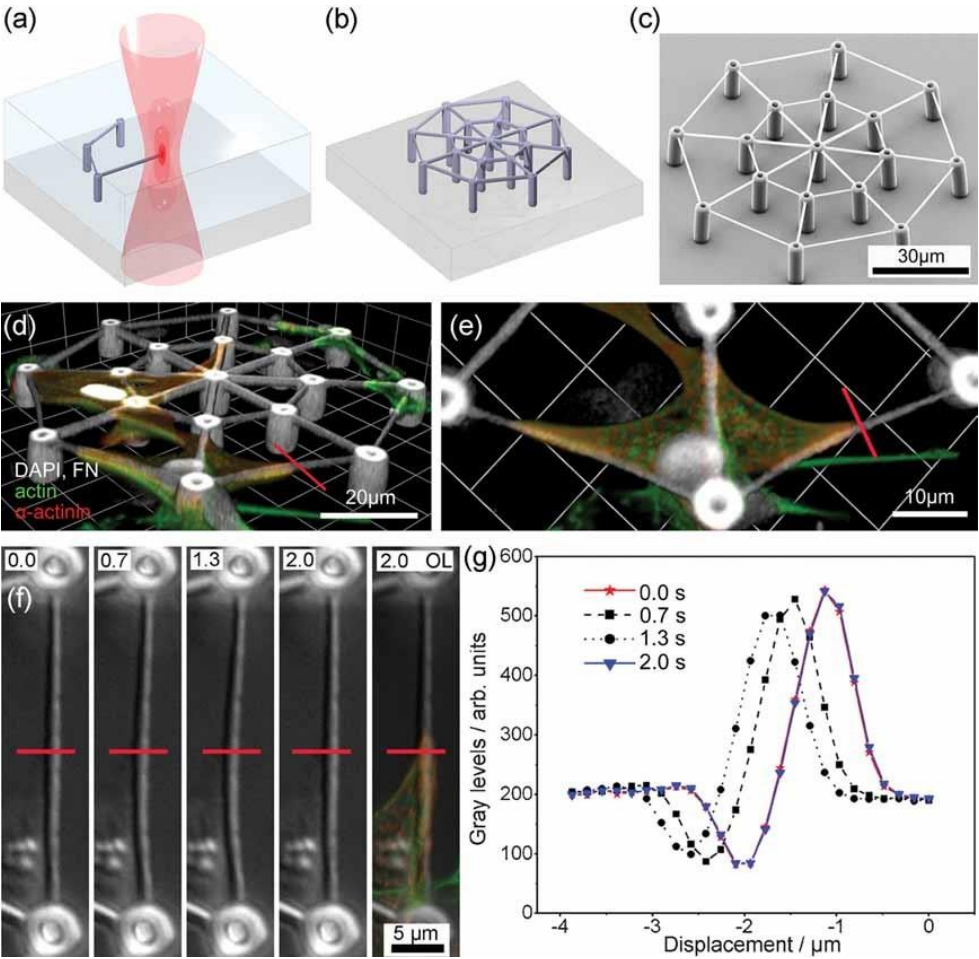
**Fig 1-16 Illustration of one of the examples where DLW was used to perform research on biological cells. a,b: DLW writing process; c: SEM image of the written structure; d,e: cells on the scaffold; f: images of the cell bending the beam; g: measurement of the bending of the beam using grey levels along the red lines in f. Reprinted with permission from Ref. 8**.
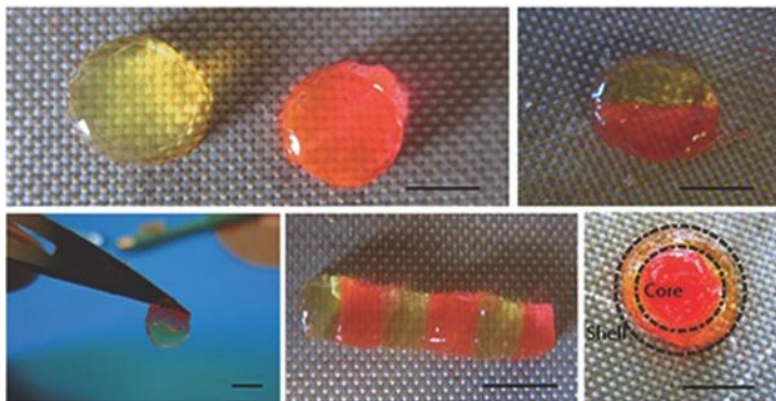
**Fig 1-17 Illustration of the self-integration properties of hydrogel based on hydrogen bonds between Ureido-pyrimidinone functionalised dextran polymers. Same hydrogel, one in the original colour and one dyed pink, integrated into one polymer network, generating different shapes. Reprinted with permission from Ref.[133]**

The third type of polymer networks, i.e. associative polymeric networks (**Fig 1-12**), break and reform their bonds upon external stimuli while maintaining the same number of crosslinks, e.g. via disulphide chemistry[107] and transesterifications.[110] A constant (yet dynamic) number of crosslinks enables the rearrangement of the topology of the polymer network and gives rise to a whole new class of polymers and vitrimers, which display self-healing and shape memory properties.[135] The addition of conducting capabilities in self-healing and recyclable vitrimers shows promise for vitrimer use in fuel cells, batteries and membranes.[113] Vitrimers became an attractive topic of research due to their potential to be reprocessed, recycled and synthesised from bio-based resources.[135-136] Associative polymeric networks have also been used in actuators.[137-138] Polyanhydride-based polymer networks are one example of associate networks that possess thermally controlled shape memory capabilities (**Fig 1-18**). In combination with their biocompatibility and degradability, polyanhydride polymer networks have shown potential in biomedical applications, such as degradable implants or controllable localised drug delivery.[139-141] They show potential as polyanhydride polymer networks can predictably degrade over time, slowly releasing the drug at the target location in the body, preventing unnecessary damage to other organs and eliminating the need for extra surgical intervention.[142] Self-healing of associate polymer networks have been demonstrated to operate at mild temperature triggers (37 °C) using sterically hindered urea bonds[105] and at ambient conditions without external stimulus by utilising diarylbibenzofuranone-based bonds.[103, 143]
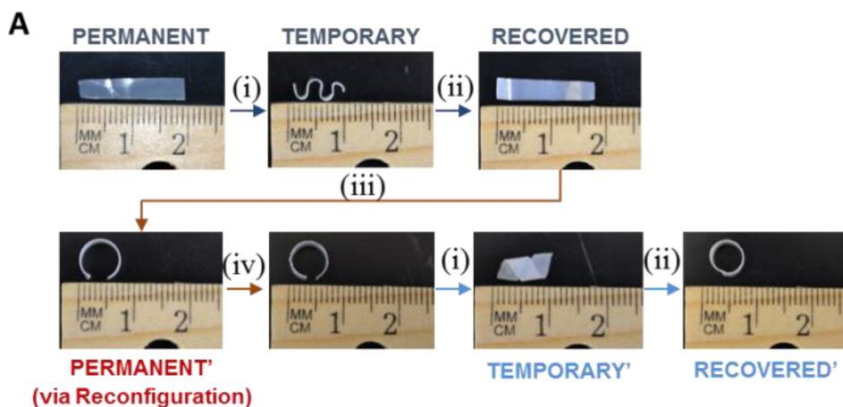
**Fig 1-18 Illustration of shape memory and reconfiguration capabilities of polyanhydride/poly(ε-caprolactone) polyurethane composite. (i) The sample can be temporarily deformed, yet subsequently (ii) the original shape can be restored. (iii-iv) the material can be reprogrammed and a new permanent shape (a ring) can be fixed, which again can be restored after temporary deformation. Adapted with permission from Ref[141]. Copyright 2021 American Chemical Society**

A combination of network types described above and triggers can offer additional advantages for dynamic polymer networks.[131] For example, the use of two photoreactive groups, which are triggered by a different wavelength of light (i.e. orthogonally), can offer additional control over the reaction.[48] Experiments using a combination of dynamic covalent and hydrogen bonds in a polymeric network showed that covalent bonds restricted creep, while the hydrogen bonds offered partial self-healing at ambient conditions.[104] Polymer networks containing a combination of disulphide bonds and hydrogen bonds display excellent self-healing properties under ambient conditions.[144] Furthermore, using an interpenetrating polymer network containing the two different bond types results in a material that displays superior mechanical properties compared to when both types of dynamic bonds are integrated into one single polymer network.[116]

Knowledge of the polymer network structure and mechanical property relationship in the polymer network is key for the successful use of dynamic materials.[139] Both the molecular structure of a polymer network and the externally controlled dynamic changes impact the final mechanical properties of the dynamic polymer network.[139, 145-147] Thus, a comprehensive model of the dynamic polymer network is required to predict mechanical properties. Therefore, one of the ultimate challenges in dynamic polymeric materials lies in the ground-up construction of an extensive theoretical framework, which connects the desired mechanical properties of the dynamic polymeric material to the conditions required (e.g. temperature, time, monomer type) to synthesise the polymer network.

The use of dynamic bonds is not limited to large scale polymeric networks, but can also be used to construct single-chain nanoparticles (SCNP). Herein, the synthesis and folding of SCNPs will be considered, because they are envisioned to be a stepping stone for the construction of an extensive model connecting the changes in the structure of the dynamic polymeric materials with the dynamic fission and formation of bonds (i.e. anthracene reversible photocycloaddition (**§1.2.3**)). Tracking the reaction progress during the intramolecular crosslinking of single polymer chains in solution is simpler than for large scale polymer networks. SCNPs are introduced in detail in the section below (**§1.4.2**).

### 1.4.2 Single-chain nanoparticles

Analogous to dynamic polymer networks, dynamic bonds can be used to form polymeric nanoparticles. These nanoparticles can be formed in two ways: intermolecular cross-linking of several chains giving rise to star-like nanogels[148-154] and polymeric micelles[75, 155-156] or intramolecular cross-linking of one chain giving rise to SCNPs (**Fig 1-19**).[35, 157-164]
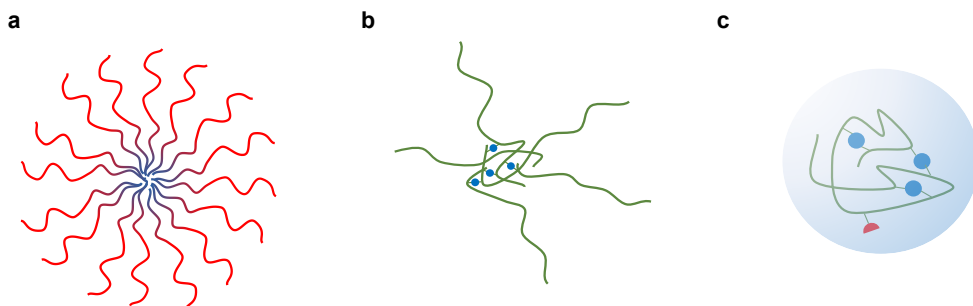
**Fig 1-19 Illustration of different polymeric nanoparticles a: polymeric micelle; b: star-like nanogel; c: SCNP.**

Star-like nanogels have an interesting architecture, which can be formed in a variety of ways, including crosslinking linear diblock copolymers at the core.[165] Using dynamic crosslinks for the core makes these star-like nanogels especially desirable as nanocarriers in drug delivery systems, as the dynamic bonds introduce a controllable degradability function.[152, 165] Polymeric micelles, formed by self-assembled block copolymers, are also of interest as sensors, as well as in drug delivery, where they respond to triggers resulting in the micelle disassembly.[75, 156, 165]

SCNPs are nanoparticles that are formed from a single polymer chain, which is capable of intramolecularly folding with the help of crosslinkers. The folding of SCNPs can be realised via a variety of reaction types

including photocycloadditions (**§1.2.2**). SCNPs are of interest due to their potential applications in a wide range of fields, for example as nanoreactors, or in catalysis.[35, 157-162, 166-170]

The ability to control the size and conformation of the folded SCNP is critical for the intended application.[35, 171-174] For example, when SCNP is used as a nanoreactor for gold nanoparticle formation, a higher amount of crosslinks in the SCNP leads to a faster rate of gold nanoparticle formation, hence altering the number of crosslinks enables control over particle formation kinetics.[35] The SCNP size can also influence the catalytic activity, for example, Perez-Baena et al. showed that smaller nanoparticles exhibited higher catalytic activity in the reduction of α-diketones.[171] The products of the reduction of α-diketones are important in the further synthesis of complex molecules.[175]

The design of the desired SCNP can be manipulated using several key synthesis and process conditions parameters: initial polymer chain length,[176-177] architecture of its crosslinkers (functionality, spacer length, etc.), environment during folding (e.g. solvent),[174, 177-178] and the number of crosslinks formed.[176-177, 179-182] The size of SCNP decreases with the decreasing polymer average molar mass.[177] SCNP contraction increases with increasing crosslinking density.[177] A simultaneous increase in (i) the polymer chain average molar mass and (ii) the amount of crosslinker leads to stronger reductions of the SNCP size (as illustrated in **Fig 1-20**).[176] When it comes to the architecture and type of the crosslinkers used, flexible, trifunctional crosslinkers produce more compact nanoparticles in comparison to bifunctional crosslinkers due to a higher amount of crosslinks that can be formed.[181] The use of longer crosslinkers and multifunctional precursors increases loop sizes in the SCNPs leading to more spherical nanoparticles.[180] Finally, solvent also has an important effect on the SCNP folding behaviour. The SCNP contraction was found to be higher in a poor solvent than in a good solvent for a similar amount of crosslinks due to a higher probability of larger loops being formed.[177] Different solvents were used to change the catalytic site distribution in SCNPs.[174] Notably, good solvents result in an even distribution of the catalytic sites, while a more selective solvent (good solvent for some parts of the molecule and poor solvent for the other parts) results in clusters of catalytic sites.[174] Additionally, for polymers containing a mix of solvophilic units and solvophobic crosslinkers, the solvent helps to avoid intermolecular reactions during folding.[183]

Modelling of the SCNP folding will be explored in more detail in **Chapter 4**. **Chapter 4** aims to establish control over the kinetics of the SCNP folding and estimating the average size of the SCNP at different stages of folding.
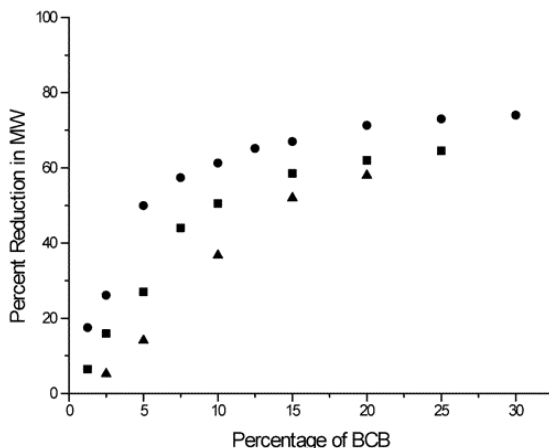
**Fig 1-20 Visualization of the influence of the average molecular weight of the polymer chains and percentage of crosslinker (benzocyclobutene (BCB)) present on those polymer chains on the contraction of the single-chain nanoparticles. Triangles stand for polymers with M_w ~44 000 g mol⁻¹, squares - ~110 000 g mol⁻¹ and circles - ~230 000 g mol⁻¹. Polymers with higher molecular weight and a higher percentage of the crosslinker present experience higher contraction. Reprinted with permission from Harth, E. et al.[176] Copyright 2021 American Chemical Society.**

## 1.5    Kinetic modelling techniques

To understand chemical reactions, and polymerisations specifically, experiments, simulations or a combination of both can be carried out to gain the most insight into the reaction. Such simulations rely on mathematical modelling of the reaction kinetics, as an example. For modelling polymerisation kinetics specifically, two classes of methods exist deterministic methods and stochastic methods. The deterministic method employs continuous-time progress and requires solving a set of differential equations.[184] The stochastic method employs a reaction probability density function.[184] Time progresses discretely in a random–walk manner in the stochastic method.[184] In reality chemical reactions happen discretely, i.e. reaction event by reaction event, therefore, the stochastic method is more representative of reality than the deterministic method. The deterministic method approximates a discrete reality, i.e. the change in the number of reactive molecules, with a continuous mathematical function, which is affordable if the number of reactive molecules is sufficiently large. Note that neither the stochastic nor the deterministic methods for prediction of kinetics explicitly describe collisions of molecules before they react, as this would require molecular dynamics (MD) simulations, which are typically not used to predict reaction kinetics. The next sections present an introduction to both methods (**§1.5.1-1.5.2**). We focus mostly on the stochastic methods as they are envisioned for use in **Chapters 4** and **5** of the current thesis to model RAFT polymerisation of SCNP (**§1.3.2**) and DLW writing of polymer networks (**§1.3.3**), respectively.

### 1.5.1    **Deterministic methods**

As mentioned above, modelling a reaction via a deterministic method involves solving a set of differential equations. In the case when the reaction involves a large number of species, such as in polymerisations, a large number of differential equations are required. These large sets of differential equations can generally not be solved analytically.[185-186] Therefore, to solve the problem of a large number of differential equations, numerical methods are often required.[186] One of the most famous numerical methods, originally developed by Bamfort et al., is the method of moments.[187] The method of moments allows to significantly simplify the set of differential equations by representing the distribution of polymer species by their statistical averages.[188-190] This speed improvement, however, comes at the cost of losing the information about the entire polymer distribution, instead only yielding information about average chain properties.[188-190] Because of this, the method of moments is not highly suitable to account for chain length dependence of reactions (and their rate coefficients), although some work has been carried out to resolve this restriction.[188]

An additional challenge for a deterministic method presents itself in a form of stiffness of the system of the differential equations, which arises due to the presence of different time scales on which various reactions proceed.[191] In the case of the polymerisation reaction, significantly more propagation events happen in a given time than termination events, even though the rate coefficient for the termination reaction is always higher than the rate coefficient for the propagation reaction.[2] The actual rate of the propagation reaction is higher than the termination reaction because the reaction rates are a product of both the rate coefficients and concentration of the reactant species. Part of the stiffness issue can also originate from (some of the) rate coefficients being dependent on the length of the chain.[186] As a compromise between reducing the number of differential equations, and eliminating stiffness, the assumption of the quasi-steady state can be used.[191, 193-194]

Apart from the method of moments, numerous other deterministic methods exist.[195-199] For example, another popular method, discretized Galerkin h-p method, is commercially implemented in the PREDICI® modelling software.[200-201] The method can provide more information on the polymer chains, e.g. average composition as a function of chain length. [200] The fixed pivot method achieves simplification of the system of the equations by grouping chains within the same chain length range together and representing the group by an average chain, called "the pivot".[201] The challenge for both methods regarding the simulation time, however, remains, because as soon as the complexity of the system is increased, the simulation time also increases.[200-201] The deterministic methods will not be discussed further as the current thesis is concerned with stochastic methods (see next section).

### 1.5.2    Stochastic methods

Stochastic modelling methods have become increasingly popular since the early 1990s and continue to gain importance as computational power increases year by year. Stochastic methods can be used for a variety of physical processes, including chemical reactions. One of the most commonly applied techniques in stochastic modelling of chemical kinetics is the so-called kinetic Monte Carlo (kMC) method which derives from Daniel Gillespie's algorithm published in 1977.[184] The original Gillespie algorithm, developed for a simple reaction, transforms reaction rates into probabilities and uses the following steps to proceed (also illustrated in **Fig 1-21**):[184]

1.  The input of initial conditions and amounts.

2.  Calculation of reaction probabilities for given conditions.

3.  Generation of two random numbers between 0 and 1.

    a.  The first is correlated to the time step in which the reaction occurs.

    b.  The second decides which reaction will occur in this step.

4.  Update all the conditions and amounts and return to step 2.

The iterations through these four basic steps continue until the end criteria are satisfied (e.g. until the algorithm reaches a certain time or conversion). A challenge associated with kMC is that the number of molecules in the simulation needs to be within an optimum range. If the number of molecules in the reaction system is too low, noisy or inaccurate results are obtained, if too high, computational costs become too high. To a certain extent, a low number of molecules in the reaction system could be compensated for by running the code several times, which, of course, increases the computational time, otherwise, an increase in the number of molecules is required.[185] To overcome this challenge, and increase the effectiveness and speed of the simulation, a variety of methods have been developed.

The first method is $\tau$-leaping, originally developed by Gillespie for general chemical reactions, which allows shortening the simulation time via the establishment of time subintervals in which the probabilities of reactions do not change considerably. Since the set of reactions is known, the calculation of each reaction step (step 3b) can be skipped within the subintervals.[202] The time subintervals need to be carefully selected because $\tau$-leaping comes at a cost of accuracy.[203] The $\tau$-leaping method was later applied to polymerisation reactions by Brandão et al.,[203] because initiation and termination probabilities do not change strongly after tens or hundreds

of propagation reaction events. Various forms of the method were developed to adapt the model according to the stiffness of the reaction system and to speed up the calculations.[191, 204]
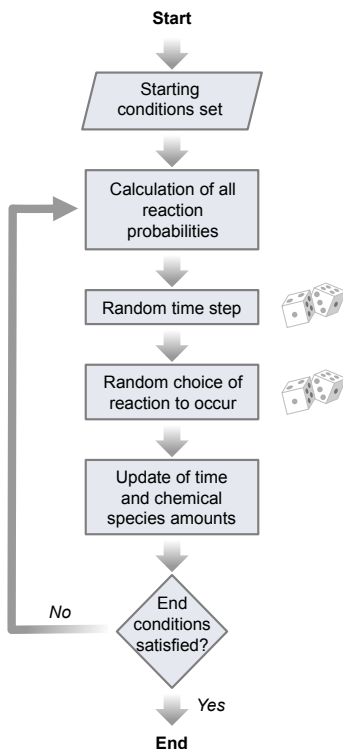


**Fig 1-21 Summary of the main kMC steps.**

Several other methods have also been introduced to improve the speed of the simulation. The first is the parallel Monte Carlo method, which involves the division of the reaction system into several smaller sections (volumes), which can be modelled separately.[205] Occasional synchronisation of the whole reaction system homogenizes (i.e. mixes) all the sections.[205] Another method is the scaling relationship method, which improves the simulation speed by reducing the reaction system size below the normal minimum number and employing scaling factors.[206] Scaling factors are applied to the radical reaction rate coefficients to compensate for the changes in the propagation-termination reaction rate proportions.[206]

Finally, in an attempt to combine the best of the two worlds, hybrid methods combine elements of deterministic and stochastic methods.[186] For example, for free radical polymerisation propagation, the steps normally occupying a large part of the kMC simulation time, i.e. propagation, could be solved via deterministic methods, while the rest, i.e. initiation and termination, could be sampled via stochastic methods.[192, 207]

**Storage methods**

The storage of information plays an incredibly important role in any stochastic simulation. The method of information storage defines the level of detail that will be available about the individual polymer chains. Information about polymers can be stored in binary trees or matrixes.

Binary trees (**Fig 1-22a**) allow for the effective storage of not only information on the polymer chains,[208] but also on the reaction probabilities.[205] In binary trees, leaf nodes contain information on, for instance, the number of chains with length i, where the number of the leaf nodes (bottom row in **Fig 1-22a**) corresponds to the number of different chain lengths.[208] The binary trees are stored in the form of arrays in the code.[208] While binary trees achieve efficient storage of information, the information stored only reflects distributional properties, e.g. chain length (and sometimes composition), without detailing monomer connectivity along the backbone. To store detailed information on the specific monomer sequences in the polymer chain, matrices are required.[209-210] Matrices can directly record the unit sequences, as illustrated in **Fig 1-22b**, and subsequently, visualize them.[209-210] Information on the position of radicals or other chemical species of interest can be effectively stored in separate arrays.[211] If the polymer chain is a copolymer (i.e. polymer chain consisting of two different monomers) a shorthand can be used, where the number of repeating units is recorded rather than a marker for the monomer.[212] Furthermore, encoding the sequence via a binary number system is also possible.[213] Matrices can store additional information on the polymer chains, for example, the total number of units, certain monomers, or even the number of the reaction events simulated.[214] The matrix-based method of information is considered in **Chapter 4** to access detailed information on the monomer sequences in single-chain nanoparticles.

The information storage methods described above are insufficient for polymer networks or branched chains due to an inability to record the information about branching. Thus, more sophisticated methods need to be used for these more complex polymer systems. For instance, one method employed for branched chains uses topology arrays to store all the information on the polymer chain topology.[216] Specifically, each column represents a polymer chain and each row position corresponds to a particular property of the polymer chain, such as size, total chain length, number of branches, the position of branches, or number of units in the polymer chain backbone.[216]
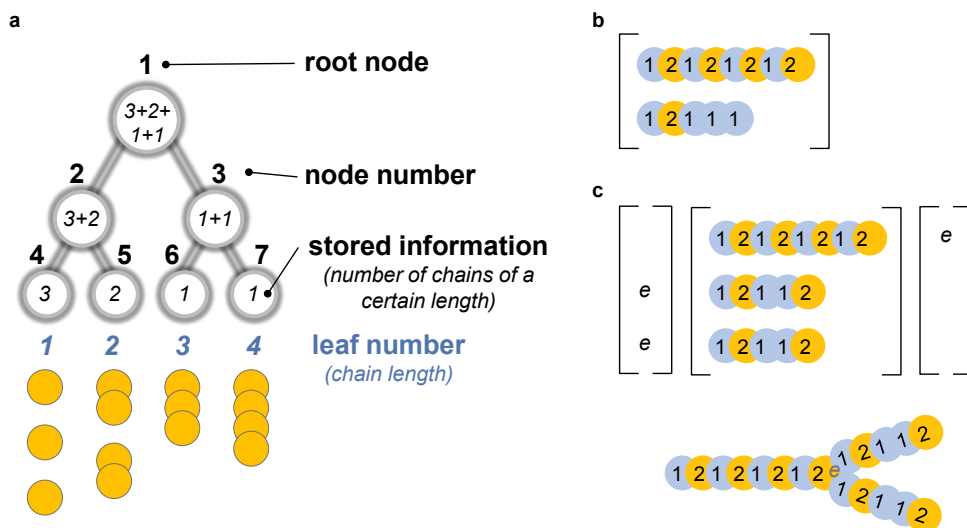
**Fig 1-22 Illustration of a: example of a binary tree illustrated for storage of chain of different length, note this illustration is an artist's impression, the tree is not limited to 4 leaf nodes; b: the matrix for storage of explicit monomer sequence for linear polymer chains; c: matrix for a polymer network.**[208-209, 215]

Another method capable of explicitly recording polymer network structure (illustrated in **Fig 1-22c**) uses a topology matrix in combination with connectivity arrays - where the topology matrix records the sequence of the monomer units, while connectivity arrays record the connection points.[215] Such an arrangement allows for an explicit recording of the polymer network structure that can be visualised at a later stage.[215] This method is envisioned for use in **Chapter 5** to record the DLW polymer network structure.

The benefit of using $k$MC is substantial, as it affords the ability to obtain in-depth insights into the molecular structure of the individually formed polymer chains/segments/molecules, as opposed to a deterministic approach.[207, 217-218] A deterministic approach requires less computational effort compared to $k$MC but does not have the benefit of the availability of the explicit molecular structures of individual chains and, as a result, is challenging to incorporate radical length-dependent diffusion coefficients.[207, 217-218]

### 1.5.3 Modelling of SCNP synthesis

The modelling of SCNP particle synthesis via $k$MC can be divided into two levels. The first level is modelling the synthesis of the polymer chains, and second is modelling the folding of the polymer chain via crosslink formation. Using the matrix-based stochastic method described in Section **§1.5.2**, the synthesis of polymer chains via RAFT polymerisation (**§1.3.2**) can be modelled. This provides access to detailed information about

the resultant polymer chains, including individual chain lengths and the exact positions of the crosslinkers along the backbone.

The knowledge of the individual chain lengths makes it possible to visualise the individual chains in 3D space via a random walk.[216] In turn, the placement of a polymer chain in a 3D space enables a straightforward calculation of the size of the polymer chain, which is critical knowledge for potential SCNP applications (**§1.4.2**). The size of the polymer chain is expressed via radius of gyration, $R_g$, which is defined as:

$$R_g^2 = \frac{1}{2(N+1)^2} \sum_{i,j=0}^{N} \left\langle \left( r_i - r_j \right)^2 \right\rangle$$

eq 1-11 [219]

where $r_{i,j}$ is the centre of mass of monomers i or j and $(N + 1)$ is the total number of monomer units.

Knowledge of the individual monomer positions gives an insight into segment length distribution, i.e. the distribution of the distances between two crosslinkers. Segment length between the crosslinker units is envisioned to be critical for the second step of the *k*MC SCNP modelling, where the folding via anthracene dimerization reaction is modelled. A method for *k*MC modelling of RAFT polymer synthesis and subsequent folding of the SCNP is proposed in **Chapter 4** of the current thesis.

### 1.5.1      Modelling of polymerisation via DLW

Very few detailed modelling studies have been undertaken regarding the network formation during DLW (**§1.3.3**). Two examples of such detailed polymerisation modelling for DLW are the studies of Pikulin et al.[220] and Uppal et al.[97] Pikulin et al. theoretically studied how molecular diffusion of the radical affects the resolution limits of the resulting 3D structures.[220] The model considered several consecutive approximations: (i) neglecting molecular diffusion, (ii) accounting for the diffusion of species consisting of only a single monomer, (iii) accounting for the diffusion of species consisting of up to two monomers, and so on, allowing for a step-by-step approach to assess diffusion effects of different radicals on the resulting material.[220] One drawback of this study is that heat transport and non-local effects, e.g. contraction, were not considered.[220] On the other hand, Uppal et al. developed a model using MATLAB®, which investigated spatial temperature variation across the focal point at the end of a dark time, as well as spatial distributions of radical, photoinitiator, monomer and inhibitor within the duration of the light pulse and dark time. This model also considered two pulse rates, which allowed for insights into the effects that pulse frequency has on the dynamics of polymerisation and the resulting voxel size.[97] These studies underline the importance of carefully considering the influence of diffusion, and light pulse configurations when modelling such reactions. Therefore, the establishment of a correlation between the DLW conditions, like laser power and writing speed, and the written networks formed as a result,

is an important challenge when it comes to modelling polymer networks formed via DLW. Modelling of the polymerisation reaction during DLW is discussed further in **Chapter 5** of the current thesis.

## 1.6 Thesis outline

Connecting and predicting the chemical structure of dynamic polymer networks with the resulting mechanical properties is a highly complex challenge. Therefore, the challenge needs to be segmented into smaller steps. The current thesis is divided into several chapters, which are organised in increasing complexity, starting from the exclusive dimerisation reaction of anthracene solution, subsequently adding the dimer cleavage reaction and, finally, modelling the reaction in a complex environment (i.e. anthracenes are attached to a polymer chain). A road map to the current thesis is presented in **Fig 1-23**.

The first step corresponds to **Chapter 2** (the first published paper; **Fig 1-23a**), where the framework model is presented for exclusive anthracene photodimerization in solution. The model is developed in such a way that the concentration of anthracene and its dimer can be readily predicted using Excel. An extensive number of details regarding the reaction is readily retrievable, e.g. integral and differential quantum yields. A simple experimental methodology for the determination of the rate coefficient ratios is established. Moreover, action plot experiments assess the wavelength-depended anthracene reactivity in the $\lambda = 375 - 430$ nm range. The work presented in this chapter was conducted collaboratively with Dr Marvin Gernhardt (QUT).

The second step corresponds to **Chapter 3** (the second published paper; **Fig 1-23b**). In **Chapter 3**, the anthracene dimer photocleavage is added to the reaction scheme in addition to the anthracene photodimerization reaction. The experimental methodology for determining the rate coefficient ratios in the region of competitive anthracene dimer photocleavage reaction and anthracene photodimerization is described. Action plots for both anthracene dimer photocleavage reaction and anthracene photodimerization reaction are measured and reported in the 260 – 330 nm range. The work in this chapter was conducted in collaboration with MSc Daniel Kodura (QUT).

The next step is **Chapter 4** (**Fig 1-23c**), where the exclusive anthracene dimerization model from **Chapter 2** is extended towards an application in the intramolecular folding of single polymer chains (into SCNPs) as an intermediate step before moving on to intramolecularly crosslinked polymer networks. The model proposes a method for the prediction of the reaction progress on average for the total population of polymers, as well as individual chains. The reaction progress of the polymer chain population on average was predicted simply using Excel, while individual chain predictions require kinetic Monte Carlo (kMC) modelling technique. The

work in this chapter was conducted collaboratively with MSc Daniel Kodura (QUT) and ir. Francisco Arraez (UGhent).

Finally, **Chapter 5** (**Fig 1-23d**) discusses and summarises how the rate coefficients may be employed in the future for modelling dynamic polymer networks obtained via DLW. Here, the network properties result from the interplay of the non-dynamic part of the network that is defined by its synthesis and the dynamic crosslinks that are controlled photochemically. Therefore, the ability to model the polymer network structure that results from DLW in detail is important to the ability of the model to predict the mechanical properties of the resulting dynamic polymer networks.
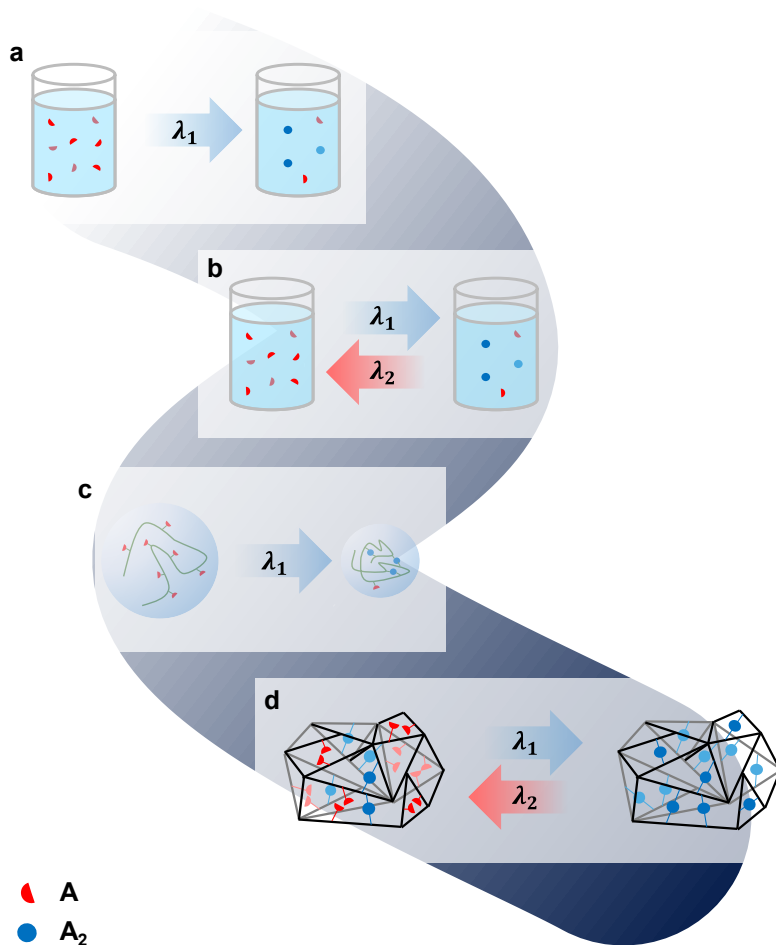
**Fig 1-23 Increasing levels of complexity in this PhD work. a: first step of kinetic understanding of exclusive photodimerization reaction in solution (Chapter 2); b: understanding of competitive dimerization and dimer cleavage in solution at any wavelength (Chapter 3); c: implementation and conformational control in single-chain nanoparticles with focus at exclusive photodimerization (Chapter 4); d: implementation of photochemical reaction in network materials at any wavelength (Chapter 5).**

# CHAPTER 2. PAPER 1. TIME-DEPENDENT DIFFERENTIAL AND INTEGRAL QUANTUM YIELDS FOR WAVELENGTH-DEPENDENT [4+4] PHOTOCYCLOADDITIONS

## 2.1   Abstract

The [4+4] photocycloaddition of anthracene is one of most relevant photoreactions and widely applied in materials science, as it allows to remote-control soft matter material properties by irradiation. However, highly energetic UV irradiation is commonly applied, which limits its application. Herein, the wavelength dependence of the photodimerization of anthracene is assessed for the first time, revealing that the reaction is actually induced just as effectively with mild visible light (410 nm). To fully establish [4+4] cycloadditions within defined chemical environments, a conceptual framework for the solution kinetics of the photo-dimerization up to long reaction times is established by developing a novel photoreaction rate law that is dependent on individual rate coefficients of the key reactions steps. These coefficients can be determined based on low conversion photochemical experiments. Both differential and integral quantum yields can subsequently be predicted that are strongly time dependent, highlighting the need of a detailed reaction pathway analysis. The presented approach simplifies a complex photochemical scenario, making the photochemical anthracene dimerization, or potentially any other photochemical dimerization, amenable to a time dependent understanding at the elementary reaction level.

## 2.2   Introduction

Following Ciamician's vision of light fueled chemical reactions,[12] the field of photochemistry has flourished over the last century and given rise to a plethora of light-based fabrication techniques. The very first light induced bond forming reaction dates back even further, with Fritzsche reporting in 1867 the [4+4] photocycloaddition of anthracene **A** (**Fig 2-1;** R=H) upon exposure to sunlight.[221] Ever since, the photochemistry of anthracene was explored in more than 25,000 scientific publications, exploiting its fluorescence,[222] charge mobility[223-224] and especially photodimerization to dimer **A₂** (**Fig 2-1**; R=H).[225]
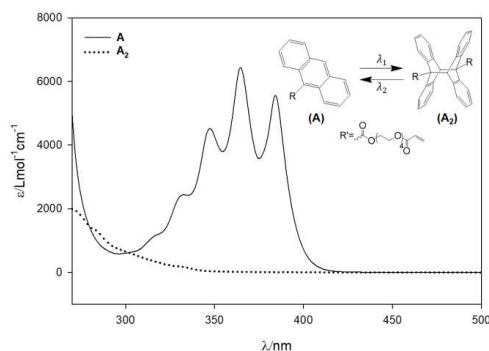
**Fig 2-1 Molar extinction coefficients of anthracene (A) and its photodimer (A₂) in CHCl₃; most basic A: R=H; A in the present work R=R'; $\lambda_1$ and $\lambda_2$ represent two wavelengths for dominance of the photocycloaddition and photocycloreversion reaction (threshold value of 300 nm).**

A particularly attractive feature of the photodimerization of **A** is its reversibility, which can be induced both thermally and photochemically. As a consequence, **A** can be readily utilized as a remote-controlled covalent binding site. Notably, it can be cleaved and reformed through combinations of light and heat or solely by using different wavelengths of light.[17] For instance, as illustrated in **Fig 2-1**, a separate wavelength ($\lambda$) window exists regarding maximal molar extinction coefficients for **A** and **A₂**, indicative of such reversibility ($\lambda_1 > 300$ nm and $\lambda_2 < 300$ nm in **Fig 2-1**[49, 60]). As a remote controlled binding site, **A** found a vast amount of applications including nanoparticles,[226] DNA ligation[227] and binding,[228] polymerisations,[229] polymer ligation,[230-231] photo patterning,[232-233] self-healing materials,[234] and single chain nanoparticles.[47, 235]

While the underlying photochemistry of the dimerization of **A** has been investigated in great detail over the last century,[49, 236] critical kinetic aspects have still been neglected. For example, only recently the activation wavelengths have become of genuine interest. Since the use of highly energetic UV light strongly limits areas of application, recent research efforts aim to shift the trigger wavelengths of photoreactions into the visible light regime.[90, 237] By using mild visible light to exert photoreactions, photodamage of the surrounding matrix and biological tissue typically caused by UV light can be avoided. To initiate [4+4] cycloadditions outside of the classically applied UV regime with mild visible light, extension of the conjugated system in order to affect the HOMO-LUMO gap has proven to be a successful strategy.[19, 47, 232] However, the required functionalization of **A** (R group in **Fig 2-1**) increases the synthetic complexity. More critically, the activation wavelengths of synthetically readily accessible anthracene derivatives are until today still unexplored, since absorbance spectra and photoreactivity are not necessarily congruent.[46, 57-59] Herein, we close this gap in the rich history of anthracene chemistry and provide the first wavelength dependent study of its photodimerization. The

resulting action plot reveals at which wavelengths and how efficiently the anthracene dimerization can be initiated.

Moreover, we focus on the complete kinetics with specifically the aim of a more fundamental understanding of the interplay of the photochemical reactions at any time *t* as a function of the initial conditions. The efficiency of photochemical reactions depends on the ease of product (in general C; here **A₂**) formation, which is commonly reflected by the quantum yield, Φ, which is a measure of how much C is formed per absorbed photon.[238] There are two types of quantum yields: (i) the differential or instantaneous quantum yield, $\Phi_{diff}$, that focuses on the variation at a given time *t* and $\lambda$, **eq 2-1** (with $I_a$ the photon absorption rate in mol s$^{-1}$ and $n_C$ the number of moles of C, both at *t*), and (ii) the integral or cumulative quantum yield $\Phi_{int}$ which reflects the overall/integrated contribution until *t*, **eq 2-2** (with $R_C = dn_C/dt$).[1]

$$\Phi_{diff}(\lambda, t) = \frac{\frac{dn_C}{dt}}{I_a} \qquad\qquad \text{eq 2-1}$$

$$\Phi_{int}(\lambda, t) = \frac{\int R_C dt}{\int I_a dt} \qquad\qquad \text{eq 2-2}$$

$R_C$ needs to be thus known at any *t* to solve **eq 2-1** and **eq 2-2**, which is less trivial for more complex reaction schemes with more reaction channels being active and more time varying concentrations. Such time dependencies are, however, often ignored and instead a low time (averaged) Φ or only the initial $\Phi_{diff}$ is considered or derived in many studies.[49, 69, 239]

In general, one needs information on the concentration of every reactant/product along the complete reaction time range. For the photon absorption step, the time dependency is often covered through the application of the Beer-Lambert's law, allowing to calculate the number of incident photons absorbed.[49, 63, 238, 240] For instance, Parnis and Oldham provided an analytical solution of the photochemical unimolecular reaction with no product absorption based on the Beer-Lambert law and showed that $\Phi_{diff}$ or $\Phi_{int}$ was not affected by the mixing of the reaction solution as a function of *t*.[240] An alternative method of treating excitation processes was suggested by Hippler, which still relies on Beer-Lambert's law, yet views the excitation process as a bimolecular process between a molecule (e.g. **A**) and a photon. The non-homogeneous nature of the photon absorption has been accounted for by providing parallels with molecular beam and cavity ring-down experiments.[239] If a photochemical reaction is bimolecular, non-linear relationships for $\Phi_{diff}$ and the concentration of reactants have been also reported. For example, $\Phi_{diff}$ for the photocycloaddition of **A** has been expressed as:[49]

$$\Phi_{diff}(\lambda, t) = \frac{k_{dimerization} c_A}{k_{life\,time} + \sum_i k_{bimolecular,i} c_A}$$ <div style="text-align: right">eq 2-3</div>

in which $c_A$ is the concentration of **A** at time *t*, $k_{lifetime}$ the rate coefficient governing the lifetime of the exited state of **A** (${}^1$**A**), $k_{dimerization}$ the rate coefficient of dimerization, and $k_{bimolecular,i}$ the rate coefficient for the $i^{th}$ bimolecular reaction considered.

Non-linear relationships become especially critical if the conditions used for the sample irradiation do not allow for the assumption of a homogeneous photon absorption, as pointed out by Saltiel.[63] He accounted for this non-uniformity by separating the reaction volume into layers with the separate calculation of $\Phi_{diff}$ and concentrations for each layer. Slight differences in overall $\Phi_{diff}$ were however only noted based on whether the layer division was used or not.[63]

The aforementioned contributions apply to continuous irradiation light sources. If pulsed lasers are used to irradiate a sample, the additional presence of dark times could affect the concentration gradients of the reacting species. We previously accounted for the presence of such dark times by developing a multilayer model that allows under conditions of competitive product absorption the estimation of $\Phi_{int}$ for two extreme cases, i.e. complete mixing between the laser pulses and a total absence of mixing, based on experimentally given (overall) conversions.[241] However, these extreme cases do not reflect the native state in solution and a more comprehensive model is therefore critically required, specifically for more complex reaction schemes.

To fully utilize the potential of **A** to act as a remote-controlled binding site in polymer network based materials applications, it is fundamental to understand precisely how the formation of crosslinks proceeds along the complete time/conversion range, as it codetermines the resulting change in material properties. Being able to predict the progress of a detailed photochemical reaction scheme for any given set of irradiation conditions is therefore paramount. Modelling the kinetics of photochemical reactions is not a straightforward task, due to their dependence on a multitude of parameters.

Thus, we develop for the solution dimerization of **A** under pulsed laser irradiation a versatile kinetic model for the complete time range at a given $\lambda$ as a starting point to readily predict the photochemical reaction progress as a function of the key reaction steps for a wide range of absorption conditions. We demonstrate that $\Phi_{diff}$ changes significantly with increasing time, so that the time evolution of $\Phi_{diff}$ and $\Phi_{int}$ are largely different, highlighting the need of detailed concentration tracking for bimolecular photochemical reactions.

## 2.3    Results and Discussion

### 2.3.1 Wavelength dependence of the photokinetics.

To generate a blueprint of the λ dependence of the [4+4] cycloaddition and to describe its photokinetics within soft matter materials, studies have to be carried out with an anthracene derivative that allows for the incorporation in view of the final application. We are focusing on an anthracene derivative, which is functionalized in the 9-position with a carboxylate ester carrying a terminal acrylate unit. A polyethylene glycol (PEG) fragment is also present in the structure (**Fig 2-1;** R=R') to widen the monomer solubility range, thus making it easier for use in various applications. Furthermore, **A** is a viscous liquid at ambient conditions and is readily incorporated into polymeric materials using a plethora of fabrication techniques, ranging from bulk polymerisation to additive manufacturing.[13, 242]

A fundamental criterion for the design of photo-controlled soft matter materials is the λ applied to trigger photoreactions within the material, with a longer trigger λ lowering the risk of unspecific photodamage to the surrounding matrix of the material and simultaneously increasing the penetration depth of radiation, allowing for a more homogeneous realization of the photoreaction within the material. To determine the most suitable λ to effect photoreactions, classically, absorption spectra are used.[243-244] However, absorption spectra exclusively represent the ground state and do not reveal the transition from which the sought-after photoreaction occurs. To quantify the λ dependent reactivity, we recently began to monitor photoreactions at different λ of monochromatic laser irradiation - yet using the same number of photons along the whole experiment.[46, 57-59] The resulting action plots reveal the conversion as a function of λ.
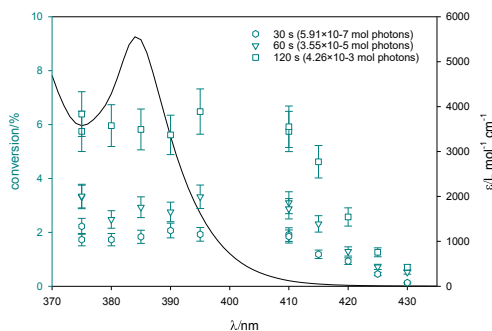


**Fig 2-2 Conversion of A (R=R') in CH₂Cl₂ after irradiation at 30, 60 and 120 s at different wavelengths (λ = 375-430 nm), along with its molar extinction coefficient. All of the samples were irradiated at a photon rate of 1.97 × 10⁻⁸ mol s⁻¹; initial concentration of at any time t (c_A0) of 0.0174 mol L⁻¹, sample volume: 250μL. Error bars here represent error propagation calculations based on the uncertainties of the equipment used. All error bars are in the acceptable range of around 13% of the value. Please refer to SI for more detailed information.**

To investigate the λ dependent photoreactivity of **A**, deoxygenated samples of **A** were irradiated for different time intervals at λ values between 375 and 430 nm with monochromatic pulsed laser irradiation in DCM. The conversions were monitored using $^1$H–nuclear magnetic resonance (NMR) spectroscopy, following the well-known shift of the proton in 10-position of the anthracene ring.[74] The obtained action plot (**Fig 2-2**) displays comparable conversions of **A** into its [4+4] photoadduct from around 2% (30 s or $5.91 \times 10^{-7}$ mol photons), to 3% (60 s or $3.55 \times 10^{-5}$ mol photons) and 6% (120 s or $4.26 \times 10^{-3}$ mol photons) between 375 nm to 410 nm. Only when exceeding 410 nm, the conversion begins to decrease for the selected time interval. However, even at 430 nm 0.7% conversion is still detectable after 120 s (or $4.26 \times 10^{-3}$ mol photons) of irradiation. These observations are critical, as the dimerization of anthracene is classically initiated with highly energetic UV light (low λ), even though violet visible light of 410 nm yields the same conversion in the investigated concentration regime. Especially taking into account the high synthetic efforts usually required to redshift the activation wavelengths of photoligations, it is of key importance that the photodimerization of **A** is indeed visible light reactive. Please refer to the **Fig A-5** of the Supporting Information for the comparison of the fractions of light absorbed at the different wavelengths.

### 2.3.2 Photoreaction rate law development.

With the λ range of photochemical reactivity being revealed, a kinetic model can be developed to describe and predict the time dependencies of the photoreaction at a given λ and any *t*. In order to derive kinetic expressions for the photodimerization of **A**, a detailed photodimerization mechanism should in principle be investigated (**Fig 2-3a**).[49, 61, 63] The mechanism involves the formation of **A$_2$** through two possible routes. The first one is based on a singlet excited state $^1$A forming an excimer with another A in the ground state, which in turn forms **A$_2$**.[49, 61, 63] Another pathway involves a triplet-triplet annihilation (TTA) route, which is prevalent in the case where triplet state sensitizers are present.[49] Radiative and nonradiative deactivations complement these reaction pathways.

To develop a practical kinetic model of the dimerization, two simplifications have been made. To make the model applicable towards catalyst free applications, no sensitizers have been added in the investigation. Additionally, all experiments were performed at concentrations > 5m mol L$^{-1}$, where concentration quenching suppresses TTA, allowing to neglect the TTA route.[49, 63, 245] A further simplification is neglecting the isolated excimer formation, simplifying the reaction scheme to 4 (lumped) reactions as shown in **Fig 2-3b**, in line with the first example from Castellan, Desvergne and Lapouyade.[49] The associated molar rate of photon absorption

at a given time *t* (derivation in Section A.1.1 of the Supporting Information) in a volume V ($\mathcal{J}_a$; mol <sub>abs. photons</sub> L$^{-1}$ s$^{-1}$,) reflecting the formation rate of $^1$A in **Scheme 1b** follows from: [246-247]

$$\mathcal{J}_a(c_A) = \frac{E_{pp}T_\lambda f}{E_\lambda N_A V}(1 - 10^{-\varepsilon c_A L})$$

eq 2-4

With $f$ the laser frequency in $\text{pulses s}^{-1}$, $N_A$ the Avogadro number ($6.02 \times 10^{23} \text{ mol}^{-1}$), $E_{pp}$ the energy per pulse of photons reaching the sample in $\text{J pulse}^{-1}$, $T_\lambda$ the glass transmittance at wavelength λ, $\varepsilon$ the molar extinction coefficient of **A** in $\text{L mol}^{-1} \text{ cm}^{-1}$ at λ, L the maximum light path length in cm, and $E_\lambda$ the energy of one photon at wavelength λ ($\text{J photon}^{-1}$). The latter variable is given by $\frac{hc}{\lambda}$ with h being Planck's constant ($6.64 \times 10^{-34} \text{J s}$) and c the speed of light being $3 \times 10^8 \text{ m s}^{-1}$. Note that "($c_A$)" is explicitly used in **eq 2-4** to highlight the dependence on $c_A$ (and thus time).
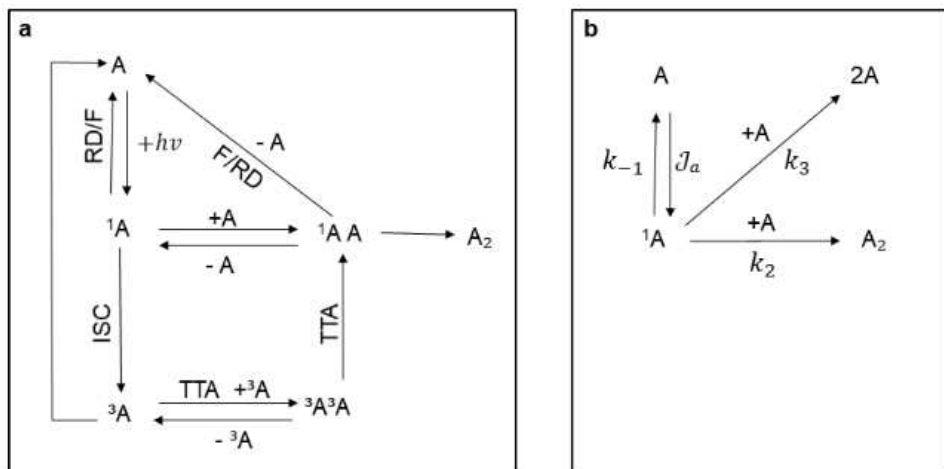


**Fig 2-3 Left: Reaction mechanism of the photodimerization of A at wavelength λ with triplet state sensitizers;[49, 61, 63] Right: simplification of left scheme as performed in the present work (no triplet state sensitizers);[49] TTA: triplet-triplet state annihilation, RD: radiationless deactivation, F: fluorescence; ISC: intersystem crossing; $^1$A represents singlet excited state for A, $^1$AA: excimer, $^3$A: triplet excited state for A, $^3$A$^3$A: triplet encounter pair, hν photon energy, J; k$_{-1}$: rate coefficient for de-excitation through various events, s$^{-1}$; k$_2$: rate coefficient for dimerization, L mol$^{-1}$ s$^{-1}$; k$_3$ rate coefficient for de-excitation through concentration quenching, L mol$^{-1}$ s$^{-1}$; J$_A$: molar rate of photon absorption, mol L$^{-1}$ s$^{-1}$ (eq 2-4).**

Assuming homogenization as well as the steady state approximation for the calculation of the concentration of the singlet excited species $^1$A,[49, 73] the general photoreaction rate law becomes (the full derivation can be found in Section A.1.2 of the Supporting Information):

$$\frac{dc_A}{dt} = -2\left[\frac{k_2\mathcal{J}_a(c_A)}{(k_2+k_3)c_A+k_{-1}}\right]c_A \qquad \text{(general rate law)}$$

eq 2-5

Depending on the relative importance of the rate coefficients and experiment set up parameters (i.e. $\lambda$, sample height, etc.) in **eq 2-5**, apparent overall reaction orders with respect to A between 0 and 2 can be obtained. In what follows limiting cases corresponding to apparent reaction orders of 0, 1, and 2 are derived.

For the (apparent) reaction order to be zero, $c_A$ needs to be in a range in which $(k_2 + k_3)c_A \gg k_{-1}$ meaning that the $k_{-1}$ term, corresponding to the monomolecular de-excitation events, becomes negligible in comparison to term for the bimolecular events $(k_2 + k_3)$. Additionally, within the $\mathcal{J}_A$ term, **eq 2-4**, $\varepsilon L c_A$ has to be sufficiently large so that small changes in $c_A$ do not lead to significant changes in the fraction of light absorbed, thus appearing to be independent of concentration.[248] Under such conditions **eq 2-5** reduces to **eq 2-6** reflecting zero-order kinetics:

$$\frac{dc_A}{dt} = -2\left[\frac{k_2\left(\frac{E_{pp}T_\lambda f}{E_\lambda N_A V}\right)}{(k_2 + k_3)}\right] \qquad \text{(0}^{\text{th}} \text{ order limit)} \qquad \text{eq 2-6}$$

The case of an apparent reaction order of one can be achieved under two circumstances. If the $\varepsilon L c_A$ term in $\mathcal{J}_A$, **eq 2-4**, is still large and thus $\mathcal{J}_A$ appears independent of $c_A$,[248] and simultaneously $(k_2 + k_3)c_A \ll k_{-1}$, making $(k_2 + k_3)c_A$ negligible **eq 2-5** reduces to:

$$\frac{dc_A}{dt} = -2\left[\frac{k_2\left(\frac{E_{pp}T_\lambda f}{E_\lambda N_A V}\right)}{k_{-1}}\right] c_A \qquad \text{(first 1}^{\text{st}} \text{ order limit )} \qquad \text{eq 2-7}$$

The second circumstance is characterized by $(k_2 + k_3)c_A \gg k_{-1}$, but $\varepsilon L$ is sufficiently small under the concentrations used allowing to approximate $\mathcal{J}_A$ being proportional to $c_A$.[248] This implies that **eq 2-5** becomes:

$$\frac{dc_A}{dt} = -2\left[\frac{k_2\left(\frac{E_{pp}T_\lambda f}{E_\lambda N_A V}\right)2.303\varepsilon L}{(k_2 + k_3)}\right] c_A \qquad \text{(second 1}^{\text{st}} \text{ order limit)} \qquad \text{eq 2-8}$$

The case of an apparent reaction order of two is possible under conditions where $\varepsilon c_A L$ is again small enough, so that $\mathcal{J}_A$ is proportional to $c_A$,[248] while $(k_2 + k_3)c_A \ll k_{-1}$ making $(k_2 + k_3)c_A$ negligible. This allows the simplification of **eq 2-5** to:

$$\frac{dc_A}{dt} = -2\left[\frac{k_2\left(\frac{E_{pp}T_\lambda f}{E_\lambda N_A V}\right)2.303\varepsilon L}{k_{-1}}\right] c_A^2 \qquad \text{(2}^{\text{nd}} \text{ order limit)} \qquad \text{eq 2-9}$$

From photoreaction rate law to time dependent concentrations.

The integration of the general rate law (**eq 2-5**) is not accompanied by a closed-form expression due to its non-linear $c_A$ dependency, complicating its application. Therefore, an approximated semi-analytical approach is being followed. By focusing on the factor inside the rectangular brackets in **eq 2-5** an apparent rate coefficient $k_{app}$ can be introduced

$$k_{app} = \frac{k_2 \mathcal{J}_a(c_A)}{(k_2+k_3)c_A + k_{-1}}$$ eq 2-10

This implies for the general rate law formulation:

$$\frac{dc_A}{dt} = -2k_{app}(c_A)c_A$$ eq 2-11

with an explicit mentioning of the $c_A$ dependence of $k_{app}$ (again notation "($c_A$)"). For *short reaction times, i.e.* for a small $c_A$ change, it can be assumed that $k_{app}$ is constant, as $c_A$ can be seen equal to $c_{A,0}$ in **eq 2-10**, so that **eq 2-11** can be integrated to **eq 2-12**

$$c_A = c_{A0}e^{-2k_{app}(c_{A0})t}$$ (small *t*) eq 2-12

Thus, **eq 2-12** can be used to determine the relation between $k_{app}$ and the initial reaction conditions ($c_{A0}$ and laser settings). In a next phase, the obtained data can be considered to assess the individual rate coefficients ($k_2$, $k_3$, and $k_{-1}$) in **eq 2-10**. Hence, short time experiments are crucial to enable the quantification of the reaction kinetics at the elementary level, i.e. to allow an explicit calculation of $k_{app}$ at any $c_A$ (and thus time) starting from the rate coefficients in **Fig 2-3b**.

For significant $c_A$ changes, i.e. long reaction times, regular updates of $k_{app}$ along the integration can be performed. In the present work, $k_{app}$ has been updated every second based on the $c_A$ of the previous integration step. As shown in **Table A2-3** in the Supporting Information, the average variation of $k_{app}$ is well below 20% justifying the mathematical shape of **eq 2-10** and the associated integration toward **eq 2-12**.

Meanwhile, the concentration of **A₂** at any time can be simply obtained as follows:

$$c_{A_2} = c_{A_20} + \frac{c_{A0}-c_A}{2}$$ eq 2-13

with $c_{A_20}$ the initial concentration of anthracene dimer.

### 2.3.3 Determination of anthracene specific rate coefficients based on short time kinetic data.

In order to determine $k_{app}$ at a wide range of conditions, several experiments were performed with limiting the conversion of **A** to maximally circa 20% to enable the use of a constant $k_{app}$ along the experiment and thus determination of $k_{app}$ using **eq 2-12** (Initial conditions considered here: 2-8 mg of **A** at start per 100-500 µL sample, complete (>99%) photon absorption). The recorded $k_{app}$ data is depicted as points in **Fig 2-4** (λ=375 nm; $1.86 \times 10^{-8}$ mol photons s⁻¹). Refer to the Section A.4.2 of the Supporting Information for the details on the experimental data on the individual fits regarding the time dependencies of $c_A$. **Fig A-9** of the Supporting Information shows similar experimental results for other wavelengths.
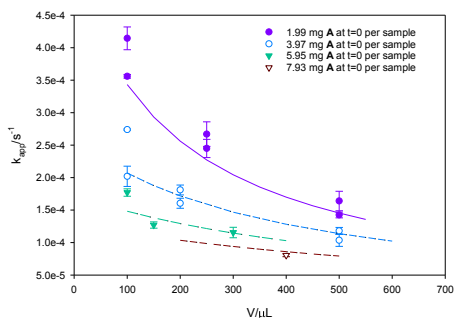
**Fig 2-4 Relevance of the initial mass amount of A and the volume of the sample (V) for the apparent rate coefficient $k_{app}$ at low times; points represent experimental data determined with the help of eq 2-12 (integrated form of general rate law (eq 2-5) up to small reaction times so that the maximal conversion is below 20% to enable the assumption of a constant $k_{app}$ for a given experiment); the lines are the result of a parameter tuning according to eq 2-14. The experimentts have been performed at 375 nm, with a 20 Hz laser and a (average) photon rate reaching the sample being $1.86 \times 10^{-8}$ mol photons s$^{-1}$. Complete photon absorption is observed during these experiments (>99%); all model parameters listed in Table A-3 of the Supporting Information. Importantly, the model also works at other laser pulse energies, as shown in Fig A-8 of the Supporting Information. Error bars represents standard error of the $k_{app}$ fit.**

Inspection of **Fig 2-4** (points) shows a clear trend with $k_{app}$ decreasing with increasing initial amount of **A** and reaction volume. It thus seems that with increasing $c_{A0}$, the relevance of the denominator in **eq 2-10** increases, therefore decreasing $k_{app}$. For each initial condition the experimentally determined $k_{app}$ at $c_{A0}$ can therefore be correlated to **eq 2-10** and thus the anthracene specific rate coefficients $k_{-1}$, $k_2$, and $k_3$ (see **Fig 2-3b**). In order to eliminate one of these three coefficients and to facilitate parameter tuning relative rate coefficients (ratios $r_1$ and $r_2$) have been first introduced. As shown in **eq 2-14**, $k_2$ and $k_3$ can be normalized with $k_{-1}$ so that:

$$k_{app}(c_{A0}) = \frac{\frac{k_2}{k_{-1}}\mathcal{J}_A(c_{A0})}{\frac{k_2+k_3}{k_{-1}}c_{A0}+1} = \frac{r_1\mathcal{J}_A(c_{A0})}{r_2 c_{A0}+1}$$ 

eq 2-14

The resulting simulated description for $k_{app}$ is also included in **Fig 2-4**, with the tuned ratios given by: $r_1 = 5.41$ L mol$^{-1}$ and $r_2 = 44.2$ L mol$^{-1}$. Considering a typical average value of $1.92 \times 10^8$ s$^{-1}$ for $k_{-1}$,[49] this implies the following individual rate coefficients, although strictly $k_{app}$ can be calculated based on $r_1$ and $r_2$ only: $k_2 = 1.04 \times 10^9$ L mol$^{-1}$ s$^{-1}$ and $k_3 = 7.46 \times 10^9$ L mol$^{-1}$s$^{-1}$. Notably, these values are of the expected order of magnitude,[49] further highlighting the relevance of the proposed method, with in particular a smaller time scale for dimerization (*ca.* $10^{-8}$ s; $1/(k_2\ c_{A0})$) compared to typical ISC time scales ($10^{-3}$-$10^{-8}$ s).[249] With the $r$ values established, it is possible to determine a critical value for $c_{A0}$ ($c_{A0,crit}$) from which bimolecular and monomolecular events switch domination and thus the overall reaction order alters. Above $c_{A0,crit}$ bimolecular events dominate (($k_2+k_3$) dominance; **eq 2-6** with $0^{th}$ order), while below, monomolecular events do ($k_{-1}$

dominance, **eq 2-7** with 1st order). As shown in **Fig A-7** of the Supporting Information $c_{A0,crit}$ is equal to 0.0226 mol L$^{-1}$ ($\lambda$ = 375 nm).

While the experiments performed to obtain the data shown in **Fig 2-4** were performed at constant laser pulse energy, two more experiments have been performed with varied energies per pulse, which are consistent with the predictions (refer to **Fig A-8** of the Supporting Information), further confirming the strength of the developed kinetic model starting from individual rate coefficients.

### 2.3.4 Application of rate law for complete time evolution of differential and integral quantum yield.

With the individual rate coefficients (or their normalizations with respect to $k_{-1}$) known, the kinetic model can be fully applied, and reactant and product concentrations and the associated quantum yields (**eq 2-1** and **eq 2-2**) can be reliably simulated. To confirm this statement three experiments have been performed in which, unlike in **Fig 2-4**, samples were irradiated until high conversion of **A** or large reaction times have been reached: one with initial conditions within the $k_{-1}$ dominance region for $\lambda$ = 375 nm ($c_{A,0}$=0.0174 mol L$^{-1}$), one with (initial) dominance of $(k_2+k_3)c_A$ for $\lambda$ = 375 nm ($c_{A,0}$ = 0.0434 mol L$^{-1}$), and one for $\lambda$ = 410 nm to verify the predictive power in absence of full photon absorption ($c_{A,0}$=0.0174 mol L$^{-1}$). The obtained experimental results for the concentration variation of **A** and **A$_2$**, and the variation of $\Phi_{int}$ are given in **Fig 2-5**.

Since in the case of complete conversion of **A**, the change in $c_A$ is significant, a small time interval of one second has been chosen for the simulations after which $k_{app}$ has been updated based on the current $c_A$ value in view of the next time step. Consecutively, the amount of **A$_2$** has been determined from **eq 2-13**. As shown in **Fig A-10** (left column) of the Supporting Information these systematic updates of $k_{app}$ are needed as significant changes (up to 100 %) are obtained in case such updates are not performed. Quantum yield predictions are similarly carried out considering $I_a$ updates, under the assumption that within one second of irradiation changes in the fraction of light absorbed can be considered negligible. **Fig A-10** (right column) of the Supporting Information shows that this update is strictly needed but the overall effect of using at any time $k_{app}(c_{A0})$ is somewhat afforded, at least to a first approximation.
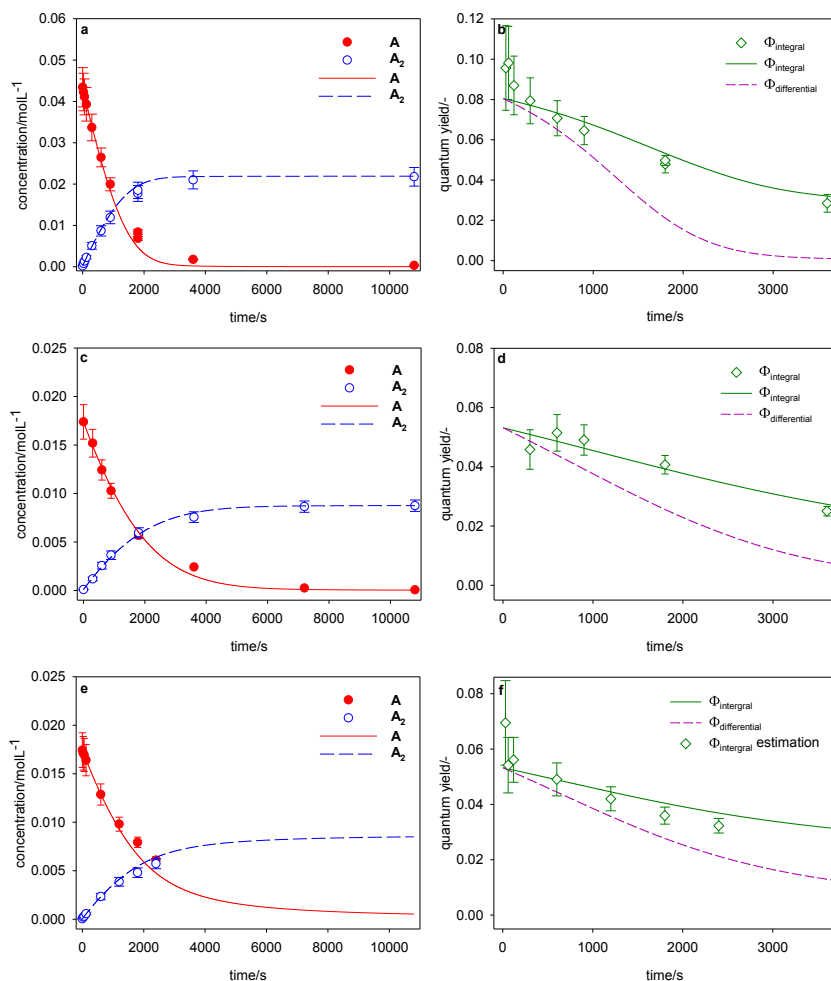
**Fig 2-5 a: Experimental and simulated anthracene A and dimer A$_2$ concentrations as a function of reaction times; b: associated differential and integral quantum yields (eq 2-1 and eq 2-2 as based on the stepwise integration of the general rate law; eq 2-5 (the update of eq 2-12 by updating k$_{app}$ based on c$_A$ of the previous time step (1s steps)) for initial A concentration of 0.0434 mol L$^{-1}$, 2 mg per sample, 401 μJ per pulse, 20 Hz, 375 nm case of initial $(k_2 + k_3)c_A$ dominance region). c-d: similar plots for initial concentration of 0.0174 mol L$^{-1}$, 2 mg per sample, 401 μJ per pulse, 20 Hz, 375 nm (initial k$_{-1}$ dominance region). e-f: similar plots (also update of J$_A$) for initial concentration of 0.0174 mol L$^{-1}$, 2 mg per sample, 355 μJ per pulse, 20 Hz, 410 nm; experimental points: symbols; lines: simulated; error bars in f are average ones based on error in b and d due to the case of incomplete absorption.**

It follows from the plots in **Fig 2-5** that the model predicts all the experimental data on concentration and $\Phi_{int}$

changes well. Therefore, the model is well suited for predictions within the investigated initial mass

concentration range (2-8 mg of **A** per 100-500 μL sample). In addition, the model allows to access $\Phi_{diff}$ at any

reaction time. It follows that this quantum yield varies strongly along the reaction, specifically for higher initial

**A** amounts (e.g. a drop larger than 80% in **Fig 2-5d**). This strong variation of $\Phi_{diff}$ is reflected in a significant lowering of $\Phi_{int}$. Thus, the approximation of photokinetics by a constant or average quantum yield as often implemented in the field is not advisable, further highlighting the relevance of the present work. In addition, as for instance illustrated in **Fig 2-5d**, larger experimental errors are obtained at very low times, highlighting the strength of a kinetic model in which such deviations can be filtered out as a continuous consistent time variation results.

## 2.4　Conclusions

The anthracene dimerization can be successfully performed in a sufficiently broad range of higher wavelengths, reaching into visible wavelength regime, orthogonally to the reverse cleavage reaction. At such wavelengths, the complete kinetics can be captured by focusing on a fundamental photoreaction rate law that is directly related to the essential reactions, considering Beer-Lambert's law and fundamental kinetic principles. Depending on the initial conditions, the overall (apparent) reaction order with respect to the anthracene concentration can vary between 0 and 2.

The corresponding rate coefficients follow from parameter tuning to low time anthracene conversion data through the introduction of an apparent rate coefficient and the stepwise updating of the latter coefficient allows to calculate the concentration variations up to complete anthracene conversion.

In addition, the differential as well as the integral quantum yield can be predicted, giving a complete picture of the progress of the reaction. Importantly, both quantum yields are strongly time dependent and, hence, the use of low time quantum yield analysis as often performed should be avoided.

The reported approach should be applicable for any photochemical dimerization reaction. Future investigations will for example treat the kinetics of the anthracene dimer cleavage, as well as a broader range of wavelengths, enabling the prediction of photochemical reaction in materials with reversible properties.

# CHAPTER 3. PAPER 2. A HOLISTIC APPROACH FOR ANTHRACENE PHOTOCHEMISTRY KINETICS

This chapter has been published as Kislyak, A.; Kodura, D.; Frisch, H.; Feist, F.; Van Steenberge, P. H. M.; Barner-Kowollik, C.; D'hooge, D. R., A holistic approach for anthracene photochemistry kinetics. *Chem. Eng. J.* **2020,** *402.*

## 3.1    Abstract

Laser-induced reversible photocycloadditions with anthracene monomer (**A**) are of key interest in generating light responsive materials. Upon dimerization (forward reaction) these species form dimers **A$_2$** that can be cleaved to regenerate the monomer A (reverse reaction). Thus, if such moieties are incorporated in a polymer network, light-shaping of the material properties becomes possible. The photocycloaddition of **A** is mostly displayed as a simple wavelength (λ) gated on/off switch with long UV light inducing bond formation and short UV light bond cleavage. However, the real situation is far more complex as the forward and reverse reactions are concomitantly initiated in the shorter λ regime and their competition is strongly influenced by the reaction conditions. Herein, we report a λ dependent kinetic study to determine the forward and reverse photochemical reactivity, which can serve as a blueprint to design large-scale polymeric network materials. We introduce fundamental photoreaction rate laws for cases of exclusive dimerization, exclusive dimer cleavage, and competitive absorption and reactions. The λ-dependent kinetic parameters are determined based on a protocol covering dedicated short timescale experiments under specific conditions, either starting with a dominant presence of A or **A$_2$**. Model validation is performed using long time scale irradiation experimental data. In particular, the λ region between 260 and 330 nm is explored to determine the optimum λ for **A$_2$** cleavage and to showcase the concentration variations of **A** and **A$_2$** at various λ, including both situations of reactant depletion and equilibrium settlement.

## 3.2    Introduction

Over the last century light has become a fundamental tool in materials science and enabled a wide variety of light-based fabrication techniques spanning from 2D photolithography [250-251] to additive manufacturing [252-254]. Light-based fabrication techniques make use of the spatiotemporal control of light induced reactions to gate when and where a reaction is active[241]. Importantly, light holds the potential to control which reaction is specifically triggered, since certain photoreactive electronic transitions are only excited by light of matching

energy. This largely untapped level of control was only recently utilized for curing of photoresists at different wavelengths[53, 255]. In addition to the direct fabrication of polymeric materials, light is widely applied during polymer post-fabrication and modification, as the reaction state of incorporated photo-active moieties readily enables a variation in macroscopic properties [13, 31, 232, 256-258].

Especially, as shown in **Fig 3-1a**, anthracene (**A**) is an attractive photoreactive group for the design of light gated materials as it is able to undergo a [4+4] photocycloaddition affording photodimer (**A₂**) that can be cleaved to **A** either photochemically [49], thermally [49] or mechanically[259]. Such an abundance in **A₂** synthetic cleavage pathways is a powerful base for the use of anthracene moieties in for instance optical storage devices [260], drug delivery [60], mechanical damage detection[259], and photovoltaic materials [261]. The photochemical route is especially attractive as it allows for remote control. While the many reported **A/A₂** based photo-chemical modifications highlight the underlying potential of photochemistry for light-controlled materials, key fundamental challenges have not been addressed yet and critically limit their further development.
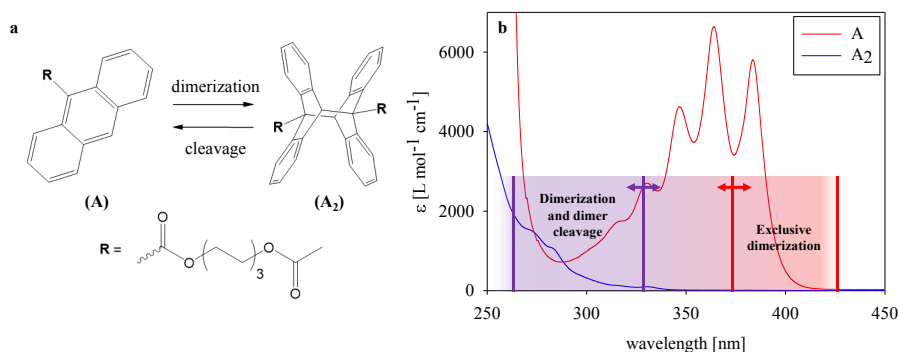


**Fig 3-1 a: Chemical structure of anthracene (A) and its photodimer (A₂); b: corresponding molar attenuation coefficients as a function of the wavelength (λ) in dichloromethane; region of exclusive dimerization (red) and competition between dimerization and dimer cleavage (purple). The double arrows represent the currently unknown exact location of the demarcation lines.**

A major challenge is, for instance, the accurate prediction of the photokinetics and thus the time dependence of the concentration variations of reactants, intermediates and products at a given wavelength. Knowledge of the kinetics is vital for the dedicated chemical control with specific and local variations in material properties. It is known that **A** photo-dimerization can proceed without interference from the presence/formation of **A₂** in λ regions of exclusive **A** absorption (λ >> 300 nm) [49]. On the other hand, **A₂** photo-cleavage mainly proceeds in *e.g.* the 250 to 290 nm region in which the formed **A** is still absorbing as can be seen in **Fig 3-1b**, and be dimerized successfully [49]. Thus, depending on the wavelength, the selectivity toward **A/A₂** formation can be significantly affected. However, it is unclear at which wavelength one actually progresses from exclusive

dimerization to a competitive situation with both photo-active dimerization of **A** and **A₂** cleavage, as illustrated by the double arrows in **Fig 3-1b**. It is additionally not fully known if at the lower wavelengths, exclusive **A₂** cleavage occurs. Limited studies have also focused on possible matrix effects, therefore the change of the photokinetics *e.g.* upon replacing the conventional reaction medium of a solvent such as dichloromethane (DCM) by a polymer-rich environment [262].

The desire for detailed knowledge on wavelength dependent photokinetics goes hand in hand with the reliable determination of the quantum yield, Φ. For irreversible reactions one can distinguish between the differential and integral quantum yield: $\Phi_{diff}$ and $\Phi_{int}$. These are respectively defined as the fraction of the photon absorption rate leading to the (desired) product formation at the selected time *t* and the cumulative fraction of absorbed photons leading to this product up to *t*. For reversible systems, $\Phi_{int}$ has no meaning and there are two instead of one $\Phi_{diff}$ contributions: one for the forward reaction and one for the reverse reaction, which in the present work are respectively denoted as $\Phi_{diff,A}$ and $\Phi_{diff,A2}$. Once in the photostationary equilibrium state, no net change in the observed concentration for **A** and **A₂** occurs as the forward and reverse overall reaction rates match ($r_{A-A2} = r_{A2-A}$ (mol s⁻¹)), which implies following balancing between $\Phi_{diff,A}$ and $\Phi_{diff,A2}$:

$$\Phi_{diff,A}\, I_A = \Phi_{diff,A2}\, I_{A2} \qquad\qquad \text{eq 3-1}$$

in which $I_A$ and $I_{A2}$ are the corresponding (overall) rates of photon absorption (mol s⁻¹).

Limited focus has been on the determination of the complete time dependence of the reaction kinetics and quantum yield of competitive photochemical reactions with **A** and/or **A₂**. In many situations, attention is preferentially placed on the changes in the material properties resulting from the photo-reversibility of the anthracene [4+4] photocycloaddition [13, 29]. In the photokinetics of the associated species, typical emphasis is either only on low reaction times, at which the **A** or **A₂** concentration can be assumed negligible (at least to a first approximation), or on deliberately very large reaction times with equilibrated conditions. The latter conditions are often investigated due to claimed difficulties associated with curve fitting from time dependent behaviour [262]. For example $\Phi_{diff,A2}$ has been determined using initial slopes from the temporal variation in fluorescence intensity or sample absorbance spectra [72, 262-263]. Alternatively, $\Phi_{diff,A2}$ has been assessed under equilibrium conditions based on **eq 3-1** assuming λ independency for $\Phi_{diff,A}$ [49, 262]. Furthermore, a determination of individual rate coefficients and rates envisaging a more fundamental quantification of $\Phi_{diff}$ values is mostly limited to the determination of the mechanism of **A₂** cleavage [70-71]. For example, Yamamoto *et al.* proposed three **A₂** cleavage pathways depending on the temperature[71]. The first pathway mainly proceeds through an **A₂** non-relaxed singlet excited state and an intermediate, possibly electronically excited tight complex (220 -

300 K), the second pathway through a singlet excited state and an excimer (120 – 190 K)[49, 70-71] and the third pathway involves a triplet state (77 – 110 K) [71]. In addition, Iannone and Scott suggested a triplet route proceeding by a two photon process [72].

It is although important to address the main reaction steps or sequences in any kinetic (modelling) study [217, 264-268], implying for the $A/A_2$ reversible system under investigation at ambient conditions in DCM at least a reaction scheme with the complexity as depicted in **Fig 3-2** (case 3). Here the red arrows describe the forward process (dimerization of **A** to $A_2$) considering a sufficient number of side reactions and the blue arrows relate to the reverse process (dimer cleavage so from $A_2$ to **A**). In this subfigure, the excitation of both species in the reaction mixture with volume *V* is explicitly considered based on photon absorption rates, which are denoted on a volumetric basis as $J_A$ and $J_{A2}$ ($J_x = I_x V^{-1}$). In agreement with literature, data intersystem crossing is not considered due to the use of experimental conditions favouring the excimer route for $A_2$ formation (low concentrations and the absence of triplet state sensitizers) and considering typical time scales [49, 63, 245, 264]. Upon ignoring the $A_2$ cleavage and dimerization of **A** in **Fig 3-2** (case 3), one obtains respectively the limiting cases as displayed in **Fig 3-2** (case 1) and **Fig 3-2** (case 2). Case 2 is thus consistent with literature data focusing at the temperature range from 220-300 K, as explained above [71]. Case 1 is consistent with our previous work on exclusive dimerization at high λ [264].

Lacking in the field is the accurate prediction of the complete reaction progress from the start ($t = 0$ s) up to the phase at which the photostationary state is reached ($t \geq t_{eq}$) or a reactant is depleted for a general set of initial conditions and fully accounting for all relevant rate coefficients, thus $k_{-1}$, $k_2$, $k_3$, $k_{-4}$, and $k_5$ in the bottom case in **Fig 3-2**. In the present work, we address this challenge by building on our previously reported kinetic modelling study on the exclusive dimerization of **A** (case 1 in **Fig 3-2**) [264], in which we highlighted the varying nature of $\Phi_{diff,A}$ and $\Phi_{int}$ during the complete irradiation. We present a holistic framework for a $A/A_2$ photoreaction as defined in **Fig 3-1** and **Fig 3-2** with the possibility that both dimerization and $A_2$ cleavage are competing for photons, allowing to obtain a clear picture of the complete timescale of the reaction progress. The forward and reverse photoreaction rate laws are derived based on individual reaction steps with the corresponding rate coefficients (or ratios of such coefficients) determined *via* an advanced experimental protocol, depending on the relative absorbance of **A** and $A_2$ at the selected wavelength. We demonstrate that the developed kinetic model can be applied under a wide range of reaction conditions including variations in the initial concentrations of **A** and $A_2$ as well as λ.

## 3.3    Experimental details

### 3.3.1 Materials

Unless stated otherwise, all chemicals and solvents were used as received from the supplier without further purification. Following chemicals and suppliers are considered: acetyl chloride (reagent grade 98%, Sigma-Aldrich), ammonium chloride (Merck), anthracene-9-carboxylic acid (99%, Sigma-Aldrich), chloroform-$d_1$ (Sigma-Aldrich), dichloromethane (DCM, Thermo Fisher Scientific, after drying and purification with SP-1 Stand Alone Solvent Purification System LC Technology Solutions Inc.), dimethylsulfoxide-$d_6$ (Sigma-Aldrich), 1,6-hexanediol (99%, Sigma-Aldrich), magnesium sulfate (anhydrous, Merck), methanol (Thermo Fisher Scientific), pyridine (anhydrous, 99.8%, Sigma-Aldrich), thionyl chloride (reagent grade 97%, Merck), and triethylamine (anhydrous ≥99%, Sigma-Aldrich).

### 3.3.2 Synthetic procedures

For the synthesis procedure to anthracene **A** in **Fig 3-1** the reader is referred to Section B.1 of the Supporting Information. Prior to each experiment, the solvent DCM was de-acidified with basic Al-oxide and degassed with several freeze pump thaw cycles. Degassed DCM was placed into a glovebox operated under nitrogen atmosphere. Both dried **A** and **A₂** (viscous liquid in appearance) were also placed into this glovebox. Stock solutions were made and placed into 0.7 mL quartz glass laser vials that were sealed. An overview of the initial conditions of all experiments is provided in **Table B 2-4** of the Supporting Information. Herein, dichloromethane (DCM) was chosen in view of the solubility of the target molecule in the solvent, as well as the solvent's UV-cut off. Furthermore, triplet sensitising solvents should be avoided as they are known to induce the triplet-triplet annihilation (TTA).

The contents of these vials were irradiated using a tuneable 20Hz Opolette laser (refer to **Fig B-9** in the Supporting information for the experimental set-up). The energy per pulse ($E_{pp}$; J pulse$^{-1}$) and the standard deviation of energy per pulse were recorded before and after irradiation (see also **Table B-5** of the Supporting Information). The same laser experimental set up was used as in our previous work[264]. The glass transmittance, $T_\lambda$, was measured at each λ following the same the procedure as reported by Menzel e*t al.*[59] The values are given in **Table B-5** of the Supporting Information.

### 3.3.3 Analysis

The experimental conversion of **A/A₂** ($x_{A/A2}$) was calculated using $^1$H-nuclear magnetic resonance (NMR) data, for which samples were dried and re-dissolved in deuterated chloroform, which was de-acidified with basic Al-

oxide prior to use. ^{1}H-NMR was measured on a Bruker 400Hz NMR available in the Central Analytical Research Facility (CARF) operated by the Institute for the Future Environments at QUT. Details on assignment of peaks are included in Section B.1 of the Supporting Information.

## 3.4 Results and discussion

In the present work, our initial focus is on the derivation of photoreaction rate laws for the three cases in **Fig 3-2**. We subsequently move to use these laws to map **A** and **A₂** variations ultimately up to large times at any set of initial conditions. An experimental protocol with two stages is introduced for this purpose, with the first stage allowing to determine the relevant kinetic parameters at small times and the second stage addressing the extension to larger times. Experiments on short times scales avoid equilibrium establishment or strong reactant depletion (e.g. 5% conversion; minute time scale), while long term experiments aim at doing so, thus implying conversions >> 5% on e.g. hour scale). Finally, we illustrate that the protocol can be successfully applied for the experimental **A/A₂** system defined in **Fig 3-1** and allows to access the temporal variations of important photokinetic relevant phenomena.
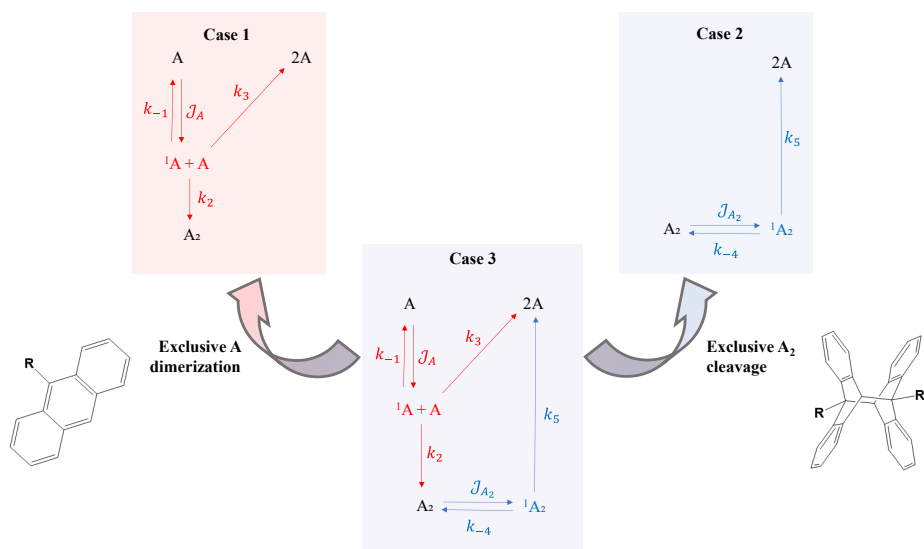


**Fig 3-2 Reaction mechanisms under ambient conditions to describe [4+4] photocycloaddition kinetics with anthracene monomer A and dimer A₂ in a solvent such as dichloromethane; Case 1: exclusive dimerization of A; [70] Case 2: exclusive cleavage of A₂; Case 3: competitive dimerization and dimer cleavage. ¹A represents anthracene in a singlet excited state and ¹A₂ anthracene dimer in a non-relaxed singlet excited state; k₋₁ and k₋₄: de-excitation rate coefficients, s⁻¹; k₂: dimerization rate coefficient, L mol⁻¹ s⁻¹; k₃: concentration quenching rate coefficient, L mol⁻¹ s⁻¹; k₅: dimer cleavage rate coefficient, s⁻¹; $\mathcal{J}_{A_2}$ and $\mathcal{J}_A$: photon volumetric absorption rate for A₂ and A species in mol L⁻¹ s⁻¹. Intersystem crossing for the forward reaction can be neglected based on previous work. [70]**

### 3.4.1 Derivation of photoreaction rate laws and their integration to simulate anthracene monomer and dimer concentration variations

**Case 1: exclusive dimerization**

The first case, *i.e.* exclusive dimerization (left top box in **Fig 3-2**), is applicable if there is no **A₂** cleavage and absorption, and has been treated extensively in our recent contribution [264]. For clarity the main derivation steps, assuming perfect mixing, are included in the Supporting Information with the general photoreaction rate law given by [264]:

$$\frac{dc_A}{dt} = -2k_{+\text{app}}(c_A)c_A \qquad\qquad \text{eq 3-2}$$

in which $c_A$ is the concentration of A and $k_{+\text{app}}$ is a (forward) apparent rate coefficient (s$^{-1}$). Note that $k_{+\text{app}}$ is also dependent on the wavelength, $\lambda$, however here we do not explicitly highlight this to simplify the notation. The term apparent is used, as after application of the quasi-steady state approximation (QSSA) for the determination of the concentration of the concentration of exited A species (A$^1$) no classical thus intrinsic rate coefficient is obtained. Instead, a combination of the molar absorption rate $\mathcal{J}_A(c_A)$ and rate coefficients defines $k_{+\text{app}}(c_A)$ with in general a complicated $c_A$ dependence:

$$k_{+\text{app}}(c_A) = \frac{\frac{k_2}{k_{-1}}\mathcal{J}_a(c_A)}{\left(\frac{k_2}{k_{-1}}+\frac{k_3}{k_{-1}}\right)c_A+1} \qquad\qquad \text{eq 3-3}$$

In **eq 3-3**, the $c_A$ dependency of $\mathcal{J}_A(c_A)$ is expressed as [246, 269]:

$$\mathcal{J}_A(c_A) = \frac{E_{\text{pp}}T\lambda f}{E_\lambda N_A V}(1 - 10^{-\varepsilon_A c_A L}) \qquad\qquad \text{eq 3-4}$$

in which $f$ is the frequency of the laser pulses (pulses s$^{-1}$), $E_\lambda$ the energy of a single photon of wavelength $\lambda$ (J photon$^{-1}$), $N_A$ the Avogadro number, $L$ the light path length (cm), and $\varepsilon_A$ the molar attenuation coefficient of **A** (L mol$^{-1}$ cm$^{-1}$).

Note that $k_{+\text{app}}(c_A)$ is related to the differential quantum yield $\Phi_{\text{diff,A}}\left(=\frac{k_2 c_A}{(k_2+k_3)c_A+k_{-1}}\right)$ so that the general photoreaction rate law can also be written as:

$$\frac{dc_A}{dt} = -2\,\Phi_{\text{diff,A}}\,\mathcal{J}_A(c_A) \qquad\qquad \text{eq 3-5}$$

It further follows from **eq 3-3** that two ratios of two rate coefficients can be kinetically relevant: $k_2/k_{-1}$ and $k_3/k_{-1}$. Here, $k_2/k_{-1}$ represents the ratio between the reactivity for the dimerization reaction and **A** de-excitation, while $k_3/k_{-1}$ stand for the ratio between the reactivity for de-excitation of $^1$A via concentration quenching versus de-excitation of $^1$A by itself. For small times, these ratios can be determined by measurements of the temporal variation of $c_A$ for various initial $c_A$ concentrations ($c_{A0}$ values) so that it can be assumed in the kinetic

description for each experiment that $k_{+app}(c_A)$ can be evaluated at $c_{A0}$ [264]. In other words, it holds per experimental condition up to sufficiently small times that **eq 3-2** can be converted into:

$$c_A = c_{A0}e^{-2k_{+app}(c_{A0})t}$$

eq 3-6

The concentration of **A₂** ($c_{A2}$) can be calculated in parallel from a mass balance over A-based species denoting $c_{A20}$ as the initial dimer concentration:

$$c_{A2} = c_{A20} + \frac{c_{A0}-c_A}{2}$$

eq 3-7

For larger times, the aforementioned assumption is not allowed and, hence, eq 3-6 must be replaced by the stepwise integration of **eq 3-2**, starting from a given $c_{A0}$ value and taking time steps $\Delta t$:

$$c_{A,t+\Delta t} = c_{At}e^{-2k_{+app}(c_{A,t})\Delta t}$$

eq 3-8

This stepwise numerical integration implies that $k_{+app}(c_A)$ needs to be updated with the previous $c_A$ after each $\Delta t$ (*e.g.* 1 s). For posteriority and to keep the overview of the discussion which is about to follow, the key kinetic equations for the exclusive dimerization case are summarized as the first entry in **Table 1**. Limiting situations for **eq 3-2** have been covered in detail in our previous contribution [264] and involve apparent reaction orders of 0, 1 and 2 with respect to **A**.

**Case 2: exclusive dimer cleavage**

The second case is the exclusive **A₂** cleavage pathway (right top box in **Fig 3-2**), which could be valid at shorter wavelengths at which **A₂** starts to absorb. For the actual experimental system under investigation this implies roughly λ < 340 nm, as deducible from **Fig 3-1b**. A closer inspection shows that in this wavelength range **A** has still a comparable molar attenuation coefficient and thus may have a significant influence on the reaction progress. Here, we therefore consider a limiting (theoretical) case in which **A** does not absorb significantly. In other words, Case 2 is thus the mirror image of Case 1.

A similar derivation of the photokinetics, assuming perfect mixing and applying the QSSA to calculate the concentration of the excited species (here $^1A_2$, see Supporting Information), can thus be followed as for Case 1. This leads to a photoreaction rate law in which the (reverse) apparent rate coefficient $k_{-app}(c_{A2})$ (mol L⁻¹ s⁻¹) can be introduced that is a function of $c_{A2}$:

$$\frac{dc_{A_2}}{dt} = -k_{-app}(c_{A2}) = \frac{-\mathcal{J}_{A_2}(c_{A2})\frac{k_5}{k_{-4}}}{1+\frac{k_5}{k_{-4}}}$$

eq 3-9

in which the $c_{A2}$ dependency of the molar absorption rate $\mathcal{J}_{A_2}(c_{A2})$ is given by (**eq 3-4** replacing $c_A$ by $c_{A2}$):

$$\mathcal{J}_{A_2}(c_{A2}) = \frac{E_{pp}T_\lambda f}{E_\lambda N_A V}(1 - 10^{-\varepsilon_{A_2}c_{A_2}L})$$

eq 3-10

Note that $k_{-app}$ is also dependent on $\lambda$, however again we simplify the notation. The photokinetics are now determined by another ratio of two rate coefficients: $k_5/k_{-4}$, which represents the competition between reaction of dimer cleavage and the excitation of the anthracene dimer. Note that it is opted here to put $k_{-4}$ in the denominator to be analogous with the former two ratios for which the denominator is $k_{-1}$, also a de-excitation rate coefficient. Analogously to Case 1, a link with the differential quantum yield here $\Phi_{\text{diff,A2}}\left(=\frac{k_5}{k_{-4}+k_5}\right)$ can be made:

$$\frac{dc_{A_2}}{dt} = -\Phi_{\text{diff,A}_2}\,\mathcal{J}_{A_2}(c_{A2}) \qquad\qquad \text{eq 3-11}$$

**eq 3-9** can be readily solved for two limiting situations, depending on the numerical value of the product of $c_{A_2}$, the $A_2$ molar attenuation coefficient $\varepsilon_{A_2}$, and $L$. This product, $\varepsilon_{A_2}c_{A_2}L$, gives rise to two apparent orders of reaction, with the first situation corresponding to a condition with $\varepsilon_{A_2}c_{A_2}L$ large enough to neglect the exponential term in **eq 3-10** so that $\mathcal{J}_{A_2}(c_{A2})$ becomes independent of $c_{A_2}$ and thus:

$$\frac{dc_{A_2}}{dt} = -\frac{k_5}{k_5+k_{-4}}\left(\frac{E_{pp}T_\lambda f}{E_\lambda N_A V}\right) \qquad (0^{\text{th}} \text{ order limit}) \qquad \text{eq 3-12}$$

The second limiting situation occurs if $\varepsilon_{A_2}c_{A_2}L$ is small so that $\mathcal{J}_{A_2}(c_{A2})$ becomes directly proportional to $c_{A_2}$ so that:

$$\frac{dc_{A_2}}{dt} = -\frac{k_5}{k_5+k_{-4}}\left(\frac{E_{pp}T_\lambda f}{E_\lambda N_A V}\right)2.303\varepsilon Lc_{A_2} \qquad (1^{\text{st}} \text{ order limit}) \qquad \text{eq 3-13}$$

Globally these limits are not guaranteed and the integration of the general rate law, **eq 3-9**, is rather cumbersome. As explained in the Supporting Information) one can derive:

$$c_{A_2} = \frac{\lg\left(1-\left(1-10^{\varepsilon_{A_2}c_{A_2 0}L}\right)10^{-\frac{k_5}{k_5+k_{-4}}t\varepsilon_{A_2}L\frac{E_{pp}T_\lambda f}{E_\lambda N_A V}}\right)}{\varepsilon_{A_2}L} \qquad \text{eq 3-14}$$

Considering again the mass balance over A-based species it follows in any case:

$$c_A = c_{A0} + 2(c_{A20} - c_{A2}) \qquad\qquad \text{eq 3-15}$$

For posteriority and to keep the overview of the discussion which is about to follow, the key equations for exclusive dimer cleavage are summarized as the second entry in **Table 1**.

**Case 3: competitive dimerization and dimer cleavage**

The last case considers a scenario with competitive photon absorption by **A** and **A$_2$** so that the detailed reaction scheme in **Fig 3-2** (bottom box) needs to be considered. To derive the associated general photoreaction rate law first the rates of photon absorption by **A** and **A$_2$** need to be generalized towards the situation of competitive

absorption. Assuming perfect mixing, the volumetric rates of photon absorption that are depending both on $c_A$ and $c_{A2}$ are given by [27]:

$$\mathcal{J}_A(c_A, c_{A2}) = \frac{E_{pp}T_\lambda f}{E_\lambda N_A V} \frac{\varepsilon_A c_A}{\varepsilon_A c_A + \varepsilon_{A_2} c_{A_2}} \left(1 - 10^{-(\varepsilon_A c_A + \varepsilon_{A_2} c_{A_2})L}\right) \qquad \text{eq 3-16}$$

$$\mathcal{J}_{A_2}(c_A, c_{A2}) = \frac{E_{pp}T_\lambda f}{E_\lambda N_A V} \frac{\varepsilon_{A_2} c_{A_2}}{\varepsilon_A c_A + \varepsilon_{A_2} c_{A_2}} \left(1 - 10^{-(\varepsilon_A c_A + \varepsilon_{A_2} c_{A_2})L}\right) \qquad \text{eq 3-17}$$

Note that these equations reduce to **eq 3-4** and **eq 3-10** if respectively $A_2$ and $A$ are not absorbing. Applying the QSSA for the calculation of the concentration of both excited intermediary species $^1A$ and $^1A_2$, the following photorate law can be derived, as explained in the Supporting Information:

$$\frac{dc_A}{dt} = \frac{-2k_2 \mathcal{J}_A(c_A, c_{A2})}{(k_2 + k_3)c_A + k_{-1}} c_A + \frac{2k_5 \mathcal{J}_{A_2}(c_A, c_{A2})}{k_5 + k_{-4}} \qquad \text{eq 3-18}$$

This photorate law can be elegantly rewritten based on the forward and a reverse apparent rate coefficients, as introduced in Case 1 and 2 but updating the calculation method of $\mathcal{J}_A$ and $\mathcal{J}_{A_2}$:

$$k_{+app}(c_A, c_{A2}) = \frac{\frac{k_2}{k_{-1}} \mathcal{J}_A(c_A, c_{A2})}{\left(\frac{k_2}{k_{-1}} + \frac{k_3}{k_{-1}}\right)c_A + 1} \qquad \text{eq 3-19}$$

$$k_{-app}(c_A, c_{A2}) = \frac{\frac{k_5}{k_{-4}} \mathcal{J}_{A_2}(c_A, c_{A2})}{1 + \frac{k_5}{k_{-4}}} \qquad \text{eq 3-20}$$

so that:

$$\frac{dc_A}{dt} = -2 \, k_{+app}(c_A, c_{A2})c_A + 2k_{-app}(c_A, c_{A2}) \qquad \text{eq 3-21}$$

Analogously to the previous two cases (Case 1 and Case 2) **eq 3-21** can be written in terms of the (updated) differential quantum yields:

$$\frac{dc_A}{dt} = -2\Phi_{diff,A} \, \mathcal{J}_A(c_A, c_{A2}) + 2\Phi_{diff,A_2} \, \mathcal{J}_{A_2}(c_A, c_{A2}) \qquad \text{eq 3-22}$$

The kinetic law for a photochemical reaction is typically expressed as a product between a differential quantum yield and the volumetric rate of photon absorption without defining apparent rate coefficients. However, herein, the focus is on solving continuity equations, thus time dependencies, for which apparent rate coefficients are convenient notations as they display the main concentration changes as for conventional chemical reactions aligning photochemical with chemical reaction kinetics. It further follows that in the most complex Case 3 three ratios of two rate coefficients come forward: $k_2/k_{-1}$, $k_3/k_{-1}$ and $k_5/k_{-4}$. A joint determination of these three ratios is complicated and it is recommended to use dedicated (initial) reaction conditions so that more simplified formulas can be used ideally close to the more basic formulas as derived for Case 1 and 2. In the present work the experimental protocol, as included in **Fig 3-3** (so-called stage 1), is proposed. Here focus is deliberately only at the small times with experiments conducted starting from the **A** or **A₂** side of the overall reaction.

Parameters are determined one-by-one to minimize parameter correlation and to facilitate the use of basic regression tools.

For small times, to a first approximation the second term of the right hand size of **eq 3-21** regarding $A_2$ cleavage can be neglected upon considering the dominant presence of **A** at the start ($c_{A20} \approx 0$ mol L$^{-1}$; $c_{A0} \neq 0$ mol L$^{-1}$). The general photoreaction law based on differential quantum yields, eq 3-21, then becomes **eq 3-2** so that with a variation of $c_{A0}$, $k_2/k_{-1}$ and $k_3/k_{-1}$ can be determined (step 1-3 in **Fig 3-3**) by using **eq 3-3** and **eq 3-6**. Ideally, the last ratio $k_5/k_{-4}$ should be determined in a similar way by starting with dominantly $A_2$ ($c_{A0} \approx 0$ mol L$^{-1}$; $c_{A20} \neq 0$ mol L$^{-1}$) so that **eq 3-21** becomes equivalent with **eq 3-9**. Fitting can thus be performed based on the related **eq 3-14** considering only small time data.

**Fig 3-3 Stage 1 of the experimental protocol proposed in the present work to study photokinetics for the system defined in Fig 3-1 considering the reaction scheme in Fig 3-2. Stage 1 is used to the determine the required kinetic parameters: three ratios of rate coefficients with always focus on small reaction times; $k_{+app}(c_A)$ is an apparent rate coefficient for dimerization of A and $k_{-app}(c_A, c_{A2})$ the apparent rate coefficient for $A_2$ cleavage; $J_A(c_A, c_{A2})$ and $J_{A2}(c_A, c_{A2})$ are volumetric photon molar absorption rates for A and $A_2$; $X_A$ and $X_{A2}$: conversions for A and $A_2$; if limited A absorption eq 23 needs to be replaced by eq 14 and there is no input needed from step 3; if there is strong A absorption then eq 23 needs be replaced by eq 24 & eq 25.**

However, if competitive **A** absorption cannot be neglected, which is likely for the actual experimental system under investigation, one should use the detailed photoreaction rate law **eq 3-21** with plugged in values for $k_2/k_{-1}$ and $k_3/k_{-1}$ as determined from step 1-3 in **Fig 3-3**. With limited **A** absorption one can evaluate both $k_{+app}(c_A, c_{A2})$ and $J_{A_2}(c_A, c_{A2})$ at the initial concentrations so that (see Supporting Information):

$$c_{A2} = c_{A20} +$$

$$+ \frac{1}{2}\left[ c_{A0} - \frac{k_{-app}(c_{A0},c_{A20}) - [k_{-app}(c_{A0},c_{A20}) - k_{+app}(c_{A0},c_{A20})\,c_{A0}]\exp[-2k_{+app}(c_{A0},c_{A20})t]}{k_{+app}(c_{A0},c_{A20})} \right]$$

eq 3-23

and the only unknown is $k_5/k_{-4}$, taking into account **eq 3-20**. Note that upon substituting $k_{-app}(c_A, c_{A2})= 0$ mol L$^{-1}$ s$^{-1}$ this equation reduces to the combination of **eq** 3-6 and **eq** 3-7, highlighting the overall consistency of the derivation. This first alternative solution for the determination of $k_5/k_{-4}$ is highlighted by steps 4-6 in **Fig 3-3** with input from step 3 in **Fig 3-3**. We can thus deduce that one first needs to study dimerization and then **A$_2$** cleavage, which is a new insight in the field with an intuitive desire to directly go to **A$_2$** cleavage as it is characterized by a simpler reaction scheme (*cf.* **Fig 3-2**).

Note that with stronger **A** absorption - even at these small times - a stepwise integration is needed defining a second alternative solution for the tuning of the last ratio $k_5/k_{-4}$. Per $\Delta t$ the two $k_{app}(c_A, c_{A2})$ terms on the right hand side of **eq 3-21** are then considered constant so that:

$$c_{A,t+\Delta t} =$$

$$= \frac{k_{-app}(c_{A,t},c_{A2,t}) - [k_{-app}(c_{A,t},c_{A2,t}) - k_{+app}(c_{A,t},c_{A2,t})\,c_{A,t}]\exp[-2k_{+app}(c_{A,t},c_{A2,t})\Delta t]}{k_{+app}(c_{A,t},c_{A2,t})}$$

eq 3-24

$$c_{A2,t+\Delta t} = c_{A20} + \frac{c_{A0}-c_{A,t+\Delta t}}{2}$$

eq 3-25

**eq 3-24** and **eq 3-25** can be also used to predict the reaction kinetics up to large times with $k_{+app}(c_A, c_{A2})$ and $k_{-app}(c_A, c_{A2})$ further updated at every $\Delta t$ until the final time is reached using the previous values for $c_A$ and $c_{A2}$ (**Fig 3-4**; so-called stage 2). Initialization is performed based on the specific initial concentrations. It is although recommended to first perform a model validation for a reference set of initial conditions (stage 2a in **Fig 3-4**). Furthermore, upon substituting $k_{-app}(c_A, c_{A2}) = 0$ mol L$^{-1}$ s$^{-1}$ **eq 3-24** reduces to **eq** 3-8, reconfirming the overall consistency of the derivation. Again for posteriority and to keep the overview of the discussion which is about to follow, the key equations for Case 3 are summarized as the third entry in **Table 3-1**.

**Table 3-1: Overview of key equations as put forward in the present work to describe the photokinetics according to Fig 3-2 for the complete reaction time (t) range so up to large t values; also given are restrictions; the kinetic parameters (k₂/k₋₁, k₃/k₋₁ and k₅/k₄) should be obtained by following the experimental protocol displayed in Fig 3-3; for entry 1 and 3 a stepwise integration is needed (time step Δt).**

| Overall reaction scheme | Photoreaction rate law for A or A₂ | $c_A$ and $c_{A2}$ variation as a function of $t$ | Restrictions |
|---|---|---|---|
| 2A → A (Case 1)[264] | $\dfrac{dc_A}{dt} = -2k_{+app}(c_A)c_A$ | $c_{A,t+\Delta t} = c_{A,t}e^{-2k_{+app}(c_{A,t})t}$ $$c_{A2,t} = c_{A20} + \frac{c_{A0}-c_{A,t}}{2}$$ | insignificant A₂ absorption $c_{A0} \neq 0$ mol L⁻¹ |
| A₂ → 2A (Case 2) | $\dfrac{dc_{A2}}{dt} = -k_{-app}(c_{A2})$ | $$c_{A2} = \frac{\lg\left(1 - (1-10^{\varepsilon_{A2}c_{A2,0}L})10^{-\frac{k_5}{k_5+k_{-4}}t\varepsilon_{A2}\frac{E_{pp}T_\lambda f}{E_\lambda N_A V}}\right)}{\varepsilon_{A2}L}$$ $$c_A = c_{A,0} + 2(c_{A2,0} - c_{A2})$$ | insignificant A absorption $c_{A2,0} \neq 0$ mol L⁻¹ |
| 2A ⇄ A₂ (Case 3) | $\dfrac{dc_A}{dt} = -2k_{+app}(c_A, c_{A2})c_A$ $+ 2k_{-app}(c_A, c_{A2})$ | $$c_{A,t+\Delta t} = \frac{k_{-app}(c_{A,t},c_{A2,t}) - [k_{-app}(c_{A,t},c_{A2,t}) - k_{+app}(c_{A,t},c_{A2,t})c_{A,t}]\exp[-2k_{+app}(c_{A,t},c_{A2,t})\Delta t]}{k_{+app}(c_{A,t},c_{A2,t})}$$ $$c_{A2,t} = c_{A2,0} + \frac{c_{A0}-c_{A,t}}{2}$$ | $c_{A,0} \neq 0$ mol L⁻¹ᵃ |

***Definition of apparent rate coefficients[b] and related volumetric photoabsorption rates***

$$k_{+app}(c_A, c_{A2}) = \frac{\frac{k_2}{k_{-1}}J_a(c_A, c_{A2})}{\left(\frac{k_2}{k_{-1}}+\frac{k_3}{k_{-1}}\right)c_A+1} \quad \text{with} \quad J_A(c_A, c_{A2}) = \frac{E_{pp}T_\lambda f}{E_\lambda N_A V}\frac{\varepsilon_A c_A}{\varepsilon_A c_A + \varepsilon_{A2}c_{A2}}\left(1 - 10^{-(\varepsilon_A c_A + \varepsilon_{A2}c_{A2})L}\right)$$

$$k_{-app}(c_A, c_{A2}) = \frac{k_5 J_{A2}(c_A, c_{A2})}{k_5+k_{-4}} \quad \text{with} \quad J_{A2}(c_A, c_{A2}) = \frac{E_{pp}T_\lambda f}{E_\lambda N_A V}\frac{\varepsilon_{A2}c_{A2}}{\varepsilon_A c_A + \varepsilon_{A2}c_{A2}}\left(1 - 10^{-(\varepsilon_A c_A + \varepsilon_{A2}c_{A2})L}\right)$$

ᵃ if not: use default value of 10⁻¹⁰ mol L⁻¹; ᵇ written down for Case 3; for the other cases these equations can be simplified considering the related volumetric absorption rates as given by **eq 3-4** and **eq 3-10**; general case (Case 3) can be simplified to Case 2 or Case 1 depending on the conditions to fulfilled as stated in the restrictions column.
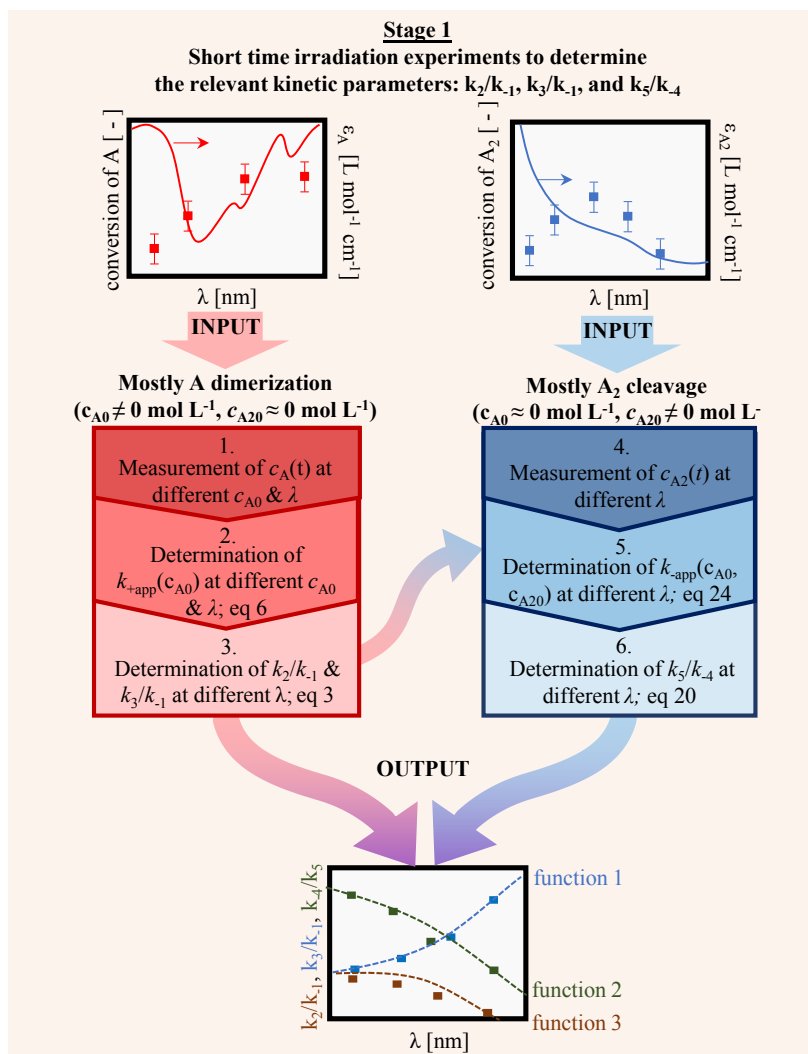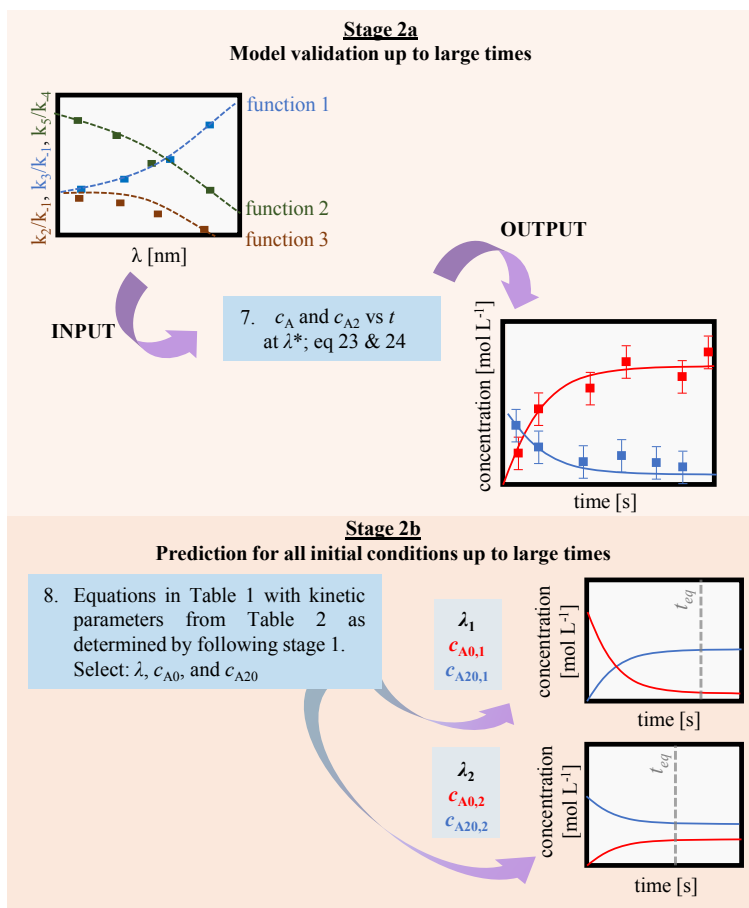
**Fig 3-4 Stage 2 of the experimental protocol proposed in the present work to study photokinetics for the system defined in Fig 3-1 considering the reaction scheme in Fig 3-2 (stage 1 in Fig 3-3 gives the wavelength dependent input functions). Stage 2 aims at the prediction of the concentration variations up to large reaction times for any reaction condition thus for a selected wavelength and set of initial concentrations; stage 2a includes (extra) model validation for a given wavelength $\lambda^*$; $k_{+app}$ is an apparent rate coefficient for dimerization of A and $k_{-app}$ the apparent rate coefficient for $A_2$ cleavage; $J_A(c_A, c_{A2})$ and $J_{A2}(c_A, c_{A2})$ are photon molar absorption rates for A and $A_2$; $X_A$ and $X_{A2}$: conversions for A and $A_2$; $t_{eq}$: time at which equilibrium is reached.**

Finally, it should be noted that in Case 3 at sufficiently large times an equilibrium is possible so that **eq 3-22**

reduces to **eq 3-1** in agreement with the state of the art in the physics field [49] but also highlighting the internal

thermodynamic consistency of this work. For completeness it is mentioned here that **eq 3-1** can be rewritten

as an implicit function of the equilibrium concentration $c_{A,eq}$ (see Supporting Information):

$$\frac{\frac{k_2}{k_{-1}}c_{A,\,eq}}{\frac{(k_2+k_3)}{k_{-1}}c_{A,\,eq}+1}\,g_A = \frac{1}{1+\frac{k_{-4}}{k_5}}\,g_{A_2} \qquad\qquad \text{eq 3-26}$$

in which $g_A$ and $g_{A_2}$ are auxiliary functions defined as:

$$g_A = \frac{\varepsilon_A c_{A,\,eq}}{\varepsilon_A c_{A,\,eq} + 0.5\varepsilon_{A_2}(c_{tot,A} - c_{A,\,eq})} \qquad \text{eq 3-27}$$

$$g_{A_2} = \frac{\varepsilon_{A_2}(c_{tot,A} - c_{A,\,eq})}{\varepsilon_A c_{A,\,eq} + 0.5\varepsilon_{A_2}(c_{tot,A} - c_{A,\,eq})} \qquad \text{eq 3-28}$$

in which in turn $c_{tot,A}$ is the total concentration of A-based moieties:

$$c_{tot,A} = c_{A,0} + 2c_{A_2,0} \qquad \text{eq 3-29}$$

Hence, if the three ratios $k_2/k_{-1}$, $k_3/k_{-1}$ and $k_5/k_{-4}$ are known according to **Fig 3-3** then **eq 3-26 - eq 3-29** can be

solved (*e.g.* in MS-Excel) with respect to $c_{A,\,eq}$. Alternatively the kinetic model

can be run until the variation in $c_A$ is negligible. The equilibrium dimer concentration $c_{A2,eq}$ can be determined

in any case from the mass balance evaluated at equilibrium:

$$c_{A2,eq} = c_{A20} + \frac{c_{A0} - c_{A,eq}}{2} \qquad \text{eq 3-30}$$

## 3.4.2 Application of stage 1 of protocol: evaluation of λ dependence for $k_2/k_{-1}$, $k_3/k_{-1}$ and $k_5/k_{-4}$

**Dimerization experiments**

We now shift to the actual application of the experimental protocol for the **A/A₂** system as defined in **Fig 3-1a**.

As indicated in **Fig 3-3** (stage 1; top input boxes) action plots need to be provided as input. In line with the

protocol preference is given to first focus on small time experiments with a negligible initial amount of **A₂** ($c_{A20}$

≈ 0 mol $L^{-1}$; $c_{A0} \neq 0$ mol $L^{-1}$; left top box). **Fig 3-5a** displays the corresponding action plot in which **A** has been

irradiated in the range from 260 to 330 nm (and even up to 375 nm), selecting a reference initial **A**

concentration: $c_{A0}$=0.0174 mol $L^{-1}$. For this action plot, at each λ, **A** has been irradiated with the same number

of photons [46, 57-59] considering three time intervals: 30 s (receiving around 5.62 × $10^{-7}$ mol photons), 60 s

(receiving 1.11 × $10^{-6}$ mol photons) and 120 s (receiving 2.23 × $10^{-6}$ mol photons). The **A** conversion ($x_A$) has

been tracked through the shift in $^1$H-NMR spectra[264] and remains below 5 mol%. The negligible impact of **A₂**

is defendable at $c_{A0}$=0.0174 mol $L^{-1}$ as the fraction of light absorbed by **A₂** species at the end of each

experiment remains below 2.5% (**Fig B-11** in the Supporting Information). In other words, the region from 260

to 330 nm features negligible **A₂** cleavage under reference conditions and small times. Furthermore, previous

work already highlighted that the region around 375 nm features no cleavage at all, due to a lack of **A₂**

absorption[264].
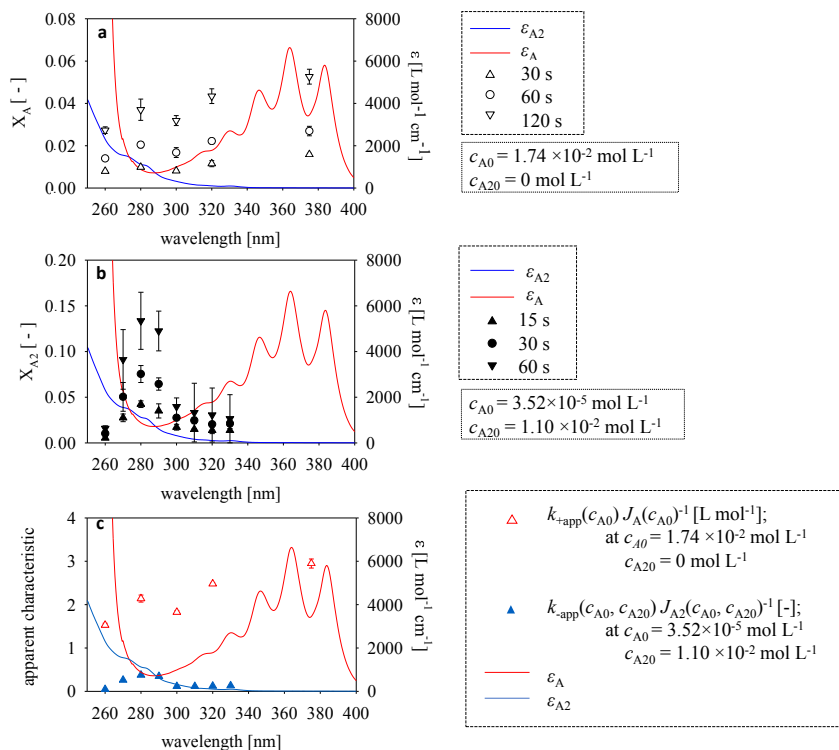
**Fig 3-5 Application of stage 1 of protocol in Fig 3-3 for the experimental system defined in Fig 3-1: action plots and attenuation coefficients for dimerization of A and cleavage of $A_2$ followed by the evaluation of the wavelength dependence of the forward ($k_{+app}(c_{A0})$; $s^{-1}$) and reverse apparent rate coefficient ($k_{-app}(c_{A0}, c_{A20})$; mol $L^{-1}$ $s^{-1}$) as introduced in Table 1; a: A dimerization action plot at 0.0174 mol $L^{-1}$ in dichloromethane (DCM) with negligible amount of $A_2$. A is irradiated at $1.86 \times 10^{-8}$ mol photons $s^{-1}$ for 30, 60 and 120 s. b: $A_2$ cleavage action plot at 0.0110 mol $L^{-1}$ in DCM with a very low A amount ($3.52 \times 10^{-5}$ mol $L^{-1}$). $A_2$ is irradiated at $1.85 \times 10^{-8}$ mol γ $s^{-1}$ for 15, 30 and 60 s; c: For the same initial conditions in a and b, the determined $k_{+app}(c_{A0})$ and $k_{-app}(c_{A0}, c_{A20})$ at low times as plotted after division through the corresponding volumetric absorption rates (J values; L $mol^{-1}$ $s^{-1}$), hence in this subplot focus is on the plotting of the apparent characteristics $k_{+app}(c_{A0}) J_A(c_{A0})^{-1}$ and $k_{-app}(c_{A0}, c_{A20}) J_{A2}(c_{A0}, c_{A20})^{-1}$; this implies the application of eq 31 (as related to eq 3) and eq 35 (as related to eq 9). In this subplot, the attenuations coefficients are also repeated.**

A closer inspection of **Fig 3-5a** reveals an overall decrease in $x_A$ (hollow symbols) from 375 nm down to 260 nm (right to left on $x$-axis; $c_{A0}$=0.0174 mol $L^{-1}$), which suggests a decrease in **A** dimerization reactivity for a lower λ. To confirm this statement we need to determine the λ dependence of the initial $k_{+app}$ values, thus apply **eq** 3-6 at various λ. As shown in **Table B 3-1** of the Supporting Information (first four entries) indeed these initial $k_{+app}$ values go down for a lower λ ($c_{A0}$=0.0174 mol $L^{-1}$). As shown in **Fig 3-5c** (red open triangles; left-axis; the apparent characteristics here refer to $k_{+app}(c_{A0})J_A(c_{A0})^{-1}$ and $k_{-app}(c_{A0}, c_{A20}) J_{A2}(c_{A0}, c_{A20})^{-1}$), globally $k_{+app}(c_{A0})J_A(c_{A0})^{-1}$ also drops for a lower λ ($c_{A0}$=0.0174 mol $L^{-1}$), hence, the action plot data under reference conditions ($c_{A0}$=0.0174 mol $L^{-1}$) are consistent with this apparent characteristic.

As indicated by step 1-3 in **Fig 3-3** parameter tuning can be subsequently performed toward $k_2/k_{-1}$ and $k_3/k_{-1}$ at each λ considering **eq 3-3** with various $c_{A0}$ values, so not only focusing on $c_{A0}$=0.0174 mol L$^{-1}$ as in **Fig 3-5** but still covering small time data. To make a link to **Fig 3-5c**, which only addresses the specific case $c_{A0}$=0.0174 mol L$^{-1}$, it is opted here to rewrite **eq 3-3** as follows:

$$k_{+\text{app}}(c_{A0})\mathcal{J}_a(c_{A0})^{-1} = \frac{\frac{k_2}{k_{-1}}}{\left(\frac{k_2}{k_{-1}}+\frac{k_3}{k_{-1}}\right)c_{A0}+1} \qquad\qquad \text{eq 3-31}$$

Note we do no introduce a new symbol on the left hand size to explicitly show that by taking this ratio the $\mathcal{J}_a(c_{A0})$ dependence is wiped out from $k_{+\text{app}}(c_{A0})$. The raw $k_{+\text{app}}(c_{A0})\mathcal{J}_a(c_{A0})^{-1}$ data at different λ with $c_{A0}$ values between 0.0436 and 0.00872 mol L$^{-1}$ are given in **Table B 3-1** and **B 3-2** of the Supporting Information. Experimentally three well-spread wavelengths are selected, namely λ equal to 260, 280 and 375 nm. Specifically, at 280 nm, the **A$_2$** absorption is below 5% at the end of all the experiments thus for all $c_{A0}$ cases (**Table B 5** and **B 3-6** of the Supporting Information). The maximum experimental **A$_2$** conversion is below 7%, indicating that **A$_2$** cleavage is relatively insignificant and thus the protocol as defined by steps 1-3 in **Fig 3-3** can be still followed. In other words to a first approximation **eq 3-31** can be used for all $c_{A0}$ values with the plot of $k_{+\text{app}}(c_{A0})\mathcal{J}_a(c_{A0})^{-1}$ against $c_{A0}$ given in **Fig B-9** of the Supporting Information. The associated tuned parameters at λ equal to 280 nm are $k_2/k_{-1}$ = 4.5 L mol$^{-1}$ and $k_3/k_{-1}$ = 45.7 L mol$^{-1}$ and are included in **Table 3-2**. Furthermore, at 260 nm, the experimental **A$_2$** conversion is maximally 5% with the corresponding maximum **A$_2$** absorption below 0.16%. Hence, again the protocol in step 1-3 in **Fig 3-3** can be followed. Parameter tuning can thus be performed in the same manner as for 280 nm (**Fig B-10** of the Supporting Information) resulting in $k_2/k_{-1}$ = 1.9 L mol$^{-1}$ and $k_3/k_{-1}$ = 10.5 L mol$^{-1}$ (see also **Table 3-2**). Regarding the third λ of 375 nm (exclusive dimerization) the plot of $k_{+\text{app}}(c_{A0})\mathcal{J}_a(c_{A0})^{-1}$ against $c_{A0}$ data is overlaid with the data from our previous work [264], as shown in **Fig B-11 - B-12** of the Supporting Information. The anthracene side-chain substituent is different from the present work, however, the same kinetic parameters ($k_2/k_{-1}$ = 5.4 L mol$^{-1}$ and $k_3/k_{-1}$ = 38.8 L mol$^{-1}$; see also **Table 3-2**) can be safely used[264]. Hence, the two ratios are mainly determined by the core of the structure of **A** and not its side chains.

Comparing the data for 375, 280 and 260 nm in **Fig 3-5c** and corresponding ratios of rate coefficients in the second and third column in **Table 3-2** it follows that the initial $k_{+\text{app}}(c_{A0})$ values decrease rather steadily with shorter wavelength and the $k_2/k_{-1}$ value is decreasing slightly upon going from 375 to 280 nm, followed by a more drastic drop from 280 to 260 nm, as also shown in **Fig B-13a** of the Supporting Information. Analogously, $k_3/k_{-1}$ is decreasing going from 375 nm to 260 nm as shown in **Fig B-13b** of the of the Supporting Information.

A decrease in $k_2/k_{-1}$ with a shorter λ indicates that for an increased photon energy the excited **A** is more likely to de-excite rather than to proceed with the dimerization reaction. A decrease of $k_3/k_{-1}$ with a shorter λ points to a favouring of de-excitation *via* the direct compared to the quenched route with decreasing λ.

**Table 3-2. Wavelength (λ) dependent values for $k_2/k_{-1}$, $k_3/k_{-1}$ and $k_5/k_{-4}$ as determined for the photokinetics in Fig 3-2 considering the experimental system defined in Fig 3-1; for a λ of 260, 280 and 375 nm they result from the protocol in Fig 3-3 (stage 1); also given are formulas based on these measured data to predict at any λ the 3 kinetic parameters; examples of such predictions are also included in this table covering a λ range between 260 and 375 nm.**

| wavelength [nm] | $k_2/k_{-1}$ [L mol⁻¹] | $k_3/k_{-1}$ [L mol⁻¹] | $k_5/k_{-4}$ [-] |
|---|---|---|---|
| **375** | 5.4[a,b] | 38.8[a,b] | n.a. |
| **330** | 5.4[c] | 44.5[c] | 0.15[b,c] |
| **320** | 5.3[c] | 44.1[c] | 0.14[b,c] |
| **310** | 5.2[c] | 43.3[c] | 0.13[b,c] |
| **300** | 5.1[c] | 41.9[c] | 0.13[b,c] |
| **290** | 4.8[c] | 39.3[c] | 0.53[b,c] |
| **280** | 4.5[b] | 45.7[b] | 0.60[b,c] |
| **270** | 3.5[c] | 26.1[c] | 0.35[b,c] |
| **260** | 1.9[b] | 10.5[b] | 0.05[b,c] |

**Formulas at any λ**

$$\frac{k_2}{k_{-1}} = 5.4 + (1.9 - 5.4)\exp(-0.06(\lambda - 260)) \text{ L mol}^{-1}$$

$$\frac{k_3}{k_{-1}} = 45.0 + (10.5 - 45.0)\exp(-0.06(\lambda - 260)) \text{ L mol}^{-1}$$

$$\frac{k_5}{k_{-4}} = \frac{0.7}{0.45\sqrt{2\pi}}\,exp\left(-0.5\left(\frac{ln(\lambda-250)-3.4}{0.45}\right)^2\right)$$

**[a] consistent with Kislyak *et al.* [264]; [b] input for construction of the formula in the same column; [c] obtained considering the formulas eq 3-32 and eq 3-33.**

For general applicability, **eq 3-32 & eq 3-33** below, as well as at the bottom of **Table 3-2** display the associated λ dependent formulas assuming exponentially based profiles as found most suited to describe the $k_2/k_{-1}$ and $k_3/k_{-1}$ experimental data, as shown by the lines in **Fig B-13a** and **Fig B-13b** of the Supporting Information.

$$\frac{k_2}{k_{-1}} = \mathbf{5.4} + (\mathbf{1.9} - \mathbf{5.4})\exp(-\mathbf{0.06}(\lambda - \mathbf{260})) \qquad \text{eq 3-32}$$

$$\frac{k_3}{k_{-1}} = \mathbf{45.0} + (\mathbf{10.5} - \mathbf{45.0})\exp(-\mathbf{0.06}(\lambda - \mathbf{260})) \qquad \text{eq 3-33}$$

For illustration purposes evaluations of $k_2/k_{-1}$ and $k_3/k_{-1}$ at other λ values according to these formulas (**eq 3-32 and eq 3-33**) are also included in column 2 and 3 of this table. It should be stressed that the current work is

the first to highlight the λ dependence of photokinetics on the level of a detailed reaction scheme as included in **Fig 3-2**. It is clear that such dependencies are strong at least already for the dimerization and therefore future kinetic studies should be directed to a more dedicated analysis following protocols as defined in **Fig 3-3**.

**$A_2$ cleavage experiments**

With step 1-3 in the protocol of **Fig 3-3** completed (determination of λ dependent kinetic parameters related to dimerization) we can now shift to step 4-6 in **Fig 3-3** (determination of λ dependent kinetic parameters related to dimer cleavage), focusing on one well-chosen set of initial conditions at which we start with **$A_2$** and a very low amount of **A** ($c_{A20} \approx 0$ mol L$^{-1}$; $c_{A0} \neq 0$ mol L$^{-1}$). Again an action plot is first needed as input (top right box in **Fig 3-3**) in the region between 260 and 330 nm. We select as initial conditions: $c_{A20} = 1.10 \times 10^{-2}$ mol L$^{-1}$ and $c_{A0}$ = $3.52 \times 10^{-5}$ mol L$^{-1}$ thus having negligible amount of **A** present at the start. **$A_2$** is irradiated for 15 s (receiving $2,79 \times 10^{-7}$ mol photons), 30 s (receiving $5,57 \times 10^{-7}$ mol photons) and 60 s (receiving $1,11 \times 10^{-6}$ mol photons) with the results shown in **Fig 3-5b**. Among all the cases the conversion of **$A_2$** ($x_{A2}$) has reached at most 13% and the relation with λ is now less straightforward with $x_{A2}$ small at 330 nm, increasing towards shorter λ with a peak around 280 nm, and then decreasing again towards 260 nm. More importantly, the fraction of light absorbed by **A** is significant and reaches 60% during the experiment in some cases (see **Fig B-16** of the Supporting Information). Hence, we cannot study a pure **$A_2$** cleavage, since competitive dimerization is always there, even at the smaller reaction times as covered here.

This implies that for the determination of $k_{-app}(c_A, c_{A2})$ and $k_5/k_{-4}$ at a given λ we cannot use **eq 3-14** or **eq 3-23** but we need to use **eq 3-24** and **eq 3-25** with plugged in values for $k_2/k_{-1}$ and $k_3/k_{-1}$ at this specific λ, as following from the first two formulas in **Table 3-2** considering stepwise integration (step 6 in **Fig 3-3**). As shown by the last column in **Table 3-2** and **Fig B-18c** of the Supporting Information a strong λ dependency is observed for $k_5/k_{-4}$ with very low values at low λ, high values at intermediate λ and again very low values at higher λ. As shown by the line in **Fig B-18c** of the Supporting Information a probability density like function (**eq 3-24**) allows to describe these experimental data to an acceptable degree also bearing in mind that toward higher λ (> 330 nm) this equation is less relevant due to an almost negligible **$A_2$** absorption. The corresponding initial $k_{-app}(c_{A0}, c_{A20})$ data are shown in **Fig B-17** and **Table B-3** of the Supporting Information and confirm the last statement with vanishing values at these higher λ.

This complex λ dependency for **$A_2$** cleavage is also observable based on the blue full triangles in **Fig 5c** which

$$\frac{k_5}{k_{-4}} = \frac{0.7}{0.45\sqrt{2\pi}} exp\left(-0.5\left(\frac{ln(\lambda-250)-3.4}{0.45}\right)^2\right) \qquad \text{eq 3-34}$$

represent λ dependent $k_{-app}(c_{A0}, c_{A20}) \mathcal{J}_{A_2}(c_{A0}, c_{A20})^{-1}$ data that are linked to **eq 3-9**:

$$k_{-app}(c_{A0}, c_{A20})J_{A_2}(c_{A0}, c_{A20})^{-1} = \frac{k_5/k_{-4}}{1+k_5/k_{-4}}$$ eq 3-35

Interestingly, these kinetic data according to **eq 3-35** follow the same trend as the individual action plot data in **Fig 3-5b** so that the overall consistency of the protocol proposed in **Fig 3-3** is again demonstrated. Moreover, to evaluate the impact of uncertainties in $k_2/k_{-1}$ and $k_3/k_{-1}$ for the subsequent determination of $k_5/k_{-4}$ a sensitivity analysis has been performed. No major changes in the calculated values of $k_5/k_{-4}$ and, therefore, the $k_{-app}(c_{A0}, c_{A20})J_{A2}(c_{A0}, c_{A20})^{-1}$ values are found, as shown in **Table B-8** of the Supporting Information.

Considering the determined kinetic parameters in **Table 3-2** ($k_2/k_{-1}$, $k_3/k_{-1}$ and $k_5/k_{-4}$) it is highlighted in **Fig 3-5** that a dominance of the forward or reverse reaction is dependent on the volumetric absorption rate of **A** and **A$_2$** ($J$ values), which is a function of λ, and the relative importance of the forward and reverse volumetric reaction rate, which is also a function of λ. Here focus is on the initial rates thus adding for the forward apparent reactivity $c_{A0}$, as $k_{+app}(c_{A0}, c_{A20})c_{A0}$ and $k_{-app}(c_{A0}, c_{A20})$ have the same dimension of L mol$^{-1}$ s$^{-1}$ and are the two terms in the general photoreaction rate law, **eq 3-20**. In **Fig 3-5a** the focus is on $c_{A20}=1.10 \times 10^{-2}$ mol L$^{-1}$ and $c_{A0}= 3.52 \times 10^{-5}$ mol L$^{-1}$ (same situation as in **Fig 3-5b** thus with a dominance of **A$_2$** presence) and in **Fig 3-5b** on $c_{A0}=10^{-2}$ mol L$^{-1}$ and $c_{A20}= 10^{-3}$ mol L$^{-1}$ (thus situation with both **A** and **A$_2$** presence but a dominance of the former). In any case, in **Fig 3-6** the $J$ values (spheres) possess the highest values and the intensity of the impact of the actual reactions can be observed by the relative lower position of the diamonds (actual rates) with respect to these spheres. Red symbols are used for dimerization and blue symbols for dimer cleavage.
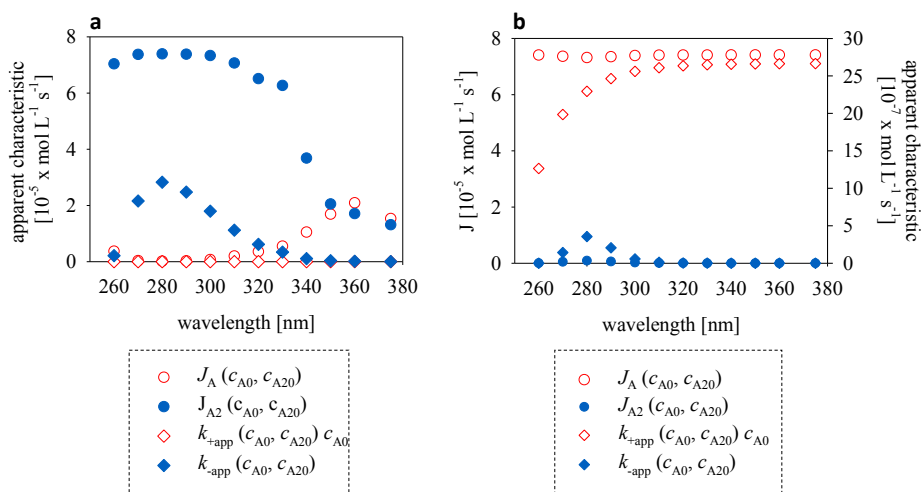


**Fig 3-6 Simulated molar photon absorption rates J$_A$(c$_{A0}$, c$_{A20}$) and J$_{A2}$(c$_{A0}$, c$_{A20}$) (both in L mol$^{-1}$ s$^{-1}$) and the apparent characteristics k$_{+app}$(c$_{A0}$, c$_{A20}$)c$_a$ and k$_{-app}$(c$_{A0}$, c$_{A20}$) (both in L mol$^{-1}$ s$^{-1}$) at the start (t = 0 s) in subplot a with**

$c_{A20}$=1.10× $10^{-2}$ mol $L^{-1}$ and $c_{A0}$= 3.52 × $10^{-5}$ mol $L^{-1}$ thus identical to the experimental conditions of the $A_2$ cleavage action plot in Fig 5b; and in subplot b with $c_{A0}$=$10^{-2}$ mol $L^{-1}$ and $c_{A20}$= $10^{-3}$ mol $L^{-1}$ thus conditions with both monomer and dimer but a dominance for the former. Results based on the formulas mentioned in Table 3-2.

Acknowledging the presence of **A** the highest (initial) apparent dimerization rate is observed around 375 nm at which there is no competition with **$A_2$** cleavage. The (initial) dimerization rate is decreasing from 330 nm to 260 nm, as specifically clear in **Fig 3-3b**. The molar attenuation of **A** shows more variability and is overall increasing from negligible > 400 nm to a maximum at 365 nm so close to the maximal forward initial apparent rate highlighting the need of strong **A** absorption for a subsequent sufficiently high reaction rate, then overall decreasing to a minimum around 290 nm. From this minimum, the molar attenuation of **A** increases however strongly towards 260 nm, indicative of a potential changing situation toward a dominant dimerization at the lower λ. As shown in **Fig 3-6a**, the maximum of the initial apparent **$A_2$** cleavage rate (with dimer present) is in turn found to be around 280 nm, while the molar attenuation coefficient of **$A_2$** is continuously increasing from negligible at 350 nm to 260 nm. Hence, despite the still high $J_{A2}(c_{A0}, c_{A20})$ values at the lowest λ values the reverse chemical reaction as such becomes less relevant. In contrast the $J_A(c_{A0}, c_{A20})$ value goes strongly up in this region of the lowest λ values and the forward chemical reaction can be more relevant again, at least on a relative basis an specifically if the A concentration is sufficiently high as is the case **Fig 3-6b**. Anyways the lowest λ values induce a lower initial apparent rate in both directions.

### 3.4.3 Application of stage 2 of the protocol: model validation

With $k_2/k_{-1}$, $k_3/k_{-1}$ and $k_5/k_{-4}$ determined according to stage 1 in **Fig 3-3** and the corresponding results specified by λ dependent functions at the bottom in **Table 3-2** we can now predict the photokinetics up to any time for all sets of relevant initial conditions thus for variations in $c_{A0}$ and $c_{A20}$ on the one hand and λ on the other hand. An example is provided in **Fig 3-7** considering a situation with competitive **A** dimerization and **$A_2$** cleavage taking λ equal to 280 nm. Also experimental data are included to enable further model validation thus the execution of stage 2a in **Fig 3-4**.

More in detail, **$A_2$** has been dissolved in DCM ($c_{A20}$ = 1.10 ×$10^{-2}$ mol $L^{-1}$) and irradiated for various times at 280 nm and 538 µJ pulse$^{-1}$. The corresponding experimental data are included as coloured symbols in **Fig 3-7** with the blue and red symbols describing the concentration variation of **$A_2$** and **A** respectively. As long time data are targeted a stepwise integration has been performed according to **eq 3-24** and **eq 3-25** (Case 3). While the **A** species has not been initially detected *via* $^1$H-NMR a default correction has been considered for the simulations setting $c_{A0}$ equal to $10^{-10}$ mol $L^{-1}$. The simulation results are included as lines in **Fig 3-7** and describe the experimental data well and automatically correct for small experimental discrepancies. As recently

indicated in Van Steenberge *et al.*[270] one of the strengths of a kinetic model if fed with sufficient variations in experimental data is to correct for inconsistencies as sometime difficult to assess purely experimentally. It can be additionally induced that $t_{eq}$ is close to 3000 s, which is more difficult based on the experimental data with inherent a non-steady-state-like character.
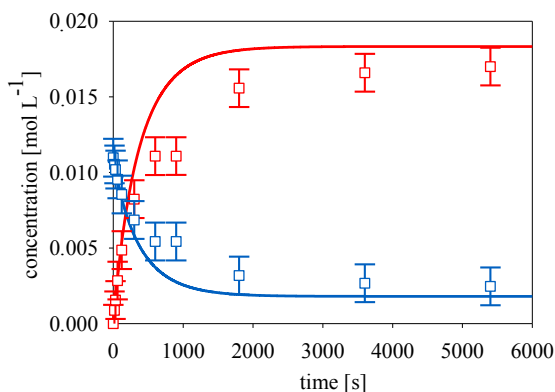


**Fig 3-7 Model validation for initial conditions with competitive dimerization and dimer cleavage up to large time; conditions: 280 nm, 20 Hz laser pulses, 538 μJ pulse$^{-1}$, initial A$_2$ concentration of $1.10 \times 10^{-2}$ mol L$^{-1}$; no monomer A initially (formally in the simulation $c_{A0}$ equal to $10^{-10}$ mol L$^{-1}$); dichloromethane (DCM) as solvent. Experimental data: blue squares represent A$_2$ concentration while red squares represent A concentration; error bars represent average error of all the samples within the overall run; simulations based on step-wise integration as specified in the second entry of Table 1; parameters from Table 2; extra details in Table B 3-5 of the Supporting Information.**

Supported by the kinetic model validation of the $k_2/k_{-1}$, $k_3/k_{-1}$ and $k_5/k_{-4}$ parameter values at small times (**Fig 3-5** and **Table 3-2**) and their combined extra model validation up to large times in **Fig 3-7** we can now fully use the kinetic model to obtain insights in the overall photochemical process. This is demonstrated in **Fig 3-8** and **Fig 3-9** differentiating between three situations (the more basic situation 1 and 3 in **Fig 3-8** and the more complex situation 2 in **Fig 3-9**). The first situation (**Fig 3-8a**) is at low λ (260 nm) with a competitive absorption for **A** and **A$_2$** starting from a mixture of **A** and **A$_2$** (but dominantly the former). The second situation (**Fig 3-9**) is also with strong competitive absorption but also strong competitive reaction but at higher λ (280 nm) and starts only with **A** or **A$_2$**. The third situation (**Fig 3-8b**) is at a very high λ (375 nm) with exclusive **A** absorption thus by default only starting from **A**. The left graph covers for each situation the concentration variation of **A** and **A$_2$** up to large times, whereas the right graph highlights each time extra kinetic information.

It is shown in **Fig 3-8a** that for the first situation equilibrium is eventually reached for the **A** and **A$_2$** concentration ($t_{eq}$ of *ca.* 10000 seconds). The associate apparent rate coefficients are plotted in the right graph as dashed

dotted lines with an additional black full line dedicated to the fraction of the volumetric photon rate absorbed by the **A** species. As highlighted in the discussion of **Fig 3-6** at lower $\lambda$ a dominance of $J_A$ is possible specifically if **A** is sufficiently present at the start. This is valid in the first situation ($J_A$ relative contributions over 80%; **Fig 3-8a**; right), explaining the on average dominant dimerization before equilibrium setting, as witnessed by the stretched decay of the red line in **Fig 3-8a** (left). This is also nicely illustrated in **Fig B-19** in the Supporting Information, indicating that $k_{+app}$ ($c_A$, $c_{A2}$) $c_A$ decreases more that $k_{-app}$ ($c_A$, $c_{A2}$) increases until the equilibrium point is reached.

In the second very competitive situation both for absorption and reaction (**Fig 3-9**), it follows that equilibrium is rapidly reached ($t_{eq}$ of *ca.* 2000 seconds). The fast kinetics are confirmed by two mirror set of initial conditions. In **Fig 3-9a(i)** and **Fig 3-9b(i)** we respectively start with $A_2$ and **A** (full lines) and twice the same equilibrium concentrations result. In **Fig 3-9a(ii)** and **Fig 3-9b(ii)** graphs, the associated apparent rate coefficients are plotted as dashed lines and eventually constant values are obtained consistent with this equilibrium setting. On the right axis the fraction of light absorbed by either of the species is also shown.

In the third situation (**Fig 3-8b**), it is clear that **A** can be fully consumed as a vanishing **A** concentration value results at the higher reaction times (above 6000 seconds). As shown in the right graph the photokinetics are quite dynamic for this situation with first an increasing $k_{+app}(c_A)$ and then a decreasing one (red line). The increase is due to the depletion of **A** and thus a lesser importance of the disturbing bimolecular concentration quenching reaction ($k_3$ in **Fig 3-2**) as opposed to the desired bimolecular reaction resulting in the formation of $A_2$ ($k_2$ in **Fig 3-2)**, as also deducible from the mathematical shape of **eq 3-3**. The decrease of $k_{+app}(c_A)$ at larger times can be directly related to the Beer-Lambert law once **A** is less present. Under such conditions $J_A$ is no longer close to its initial value but the correction factor $1 - 10^{-\varepsilon_A c_A L}$ in **eq 3-4** matters.
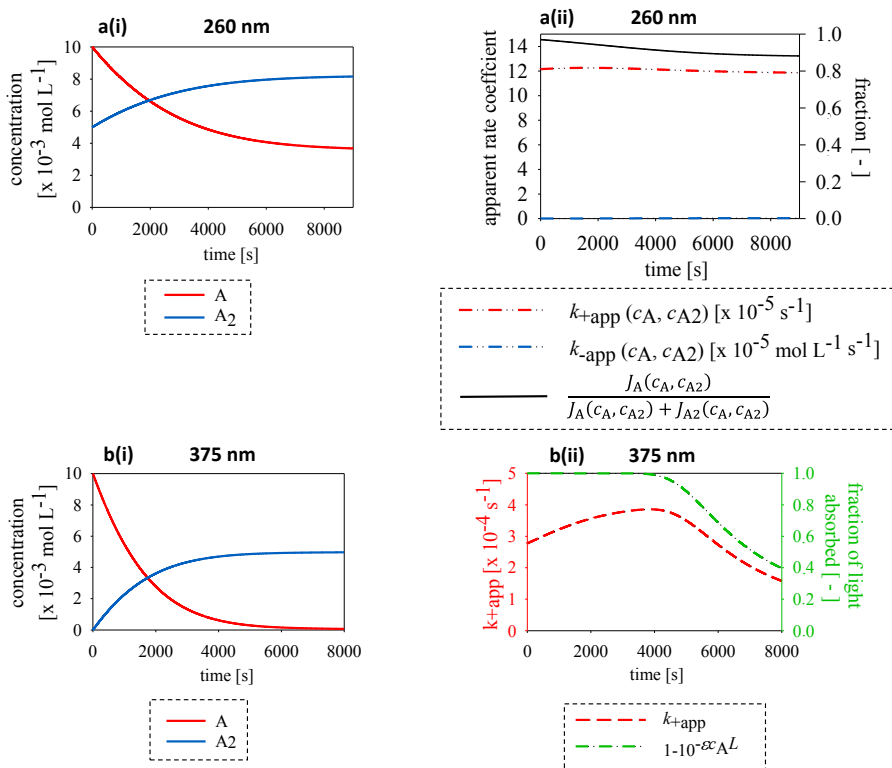
**Fig 3-8 Simulation of concentration variations for monomer A (red full lines) and dimer A$_2$ (blue full lines) for two wavelengths (λ values) with various initial concentrations considering the λ dependencies specified at the bottom in Table 3-2 and following stage 2 of the protocol in Fig 3-4 thus the equations in Table 3-1 as valid up to large time. Initial conditions for a are: λ=260 nm, $c_{A0}$ = 10$^{-2}$ mol L$^{-1}$ and $c_{A20}$ = 5×10$^{-3}$ mol L$^{-1}$; initial conditions for b are: λ= 375 nm $c_{A0}$ = 10$^{-2}$ mol L$^{-1}$ and $c_{A20}$ = 0 mol L$^{-1}$; all cases with the same volumetric flow rate of photons 7.4×10$^{-5}$ mol L$^{-1}$ s$^{-1}$; a: case with dominant forward apparent reactivity (see extra right graph) with competitive absorption (Case 3); b: case of exclusive dimerization (Case 1) with the right graph displaying the variation of the forward apparent rate coefficient and fraction of light absorbed. Same volumetric flow rate of photons 7.4×10$^{-5}$ mol L$^{-1}$ s$^{-1}$ in both cases.**
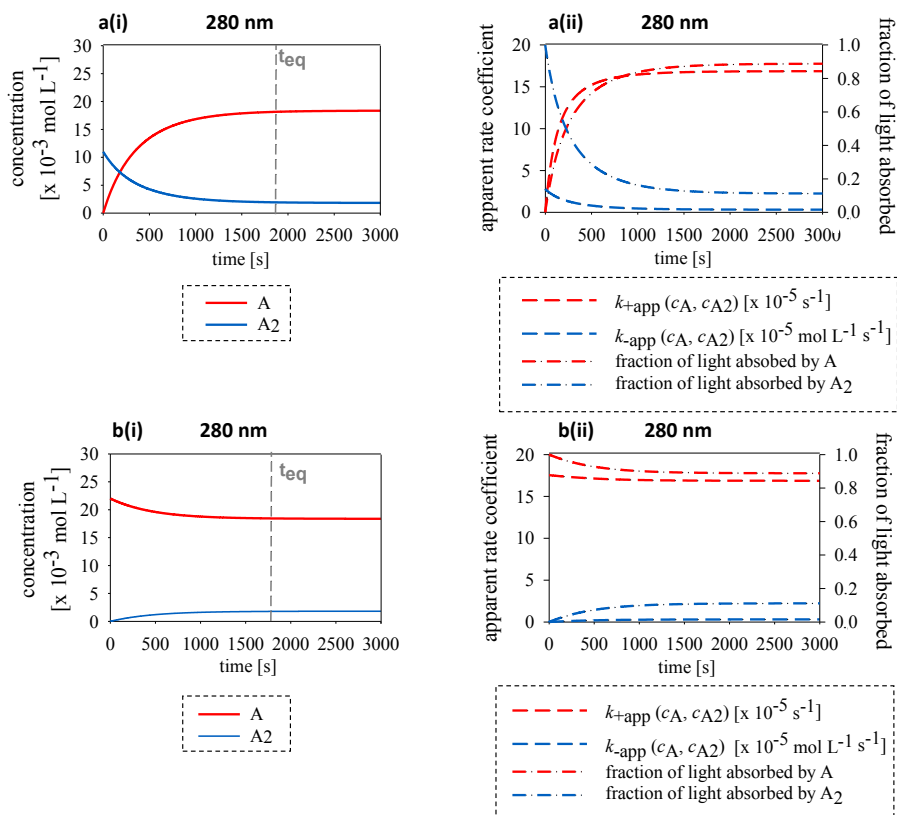
**Fig 3-9 Simulation regarding reaching the same equilibrium composition with two different initial concentrations considering the case with strong competition at 280nm (Case 3). Concentration variations for monomer A (red full lines) and dimer $A_2$ (blue full lines) are shown by the graphs on the left (i); graphs on the right (ii) show corresponding variations in apparent rate coefficients $k_{-app}(c_A, c_{A2})$ and $k_{+app}(c_A, c_{A2})$;and fraction of light absorbed by either of the species. a: $\lambda = 280$ nm, $c_{A0} = 1 \times 10^{-10}$ mol $L^{-1}$ (to be read as 0 mol $L^{-1}$) and $c_{A20} = 1.1 \times 10^{-2}$ mol $L^{-1}$, b: $\lambda = 280$ nm, $c_{A0} = 2.2 \times 10^{-2}$ mol $L^{-1}$ and $c_{A20} = 0$ mol $L^{-1}$ (hence same $c_{tot,A}$ (eq 29) as for a). Same volumetric flow rate of photons $7.4 \times 10^{-5}$ mol $L^{-1}$ $s^{-1}$.**

## 3.5    Conclusions

A fundamental photokinetic framework based on chemical engineering principles and differentiation between photon absorption and subsequent reaction is presented to study to dimerization of **A** and its reverse $A_2$ cleavage at any $\lambda$ and set of initial concentrations. The $\lambda$ region from 375 to 260 nm is explored both experimentally and by kinetic simulations to identify a region of simultaneous **A** dimerization and $A_2$ cleavage from 330 to 260 nm. Above 330 nm and toward 260 nm one tends to dominant and in the limit for specially 375 nm exclusive dimerization. For the region close to 260 nm this is specifically true with sufficiently high initial **A** amounts.

An experimental protocol is put forward to determine the relevant kinetic parameters and to validate the kinetic model up to large times. Critical is at a first stage the consideration of dedicated short time scale experiments to determine three ratios of rate coefficients (always with a de-excitation rate coefficient in the denominator) considering as input value measured (initial) apparent reactivities. The short time scale experiments show that the initial (apparent) dimerization reactivity of **A** is slowly decreasing with decreasing wavelength, while the (apparent) **A$_2$** cleavage reactivity is increasing with a peak around 280 nm, then again decreasing with shorter λ. Measurements of these initial apparent reactivities at several λ enables the subsequent determination of λ dependent kinetic parameters, as currently unavailable in the field.

In a second stage of the protocol, the focus can be been shifted to large times irradiations. Here, we have first successfully benchmarked simulated data against experimental data involving a simultaneous dimerization of **A** and **A$_2$** cleavage. We subsequently highlighted the potential of the simulation tool to predict the photokinetics at any wavelength and any set of initial concentrations. Specific focus has been on the time dependent variation of relative absorption rates and apparent kinetic parameters, and the determination of the reaction time of either equilibrium setting or the complete depletion of the reactant. Hence, the combination of experimental and modelling work has allowed to fully understand the reversibility of photocycloaddition reactions with the proposed protocol also applicable for other photoreactions thanks to its generic nature.

Future work will expand the present work towards larger molecules in the limit polymeric systems, in which the anthracenes will be present on the polymer backbones. Such applications are useful for designing macroscopic properties of next-generation polymeric materials by light and to further study the relation of potential matrix effects and photokinetics at the level of the individual reaction.

.

# CHAPTER 4. CONFORMATIONAL CONTROL OF INDIVIDUAL SINGLE-CHAIN NANOPARTICLES

The following chapter is part of a future publication in preparation: 'Conformational Control of Individual Single-Chain Nanoparticles'. Anastasia Kislyak, Francisco J. Arraez, Daniel Kodura, Mariya Edeleva, Fabian Blößer, Hendrik Frisch, Paul H.M. Van Steenberge, Dagmar R. D'hooge, Christopher Barner-Kowollik

## 4.1 Introduction

The field of single-chain nanoparticle (SCNP) synthesis strives towards the most intricate level macromolecular design can afford, i.e. controlling the conformation of each polymer chain according to – ideally – a predetermined folding pattern.[162] The potential that rests within synthetic polymer chains can be connected to natural phenomena. Perfectly folded polypeptides give rise to a plethora of biological functions, ranging from enzymatic reaction control to macroscopic movement.[271] If synthetic polymer chain conformation could be realized with a comparable precision, we would be able to define the chemical and physical behaviour of specific chemical groups within chains as a function of intramolecular connections. Such progress in the field of synthetic polymer chemistry could unleash the application potential associated with the natural inspiration of SCNPs, i.e. proteins.[271] In the context of the current thesis, understanding the intramolecular crosslinking processes of SCNPs via a holistic modelling approach serves as a blueprint for complex dynamic network modelling.

While key advances have already been made in SCNP synthesis as demonstrated by applications in nanoreactor technology,[35, 162] metal ion sensing,[161] nanocarriers,[160] catalyses,[158-159] and contrast agents for magnetic resonance imaging,[157] the dream of perfect command over the single-chain conformation remains elusive.[157, 159, 271] The challenge is mainly a consequence of research efforts being focused on average chain folding, neglecting structural differences at the individual polymer chain and functional group level. In practice, during polymer synthesis, chain-to-chain deviations are unavoidable.[185, 200, 270, 272-274] Chain-to-chain deviations – even in the case when sequence-defined polymers are used – imply a non-uniform starting position for the subsequent folding process, complicating the achievement of a well-defined 3D folding process.[275] However, the uniformity of the chains during folding is critical because small protein conformational deviations, either through incorrect folding or subsequent unfolding, lead to serious consequences in biological contexts.[276] Analogously, the SCNP conformation and size are of immense application importance.[35, 171-174, 277] For example, the SCNP crosslinking density (and thus conformation) can control gold nanoparticle formation

kinetics[35] and the SCNP size can control the effectiveness of organocatalysis.[171] Intriguingly, SCNP design can rely on several types of crosslinking bonds, both covalent bond formation and dynamic non-covalent interactions can be utilized.[35, 48, 80, 278-279] The folding of proteins, in comparison, relies predominantly on non-covalent interactions such as hydrogen bonding.[276] The correct way of folding proteins is crucial to enable their specific function and is limited to a narrow solvent range and temperature window.[280] Any deviation from such stringent conditions would lead to unfolding or incorrect folding of the polymer. In contrast to the non-covalent bonding in proteins, more robust covalent bonds, resulting from e.g. anthracene dimerization, allow overcoming this restriction in SCNPs. However, since these covalent bonds are much stronger and thus harder to break, they generally lead to conformations that are far away from the global minimum in the energy conformational landscape. The resulting unpredictable conformations are undesirable for applications (e.g. supramolecular assembly, catalysis). Therefore, the effect of the folding process on the final macromolecular architecture is just as critical for covalent-based SCNPs as it is for proteins. The challenging task of elucidating the complex relationship between contraction, molar mass of the chain, crosslinker amounts and bulkiness in building the desired final macromolecular architecture of the SCNPs was only recently explored using experimental techniques including SEC-MALS and MS.[176-177, 179-181]

Among the covalent bond-forming reactions, those induced by light are especially attractive because the chain contraction can be precisely controlled at a given wavelength, $\lambda$, and combined with other orthogonal types of reactions.[47-48, 281-282] For instance, our team has pioneered photonic fuel-driven single-chain folding using [2+2] cycloadditions, and exploited steric confinement to substantially increase the folding quantum efficiency.[58] A prominent example of a light-induced reaction for SCNP folding is the [4+4] photocycloaddition of anthracene (**A**) (**Fig 4-1**).[80] When anthracene molecules are irradiated in free solution, i.e. not anchored to polymer chains, long wavelengths (e.g. $\lambda > 300$ nm) allow for exclusive **A** dimerization, while shorter wavelengths ($\lambda < 300$ nm) initiate competitive **A** dimerization and its dimer (**A$_2$**) cleavage.[60, 264, 283] The core reaction mechanism of the **A** dimerization is depicted in **Fig 4-1** and starts from an **A** moiety absorbing a photon, which elevates it into a singlet excited state. The excited species **A$^1$** either reacts with another **A** to form the desired dimer **A$_2$**, de-excites or undergoes concentration quenching. Triplet-triplet annihilation is ignored here, due to the absence of triplet sensitizers.[49] Attachment of **A** moieties onto polymer chains, in contrast with the free solution, will restrict **A** movement. Such confinement may lead to a different photo-kinetic behaviour compared to non-polymeric systems.[284]

Our understanding of the kinetics of light-induced folding at the molecular, elementary level remains limited. To address this critical gap in understanding photo-induced folding, we herein fuse photochemical macromolecular design featuring [4+4] cycloadditions with kinetic Monte Carlo (*k*MC) simulations to fundamentally map individual covalent bond formation in 3D,



**Fig 4-1 Simplified reaction mechanism of anthracene photocycloaddition.**[49, 264]

ultimately allowing to evaluate SCNP-to-SCNP folding deviations. This is a largely unexplored research area, going beyond standard molecular dynamic (MD) simulations.[171, 183, 285-288] Such MD simulations consist of equilibrating "idealized" chains with randomly distributed crosslinking groups along the polymer backbone, which do not represent the real distribution of crosslinking groups. As a consequence, these simulations do not benchmark against experimental polymerisation data nor do they result from kinetic modelling predictions of actual polymerisations. Also, they define chemical interactions by so-called capture distance criteria[285, 287] rather than relying on chemical reactivities determined from kinetic studies.

Analysis of the protein 3D conformation is achievable via X-ray crystallography.[289] However, obtaining information about the 3D conformation of SCNPs is generally challenging owing to its variations in dispersity and monomer sequence preventing the crystallization required for X-ray crystallography. Therefore, a different approach must be used to obtain such in-depth information on SCNPs.

In this chapter, a model for obtaining an encompassing picture of photochemical chain folding using exact knowledge of the positioning of the photoreactive groups within the chains is proposed. Photoreaction rate laws are derived to describe the folding kinetics for an average (with respect to chain length and composition) chain in a solution. Matrix-based kinetic *k*MC platform enables visualisation of the molecular structure of individual chains. Positioning of the functional groups was predicted from reversible addition-fragmentation chain transfer (RAFT) polymerisation kinetics. 3D folding deviations between individual chains could be modelled predicting the evolution of the radius of gyration distributions. 3D conformations of individual SCNPs and chemical constitutions were subsequently accessed, opening the pathway to predict macroscopic SCNP behaviour from chemical variations and diffusion restrictions both during chain synthesis and subsequent folding, unlocking an extensive level of detail about the formed SCNPs. Finally, experiments required for the validation of the model are discussed.
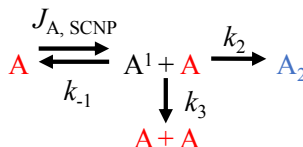
## 4.2　Model derivation

In the following section, a model is derived theoretically first on average assuming all chains to be identical (**§4.2.1**), then chain-to-chain deviations are established via kMC (**§4.2.2**).

### 4.2.1 Theoretical folding of identical chains

We initially study the chain folding kinetics assuming identical highly flexible linear chains. For illustrative purposes, emphasis is on λ = 375 nm, wavelengths where **A₂** photon absorption is negligible and, therefore, only dimerization takes place.[49] By assuming sufficiently diluted conditions, intermolecular reactions can be ignored so that each chain eventually results in an SCNP, as highlighted in **Fig 4-2b**, implying that only intramolecular dimerization reactions occur according to the mechanism depicted in **Fig 4-1**.[49]

| **A** | **B** | **C** |
|---|---|---|
| Pseudo-homogeneous A concentration | Concentration of chains in solution | Concentration of A within the defined chain volume |
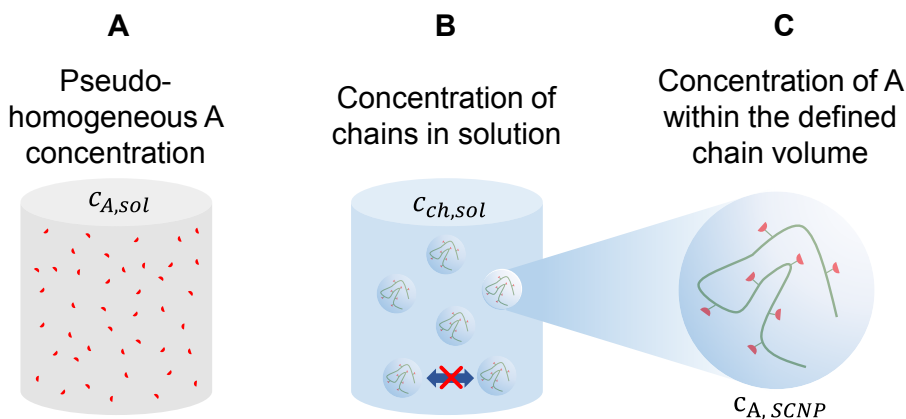


**Fig 4-2 Molar concentrations to define ideal folding with identical highly flexible linear chains; $c_{A,SCNP}$ - relates to A moieties in a single chain nanoparticle (SCNP), i.e. single-molecule volume, $c_{ch,sol}$ to polymer chains in the solution, and $c_{A,sol}$ to the pseudo-homogeneous concentration of A moieties in the solution. The red cross in subplot b highlights that intermolecular reactions are not considered, which implies sufficiently diluted conditions (low $c_{ch,sol}$).**

Essential in the photodimerization mechanism (refer to **Fig 4-1**) is the realization of the activated state for **A** in an SCNP environment. The volumetric rate of light absorbed at a given time *t* in a particle (such as in **Fig 4-2c**) ($J_{A,SCNP,t}$ **eq 4-1**) follows from (i) applying the law of Beer-Lambert for the entire mixture, assuming freely moving **A** moieties due to high chain flexibility, and (ii) dividing the absorbed light between the SCNPs. $J_{A,SCNP,t}$ is, therefore expressed as:

$$J_{A\,SCNP\,t}\left(c_{A,sol},t\right) = \frac{\frac{E_{pp}T\lambda f}{E_\lambda N_A V_{sample}}\left(1-10^{-\varepsilon_A c_{A,sol,t}L}\right)}{c_{ch,sol,0}\,N_A V_{SCNP,t}} \qquad \text{eq 4-1}$$

where, as in previous chapters, $E_{pp}$ is energy pre pulse, J, $T_\lambda$ is glass transmittance, $f$ is laser frequency, Hz, $E_\lambda$ the energy of a photon of wavelength, $\lambda$, $N_A$ – Avogadro number, $V_{sample}$ – volume of the irradiated sample, L, $\varepsilon_A$ is a molar attenuation coefficient, L mol$^{-1}$ cm$^{-1}$, $c_{A, sol,t}$ is a pseudo-homogeneous concentration of **A** moieties in the solution, mol L$^{-1}$ (**Fig 4-2a**), $L$ is light path, cm, $c_{ch, sol,0}$ is concentration of polymer chains in the solution (**Fig 4-2b**), $V_{SCNP,t}$ – defined volume of a polymer chain, e.g. hydrodynamic volume, L.

Once $J_{A,SCNP,t}$ is calculated, the $t$ variation of the moles of A moieties in an SCNP, $\left(\frac{dn_{A,SCNP,t}}{dt}\right)$, becomes accessible. This is illustrated in **Fig 4-3a**, assuming that the hydrodynamic volume is constant ($V_{SCNP,H,0}$). Here, $k_{+app,ideal}$ is an apparent rate coefficient for dimerization representing not only the activation but also the other individual reactions in **Fig 4-1c**. This apparent rate coefficient has been introduced in **Chapter 2** (also Section C.1 of the Appendix) in the absence of chains and is thus an ideal value that ignores any effect of confinement of the polymer chain.[264] However, in practice, a decrease of $V_{SCNP,t}$ is expected, which could be captured by a Zimm and Stockmayer contraction factor, *g*,[290-291] as demonstrated in Section C.2 of the Appendix. The Zimm and Stockmayer contraction factor is defined as a ratio of the mean square radius of gyration of a branched-chain to a linear one.

As shown in **Fig 4-3c**, a correction factor *z* is proposed to be introduced connecting $k_{+app,ideal}$ with $k_{+app}$ to account for mobility constraints or confinement during folding. At the start, no **A** dimerization reaction has taken place yet and as a result, all **A** moieties should indeed be able to move rather freely. In contrast, if initial dimerization has occurred, further dimerization could be hindered due to the decreased mobility of **A** moieties as well as unfavourable spatial arrangements, albeit that a volume contraction has brought them closer to each other (**Fig 4-3b**). Additionally, the **A** conversion ($X_A$) is limited. If an odd number of **A** molecules has been incorporated in the chains, it is stoichiometrically impossible for the last remaining **A** moiety to react. Furthermore, unfavourable spatial arrangements of the **A** moieties could further limit the conversion.

In the present chapter, we propose a basic power law equation for the variation of the confinement correction factor *z* with increasing $X_A$, as shown in **Fig 4-3d**. The power *w* would be a system-dependent fitting parameter that depends on chemical building block variations. These variations include the stiffness of the polymer backbone and the spacer length for **A** units, which codetermine chain flexibility. A different *w* value per polymer/**A** system is thus considered, in **Fig 4-3d** two examples (*w=w'* and *w=w''*) are demonstrated. In long term, these *w* data were determined even more fundamentally by correlating them with physical polymer

parameters such as the stiffness ratio $C_\infty$.[292] A sample of a potential simulation result can be seen in **Fig C-4** in the Appendix.



**A  Ideal case approximation**

$$V_{SCNP,0}$$

$$n_{A,SCNP,t+\Delta t} = \\ = n_{A,SCNP,t}e^{-2k_{+app,ideal}(c_{A,sol,t},c_{A\,SCNP,t})\Delta t}$$

$$c_{A,SCNP} = \frac{n_{A,SCNP}}{V_{SCNP}} \qquad (V_{SCNP}=V_{SCNP,0})$$

**C  Confinement and limiting conversion**

$$z_{t1}$$

$$z_{t2}$$

$$z_{t3}\ \&\ X_{lim}$$

$$k_{+app}(c_{A,sol,t}, c_{A\,SCNP,t}) = k_{+app,ideal}z_t$$

**B  Volume contraction**

$$g_{t1}$$

$$g_{t2}$$

$$V_{SCNP,t} = V_{SNCP,t0}g_t^{3/2}$$

**D  Structural features**

$$w = w'$$

$$w = w''$$

$$z_t = 1 - \left(\frac{X_{A,t}}{X_{A,lim}}\right)^w$$
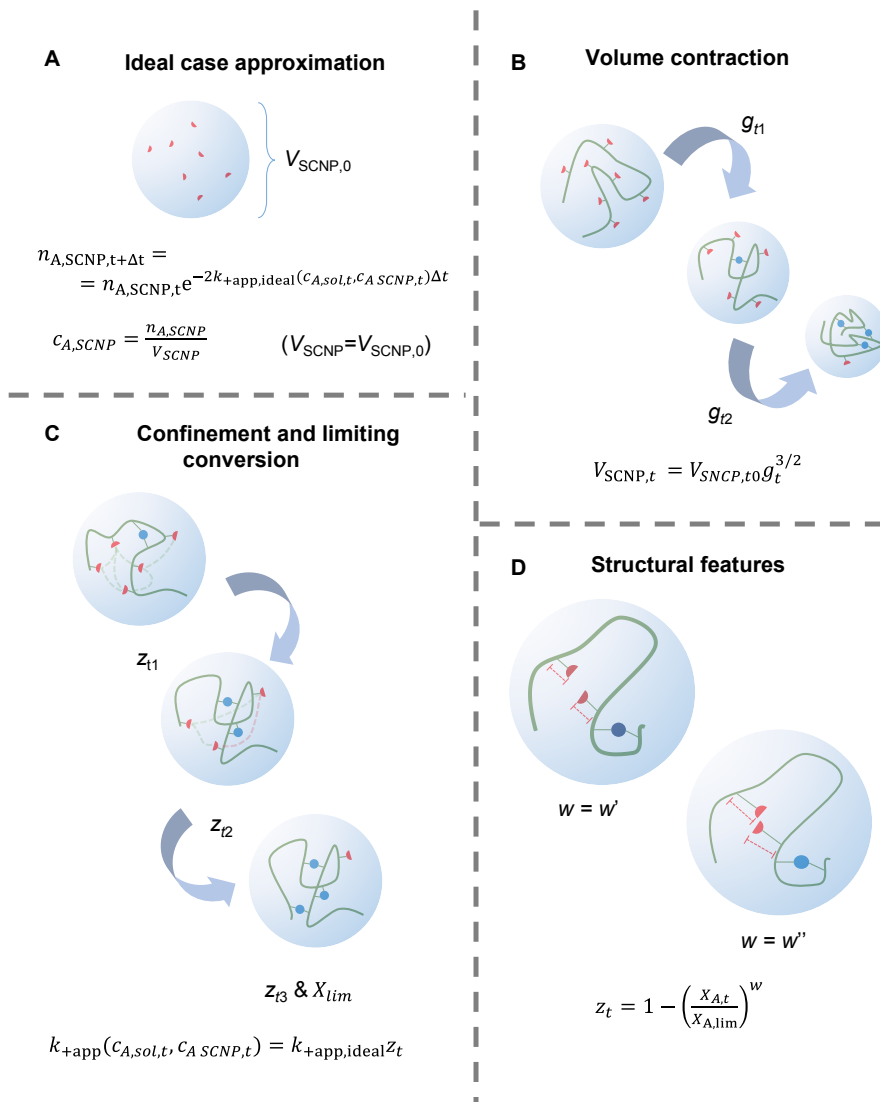
**Fig 4-3 From ideal to non-ideal folding kinetics; a: ideal case with unlimited chain flexibility so that A moieties can be considered as freely moving within a given SCNP/single molecule volume (constant hydrodynamic volume $V_{SCNP}$); b: perceived polymer chain volume contraction during folding (no constant $V_{SCNP}$), as expressed by the contraction factor $g$ (Figure C-3); c: restriction on dimerization due to an unfavourable spatial arrangement (steric hindrance) as captured by the $z$ variation up to the limiting A conversion; d: upon changing the chemical system (e.g. spacer length for A) one changes the confinement effect, as captured by a different $w$.**

### 4.2.2 Macromolecular reverse engineering to unravel the folding of individual chains

Modelling in the current section was executed by ir. Francisco Arraez. As explained in the introduction (**§4.1**), the conformation of single chains is critical for SNCP applications. An average folding interpretation is biased as it does not allow for the validation of the relevant subtle conformational 3D changes along the chains and fails in identifying multimodalities in chain configuration distributions, such as radius of gyration distribution (RGD). Non-idealities, such as different backbone **A** distances, are already encountered during the original synthesis of the to-be-folded chains. Critically, experimental synthesis techniques only allow mapping average behaviour, whereas matrix-based *k*MC simulations provide a high level of macromolecular detail (including monomer sequence and a sequence of the reaction events **Fig C-10 – C-11**).[185, 293]

Matrix-based *k*MC simulations have already been applied for several reversible deactivation radical polymerisation (RDRP) techniques, but not yet for RAFT polymerisation.[270, 294-297] **Fig 4-4a** depicts a typical test 2D simulation outcome with **A** anchored monomer units coloured in red and non-functionalized units in green and for simplicity only 400 chains depicted in stretched format, although, ~$10^6$ chains are followed during the simulation. The kinetic model parameters are provided in **Table C-1** in the Appendix and allow for well-described monomer conversion and dispersity data, as shown in **Fig C-5** of the Appendix. It follows that on average the chains consist of ~6 **A** units with only a low amount (ca. 5%; **Fig C-6b**) of them not containing **A** units. More importantly, from **Fig C-6c-d** a distribution of **A** distances can be identified, highlighting that a chain folding is non-uniform for a given chain and even different per chain considered. From the 2D visualization after RAFT polymerisation synthesis, a 3D spatial representation (**Fig 4-4c-e**) of the unfolded copolymer chains can be generated using the methodology described by Arraez *et al.* and used for studying the kinetics of RDRP brushes.[298-299] For each chain in the *k*MC ensemble, the comonomer units are placed within a unitary cubic lattice from which the squared radius of gyration ($R_g^2$) can be predicted, accounting for possible expansions and excluded volume effects. Such 3D translation can also be done for folded chains (**Fig 4-4c-e**), provided that in the 2D visualization it is identified which **A** units have undergone dimerization. For this, we need to know the dimerization possibilities for a given chain at every moment of the folding process. In other words, we need to update its **A-A** distance ($d_{A-A}$) distribution, as shown in **Fig C-6c** of the Appendix.
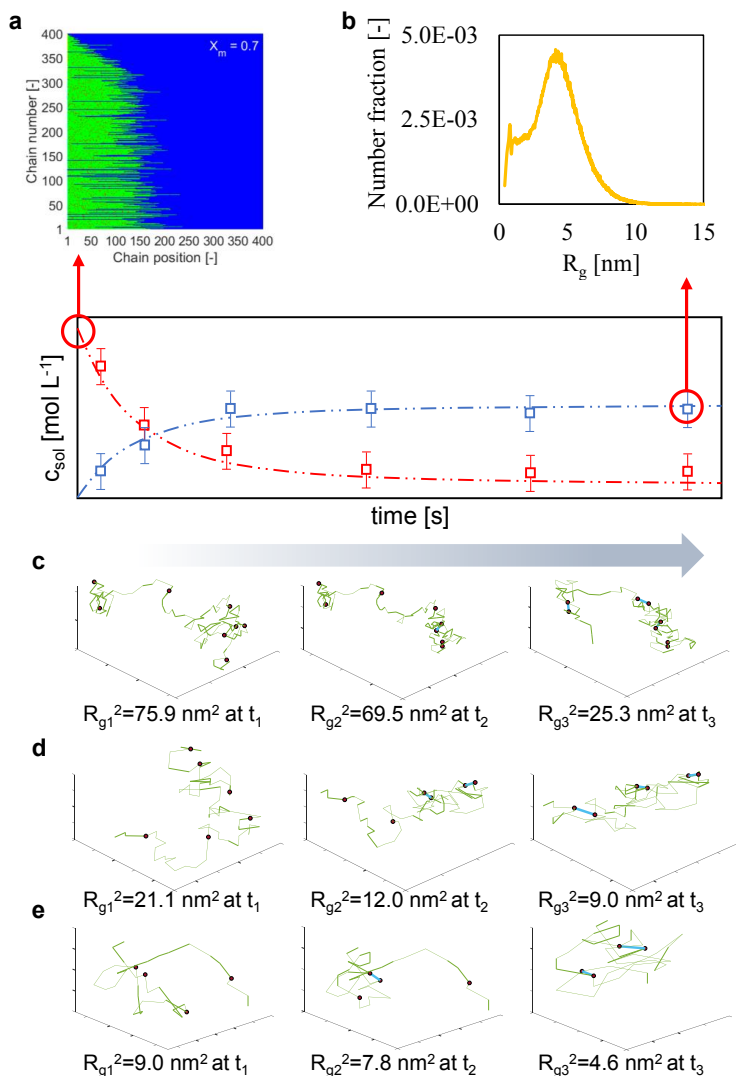
**Fig 4-4 Sample results of the kMC simulation and the information available at various stages of the simulation. a: visualization results of the modelling of the kMC polymerisation. A sample of 400 polymer chains is presented. Green dots stand for MMA units and red - for anthracene units. b: distribution of the $R_g$ values is available at the end of the folding simulation. c-e: 3D visualisation sample of 3 different chains as the folding progress.**

Not every **A-A** pair has the same likelihood to be sampled for dimerization. Pairs that are too far away from each other will not allow for **A-A** formation, however, this could change if contraction through dimerization of another **A-A** pair in the same chain has brought them closer to each other. In the present chapter, we propose

to grasp this by a fundamental dimerization apparent rate coefficient ($k_{+app,A-A}$) that is dependent on the composition of the chain:

$$k_{+app,A-A} = k_{+app,ideal}\, e^{-Bl(1-M\rho_{chain})\sqrt{d_{A-A}}}$$   eq 4-2

in which $\rho_{chain}$ is the chain crosslinking density (mol of **A₂** moieties over the mol of monomer units) of the selected chain, $l$ the bond length between two backbone monomer units, *M* and *B* are tunable system-dependent parameters. The product of $l$ and $\sqrt{d_{A-A}}$ reflects the dynamics of an ideal (Gaussian) chain. Parameter *M* is utilized to capture non-idealities concerning this Gaussian configuration, whereas parameter *B* is considered to allow for a counteracting effect through the contraction.

In the previous section (**§4.2.1),** the *z* function appeared as an empirical correction function for confinement and restricted mobility for an average chain, here the *z* function is now defined per individual chain using molecular information and forming an explicit link with the chain synthesis. Thus, **eq 4-2** can be used to sample **A**-**A** pair by **A**-**A** pair for each chain in the *k*MC ensemble, acknowledging the chain history during synthesis and folding. A sample of what the *k*₊app,A-A variation could look like as a function of time is provided in **Fig C-7** of the Appendix. Notably, this variation is consistent with the average trend in **Fig C-4**, highlighting the overall consistency of the proposed model.

From **Fig 4-4b**, it can be seen that the distributions after folding are bimodal. The first peak represents short homopolymers with a very low $R_g$ that do not participate in the folding process. The second peak represents longer copolymer chains whose $R_g$ at peak height almost coincides with the average radius of gyration. The simulation also shows that folding reduces $\langle R_g^2 \rangle$ by approximately 11%. Similarly, the variance of the RGD decreases around 20%, because longer chains contain more **A** than shorter chains, thereby folding proportionally more than shorter chains.

## 4.3    Proposed experiments for model validation

In this section, experiments will be discussed that could be used for model validation and parameter determination. First, different polymer structures that could be used are discussed, followed by experiments that could be used to determine all the necessary parameters.

To investigate the influence of various structural parameters on the system-dependent fitting parameter, *w*, a library of different polymers could be synthesised, varying different aspects of the polymer structure. Initially, several polymers could be synthesised using RAFT polymerization varying non-functional monomer to anthracene ratio (e.g. MMA:A shown in **Fig 4-5**), while keeping the chain length constant. It is expected that

up to a certain level more crosslinkers on the chain would lead to higher contractions (*g*) of the SCNP.[177]

However, it is not clear how they will affect the values of *w* and $X_{lim}$. Linker length is already known to influence

the final SCNP dimensions (longer linkers – more spherical SCNPs).[180] Therefore, it would be interesting to

investigate the influence of the linker length on the values of *w* and $X_{lim}$. To investigate the influence of the

linker length on the folding kinetics (**Fig 4-5**), a variation on the carbon linker length could be employed. It

would be ideal to have a sufficiently high variation in both to obtain a reliable trend in *w*. The current limitation

here is that the 3D visualisation of folded SCNPs and thus $R_g$ calculation in kMC code is limited by the type of

loops that the current code can process (**Fig C-8**)
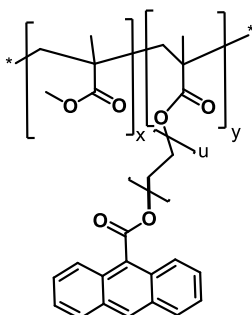


**Fig 4-5 Structure for the proposed initial library of molecules for model validation. MMA/A polymer where MMA:A ratio can be varied (x:y) as well as linker length (u).**

If an anthracene containing monomer is directly polymerized with another monomer like MMA, most certainly

there will be insufficient information on the kinetic rate coefficients for modelling the polymerization. In absence

of reliable rate coefficients, several experiments may need to be performed to adjust the polymerization rate

coefficients used in the kMC model. By tracking the conversion of the individual monomer species during

polymerization, as well as the conversion of the non-functional monomer during the homopolymerization

experiment, it would become possible to tune the rate coefficients for the kMC polymerization simulation.

Conversion of the reaction could be measured via H-NMR and polymer chain length distributions via SEC.

Once the polymer structure is known, the molar attenuation coefficient of anthracene attached to the polymer

chain needs to be measured. Knowledge of the molar attenuation coefficient is required for the calculation of

the fraction of light absorbed by the polymer chains. Molar attenuation coefficient can be determined via UV-

VIS measurements of anthracene containing polymers. UV-VIS measurement of the corresponding non-

photoreactive homopolymer could be beneficial to ensure there is no competitive absorption from moieties

other than anthracene.

Test experiments need to be conducted to test the chain free concentration limit where the intramolecular reaction occurs exclusively. The proposed model for SCNP folding is only concerned with the intramolecular reaction. However, if during the folding experiment the chain concentration in the solution is too high, intermolecular anthracene dimerization may occur, which is not accounted for by the model. Hence, test experiments need to be conducted to confirm an upper limit of the polymer concentration during the folding experiment. Anthracene containing polymer chains could be dissolved in the solvent in a variety of concentrations and folded with a 415 nm LED lamp. The resulting SCNPs could be analysed with SEC to determine unwanted intermolecular reactions through a gain in molecular weight.

The fitting parameters, α and β, from the Zimm-Stockmayer correction, need to be determined for each of the synthesised polymers to model the volume contraction factor, $g$. The dimensions of the nanoparticle, represented by the radius of gyration, $R_g$, or hydrodynamic radius, $R_H$, need to be measured at different crosslinking densities (i.e. anthracene conversions). The dimensions could, for example, be measured via diffusion-ordered NMR spectroscopy (DOSY-NMR), which would deliver $R_H$. Care needs to be taken regarding the solvent used when measuring the dimensions of the SCNPs, as the solvent can affect the SCNP size. At least three measurements are required to fit the curve for α and β.

The rate coefficient ratios for the $k_{+app,ideal}$ calculation are already available from **Chapter 2** or **3**, if the same anthracene is used, otherwise, experiments to determine rate coefficient ratios also need to be performed as described in **Chapter 2**.[264]

Finally, experiments recording the folding kinetics could be performed on each of the polymer chains determining $w$ and $X_{A,lim}$. In order to know the number of photons received by the polymer chain solution at each point in time, the experiment needs to be performed using a laser (which is available at QUT). The samples can be irradiated for different amounts of time with the same energy and the conversion is subsequently determined with the UV-VIS measurement. Since the sample size and concentration of the polymer chains in the sample is limited, it is most likely that micro cuvettes would be required to ensure a sufficient signal in the UV-VIS. H-NMR could not be used to measure the reaction conversion, as the material amounts would be too low. The resulting data on the anthracene conversion vs time (i.e. photons received) can be used to determine $w$ and $X_{A,lim}$. Collection data $w$ and $X_{A,lim}$ for different polymers trends could be identified and correlating $w$ and $X_{A,lim}$ with physical polymer parameters. Analogously, the resultant experimental data also can be used to calculate the M and B for the kMC model. Furthermore, some experiments need to be performed to evaluate the stability of the SCNP under laser irradiation to establish a

safe operation window with respect to wavelength and time of irradiation. This could be done by irradiating the SCNP with a range of wavelengths and closely monitoring the UV-VIS, NMR, SEC measurements for the subject of any undesired reactions.

## 4.4   Conclusions

Herein, a model was proposed to predict the photocycloaddition of anthracenes attached to a polymer chain based on the model developed in **Chapter 2**, where anthracene photocycloaddition was modelled free in solution. The model has the potential to reveal the interior architecture of SCNPs on an unprecedented level. The model proposed in this work would allow for obtaining the information on the average behaviour, as well as also having access to individual chain data, providing a detailed understanding of the variety of chains present in the mixture. The exact placement of photoreactive folding points along individual polymer backbones could be computationally predicted during synthesis using $k$MC simulation. 3D visualisation of the polymer chains could be done at several points during the folding process. Finally, experiments for model validation were also proposed.

As proven for the natural analogues of SCNPs, i.e. proteins, detailed knowledge of exact conformation is a prerequisite to enable comparable degree functionality in SCNPs. The proposed model would be paramount in understanding and exerting control over SCNPs. Furthermore, the proposed model would be used as a basis for developing a model for photocycloaddition of anthracenes controlling dynamic polymer networks (**Chapter 5**).

# CHAPTER 5. IMPLEMENTATION [4+4] PHOTOCYCLOADDITIONS IN NETWORK MATERIALS

In the following chapter, a preliminary literature survey was conducted to prepare the groundwork for modelling the dynamic nature of the DLW material based on anthracene units incorporated within the network using kMC. Preliminary values for the kinetic rate coefficients for modelling polymerization during DLW are given and discussed. This chapter is limited to discussing DLW without spatial variations or movement of the focus during DLW. A summary of species in the potential photoresist is presented in **§5.1**. The next sections are addressing the different types of reactions involved in the DLW process: initiation - **§5.2**, propagation - **§5.3**, termination - **§5.4** and chain transfer - **§5.5**. Finally, potential methods for the introduction of the anthracene photocycloaddition reaction are discussed in **§5.7**.

## 5.1    Summary of species

The photoresist composition considered in this chapter is based on the initial system used by another QUT student from our team, Dr Marvin Gernhardt, who aimed at generating a dynamic polymer network via DLW.[13, 32, 300] The species of the photoresist are presented in **Table 5-1**. Often, the polymerization that cures the resist is photoinitiated using Irgacure 369 (IRG369), Irgacure 819 (IRG819), 7-diethylamino-3-thenoylcoumarin (DETC) or Isopropyl thioxanthone (ITX).[86, 96] Here we use IRG369. Three types of monomers can be typically used: tri-, bi- and monofunctional monomers. Tri- and monofunctional monomers are responsible for the non-dynamic part of the polymer network, i.e. "the base network". For the role of the trifunctional monomer, either pentaerythritol tetraacrylate (PETA) or PEGTriA were proposed. The bifunctional monomer contains anthracene in its dimer form, which imparts the dynamic covalent properties – leading to adjustable material properties – to the final printed structure. Anthracene in its dimer form had to be used because using anthracene containing monofunctional monomers in the photoresist was found to be challenging. Photoresists with anthracene containing monofunctional monomers result in frequent microexplosions, restricted writing conditions and poor final polymer structure quality due to absorption of the irradiation by the anthracenes.[13] Using bifunctional monomers containing anthracene in its dimer form in the photoresist allowed to avoid the aforementioned problems.[13] Therefore, Dr Marvin Gernhardt has found that using a bifunctional monomer containing anthracene in its dimer form was an optimal solution. As a solvent propylene carbonate is used due to its high boiling point. Note that Dr Marvin Gernhardt has changed the chemical species used for his photoresist during his PhD, hence, several different tri- and bifunctional monomers were listed in **Table 5-1**.

115

The rate coefficients listed in this chapter are for the set of molecules in **Table 5-1**, however, may require updating as the photoresist composition changes in the future. Nonetheless, the model framework presented herein retains its general applicability.

In the next sections, **§5.2-§5.5**, the different reactions taking place during DLW are discussed. To simplify the writing, shorthand was used. **Tables 5-2** present the summary of the shorthand and corresponding schematic representations of different species involved in the reaction.

**Table 5-1 Summary of the species in the reference system.**
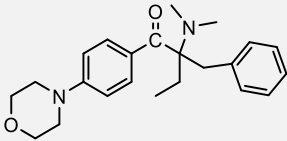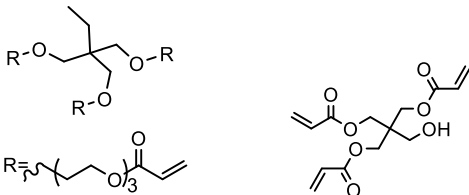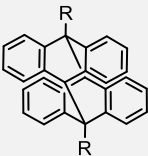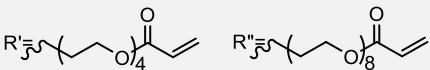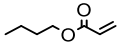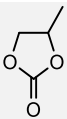
| Function | Chemical structure |
|---|---|
| Photoinitiator | <br>IRG369 |
| Trifunctional monomer | <br>PEGTriA            PETA |
| Bifunctional monomer | <br>R= R' or R"<br>anthracene dimer containing monomer |
| Monofunctional monomer | <br>butyl acrylate |
| Solvent | <br>propylene carbonate |

**Table 5-2 Summary of the shorthand and schematic representations of the monomers (left) and the species with the involvement of the monomers at the end of the radical (right).**

| Shorthand | Schematic representation | Shorthand | Schematic representation |
|---|---|---|---|
| $C$ |  | $\underset{\sim}{\approx}C\,\cdot$ |  |
| $C^{\approx}$ |  | $\underset{\sim}{\approx}C\underset{\cdot}{.}^{\approx}$ |  |
| $C_{\approx}^{\approx}$ |  | $\sim C\,\cdot$ |  |
| $C\,\cdot$ |  | $D\,\cdot$ |  |
| $D$ |  | $\sim D\,\cdot$ |  |
| $D^{\approx}$ |  | $\underset{\sim}{\approx}D\,\cdot$ |  |
| $X$ |  | $\sim X\,\cdot$ |  |
| $X\,\cdot$ |  | | |

## 5.2    Initiation reactions

The polymerisation process in the DLW can be divided into two phases: light phase (pulse duration) and dark phase (dark time). A laser used for DLW typically has frequencies in the range 80 MHz-1kHz[86, 301-302] with a typical laser pulse duration of around 100 fs and wavelength in the near-IR range.[21] Thus, the pulse duration is extremely short in comparison to the dark time. As a first approximation, it may be beneficial to model the light phase as a single event resulting in several initiator molecules reaching the excited state.

During the light phase, a photoresist is subject to irradiation, leading to photoinitiator excitation and subsequent photocleavage. First, the number of photoinitiator molecules excited by two-photon absorption per pulse, $n^{(2)}$, needs to be estimated. Since no spatial variation is modelled at first, **eq 1-10** (duplicated below; introduced in **§1.3.3**) can be used.

$$n^{(2)} = \frac{1}{2}\sigma_{2PA,\lambda}N_g\left(\frac{I}{h\nu}\right)^2$$

eq 1-10[85-86]

where $I$ – light intensity (W cm$^{-2}$), $N_g$ - number of molecules in the ground state, $h\nu$ - photon energy, J, and, finally, $\sigma_{2PA,\lambda}$ - two-photon absorption cross-section at wavelength $\lambda$, GM ($1GM = 10^{-50}$cm$^4$ s photon$^{-1}$). A two-photon absorption cross-section represents the probability of the two-photon absorption event for a given molecule at a wavelength $\lambda$.[87] $\sigma_{2PA,\lambda}$ can be measured experimentally using, for example, a Z-scan technique, where transmittance through the sample is measured.**[88]** $\sigma_{2PA,\lambda}$ was measured for IRG369 and was found to be either 27 GM or 7 GM for the peak wavelength depending on the experimental technique used (see **Table 5-3**).[88] The reported peak wavelength is 318 nm for 27 GM and 335 nm for 7 GM measurements.[88] The irradiation wavelength in the DLW set up used by Dr Marvin Gernhardt, however, is 780 nm.[303] Under the assumption that the shapes of absorption spectra for one proton and two-photon absorption are the same, Fischer et al. have been able to estimate the $\sigma_{2PA,\lambda}$ value for IRG369 at 800 nm to be 0.27 GM using: [86, 88]

$$\sigma_{2PA,\lambda} = \sigma_{2PA,\text{peak}}\frac{\sigma_{1PA,\lambda/2}}{\sigma_{1PA,peak}}$$

eq 5-1[86]

where $\sigma_{2PA,\lambda}$ is two-photon absorption cross-section at wavelength λ, GM, $\sigma_{2PA,\text{peak}}$ - two-photon absorption cross-section at peak wavelength, GM, $\sigma_{1PA,peak}$ - one-photon absorption cross-section at peak wavelength, GM, $\sigma_{1PA,\lambda/2}$ - one-photon absorption cross-section at wavelength λ/2, GM.

Using the same method, $\sigma_{2PA,\lambda}$ at 780 nm was also be approximated. According to **Fig E-1** in the Appendix, the ratio of absorbances at the peak wavelength and 390 nm is $9.22 \times 10^{-3}$, thus yielding an approximation of 0.25 GM for $\sigma_{2PA,780\text{ nm}}$.

**Table 5-3 Initiation reactions.**

| Reaction | | Parameter | Value | Reference |
|---|---|---|---|---|
| Photoinitiator dissociation | $I_2 \rightarrow I_a \cdot \ + \ I_b \cdot$ | $\Phi$ | $\Phi \approx 0.3$ $\Phi \approx 0.2$ (typical value) $\Phi = 0.3$ | [304] [305] [306] |
| | | $\sigma_{2PA,\,peak}$ | $27 GM\ (or\ 7GM)$ | [88] |
| | | $\dfrac{\sigma_{1PA,\,390}}{\sigma_{1PA,\,peak}}$ | $9.22 \times 10^{-3}$ | in-house UV-VIS (**Fig D-1**) |
| Reaction of $I_a \cdot$ radical with free monomers | $I_a \cdot + C \ \rightarrow C \cdot$ $I_a \cdot + D \ \rightarrow D \cdot$ | $k_{init\ 1C}$ $k_{init\ 1D}$ | $k_{prop\ CC}$ $k_{prop\ DD}$ | This work This work |
| | $I_a \cdot + X \ \rightarrow X \cdot$ | $k_{init\ 1X}$ | $3.6 \times 10^5\ M^{-1}s^{-1}$ in acetonitrile | [93] |
| Reaction of $I_b \cdot$ radical with free monomers | $I_b \cdot + C \ \rightarrow C \cdot$ $I_b \cdot + D \ \rightarrow D \cdot$ | $k_{init\ 2C}$ $k_{init\ 2D}$ | $k_{prop\ CC}$ $k_{prop\ DD}$ | This work This work |
| | $I_b \cdot + X \ \rightarrow X \cdot$ | $k_{init\ 2X}$ | $6.1 \times 10^6\ M^{-1}s^{-1}$ in acetonitrile | [307] |
| Reaction of photoinitiator radicals with O₂ | $I_a \cdot + \ O_2 \ \rightarrow I_a - O - O \cdot$ | $k_{I_a+O_2}$ | on the order of $10^9$ (approximated by other benzoyl radicals) | [93] |
| | $I_b \cdot + \ O_2 \ \rightarrow product$ | $k_{I_b+O_2}$ | $4.3 \times 10^9\ M^{-1}s^{-1}$ in acetonitrile | [307] |

Once the number of photoinitiator molecules excited by two-photon absorption is known, the quantum yield is needed to determine the number of molecules that will decompose and form initiating radicals. The dissociation quantum yield for IRG369 was determined to be around 0.3.[304, 306] An approximated value of 0.2 has also been used in the simulation by Kenning et al. to model photopolymerization in thick polymer systems under LED irradiation.[305] IRG369 undergoes photocleavage forming two different radicals, $I_a \cdot$ and $I_b \cdot$, shown in **Fig 5-1**, where both radicals can initiate the polymerization reaction. The rate coefficients for the initiator radicals have been measured in acetonitrile for propagation with butyl acrylate (monofunctional monomer here).[93, 307] Rate coefficients for the initiator radials propagation with the other two monomers (bi- and trifunctional monomers) are not known. Therefore, we propose to estimate their rate coefficient values as those belonging to a corresponding homopropagation of the main chain radical.
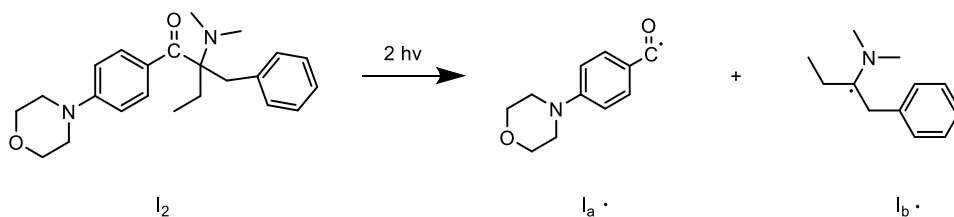
**Fig 5-1 Photoinitiator IRG369 dissociation scheme following two-photon absorption event.**

Finally, an important side reaction that takes place during DLW is the reaction of the initiator radical species with traces of molecular oxygen. Here the information is also limited: only the reaction between the $I_b \cdot$ initiator radical and oxygen has a known rate coefficient value in acetonitrile.[307] For the $I_a \cdot$ initiator radical, the value could only be appoximed by using a value with the same order of magnitude as for other benzyol radicals. While for a first approximation the polymerisation reaction during DLW could be modelled without the presence of oxygen, it is important to account for this reaction later on because the competition between the radical generation and consumption determines the possibility for the successful polymerisation reaction to occur.[101]

## 5.3   Propagation

A multitude of different propagation reactions takes place in the focal point owing to the number of monomer species. The summary of the reactions is listed in **Table 5-4-Table 5-7**. **Table 5-4** shows the propagation of the main chain radical through the addition of any free monomer listed in **Table 5-1**, i.e. monomer which has not undergone a reaction yet. An accurate rate coefficient is only available for homopropagation of the monofunctional monomer, butyl acrylate (**Table 5-4**). With the knowledge of the pre-exponential factor, $A$, and activation energy, $E_a$, the rate coefficient can be calculated via the Arrhenius' law:

$$k = Ae^{-\frac{E_a}{RT}}$$

eq 5-2

where $k$ is a rate coefficient, R is the universal gas constant (8.314 J K$^{-1}$mol$^{-1}$) and T – the temperature in K.



*tert*-butyl acrylate
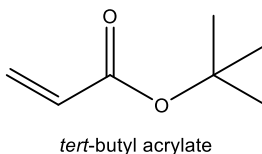
**Fig 5-2 Structure of tert-butyl acrylate that could be used to approximate homopropagation of the PETA (trifunctional monomer).**

For homopropagation of the trifunctional monomer, the rate coefficients are not known. Therefore, it is proposed that the reactivity of the trifunctional monomer could be potentially approximated by viewing each branch of the trifunctional monomer as three separate monofunctional monomers. Thus, the reactivity of each

of the double bonds in the trifunctional monomer is viewed separately. Applied to trifunctional monomer PETA, the monomer is then simplified into three acrylates, whose reactivity can be approximated by monofunctional acrylate monomers. For example, the homopropagation of monofunctional tert-butyl acrylate (see **Fig 5-2**) is known (**Table 5-4**). Tert-butyl acrylate resembles part of the PETA structure, with the exception of having one less carbon along the chain. After approximation of the reactivity of the individual functional groups, the overall reactivity of the trifunctional monomer would be three times the reactivity of one of its functional groups (e.g. $k_{prop\,CC} \approx 3 \times k_{prop\,XX}$). The homopropagation rate coefficient for bifunctional monomer is not known, therefore, a similar strategy can be used for a trifunctional monomer.

Cross propagation between the different types of monomers is also possible. To calculate the cross propagation of different monomer combinations a monomer reactivity ratio, *r*, is required. Such a monomer reactivity ratio is defined as:

$$r_{CD} = \frac{k_{propCC}}{k_{propCD}} \qquad \qquad \text{eq 5-3}$$

where $r_{CD}$ – reactivity ratio between monomer C and D, $k_{propCC}$ – homopropagation reactivity of monomer C and $k_{propCD}$ – cross propagation rate coefficient for the propagation of a macroradical with monomer unit C at the end of the radical species through the addition of the free monomer D. Rate coefficients for cross propagation between these three different monomers are also unavailable, which is not surprising because the homopropagation rate coefficients are also lacking. Therefore, reactivity ratios for all the combinations must be approximated.

Apart from the addition of unreacted free monomers, the main chain radical can propagate through the addition of dangling bonds of tri- and bifunctional monomers (**Table 5-5**). None of the rate coefficients for the reactions listed are known, therefore, approximations must be made. Inspiration could be taken from the corresponding reactions in **Table 5-4**, for which the propagation rate coefficients can be adjusted to reflect the additional steric hindrance present. Similarly to the situation in **Table 5-5**, rate coefficients for reactions in **Table 5-6** and **Table 5-7** could also be approximated.

**Table 5-4 Reactions considering the propagation through the addition of the mono-/bi-/trifunctional free monomer molecule (C, D, X).**

| Reaction equation | | Rate coefficient | Intrinsic reactivity value | Reference |
|---|---|---|---|---|
| Trifunctional monomer ($\sim C \cdot$) at the end of the radical | $\sim C \cdot + C \ \to \sim C \cdot$ | $k_{prop\,CC}$ | Data for tert-butyl acrylate $E_a = 16.45\ kJmol^{-1}$ $A = \ 11.2 \times 10^6\ Lmol^{-1}s^{-1}$ | [308] |
| | | | $3 \times k_{prop\,XX}$ | this work |
| | $\sim C \cdot + D \ \to \sim D \cdot$ | $k_{prop\,CD}$ | $\dfrac{k_{prop\,CC}}{r_{CD}}$ | this work |
| | $\sim C \cdot + X \ \to \sim X \cdot$ | $k_{prop\,CX}$ | $\dfrac{k_{prop\,CC}}{r_{CX}}$ | this work |
| bifunctional monomer (D) at the end | $\sim D \cdot + C \ \to \sim C \cdot$ | $k_{prop\,DC}$ | $\dfrac{k_{prop\,DD}}{r_{DC}}$ | this work |
| | $\sim D \cdot + D \ \to \sim D \cdot$ | $k_{prop\,DD}$ | $2 \times k_{prop\,XX}$ | this work |
| | $\sim D \cdot + X \ \to \sim X \cdot$ | $k_{prop\,DX}$ | $\dfrac{k_{prop\,DD}}{r_{DX}}$ | this work |
| monofunctional monomer (X) at the end | $\sim X \cdot + C \ \to \sim C \cdot$ | $k_{prop\,XC}$ | $\dfrac{k_{prop\,XX}}{r_{XC}}$ | this work |
| | $\sim X \cdot + D \ \to \sim D \cdot$ | $k_{prop\,XD}$ | $\dfrac{k_{prop\,XX}}{r_{XD}}$ | this work |
| | $\sim X \cdot + X \ \to \sim X \cdot$ | $k_{prop\,XX}$ | $E_a = 17.9\ kJmol^{-1}$ $A = 2.21 \times 10^7\ Lmol^{-1}s^{-1}$ | [309] |

Once intrinsic reactivity values are estimated, it is necessary to take into account the diffusional limitations imposed on the possible reaction.[274] Apparent rate coefficients, $k_a$, can be calculated as a function of the intrinsic reactivity and diffusional limitation (expressed in a form of a diffusional rate coefficient, $k_{diff}$).[274]

$$\frac{1}{k_a} = \frac{1}{k_{prop}} + \frac{1}{k_{diff}} \qquad\qquad \text{eq 5-4}[274]$$

For intramolecular reactions, distance rules, available via an in-house UGent algorithm, can be used to check if the potential reaction pair is close enough to react. The distance rule calculates the shortest path along the polymer network between the potential reaction pair as well as the number of crosslinks along that path.[274] The combination of these two variables decides whether the reaction is probable.[274]

**Table 5-5 Reactions considering the propagation of main chain radical through the addition of the dangling double bond.**

| | Reaction equation | Rate coefficient | Intrinsic reactivity value | Reference |
|---|---|---|---|---|
| **Tri-functional monomer (C) at the end** | $\sim C \cdot + C^{\approx} \rightarrow {}^{\approx}_{\sim}C \cdot$ | $k_{PDB\,CC_1}$ | $k_{prop\,CC}$ | this work |
| | $\sim C \cdot + C^{\approx}_{\approx} \rightarrow {}^{\approx}_{\sim}C.^{\approx}$ | $k_{PDB\,CC_2}$ | $k_{prop\,CC}$ | this work |
| | $\sim C \cdot + D^{\approx} \rightarrow {}^{\approx}_{\sim}D \cdot$ | $k_{PDB\,CD_1}$ | $k_{prop\,CD}$ | this work |
| **Bi-functional monomer (D) at the end** | $\sim D \cdot + C^{\approx} \rightarrow {}^{\approx}_{\sim}C \cdot$ | $k_{PDB\,DC_1}$ | $k_{prop\,DC}$ | this work |
| | $\sim D \cdot + C^{\approx}_{\approx} \rightarrow {}^{\approx}_{\sim}C.^{\approx}$ | $k_{PDB\,DC_2}$ | $k_{prop\,DC}$ | this work |
| | $\sim D \cdot + D^{\approx} \rightarrow {}^{\approx}_{\sim}D \cdot$ | $k_{PDB\,DD_1}$ | $k_{prop\,DD}$ | this work |
| **Mono-functional monomer (X) at the end** | $\sim X \cdot + C^{\approx} \rightarrow {}^{\approx}_{\sim}C \cdot$ | $k_{PDB\,XC_1}$ | $k_{prop\,XC}$ | this work |
| | $\sim X \cdot + C^{\approx}_{\approx} \rightarrow {}^{\approx}_{\sim}C.^{\approx}$ | $k_{PDB\,XC_2}$ | $k_{prop\,XC}$ | this work |
| | $\sim X \cdot + D^{\approx} \rightarrow {}^{\approx}_{\sim}D \cdot$ | $k_{PDB\,XD_1}$ | $k_{prop\,XD}$ | this work |

**Table 5-6 Reactions considering the propagation of dangling double bond radical through the addition of the free monomer.**

| Reaction equation | | Rate coefficient | Intrinsic reactivity value | Reference |
|---|---|---|---|---|
| **Tri-functional monomer (C) at the end #1** | $\widetilde{\sim}C \cdot \ + \ C \ \rightarrow \sim C \cdot$ | $k_{PDDB\ C_1C}$ | $k_{prop\ CC}$ | this work |
| | $\widetilde{\sim}C \cdot \ + \ D \ \rightarrow \sim D \cdot$ | $k_{PDDB\ C_1D}$ | $k_{prop\ CD}$ | this work |
| | $\widetilde{\sim}C \cdot \ + \ X \ \rightarrow \sim X \cdot$ | $k_{PDDB\ C_1X}$ | $k_{prop\ CX}$ | this work |
| **Tri-functional monomer (C) at the end #2** | $\widetilde{\sim}C.^{\approx} + \ C \ \rightarrow \sim C \cdot$ | $k_{PDDB\ C_2C}$ | $k_{prop\ CC}$ | this work |
| | $\widetilde{\sim}C.^{\approx} \ + \ D \ \rightarrow \sim D \cdot$ | $k_{PDDB\ C_2D}$ | $k_{prop\ CD}$ | this work |
| | $\widetilde{\sim}C.^{\approx} \ + \ X \ \rightarrow \sim X \cdot$ | $k_{PDDB\ C_2X}$ | $k_{prop\ CX}$ | this work |
| **Bi-functional monomer (D) at the end** | $\widetilde{\approx}D \cdot + \ C \ \rightarrow \sim C \cdot$ | $k_{PDDB\ D_1C}$ | $k_{prop\ DC}$ | this work |
| | $\widetilde{\approx}D \cdot + \ D \ \rightarrow \sim D \cdot$ | $k_{PDDB\ D_1D}$ | $k_{prop\ DD}$ | this work |
| | $\widetilde{\approx}D \cdot + \ X \ \rightarrow \sim X \cdot$ | $k_{PDDB\ D_1X}$ | $k_{prop\ DX}$ | this work |

**Table 5-7 Reactions considering the propagation of dangling double bond radical through the addition of the dangling double bond.**

| | Reaction equation | Rate coefficient | Intrinsic reactivity value | Reference |
|---|---|---|---|---|
| Tri-functional monomer (C) at the end | $\approx C\cdot \ + \ C\approx \ \rightarrow \ \approx C\cdot$ | $k_{PDDB\,C_1C_1}$ | $k_{prop\,CC}$ | this work |
| | $\approx C\cdot \ + \ C\approx\!\approx \ \rightarrow \ \approx C.\approx$ | $k_{PDDB\,C_1C_2}$ | $k_{prop\,CC}$ | this work |
| | $\approx C\cdot \ + \ D\approx \ \rightarrow \ \approx D\cdot$ | $k_{PDDB\,C_1D_1}$ | $k_{prop\,CD}$ | this work |
| Tri-functional monomer (C) at the end #2 | $\approx C.\approx \ + \ C\approx \ \rightarrow \ \approx C\cdot$ | $k_{PDDB\,C_2C_1}$ | $k_{prop\,CC}$ | this work |
| | $\approx C.\approx \ + \ C\approx\!\approx \ \rightarrow \ \approx C.\approx$ | $k_{PDDB\,C_2C_2}$ | $k_{prop\,CC}$ | this work |
| | $\approx C.\approx \ + \ D\approx \ \rightarrow \ \approx D\cdot$ | $k_{PDDB\,C_2D_1}$ | $k_{prop\,CD}$ | this work |
| Bi-functional monomer (D) at the end | $\approx D\cdot + \ C\approx \ \rightarrow \ \approx C\cdot$ | $k_{PDDB\,D_1C_1}$ | $k_{prop\,DC}$ | this work |
| | $\approx D\cdot + \ C\approx\!\approx \ \rightarrow \ \approx C.\approx$ | $k_{PDDB\,D_1C_2}$ | $k_{prop\,DC}$ | this work |
| | $\approx D\cdot + \ D\approx \ \rightarrow \ \approx D\cdot$ | $k_{PDDB\,D_1D_1}$ | $k_{prop\,DD}$ | this work |

## 5.4 Termination reactions

A summary of possible termination reactions considered here is provided in **Table 5-8**. Termination reactions considered are termination by a combination of radical species with each other, termination by radical trapping and termination by reaction with oxygen. Termination by disproportionation is not considered here for now. Some information regarding termination reaction rate coefficients was found for the termination of butyl acrylate and methyl acrylate (see **Table 5-8**). However, we did not find the termination reaction rate coefficients for the radical chains with tri- and bifunctional monomer at the end, therefore, approximations need to be made. In the first instance, constant termination rate coefficients can be assumed. Later, diffusional limitations can be added to optimize the rate coefficients.

The termination by combination is controlled by two types of diffusion translational and segmental (as illustrated in **Fig 5-3**).[310] The length of the polymer chains influences which of the two types of diffusions is rate-determining, resulting in three different regimes of the termination rate coefficient behaviour (**Fig 5-3**).[310] For short chain lengths, rate-determining is translational diffusion, for medium length – segmental.[310] Once

long chain lengths have been reached, the gel effects make translational diffusion rate-determining once again.[310]
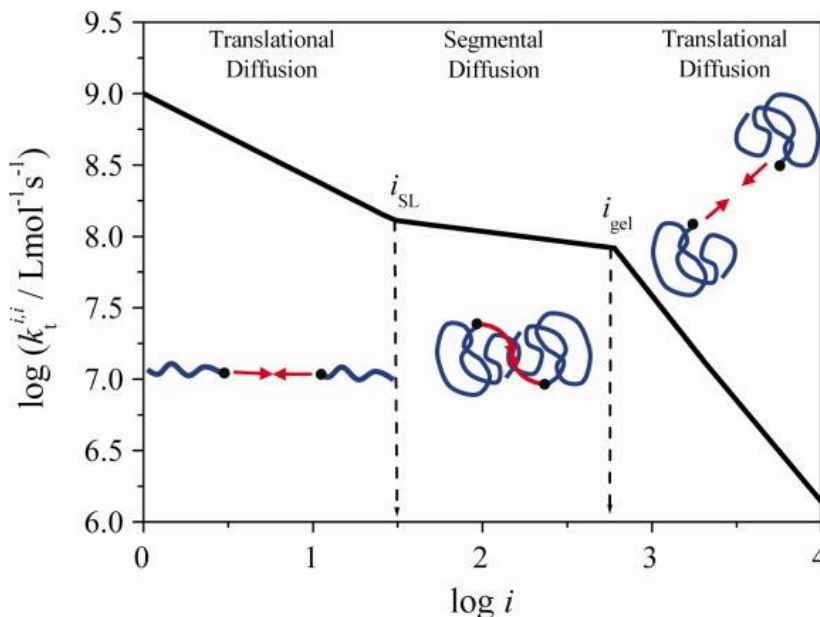


**Fig 5-3 Illustration of changes in termination rate coefficient vs chain length. Reprinted with permission from Ref.[310]**

For linear polymerisations, empirical correlations have been developed to account for the three regimes in the termination reactivity as a function of the chain length. For example, for methyl acrylate at 50 °C Johnston-Hall and Monteiro found the complete correlation to be:

$For\ i < i_{gel}$

$$k_t^{i,i} = k_t^0 \times i^{-\alpha_s}\ for\ i_x < i_{SL}$$ eq 5-5[310]

$$k_t^{i,i} = k_t^0 \times i_{SL}^{\alpha_L - \alpha_s} \times i^{-\alpha_L}\ for\ i_x \geq i_{SL}$$ eq 5-6[310]

$For\ i \geq i_{gel}$

$$k_t^{i,i} = k_t^0 \times i_{gel}^{\alpha_L - \alpha_s} \times i^{-\alpha_{gel}}\ for\ i_x < i_{SL}$$ eq 5-7[310]

$$k_t^{i,i} = k_t^0 \times i_{SL}^{\alpha_L - \alpha_s} \times i_{gel}^{\alpha_L - \alpha_L} \times i^{-\alpha_{gel}}\ for\ i_x \geq i_{SL}$$ eq 5-8[310]

where the short chain length exponent, $\alpha_s$, is $0.78 \pm 0.04$, the medium chain length exponent, $\alpha_l$, - $0.15 \pm 0.03$, and the long chain length exponent, $\alpha_{gel}$, is $(0.81x - 0.05) \pm 0.07$. The chain length for the first regime change is $i_{SL} \approx 18$ and the second one is:

$$i_{gel} = 6.90X^{-2.20}$$ eq 5-9[310]

where $X$ is the monomer conversion (or equivalently, the polymer mass fraction in case of solution polymerization). They also proposed to calculate the termination rate coefficient by a combination between two radials of different chain lengths to be calculated as:

$$k_t^{i,j} = \left(k_t^{i,i} \times k_t^{j,j}\right)^{1/2}$$ eq 5-10[310]

For butyl acrylate polymerization in toluene, at ambient pressure in the temperature range of -40 °C to 60 °C the correlation was found to be:

$$k_t(i,i) = k_t(1,1)i^{-\alpha_s} \text{ when } i \leq i_c$$ eq 5-11[311]

$$k_t(i,i) = k_t(i,i)i_c^{-\alpha_s+\alpha_l}i^{-\alpha_l} = k_t^0 i^{-\alpha_l} \text{ when } i > i_c$$ eq 5-12[311]

where $i$ stands for chain length, $i_c$ stands for a "cut-off" chain length where the regime changes from short to long chain length and is equal to $30 \pm 5$, $\alpha_s = 0.85 \pm 0.09$, $\alpha_l = 0.16 \text{ or } 0.22 \pm 0.07$. [311]

Determining the chain length in the network, however, may be ambiguous and/or difficult, obstructing the use of the correlations stated above. In a recent publication by De Keer et al., diffusional limitations were represented by diffusional rate coefficients, which together with the intrinsic rate coefficients made up an apparent rate coefficient (**eq 5-4**).[274] Additionally, distance rules were used for intramolecular reactions as was already described in **§5.3**.

Termination by radical trapping is also possible during DLW. Radical trapping occurs due to increasing polymer network density restricting some of the radical ability to participate in the further reaction.[312] However, no rate coefficients are known and, therefore, more research is needed to estimate the values. Due to the presence of oxygen in the focal point, termination by reaction with oxygen is possible during DLW. The literature of the reaction rate coefficient for the reaction of radical species with oxygen is limited, only orders of magnitude for some reactions were found. These orders of magnitude are presented in **Table 5-8**.

**Table 5-8 Reactions considering the termination by combination.**

| Reaction equation | | Rate coefficient | Intrinsic reactivity value | Reference |
|---|---|---|---|---|
| Termination by combination [a] | $\cdot C\sim_i + \cdot C\sim_j \rightarrow P$ | $k_{tCC}(i,j)$ | at 50C for methyl acrylate $Log k_t^0 = 9.0$ or $k_{tXX}(i,j)$ | 310 |
| | $\cdot C\sim_i + \cdot D\sim_j \rightarrow P$ | $k_{tCD}(i,j)$ | $k_{tXX}(i,j)$ | this work |
| | $\cdot C\sim_i + \cdot X\sim_j \rightarrow P$ | $k_{tCX}(i,j)$ | $k_{tXX}(i,j)$ | this work |
| | $\cdot D\sim_i + \cdot D\sim_j \rightarrow P$ | $k_{tDD}(i,j)$ | $k_{tXX}(i,j)$ | this work |
| | $\cdot D\sim_i + \cdot X\sim_j \rightarrow P$ | $k_{tDX}(i,j)$ | $k_{tXX}(i,j)$ | this work |
| | $\cdot X\sim_i + \cdot X\sim_j \rightarrow P$ | $k_{tXX}(i,j)$ | $E_a = 8.4 kJmol^{-1}$ $A = 1.3 \times 10^{10} Lmol^{-1}s^{-1}$ for $k_t(1,1)$ in toluene, at ambient pressure, -40C to 60C | 311 |
| Termination by combination with the initiator [a] | $\cdot C\sim_i + I\cdot \rightarrow P$ | $k_{tCI}(i,I)$ | $k_{tCC}(i,1)$ | this work |
| | $\cdot D\sim_i + I\cdot \rightarrow P$ | $k_{tDI}(i,I)$ | $k_{tCC}(i,1)$ | this work |
| | $\cdot X\sim_i + I\cdot \rightarrow P$ | $k_{tXI}(i,I)$ | $k_{tCC}(i,1)$ | this work |
| Radical trapping | $\cdot P \rightarrow (\cdot P)$ | $k_{trap}$ | | 312 |
| Termination by reaction with oxygen[b] | $\cdot P + O_2 \rightarrow POO\cdot$ | $k_{PO2}$ | order of $10^9\ M^{-1}s^{-1}$ for trapped radicals | 312 |
| | $POO\cdot + Y \rightarrow$ $\rightarrow POOH + Y\cdot$ | $k_{tranOY}$ | order of $10^8\ M^{-1}s^{-1}$ | 312 |
| | $POO\cdot + POO\cdot \rightarrow$ $\rightarrow POOOOP$ | $k_{POO2}$ | order of $10^4 - 10^8\ M^{-1}s^{-1}$ for methacrylate | 312 |

a - here $\cdot C\sim_{i\ or\ j}$, $\cdot D\sim_{i\ or\ j}$, $\cdot X\sim_{i\ or\ j}$ can represent any of the C, D and X radical species as described in **Table 5-2**.

b – here Y can represent any of the C, D and X non-radical species and $\cdot P$ - any of the C, D and X radical species.

## 5.5 Chain transfer to monomer reactions

Chain transfer reactions can take place during the DLW. These reactions are written in a summarised format (i.e. no distinction between different types of radicals) in **Table 5-9** below. Rate coefficients for chain transfer were found only for butyl acrylate (chain transfer to monomer), as expected. Therefore, the butyl acrylate transfer rate coefficient value would need to be used to approximate values for all chain transfer reactions. No intentional chain transfer agents are present in the model. Chain transfer to the initiator, solvent and polymer is not considered here for the simplicity of the model. However, it has been noted that chain transfer to a polymer can become significant further along the polymerization process.[313] Therefore, the inclusion of chain transfer to polymer could be considered in the future. A limited number of rate coefficients for chain transfer to polymer for butyl acrylate are available.[314]

**Table 5-9 Reactions considering the chain transfer to monomer.**

| Reaction equation | Rate coefficient | Intrinsic reactivity value | Reference |
|---|---|---|---|
| $\cdot C\sim_i + C \rightarrow C\sim_i + \cdot C$ | $k_{trCC}$ | $k_{trXX}$ | this work |
| $\cdot C\sim_i + D \rightarrow C\sim_i + \cdot D$ | $k_{trCD}$ | $k_{trXX}$ | this work |
| $\cdot C\sim_i + X \rightarrow C\sim_i + \cdot X$ | $k_{trCX}$ | $k_{trXX}$ | this work |
| $\cdot D\sim_i + C \rightarrow D\sim_i + \cdot C$ | $k_{trDC}$ | $k_{trXX}$ | this work |
| $\cdot D\sim_i + D \rightarrow D\sim_i + \cdot D$ | $k_{trDD}$ | $k_{trXX}$ | this work |
| $\cdot D\sim_i + X \rightarrow D\sim_i + \cdot X$ | $k_{trDX}$ | $k_{trXX}$ | this work |
| $\cdot X\sim_i + C \rightarrow X\sim_i + \cdot C$ | $k_{trXC}$ | $k_{trXX}$ | this work |
| $\cdot X\sim_i + D \rightarrow X\sim_i + \cdot D$ | $k_{trXD}$ | $k_{trXX}$ | this work |
| $\cdot X\sim_i + X \rightarrow X\sim_i + \cdot X$ | $k_{trXX}$ | chain transfer to monomer $E_A = 32.6\ (\pm 0.8)\ kJmol^{-1}$ $A = 2.9(\pm 0.9) \times 10^5\ dm^3mol^{-1}s^{-1}$ | [315] |

a – here $\cdot C\sim_i$, $\cdot D\sim_i$, $\cdot X\sim_i$ can represent any of the C, D and X radical species as shown in **Table 5-2**.

## 5.6    Non-uniformities in space and time

So far the polymerization reactions were discussed with no spatial variations of concentration and temperature in mind. However, the polymerisation reaction during DLW occurs in very small volumes (nm scale), therefore, diffusion will have a significant effect on the outcome of the DLW.[220] The diffusion of species in and out of the focal volume in combination with variation in the writing conditions (i.e. pulse frequency, writing speed, energy per pulse) results in effects such as focal point duplication, voxel growth and defines whether no polymer network structures will be formed, to begin with (**§1.3.3**).[100-101] Furthermore, spatial variations in irradiation intensity during light times within the focal volume are also present (**Fig 1-9c**). Consequently, it is reasonable to expect that the structure of the formed polymer network could be affected.

Inclusion of spatial variation of the concentration of species in the kMC model may be challenging, as nearly all kMC models assume perfect mixing. A simple first approximation approach could treat diffusion in and out of reaction volume as a "pseudo-reaction", where the rate coefficient for the "pseudo-reaction" would be a function of the diffusion coefficient. The result of the "diffusion reaction" would be an addition or exclusion of the molecule from the modelled reaction volume. Subdivision of the reaction volume into several subvolumes (by analogy with parallel kMC (**§1.5.2**)) could to some degree be used to mimic spatial variations in the concentration of species as well as photons inside the focal point (**Fig 5-4**). The results could then be used to construct the spatial profile of the network in 1D, 2D or 3D like a puzzle (**Fig 5-4**). Of course, this solution is only an approximation and is most likely to be computationally demanding, thus research into more sophisticated and more optimal methods would need to be explored.

So far the discussion only considered polymerisation of the voxel in general, however, polymer structures are written on a substrate, e.g. glass slide. Therefore, the influence of the substrate on the polymerization process needs to be investigated. The presence of the substrate limits the diffusion of the reacting species in and out of the focal point as the diffusion of the species is not possible through the substrate. Additionally, the relative position of the focal point to the substrate-photoresist interphase during DLW can be different hence affecting the adhesion of the written polymer structures to the substrate as well as whether the polymer structures will be written successfully or not.

Spatial temperature changes during DLW have been explored experimentally by Mueller et al.[316] They found that under optimal writing conditions, the average local increase in temperature was only a few degrees (~5K), however, once the conditions were no longer optimal, a significant temperature increase (~300K) and micro-explosions were observed. [316] Therefore, the importance of the inclusion of temporal and spatial temperature

variations at various writing conditions (i.e. pulse frequency, writing speed, energy per pulse) for successful

DLW (and as a consequence polymer network structure) can not be underestimated.
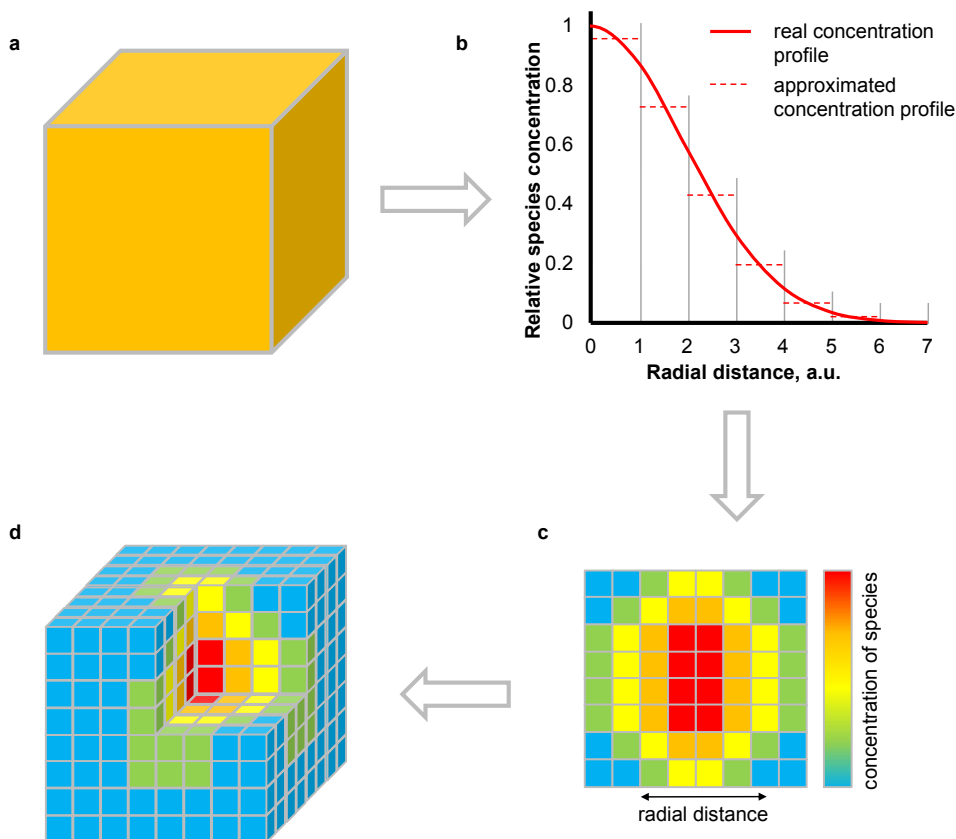


**Fig 5-4 Illustration of the proposed implementation of the spatial resolution. a: first the whole focal point region is averaged (no spatial resolution); b: subdivision into subvolumes to obtain cross-section (1D); c: assembly into a 2D representation; d: assembly into a 3D representation.**

## 5.7 Anthracene reactions in the network environment

After the generation of the main polymer network structure, we need to implement the anthracene reversible

cycloaddition reaction. The anthracene reversible cycloaddition takes place at two points in time: during DLW

and post-DLW. In this section, anthracene reaction during the DLW and potential implementation of the

reaction into kMC modelling is discussed (**§5.7.1**). Next, the implementation of post-DLW photodimerization of

anthracene in the polymer network for kMC is discussed (**§5.7.2**).

### 5.7.1 During the DLW

Following the experimental data collected in the papers by Gernhardt et al.,[13, 32] it is clear that anthracene dimer is cleaved during the DLW procedure. Several potential reasons could be responsible for the cleavage during DLW, making it difficult to include it into the kMC model for DLW. The first potential reason is that anthracene dimer cleavage reaction is known to be able to proceed thermally.[49] Uppal et al. have predicted local temperature increase during DLW in their model,[97] and Mueller et al. – experimentally.[316] A second potential reason is the possibility of multi-photon absorption due to high photon concentrations during the DLW which could lead to anthracene dimer photocleavage. Experimental data (**Fig 5-5**) shows that the amount of anthracene dimer cleaved depends on the DLW writing parameters (e.g. writing speed and laser power).[32] Higher writing speed and laser power lead to more anthracene dimer cleavage.[32] It is not clear to which proportion these two routes could be taking place or if another source of anthracene dimer cleavage is present. While thermal cleavage of dimer during writing could be introduced into the model, it may be more difficult to do so for the multi-photon absorption. Therefore, it might be beneficial to simplify the model and introduce the anthracene dimer cleavage post-writing manually. We could cleave a specific number of bonds statistically distributed through the network post-writing in one go. The drawback of this approach would be that, since the dimer cleavage occurs during the DLW, the formed anthracenes could potentially drift too far apart, which would not be captured by the model. If two anthracenes drift too far apart, the probability that they would not be able to participate in photocycloaddition reaction with each other post-DLW would increase. This situation is also indirectly confirmed by the fact that in the work of Gernhardt et al. even after 60 hours of post-DLW irradiation, fluorescence is still observed, which indicates that not all anthracene moieties were dimerised.[32] A major challenge here would be to quantify the exact proportion of anthracene dimer that has been cleaved during the DLW process. To approach this challenge it may be beneficial to simplify the system first. Several experiments could be conducted, where the anthracene dimer bifunctional monomer is substituted with another bifunctional monomer. The new bifunctional monomer should not be subject to cleaving during the DLW, but could be assumed equivalent to the anthracene dimer containing bifunctional monomer in terms of the polymerisation kinetics. The resulting polymer networks can then be treated as a reference point. Generation of a reference polymer network using different writing parameters will permit the collection of a library of data on the mechanical properties of the polymer network versus the writing parameters used. Experimental data could then be compared with the network structure generated by the code resulting in a correlation. The

correlation, in turn, could be used to estimate the anthracene conversion in the polymer networks containing anthracene.
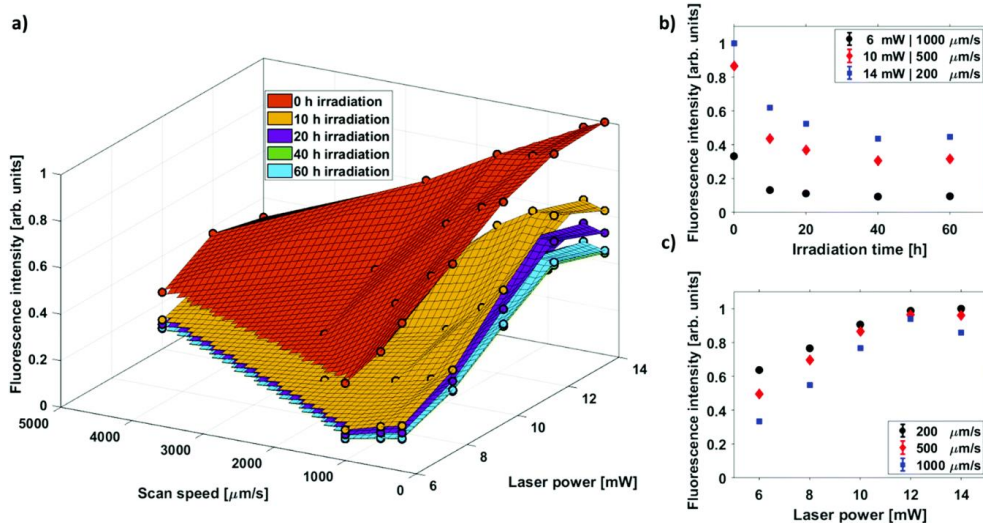


**Fig 5-5 Changes in normalised intensity of anthracene fluorescence incorporated into DLW polymer structures (92% anthracene dimer containing monomer and 8% PETA) as a function of scan speed, laser power and post-DLW irradiation with 415 nm LED. Reproduced from Ref. 1 with permission from the Chinese Chemical Society (CCS), Institute of Chemistry of Chinese Academy of Sciences (IC), and the Royal Society of Chemistry.**

### 5.7.2 Post-DLW

Once a polymer network has been generated by the kMC code and some of the anthracenes have been cleaved *in silico*, the introduction of the anthracene reversible photocycloaddition to the model in the post-DLW stage could take place. An important thing to consider here is that, since anthracene moieties are attached to the polymer network, anthracenes are even more restricted in their reaction than in the SCNP. Experimental results in **Fig 5-5** demonstrate that full conversion for anthracene photocycloaddition reaction when attached to a polymer network is not reached even after 60 hours of irradiation with a 415 nm LED. The model for anthracene dimerization, when attached to polymer chains (**Chapter 4**), could be adapted to the polymer network environment.

The first step in the adaptation would be an adjustment of how the molar rate of photon absorption, $J_A$, is calculated. The division of the molar rate of photon absorption between individuals chains is not needed, therefore, the calculation of the $J_A$ from the model for anthracene dimerization free in the solution (**Chapter 2, eq 2-4**) could be used with some adjustments. For convenience the equation **eq 2-4** is presented below:

$$\mathcal{J}_a(c_A) = \frac{E_{pp}T_\lambda f}{E_\lambda N_A V}(1 - 10^{-\varepsilon c_A L})$$ eq 2-4

The kMC modelled sample volume, *V*, becomes the volume of the irradiated polymer network, which will need to be carefully defined. The transmittance of the laser vial, $T_\lambda$, will no longer be needed as no glass is present in the way of the laser beam. The DLW written structures are much smaller than the profile of the laser beam, therefore, the energy per pulse received by the sample would need to be adjusted according to the area occupied by the DLW polymer structures. Additionally, care needs to be taken to determine if any other species, e.g. any of the other monomers used, could be competing with anthracenes for absorption.

The next step is the adaptation of the kinetic expression for the reaction of anthracene attached to the polymer network. Previously (**Chapter 4**, **eq 4-2**), when anthracenes were attached to a single polymer chain, rate coefficients for each possible pair of anthracene, $k_{+app,A-A}$, were calculated by calculating an ideal apparent rate coefficient for anthracene photodimerization in free solution and correcting for unfavourable spatial arrangement and chemical system confinement effects. A similar approach can be taken here. Apparent rate coefficients for each possible pair of anthracene in the network can be calculated by using the ideal apparent rate coefficient for anthracene photodimerization in free solution and applying several correction factors. The first factor, just like in the single polymer chain case, is a tunable system-dependent parameter that depends on the type of monomers used for the creating of the polymer network and structural features of the polymer network e.g. crosslinking density. The distance between the anthracenes could be estimated by calculating the shortest distance between the anthracenes[274] since a single polymer backbone is not present.

A second, Beer-Lambert law dependent factor, is required for the apparent rate coefficient to account for the lack of mixing because mixing for anthracenes attached to a polymer network is not possible. The closer the anthracene to the surface, the higher the chance for it to absorb the photon and react. Therefore, ideally, anthracenes that absorb a photon and reach a singlet excited state should be distributed following the Beer-Lambert law, however, no spatial resolution is absent in the kMC code. This challenge could be approached in incremental steps. The first step is to simply omit the spatial variations and model the reaction on average. However, then only the average changes in the network are accessed and the magnitude of change would be highly dependent on the chosen sample volume, *V*. The next step could be the division of the sample volume into several smaller sub-volumes by analogy with the parallel kMC approach (see **§1.5.2**) except for the homogenisation step (**Fig 5-6**). Each sub-volume would be representing a different layer of the polymer network. The average Beer-Lambert law dependent factor can be calculated based on the fraction of light absorbed by the anthracene species in the sub-volume. The anthracene pairs within each volume can then

have the same Beer-Lambert law dependent factor. The approach would enable having a degree of "spatial" resolution without the need for the explicit construction of a 3D polymer network beforehand. Finally, the third step is to have an explicit construction of a 3D polymer network first, then use the z-coordinates of anthracene moieties to define the probability of anthracene absorbing a photon and thus the Beer-Lambert law dependent factor (**Fig 5-6**).
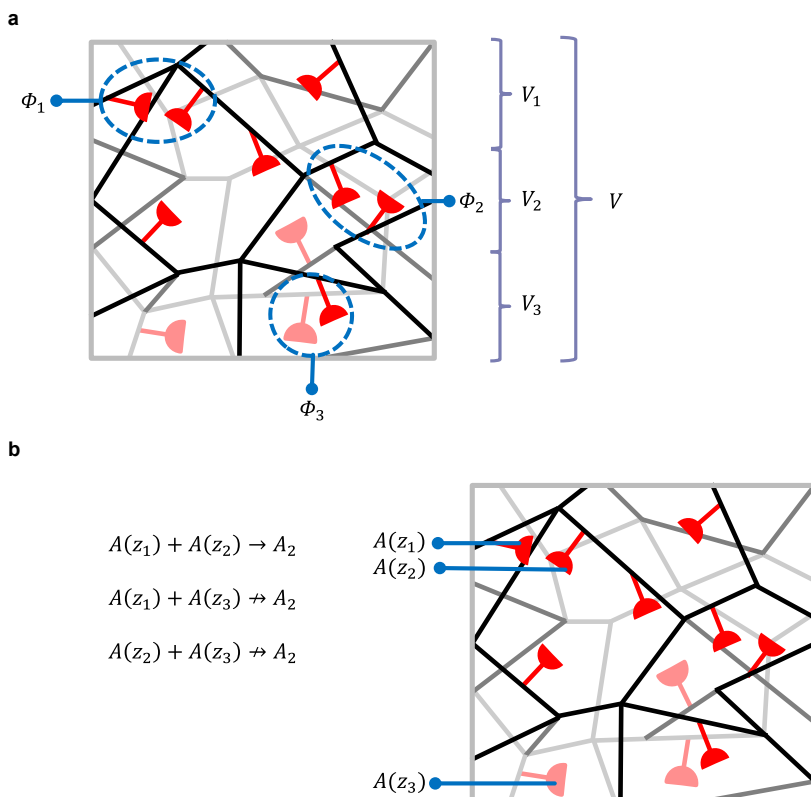


**Fig 5-6 Illustration of the potential implementation of anthracene photocycloaddition in the modelling framework. a: subdivision into subvolumes ($V_x$), where light absorption is assumed to be homogeneous (same Beer-Lambert law dependent factor, $f_{BL}$), shortest distance between the two anthracenes along the backbone of the polymer network defines the possibility of reaction; b: individual z-coordinates define the possibility to react.**

The photodimerization kinetics of anthracenes attached to a polymer network could also be modelled without the help of the kMC simulation. As a basis, we could use the expression for the photodimerisation of anthracenes attached to a polymer chain from **Chapter 4** (**Fig 4-3**), which models the reaction progress for an averaged chain. The apparent rate coefficient could be corrected for the confinement effects of the network through network correction factor, *z*. The network correction factor for SCNPs was a function of conversion

and system-dependent fitting parameter, *w*. The limiting conversion in the polymer network environment would need to be experimentally determined. However, in the future, it could be potentially expressed as a function of the DLW writing parameters (e.g. laser power) for a given chemical system.

## 5.8 Conclusions

In this chapter, rate coefficient availability and potential modelling methods have been discussed for the DLW process and post-DLW dynamics. Information regarding rate coefficients required for modelling the DLW process is lacking in the literature. Approximations for rate coefficients have been proposed, but more research is required to establish more accurate values. The missing data may need to be determined experimentally from linear polymer systems as current approximations are not sufficiently reliable. Experimental characterisation of the DLW process is challenging, therefore, benchmarking the model is non-trivial and alternative solutions may need to be explored.

Basic modelling challenges with possible implementation steps were explored here, i.e. reactions to consider and the availability of the corresponding rate coefficients. Further expansion of the DLW model is required to include but is not limited to spatial variations and diffusion of the reacting species, heat transfer and the movement of the laser focus. Possible step-by-step implementation methods of anthracene reactions during and post-DLW were explored.

# CHAPTER 6. CONCLUSIONS AND FUTURE OUTLOOK

The current chapter summarises all outcomes of the current PhD thesis and provides an outlook into the future possibilities of where the results of this thesis could lead. **§ 6.1** provides the summary of all the chapters and the achievements completed in each of them. **§ 6.2** discussed the potential directions that could be taken in the future to further develop the model established in the current thesis.

## 6.1    Conclusions

The current thesis aimed to set the foundation for the development of a complex model to predict dynamic changes in polymer network structures under an external stimulus (i.e. light) - a prerequisite for the correlation between network structure and displayed mechanical properties. The work was approached in a stepwise manner, increasing the complexity of the modelled chemical system with each chapter. The investigation commenced by exploring the photokinetics of a bond-forming reaction through exclusive anthracene photocycloaddition in solution. In a second step, a competitive photocycloreversion was added as a bond-breaking reaction. In the following chapter, the model was expanded towards single polymer chain networks (i.e. single-chain polymer nanoparticles (SCNPs)), by attaching the photoreactive unit to well-defined polymer chains. Finally, the availability of the rate coefficients and potential model construction strategy for dynamic network formation in additive manufacturing and post-manufacturing modifications were explored in the field of direct laser writing (DLW). A detailed summary of each chapter is provided below.

In **Chapter 2**, the development of a simple model framework for exclusive anthracene photodimerisation kinetics in solution was completed. The model framework is not limited to anthracene photodimerisation exclusively, but has the potential to be applied to other photodimerisations. The simplicity of the model was highlighted by the fact that the determination of individual rate coefficients was not required. Instead, an apparent rate coefficient was used. The apparent rate coefficient consists of rate coefficient ratios, which were determined by several short time (low conversion) irradiation experiments. During the short time (low conversion) irradiation experiments, the apparent rate coefficient was assumed constant, thus rate coefficient ratios could be easily calculated. Furthermore, model predictions of conversions were readily conducted using Excel and stepwise integration. An array of variables, e.g. integral and differential quantum yields, a fraction of light absorbed or apparent rate coefficient, are easily retrievable from the model. Both integral and differential

quantum yields, parameters classically used to describe photochemical reactions, were calculated throughout the entire modelled time frame, providing insight into the reaction progress. Importantly, the wavelength dependence of the anthracene photocycloaddition was explored in detail in the $\lambda = 375 - 430$ nm range, revealing that - apart from the traditionally applied harsh UV light - mild visible light ($\lambda = 410$ nm) can be used to initiate the reaction.

To capture reversible dynamic changes in networks, not only the kinetics of bond-forming reactions but also bond-breaking reactions have to be considered. Therefore, the anthracene photodimerisation model was extended in **Chapter 3** to include the competitive anthracene dimer cleavage reaction. The extension was carried out by deriving kinetic expressions for two additional scenarios. First, the kinetic expression for exclusive anthracene dimer cleavage was derived. The applicability of the kinetic expression for exclusive dimer cleavage is limited in the case of anthracene, due to a high molar attenuation coefficient of the anthracene monomer. However, the general applicability of the expression for exclusive dimer cleavage remains valid. In the following, the kinetic expression for competitive anthracene dimerisation and anthracene dimer cleavage were derived. Wavelength dependence of the anthracene photocycloaddition and cleavage were explored in detail in the $\lambda = 260 - 330$ nm range via action plots. The wavelength of $\lambda = 280$nm was determined to be the optimal wavelength for anthracene dimer cleavage. Once again apparent rate coefficients were used, one for anthracene dimerisation and one for anthracene dimer cleavage. Both apparent rate coefficients are made up of rate coefficient ratios which were determined at a range of wavelengths. A methodology for the determination of competitive anthracene dimerisation and anthracene dimer cleavage rate coefficients ratios consisted of performing several short time (low conversion) irradiation experiments. First, rate coefficient ratios were determined for anthracene dimerisation with short time (low conversion) irradiation experiments on anthracene. Anthracene dimer cleavage was assumed negligible at low conversions (i.e. exclusive anthracene dimerization assumed), hence apparent rate coefficient ratios for anthracene dimerization were able to be determined the same way as in **Chapter 2**. Anthracene dimer cleavage rate coefficients ratio was determined with short time (low conversion) irradiation experiments on anthracene dimer. Anthracene absorption was found to be significant even at low conversions, therefore, the kinetic expression for competitive anthracene dimerisation and anthracene dimer cleavage was used to calculate the rate coefficient ratio for anthracene dimer cleavage. Finally, the model allowed for the prediction of the wavelength-dependent photokinetics and equilibria at any set of initial concentrations.

**Chapter 4** organically extended the model for anthracene dimerisation in solution to intramolecular dimerisation of anthracenes attached to polymer chains. The model in **Chapter 4** proposed the adaptation of the model for anthracene dimerisation in solution by the addition of a confinement correction function. The model permits a simple calculation of the progress of the reaction for an averaged chain in Excel. Furthermore, the averaged chain model is capable of providing detailed information on the changes in various parameters, including integral and differential quantum yields as well as a volume of the polymer chain at any given point in time of the reaction. Additional insight was provided by a kMC model, which models the RAFT polymerization, to provide insight into crucial chain-to-chain deviations. Additionally, having access to individual chain structures, the kMC model calculates the probability of each potential pair of anthracenes to react. Therefore, the kMC model can model every single intramolecular anthracene dimerization event. Furthermore, the kMC code can visualise the folding process of individual polymer chains explicitly in 3D. Consequently, 3D visualization enabled the calculation of the radius of gyration for each chain after every intramolecular reaction event, giving insight into the radius of gyration distributions and the folding process itself. A series of experiments were proposed for model validation and determination of the missing model parameters, such as Zimm-Stockmayer fitting parameters for the calculation of contraction factor as well as the system-dependent fitting parameter for estimation of the steric hindrance to the photocycloaddition reaction. The model holds key potential to provide a detailed picture of the SCNP folding morphology distribution resulting from the given polymerization parameters during the synthesis (e.g. monomer ratio, temperature) and folding (e.g. irradiation time and wavelength). Such detailed insight is critical to establish control over the SCNP synthesis, which will be required for prospective applications of SCNPs.

Finally, **Chapter 5** investigated anthracene containing polymer networks created via DLW to construct a model for predicting the polymer network structure DLW and post-DLW modifications thereof. The mechanical properties of the polymer networks depend both on the dynamic (anthracene reversible photocycloaddition) and non-dynamic parts of the network (polymer backbone). Therefore, knowledge of the polymer network structure at all stages is critical for the success of the model predictions. The chapter discussed the availability of rate coefficients for the modelling of polymerisation reactions during DLW on an example of a reference system. Unfortunately, many propagation, termination and chain transfer rate coefficients were not found and would have to be estimated in the future. A strategy to implement the estimation of rate coefficients was proposed. The chapter described a stepwise approach that could be taken to build the model complexity focusing on the static voxel formation i.e. no movement. First, building the model to reflect the reaction kinetics

of the simplified reaction (omitting some of the reaction intermediate species) was proposed. Then, the gradual introduction of the diffusional limitations on the reaction rate coefficients was suggested. The kMC modelling technique does not entail spatial resolution as an inherent feature of the model. However, modelling the diffusion of species during the reaction and spatial variations of the species is critical for the successful DLW model. Therefore, options were proposed to reflect the presence of spatial variations of the species in the reaction system. The method proposed a gradual increase in complexity of the model by going from modelling voxel formation on average as a whole, then introducing 1D resolution by employing a parallel kMC inspired approach. Similarly, avenues to 2D and even 3D resolutions were proposed. Finally, anthracene reactions during and post-DLW were discussed. Introduction of the anthracene dimer cleavage reaction occurring during the DLW may be challenging, therefore, a strategy was proposed to introduce the cleaved anthracene *post factum*. Modelling of the anthracene photodimerisation reaction post-DLW would take the model proposed in **Chapter 4** as a basis with some additional adjustments due to increased restrictions of the polymer network (e.g. lack of mixing). A step-by-step approach to the potential implementation strategy was written out.

The current thesis, thus, has prepared the basis required for a highly complex model for polymer network structures of dynamic materials generated via DLW. A model for anthracene reversible photocycloaddition reaction as dynamic bonds in adaptable polymeric materials has been built from the ground up in a step-wise approach gradually increasing the complexity of the model. The required kinetic data for modelling of the DLW process via the kMC method has been discussed along with the proposed methodology for the implementation of the spatial variations of species in the kMC model.

## 6.2   Outlook

In the current section, future work that could be conducted based on the results of the current thesis will be discussed. Where appropriate, future ideas have already been mentioned in **Chapters 4** and **5**, however, here ideas are explored as to how the models discussed in the current thesis could be expanded further.

The model frameworks derived in the current thesis have the benefit of being generally applicable. Hence, the methodology of the models derived in **Chapters 2** and **3** for anthracene reversible photocycloaddition could be further explored for applicability in other photochemical reactions. [2+2] photocycloadditions would be especially promising candidates since our group is constantly developing novel, red-shifted stilbene derivatives for this class of photoreactions.[46, 317-318] Furthermore, it would be of interest to collect more experimental data regarding the reactivity of anthracene dimerization reaction in the visible region as it is of interest for more

practical applications. In the future experiment, it will also be beneficial to expand the analytical techniques to include IR and MS spectra to cross-validate the experimental results.

The model for photodimerisation of anthracene attached to the polymer chain, proposed in **Chapter 4**, could be further extended. The current algorithm for 3D visualisation of polymer chain conformations is limited by the number of different crosslinking point combinations that could be visualised by the code. Therefore, an extension of the algorithm for 3D visualisation to increase the limit would be extremely beneficial for expanding the model possibilities. A larger library of different polymers of varying structures could be explored to expand the correction factor function develop a correlation with more fundamental polymer chain structural properties like polymer chain stiffness. Reaction kinetics could be extended to include competitive anthracene dimer cleavage (as in **Chapter 3**), which would enable the modelling of reversible folding and unfolding of SCNPs. Additionally, another competitive photocycloaddition reaction could be added to the kinetic model reaction to make the model also applicable for modelling polymer chains containing two types of photoreactive groups. Such an approach would enable a deeper understanding of light-gated stepwise folding of SCNPs, which has been carried out experimentally, yet without the knowledge of the precise macromolecular architecture.[48, 319]

The inclusion of intermolecular anthracene photocycloaddition reaction kinetics should be considered because the presence of intermolecular reaction pathways in the model would increase its applicability to guide experimental design. Here, irradiation time and chain concentration could be predicted to optimize SCNP folding conditions. Furthermore, the inclusion of intermolecular reaction and anthracene dimer cleavage could potentially be the first step in extending the model to include reactions in polymeric micelles and star-like nanogels, although no doubt, much more work would need to be done to achieve model applicability for such multi-chain architectures. In **Chapters 2 - 4**, perfect mixing was assumed in a view of small reaction volume (50 – 500 µL), absence of a (magnetic) stirrer, and relatively long reaction times. However, care needs to be taken in case of application of the model to larger reaction volumes where imperfect mixing may negatively affect the reaction progress.

An extensive amount of future work could be carried out regarding the model for DLW polymer network generation and reversible anthracene photocycloaddition post-DLW. As described in **Chapter 5**, a kMC model would need to be built first to reflect the basic kinetics (i.e. no spatial variations, chain length dependence in rate coefficients) of the polymerisation reaction during the DLW. Next, the diffusional limitations could be applied to the intrinsic rate coefficients as described in the recent publication by De Keer et al.[274] The possibility of the experimental determination of specific rate coefficients for polymerisation could be explored, as this

would allow reducing the number of approximations made. Experimental measurements for benchmarking the model for kMC could be challenging. Benchmarking of the model could potentially be achieved in the future using the set-up described in the works of Wegener, where the scattering of a second continuous laser beam was used to measure monomer conversion during the DLW.[86, 101, 316] As proposed in **Chapter 5**, spatial variations of species and their diffusion would need to be incorporated into the DLW model because the diffusion plays an important role in the polymerisation reaction during DLW. Inclusion of temperature profile into the simulation would allow to study and predict the microexplosions observed during the DLW permitting additional insight into the DLW process and improved experiment design. In **Chapter 5**, the inclusion of anthracene dimer cleavage reactions during DLW was proposed to be done *post factum* manually, however, it would be beneficial to incorporate the reaction into the model. Anthracene photocycloaddition reactions would also need to be incorporated into the model to predict post-DLW changes in the polymer network structure. The proposed approach was explored in **Chapter 5**. After the establishment of the model for DLW of the single voxel, the model could be further expanded to include the movement of the focal point along the path. The inclusion of the movement of the focal point would enable to study the influence of the focal point movement on the polymer network structure as well as the resolution of the written features. Finally, the modelled dynamic polymer network structures would need to be correlated with their corresponding mechanical properties, e.g. stiffness. The correlation could be done through polymer network structural features, e.g. pore size, as described in the recent publication by De Keer et al.[274] The combination of kMC and MD simulations and experimental measurements in the De Keer et al. publication allowed to demonstrate a clear structure-property relationship between for example the experimentally measured degree of swelling and simulated polymer structural features like pore size.[274] Similarly, structural features of the DLW dynamic polymer network could be correlated with experimentally measured mechanical properties. Mechanical properties for DLW polymer networks such as hardness could be measured using nano-dynamic mechanical analysis (nano-DMA).[13] An initial correlation between the modelled polymer network structure and the experimentally measured mechanical properties could be done by first performing nano-DMA measurements on a range blank samples, i.e. bifunctional monomer containing anthracene dimer is substituted by an equivalent non-cleavable bifunctional monomer as was previously done by Gernhardt et al.[1] The non-cleavable bifunctional monomer would help to avoid anthracene dimer cleavage during writing. Additionally, it must be noted that the non-cleavable bifunctional monomer must be carefully selected as bulky anthracene structure is expected to affect the mechanical properties of the material.[1] The correlation could also potentially be used

to determine the anthracene dimerization and anthracene dimer cleavage reaction conversion, providing the means to establish and validate a model for anthracene reversible photocycloaddition reaction when attached to a polymer network.

In conclusion, the current thesis prepared the groundwork for the generation of a model for dynamic polymeric networks generated via DLW, subsequent modifications of the network structure under external stimuli and connection of the said polymer network structure to the resulting mechanical properties. The models proposed in the current thesis have general applicability and thus, in the future, could additionally be further adapted to suit different reaction systems.

# REFERENCES

1.      Braslavsky, S. E., Glossary of terms used in photochemistry, 3rd edition (IUPAC Recommendations 2006). *Pure Appl. Chem.* **2007,** *79* (3), 293-465.
2.      Albini, A., *Photochemistry Past, Present and Future*. 1st ed. 2016. ed.; Springer Berlin Heidelberg: Berlin, Heidelberg, 2016.
3.      Anderson, N. A.; Shiang, J. J.; Sension, R. J., Subpicosecond Ring Opening of 7-Dehydrocholesterol Studied by Ultrafast Spectroscopy. *The Journal of Physical Chemistry A* **1999,** *103* (50), 10730-10736.
4.      Johnson, P. J.; Halpin, A.; Morizumi, T.; Prokhorenko, V. I.; Ernst, O. P.; Miller, R. J., Local vibrational coherences drive the primary photochemistry of vision. *Nat Chem* **2015,** *7* (12), 980-6.
5.      Ernst, O. P.; Lodowski, D. T.; Elstner, M.; Hegemann, P.; Brown, L. S.; Kandori, H., Microbial and animal rhodopsins: structures, functions, and molecular mechanisms. *Chem. Rev.* **2014,** *114* (1), 126-63.
6.      Melough, M. M.; Cho, E.; Chun, O. K., Furocoumarins: A review of biochemical activities, dietary sources and intake, and potential health risks. *Food Chem. Toxicol.* **2018,** *113*, 99-107.
7.      Schreier, W. J.; Schrader, T. E.; Koller, F. O.; Gilch, P.; Crespo-Hernandez, C. E.; Swaminathan, V. N.; Carell, T.; Zinth, W.; Kohler, B., Thymine dimerization in DNA is an ultrafast photoreaction. *Science* **2007,** *315* (5812), 625-9.
8.      Nada, A. A., Professor A. Schonberg and the history of photochemistry in Egypt. *J. Chem. Educ.* **1983,** *60* (6).
9.      McKenna, W. B., Ammi majus Linn in the treatment of vitiligo. *Scott Med J* **1957,** *2* (2), 69-70.
10.     Sidi, E.; Bourgeois-Gavardin, J., The treatment of vitiligo with Ammi Majus Linn; a preliminary note. *J Invest Dermatol* **1952,** *18* (5), 391-5.
11.     Forman, S. A., The dynamic interplay between photochemistry and photography. *J. Chem. Educ.* **1975,** *52* (10).
12.     Ciamician, G., The Photochemistry of the Future. *Science* **1912,** *36* (926), 385-94.
13.     Gernhardt, M.; Blasco, E.; Hippler, M.; Blinco, J.; Bastmeyer, M.; Wegener, M.; Frisch, H.; Barner-Kowollik, C., Tailoring the Mechanical Properties of 3D Microstructures Using Visible Light Post-Manufacturing. *Adv. Mater.* **2019,** *31* (30).
14.     Protti, S.; Fagnoni, M., The sunny side of chemistry: green synthesis by solar light. *Photochem Photobiol Sci* **2009,** *8* (11), 1499-516.
15.     Barner-Kowollik, C.; Bastmeyer, M.; Blasco, E.; Delaittre, G.; Müller, P.; Richter, B.; Wegener, M., 3D Laser Micro- and Nanoprinting: Challenges for Chemistry. *Angew. Chem. Int. Ed.* **2017,** *56* (50), 15828-15845.
16.     Guvendiren, M.; Burdick, J. A., Stiffening hydrogels to probe short- and long-term cellular responses to dynamic mechanics. *Nat Commun* **2012,** *3*, 792.
17.     Frisch, H.; Marschner, D. E.; Goldmann, A. S.; Barner-Kowollik, C., Wavelength-Gated Dynamic Covalent Chemistry. *Angew. Chem. Int. Ed. Engl.* **2018,** *57* (8), 2036-2045.
18.     Van Hoorick, J.; Ottevaere, H.; Thienpont, H.; Dubruel, P.; Van Vlierberghe, S., *Polymer and Photonic Materials Towards Biomedical Breakthroughs*. Springer, Cham: 2018.
19.     Truong, V. X.; Li, F.; Forsythe, J. S., Versatile Bioorthogonal Hydrogel Platform by Catalyst-Free Visible Light Initiated Photodimerization of Anthracene. *ACS Macro Letters* **2017,** *6* (7), 657-662.
20.     Albini, A.; Dichiarante, V., The 'belle époque' of photochemistry. *Photochemical & Photobiological Sciences* **2009,** *8* (2).
21.     Engelhardt, S., Direct Laser Writing. In *Laser Technology in Biomimetics: Basics and Applications*, Schmidt, V.; Belegratis, M. R., Eds. Springer: New York, 2013; pp 13-65.
22.     Dürr, H.; Bouas-Laurent, H.; Dürr, H.; Durr, H., *Photochromism : Molecules and Systems*. Elsevier Science & Technology: Oxford, NETHERLANDS, THE, 2003.
23.     Serrano-Andrés, L.; Serrano-Pérez, J. J., Calculation of excited states: Molecular photophysics and photochemistry on display. In *Handbook of Computational Chemistry*, 2017; pp 639-725.
24.     Cassano, A. E.; Martin, C. A.; Brandi, R. J.; Alfano, O. M., Photoreactor Analysis and Design: Fundamentals and Applications. *Industrial & Engineering Chemistry Research* **1995,** *34* (7), 2155-2201.
25.     Molina, M. J.; Colussi, A. J.; Molina, L. T.; Schindler, R. N.; Tso, T. L., Reprint of: Quantum yield of chlorine-atom formation in the photodissociation of chlorine peroxide (ClOOCl) at 308nm. *Chem. Phys. Lett.* **2013,** *589*, 52-55.
26.     Läuter, A.; Suresh, D.; Volpp, H.-R., Absolute chlorine and hydrogen atom quantum yield measurements in the 193.3 nm photodissociation of CH3CFCl2 (HCFC-141b). *The Journal of Chemical Physics* **2003,** *118* (13), 5821-5830.
27.     Loubière, K.; Oelgemöller, M.; Aillet, T.; Dechy-Cabaret, O.; Prat, L., Continuous-flow photochemistry: A need for chemical engineering. *Chem. Eng. Process. Process Intensif.* **2016,** *104*, 120-132.

28.     Kaur, G.; Johnston, P.; Saito, K., Photo-reversible dimerisation reactions and their applications in polymeric systems. *Polym. Chem.* **2014,** *5* (7), 2171-2186.

29.     Dan-Thuy, V.-P.; Minh Tri, N.; Ken, O.; Hideyuki, N.; Tomohisa, N.; Qui, T.-C.-M., Controlling the nano-deformation of polymer by a reversible photo-cross-linking reaction. *Advances in Natural Sciences: Nanoscience and Nanotechnology* **2017,** *8* (2), 025003.

30.     Chung, C.-M.; Roh, Y.-S.; Cho, S.-Y.; Kim, J.-G., Crack Healing in Polymeric Materials via Photochemical [2+2] Cycloaddition. *Chem. Mater.* **2004,** *16* (21), 3982-3984.

31.     Lendlein, A.; Jiang, H.; Junger, O.; Langer, R., Light-induced shape-memory polymers. *Nature* **2005,** *434* (7035), 879-82.

32.     Gernhardt, M.; Frisch, H.; Welle, A.; Jones, R.; Wegener, M.; Blasco, E.; Barner-Kowollik, C., Multi-material 3D microstructures with photochemically adaptive mechanical properties. *Journal of Materials Chemistry C* **2020,** *8* (32), 10993-11000.

33.     Truong, V. X.; Li, F.; Ercole, F.; Forsythe, J. S., Wavelength-Selective Coupling and Decoupling of Polymer Chains via Reversible [2 + 2] Photocycloaddition of Styrylpyrene for Construction of Cytocompatible Photodynamic Hydrogels. *ACS Macro Letters* **2018,** *7* (4), 464-469.

34.     He, H.; Feng, M.; Chen, Q.; Zhang, X.; Zhan, H., Light-Induced Reversible Self-Assembly of Gold Nanoparticles Surface-Immobilized with Coumarin Ligands. *Angew. Chem. Int. Ed. Engl.* **2016,** *55* (3), 936-40.

35.     He, J.; Tremblay, L.; Lacelle, S.; Zhao, Y., Preparation of polymer single chain nanoparticles using intramolecular photodimerization of coumarin. *Soft Matter* **2011,** *7* (6).

36.     Kehrloesser, D.; Baumann, R.-P.; Kim, H.-C.; Hampp, N., Photochemistry of Coumarin-Functionalized SiO2 Nanoparticles. *Langmuir* **2011,** *27* (7), 4149-4155.

37.     Ling, J.; Rong, M. Z.; Zhang, M. Q., Coumarin imparts repeated photochemical remendability to polyurethane. *J. Mater. Chem.* **2011,** *21* (45).

38.     Chen, Y.; Chen, K.-H., Synthesis and reversible photocleavage of novel polyurethanes containing coumarin dimer components. *J. Polym. Sci., Part A: Polym. Chem.* **1997,** *35* (4), 613-624.

39.     Yang, K.; Zeng, M., Multiresponsive hydrogel based on polyacrylamide functionalized with thymine derivatives. *New J. Chem.* **2013,** *37* (4).

40.     Jalili Moghaddam, M.; Hozumi, S.; Inaki, Y.; Takemoto, K., Functional Monomers and Polymers CLXVIII. Syntheses and Photoreactions of Poly(methacrylate)s Containing Thymine Bases. *Polym. J.* **1989,** *21* (3), 203-213.

41.     Itoh, H.; Tahara, A.; Naka, K.; Chujo, Y., Photochemical assembly of gold nanoparticles utilizing the photodimerization of thymine. *Langmuir* **2004,** *20* (5), 1972-6.

42.     Doi, T.; Kashida, H.; Asanuma, H., Efficiency of [2 + 2] photodimerization of various stilbene derivatives within the DNA duplex scaffold. *Org Biomol Chem* **2015,** *13* (15), 4430-7.

43.     Li, N. Y.; Chen, J. M.; Tang, X. Y.; Zhang, G. P.; Liu, D., Reversible single-crystal-to-single-crystal conversion of a photoreactive coordination network for rewritable optical memory storage. *Chem Commun (Camb)* **2020,** *56* (13), 1984-1987.

44.     Njikang, G.; Liu, G.; Curda, S. A., Tadpoles from the Intramolecular Photo-Cross-Linking of Diblock Copolymers. *Macromolecules* **2008,** *41* (15), 5697-5702.

45.     Micic, M.; Zheng, Y.; Moy, V.; Zhang, X.-H.; Andreopoulos, F. M.; Leblanc, R. M., Comparative studies of surface topography and mechanical properties of a new, photo-switchable PEG-based hydrogel. *Colloids and Surfaces B: Biointerfaces* **2003,** *27* (2-3), 147-158.

46.     Marschner, D. E.; Frisch, H.; Offenloch, J. T.; Tuten, B. T.; Becer, C. R.; Walther, A.; Goldmann, A. S.; Tzvetkova, P.; Barner-Kowollik, C., Visible Light [2 + 2] Cycloadditions for Reversible Polymer Ligation. *Macromolecules* **2018,** *51* (10), 3802-3807.

47.     Frisch, H.; Bloesser, F. R.; Barner-Kowollik, C., Controlling Chain Coupling and Single-Chain Ligation by Two Colours of Visible Light. *Angew. Chem. Int. Ed. Engl.* **2019,** *58* (11), 3604-3609.

48.     Frisch, H.; Kodura, D.; Bloesser, F. R.; Michalek, L.; Barner-Kowollik, C., Wavelength-Selective Folding of Single Polymer Chains with Different Colors of Visible Light. *Macromol. Rapid Commun.* **2020,** *41* (1), e1900414.

49.     Bouas-Laurent, H.; Desvergne, J.-P.; Castellan, A.; Lapouyade, R., Photodimerization of anthracenes in fluid solutions: (part 2) mechanistic aspects of the photocycloaddition and of the photochemical and thermal cleavage. *Chem. Soc. Rev.* **2001,** *30* (4), 248-263.

50.     Behrendt, P. J.; Kim, H.-C.; Hampp, N., Laser-based depletion zone photoreaction: Selective synthesis of [2+2]-crossdimers of coumarin and 5-fluorouracil. *Journal of Photochemistry and Photobiology A: Chemistry* **2013,** *264*, 67-72.

51.     Cao, D.; Meier, H., The Unusual Photochemistry of Dendrimers with an Anthracene Core. *Angew. Chem. Int. Ed.* **2001,** *40* (1), 186-188.

52.     Yoshizawa, M.; Takeyama, Y.; Okano, T.; Fujita, M., Cavity-directed synthesis within a self-assembled coordination cage: highly selective [2 + 2] cross-photodimerization of olefins. *J. Am. Chem. Soc.* **2003,** *125* (11), 3243-7.

53.     Bialas, S.; Michalek, L.; Marschner, D. E.; Krappitz, T.; Wegener, M.; Blinco, J.; Blasco, E.; Frisch, H.; Barner-Kowollik, C., Access to Disparate Soft Matter Materials by Curing with Two Colors of Light. *Adv. Mater.* **2019,** *31* (8), e1807288.

54.     Wang, S. Y., 6 - Pyrimidine Bimolecular Photoproducts. In *Photochemistry and Photobiology of Nucleic Acids*, Wang, S. Y., Ed. Academic Press: 1976; pp 295-356.

55.     Cardenas-Daw, C.; Kroeger, A.; Schaertl, W.; Froimowicz, P.; Landfester, K., Reversible Photocycloadditions, a Powerful Tool for Tailoring (Nano)Materials. *Macromol. Chem. Phys.* **2012,** *213* (2), 144-156.

56.     Woodward, R. B.; Hoffmann, R., The Conservation of Orbital Symmetry. *Angewandte Chemie International Edition in English* **1969,** *8* (11), 781-853.

57.     Fast, D. E.; Lauer, A.; Menzel, J. P.; Kelterer, A.-M.; Gescheidt, G.; Barner-Kowollik, C., Wavelength-Dependent Photochemistry of Oxime Ester Photoinitiators. *Macromolecules* **2017,** *50* (5), 1815-1823.

58.     Frisch, H.; Menzel, J. P.; Bloesser, F. R.; Marschner, D. E.; Mundsinger, K.; Barner-Kowollik, C., Photochemistry in Confined Environments for Single-Chain Nanoparticle Design. *J. Am. Chem. Soc.* **2018,** *140* (30), 9551-9557.

59.     Menzel, J. P.; Noble, B. B.; Lauer, A.; Coote, M. L.; Blinco, J. P.; Barner-Kowollik, C., Wavelength Dependence of Light-Induced Cycloadditions. *J. Am. Chem. Soc.* **2017,** *139* (44), 15812-15820.

60.     Wells, L. A.; Furukawa, S.; Sheardown, H., Photoresponsive PEG-Anthracene Grafted Hyaluronan as a Controlled-Delivery Biomaterial. *Biomacromolecules* **2011,** *12* (4), 923-932.

61.     Bowen, E. J., The Photochemistry of Aromatic Hydrocarbon Solutions. In *Advances in Photochemistry*, W. A. Noyes, G. S. H. a. J. N. P., Ed. Interscience Publishers: New York, 1963; Vol. 1, pp 23-42.

62.     Menter, J.; Forster, T. H., ELECTRONICALLY EXCITED PRODUCTS IN THE PHOTODISSOCIATION OF Di-9-METHYLANTHRACENE. *Photochem. Photobiol.* **1972,** *15* (3), 289-296.

63.     Charlton, J. L.; Dabestani, R.; Saltiel, J., Role of triplet-triplet annihilation in anthracene dimerization. *J. Am. Chem. Soc.* **1983,** *105* (11), 3473-3476.

64.     Castellan, A.; Lapouyade, R.; Bouaslaurent, H., PHOTOCYCLOADDITION OF POLYNUCLEAR HYDROCARBONS IN SOLUTION .1. PHOTODIMERIZATION OF ACENES - PHOTOREACTIVE STATES AND SUBSTITUENT EFFECT. *Bulletin De La Societe Chimique De France Partie Ii-Chimie Moleculaire Organique Et Biologique* **1976,**  (1-2), 201-209.

65.     Bouas-Laurent, H.; Castellan, A.; Desvergne, J. P., From Anthracene Photodimerization To Jaw Photochromic Materials And Photocrowns. *Pure Appl. Chem.* **1980,** *52* (12), 2633-2648.

66.     Birks, J. B.; Aladekomo, J. B., THE PHOTO-DIMERIZATION AND EXCIMER FLUORESCENCE OF 9-METHYL ANTHRACENE. *Photochem. Photobiol.* **1963,** *2* (4), 415-418.

67.     Becker, H. D., Unimolecular photochemistry of anthracenes. *Chem. Rev.* **1993,** *93* (1), 145-172.

68.     Barnes, R. L.; Birks, J. B., EXCIMER FLUORESCENCE .X. SPECTRAL STUDIES OF 9-METHYL AND 9,10-DIMETHYL ANTHRACENE. *Proceedings of the Royal Society of London Series a-Mathematical and Physical Sciences* **1966,** *291* (1427), 570-&.

69.     Vember, T. M.; Mitina, V. G.; Cherkasov, A. S., Preparation and study of the mixed photodimers of anthracene and its dimeso substituted derivatives. *Theor. Exp. Chem.* **1971,** *4* (3), 238-241.

70.     Yamamoto, S.-a.; Grellmann, K.-H., The triplet state of anthracene photodimers and the wavelength dependence of the photodissociation process. *Chem. Phys. Lett.* **1982,** *85* (1), 73-80.

71.     Yamamoto, S.-a.; Grellmann, K.-H.; Weller, A., Mechanism of the photodissociation of the 9-methylanthracene photodimer. *Chem. Phys. Lett.* **1980,** *70* (2), 241-245.

72.     Iannone, M. A.; Scott, G. W., Low temperature spectroscopy and photochemistry of dianthracene. *Mol. Cryst. Liq. Cryst.* **1992,** *211* (1), 375-387.

73.     Saltiel, J.; Marchand, G. R.; Smothers, W. K.; Stout, S. A.; Charlton, J. L., Concerning the Spin-Statistical Factor in the Triplet-Triplet Annihilation of Anthracene Triplets. *J. Am. Chem. Soc.* **1981,** *103* (24), 7159-7164.

74.     Yamamoto, T.; Yagyu, S.; Tezuka, Y., Light- and Heat-Triggered Reversible Linear-Cyclic Topological Conversion of Telechelic Polymers with Anthryl End Groups. *J. Am. Chem. Soc.* **2016,** *138* (11), 3904-11.

75.     Brooks, W. L.; Sumerlin, B. S., Synthesis and Applications of Boronic Acid-Containing Polymers: From Materials to Medicine. *Chem. Rev.* **2016,** *116* (3), 1375-97.

76.     Odian, G., *Principles of polymerization*. 4th ed.; John Wiley & Sons, Inc.: Hoboken, New Jersey, 2004.

77.     Cowie, J. M. G.; Arrighi, V., *Polymers : chemistry and physics of modern materials*. Third edition. ed.; CRC Press: Boca Raton, Florida, 2007.

78.     Perrier, S., 50th Anniversary Perspective: RAFT Polymerization—A User Guide. *Macromolecules* **2017,** *50* (19), 7433-7447.

79.     Moad, G., RAFT polymerization to form stimuli-responsive polymers. *Polymer Chemistry* **2017,** *8* (1), 177-219.

80.     Frank, P. G.; Tuten, B. T.; Prasher, A.; Chao, D.; Berda, E. B., Intra-chain photodimerization of pendant anthracene units as an efficient route to single-chain nanoparticle fabrication. *Macromol. Rapid Commun.* **2014,** *35* (2), 249-253.

81.      Fischer, J.; Wegener, M., Three-dimensional optical laser lithography beyond the diffraction limit. *Laser & Photonics Reviews* **2013,** *7* (1), 22-44.

82.      Lee, K.-S.; Yang, D.-Y.; Park, S. H.; Kim, R. H., Recent developments in the use of two-photon polymerization in precise 2D and 3D microfabrications. *Polym. Adv. Technol.* **2006,** *17* (2), 72-82.

83.      Selimis, A.; Mironov, V.; Farsari, M., Direct laser writing: Principles and materials for scaffold 3D printing. *Microelectron. Eng.* **2015,** *132*, 83-89.

84.      Cumpston, B. H.; Ananthavel, S. P.; Barlow, S.; Dyer, D. L.; Ehrlich, J. E.; Erskine, L. L.; Heikal, A. A.; Kuebler, S. M.; Lee, I. Y. S.; McCord-Maughon, D.; Qin, J.; Röckel, H.; Rumi, M.; Wu, X.-L.; Marder, S. R.; Perry, J. W., Two-photon polymerization initiators for three-dimensional optical data storage and microfabrication. *Nature* **1999,** *398* (6722), 51-54.

85.      Rumi, M.; Barlow, S.; Wang, J.; Perry, J. W.; Marder, S. R., Two-photon absorbing materials and two-photon-induced chemistry. In *Adv. Polym. Sci.*, 2008; Vol. 213, pp 1-95.

86.      Fischer, J.; Mueller, J. B.; Kaschke, J.; Wolf, T. J. A.; Unterreiner, A. N.; Wegener, M., Three-dimensional multi-photon direct laser writing with variable repetition rate. *Opt. Express* **2013,** *21* (22), 26244-26260.

87.      Rumi, M.; Perry, J. W., Two-photon absorption: an overview of measurements and principles. *Advances in Optics and Photonics* **2010,** *2* (4).

88.      Schafer, K. J.; Hales, J. M.; Balu, M.; Belfield, K. D.; Van Stryland, E. W.; Hagan, D. J., Two-photon absorption cross-sections of common photoinitiators. *Journal of Photochemistry and Photobiology A: Chemistry* **2004,** *162* (2-3), 497-502.

89.      Maruo, S.; Nakamura, O.; Kawata, S., Three-dimensional microfabrication with two-photon-absorbed photopolymerization. *Opt. Lett.* **1997,** *22* (2), 132-134.

90.      Bleger, D.; Hecht, S., Visible-Light-Activated Molecular Switches. *Angew. Chem. Int. Ed. Engl.* **2015,** *54* (39), 11338-49.

91.      Cohen, E. R.; Cvitas, T.; Frey, J. G.; Holström, B.; Kuchitsu, K.; Marquardt, R.; Mills, I.; Pavese, F.; Quack, M.; Stohner, J.; Strauss, H. L.; Takami, M.; Thor, A. J., *Quantities, Units and Symbols in Physical Chemistry*. 2007.

92.      Alberti, A.; Benaglia, M.; Macciantelli, D.; Rossetti, S.; Scoponi, M., Further EPR-spin trapping studies of the photoinitiating activity of Irgacure 369. *Eur. Polym. J.* **2008,** *44* (9), 3022-3027.

93.      Colley, C. S.; Grills, D. C.; Besley, N. A.; Jockusch, S.; Matousek, P.; Parker, A. W.; Towrie, M.; Turro, N. J.; Gill, P. M. W.; George, M. W., Probing the Reactivity of Photoinitiators for Free Radical Polymerization:  Time-Resolved Infrared Spectroscopic Study of Benzoyl Radicals. *J. Am. Chem. Soc.* **2002,** *124* (50), 14952-14958.

94.      Belfield, K. D.; Schafer, K. J.; Liu, Y.; Liu, J.; Ren, X.; Stryland, E. W. V., Multiphoton-absorbing organic materials for microfabrication, emerging optical applications and non-destructive three-dimensional imaging. *J. Phys. Org. Chem.* **2000,** *13* (12), 837-849.

95.      LaFratta, C. N.; Fourkas, J. T.; Baldacchini, T.; Farrer, R. A., Multiphoton fabrication. *Angew. Chem. Int. Ed. Engl.* **2007,** *46* (33), 6238-58.

96.      Mueller, J. B. Exploring the Mechanisms of 3D Direct Laser Writing by Multi-Photon Polymerization. 2015.

97.      Uppal, N.; Shiakolas, P. S., Modeling of temperature-dependent diffusion and polymerization kinetics and their effects on two-photon polymerization dynamics. *Journal of Micro-Nanolithography Mems and Moems* **2008,** *7* (4), 043002.

98.      Zhou, X.; Hou, Y.; Lin, J., A review on the processing accuracy of two-photon polymerization. *AIP Advances* **2015,** *5* (3).

99.      Sun, H.-B.; Maeda, M.; Takada, K.; Chon, J. W. M.; Gu, M.; Kawata, S., Experimental investigation of single voxels for laser nanofabrication via two-photon photopolymerization. *Appl. Phys. Lett.* **2003,** *83* (5), 819-821.

100.     Sun, H.-B.; Takada, K.; Kim, M.-S.; Lee, K.-S.; Kawata, S., Scaling laws of voxels in two-photon photopolymerization nanofabrication. *Appl. Phys. Lett.* **2003,** *83* (6), 1104-1106.

101.     Mueller, J. B.; Fischer, J.; Mayer, F.; Kadic, M.; Wegener, M., Polymerization kinetics in three-dimensional direct laser writing. *Adv. Mater.* **2014,** *26* (38), 6566-71.

102.     Defize, T.; Thomassin, J.-M.; Ottevaere, H.; Malherbe, C.; Eppe, G.; Jellali, R.; Alexandre, M.; Jérôme, C.; Riva, R., Photo-Cross-Linkable Coumarin-Based Poly(ε-caprolactone) for Light-Controlled Design and Reconfiguration of Shape-Memory Polymer Networks. *Macromolecules* **2018,** *52* (2), 444-456.

103.     Imato, K.; Nishihara, M.; Kanehara, T.; Amamoto, Y.; Takahara, A.; Otsuka, H., Self-healing of chemical gels cross-linked by diarylbibenzofuranone-based trigger-free dynamic covalent bonds at room temperature. *Angew. Chem. Int. Ed. Engl.* **2012,** *51* (5), 1138-42.

104.     Zhang, B.; Digby, Z. A.; Flum, J. A.; Foster, E. M.; Sparks, J. L.; Konkolewicz, D., Self-healing, malleable and creep limiting materials using both supramolecular and reversible covalent linkages. *Polymer Chemistry* **2015,** *6* (42), 7368-7372.

105.  Ying, H.; Zhang, Y.; Cheng, J., Dynamic urea bond for the design of reversible and self-healing polymers. *Nat Commun* **2014,** *5*, 3218.

106.  Gräfe, D.; Gernhardt, M.; Ren, J.; Blasco, E.; Wegener, M.; Woodruff, M. A.; Barner-Kowollik, C., Enzyme-Degradable 3D Multi-Material Microstructures. *Adv. Funct. Mater.* **2020,** *31* (3).

107.  Zieger, M. M.; Mueller, P.; Quick, A. S.; Wegener, M.; Barner-Kowollik, C., Cleaving Direct-Laser-Written Microstructures on Demand. *Angew. Chem. Int. Ed. Engl.* **2017,** *56* (20), 5625-5629.

108.  Grafe, D.; Wickberg, A.; Zieger, M. M.; Wegener, M.; Blasco, E.; Barner-Kowollik, C., Adding chemically selective subtraction to multi-material 3D additive manufacturing. *Nat Commun* **2018,** *9* (1), 2788.

109.  Batchelor, R.; Messer, T.; Hippler, M.; Wegener, M.; Barner-Kowollik, C.; Blasco, E., Two in One: Light as a Tool for 3D Printing and Erasing at the Microscale. *Adv. Mater.* **2019,** *31* (40), e1904085.

110.  Montarnal, D.; Capelot, M.; Tournilhac, F.; Leibler, L., Silica-like malleable materials from permanent organic networks. *Science* **2011,** *334* (6058), 965-8.

111.  Willott, J. D.; Nielen, W. M.; de Vos, W. M., Stimuli-Responsive Membranes through Sustainable Aqueous Phase Separation. *ACS Appl Polym Mater* **2020,** *2* (2), 659-667.

112.  Lequieu, W.; Du Prez, F. E., Segmented polymer networks based on poly(N-isopropyl acrylamide) and poly(tetrahydrofuran) as polymer membranes with thermo-responsive permeability. *Polymer* **2004,** *45* (3), 749-757.

113.  Obadia, M. M.; Mudraboyina, B. P.; Serghei, A.; Montarnal, D.; Drockenmuller, E., Reprocessing and Recycling of Highly Cross-Linked Ion-Conducting Networks through Transalkylation Exchanges of C-N Bonds. *J. Am. Chem. Soc.* **2015,** *137* (18), 6078-83.

114.  Herbst, F.; Seiffert, S.; Binder, W. H., Dynamic supramolecular poly(isobutylene)s for self-healing materials. *Polymer Chemistry* **2012,** *3* (11).

115.  Wemyss, A. M.; Ellingford, C.; Morishita, Y.; Bowen, C.; Wan, C., Dynamic Polymer Networks: A New Avenue towards Sustainable and Advanced Soft Machines. *Angew. Chem. Int. Ed. Engl.* **2021**.

116.  Foster, E. M.; Lensmeyer, E. E.; Zhang, B.; Chakma, P.; Flum, J. A.; Via, J. J.; Sparks, J. L.; Konkolewicz, D., Effect of Polymer Network Architecture, Enhancing Soft Materials Using Orthogonal Dynamic Bonds in an Interpenetrating Network. *ACS Macro Letters* **2017,** *6* (5), 495-499.

117.  Chen, X.; Dam, M. A.; Ono, K.; Mal, A.; Shen, H.; Nutt, S. R.; Sheran, K.; Wudl, F., A thermally re-mendable cross-linked polymeric material. *Science* **2002,** *295* (5560), 1698-702.

118.  Fang, Y.; Du, X.; Du, Z.; Wang, H.; Cheng, X., Light- and heat-triggered polyurethane based on dihydroxyl anthracene derivatives for self-healing applications. *Journal of Materials Chemistry A* **2017,** *5* (17), 8010-8017.

119.  Wu, Y.; Wei, Y.; Ji, Y., Polymer actuators based on covalent adaptable networks. *Polymer Chemistry* **2020,** *11* (33), 5297-5320.

120.  Hu, W.; Ren, Z.; Li, J.; Askounis, E.; Xie, Z.; Pei, Q., New Dielectric Elastomers with Variable Moduli. *Adv. Funct. Mater.* **2015,** *25* (30), 4827-4836.

121.  Jiang, Z. C.; Xiao, Y. Y.; Tong, X.; Zhao, Y., Selective Decrosslinking in Liquid Crystal Polymer Actuators for Optical Reconfiguration of Origami and Light-Fueled Locomotion. *Angew. Chem. Int. Ed. Engl.* **2019,** *58* (16), 5332-5337.

122.  Greiner, A. M.; Klein, F.; Gudzenko, T.; Richter, B.; Striebel, T.; Wundari, B. G.; Autenrieth, T. J.; Wegener, M.; Franz, C. M.; Bastmeyer, M., Cell type-specific adaptation of cellular and nuclear volume in micro-engineered 3D environments. *Biomaterials* **2015,** *69*, 121-32.

123.  Hohmann, J. K.; Von Freymann, G., Influence of Direct Laser Written 3D Topographies on Proliferation and Differentiation of Osteoblast-Like Cells: Towards Improved Implant Surfaces. *Adv. Funct. Mater.* **2014,** *24* (42), 6573-6580.

124.  Marino, A.; Filippeschi, C.; Genchi, G. G.; Mattoli, V.; Mazzolai, B.; Ciofani, G., The Osteoprint: A bioinspired two-photon polymerized 3-D structure for the enhancement of bone-like cell differentiation. *Acta Biomaterialia* **2014,** *10* (10), 4304-4313.

125.  Song, J.; Michas, C.; Chen, C. S.; White, A. E.; Grinstaff, M. W., From Simple to Architecturally Complex Hydrogel Scaffolds for Cell and Tissue Engineering Applications: Opportunities Presented by Two-Photon Polymerization. *Adv Healthc Mater* **2020,** *9* (1), e1901217.

126.  Hippler, M.; Lemma, E. D.; Bertels, S.; Blasco, E.; Barner-Kowollik, C.; Wegener, M.; Bastmeyer, M., 3D Scaffolds to Study Basic Cell Biology. *Adv. Mater.* **2019,** *31* (26), e1808110.

127.  Engler, A. J.; Sen, S.; Sweeney, H. L.; Discher, D. E., Matrix elasticity directs stem cell lineage specification. *Cell* **2006,** *126* (4), 677-89.

128.  Soman, P.; Kelber, J. A.; Lee, J. W.; Wright, T. N.; Vecchio, K. S.; Klemke, R. L.; Chen, S., Cancer cell migration within 3D layer-by-layer microfabricated photocrosslinked PEG scaffolds with tunable stiffness. *Biomaterials* **2012,** *33* (29), 7064-7070.

129.  Bischofs, I. B.; Safran, S. A.; Schwarz, U. S., Elastic interactions of active cells with soft materials. *Phys Rev E Stat Nonlin Soft Matter Phys* **2004,** *69* (2 Pt 1), 021911.

130.    Palmieri, B.; Scanlon, C.; Worroll, D., 3rd; Grant, M.; Lee, J., Substrate mediated interaction between pairs of keratocytes: Multipole traction force models describe their migratory behavior. *PLoS One* **2019,** *14* (3), e0212162.

131.    Wemyss, A. M.; Bowen, C.; Plesse, C.; Vancaeyzeele, C.; Nguyen, G. T. M.; Vidal, F.; Wan, C., Dynamic crosslinked rubbers for a green future: A material perspective. *Materials Science and Engineering: R: Reports* **2020,** *141*.

132.    Saunders, L.; Ma, P. X., Self-Healing Supramolecular Hydrogels for Tissue Engineering Applications. *Macromol Biosci* **2019,** *19* (1), e1800313.

133.    Hou, S.; Wang, X.; Park, S.; Jin, X.; Ma, P. X., Rapid Self-Integrating, Injectable Hydrogel for Tissue Complex Regeneration. *Adv Healthc Mater* **2015,** *4* (10), 1491-5, 1423.

134.    Highley, C. B.; Rodell, C. B.; Burdick, J. A., Direct 3D Printing of Shear-Thinning Hydrogels into Self-Healing Hydrogels. *Adv. Mater.* **2015,** *27* (34), 5075-9.

135.    Yang, X.; Guo, L.; Xu, X.; Shang, S.; Liu, H., A fully bio-based epoxy vitrimer: Self-healing, triple-shape memory and reprocessing triggered by dynamic covalent bond exchange. *Materials & Design* **2020,** *186*.

136.    Liu, T.; Hao, C.; Wang, L.; Li, Y.; Liu, W.; Xin, J.; Zhang, J., Eugenol-Derived Biobased Epoxy: Shape Memory, Repairing, and Recyclability. *Macromolecules* **2017,** *50* (21), 8588-8597.

137.    Yang, Y.; Pei, Z.; Li, Z.; Wei, Y.; Ji, Y., Making and Remaking Dynamic 3D Structures by Shining Light on Flat Liquid Crystalline Vitrimer Films without a Mold. *J. Am. Chem. Soc.* **2016,** *138* (7), 2118-21.

138.    Takashima, K.; Rossiter, J.; Mukai, T., McKibben artificial muscle using shape-memory polymer. *Sensors and Actuators A: Physical* **2010,** *164* (1-2), 116-124.

139.    Poetz, K. L.; Shipp, D. A., Polyanhydrides: Synthesis, Properties, and Applications. *Aust. J. Chem.* **2016,** *69* (11).

140.    Stebbins, N. D.; Faig, J. J.; Yu, W.; Guliyev, R.; Uhrich, K. E., Polyactives: controlled and sustained bioactive release via hydrolytic degradation. *Biomater Sci* **2015,** *3* (8), 1171-87.

141.    Lawton, M. I.; Tillman, K. R.; Mohammed, H. S.; Kuang, W.; Shipp, D. A.; Mather, P. T., Anhydride-Based Reconfigurable Shape Memory Elastomers. *ACS Macro Letters* **2016,** *5* (2), 203-207.

142.    Langer, R., Biomaterials in drug delivery and tissue engineering: one laboratory's experience. *Acc. Chem. Res.* **2000,** *33* (2), 94-101.

143.    Urban, M. W., Dynamic materials: The chemistry of self-healing. *Nat Chem* **2012,** *4* (2), 80-2.

144.    Rekondo, A.; Martin, R.; Ruiz de Luzuriaga, A.; Cabañero, G.; Grande, H. J.; Odriozola, I., Catalyst-free room-temperature self-healing elastomers based on aromatic disulfide metathesis. *Mater. Horiz.* **2014,** *1* (2), 237-240.

145.    Chen, L.; Zhang, L.; Griffin, P. J.; Rowan, S. J., Impact of Dynamic Bond Concentration on the Viscoelastic and Mechanical Properties of Dynamic Poly(alkylurea-co -urethane) Networks. *Macromol. Chem. Phys.* **2019,** *221* (1).

146.    Shokuhfar, A.; Arab, B., The effect of cross linking density on the mechanical properties and structure of the epoxy polymers: molecular dynamics simulation. *J. Mol. Model.* **2013,** *19* (9), 3719-31.

147.    Tillman, K. R.; Meacham, R.; Rolsma, A. N.; Barankovich, M.; Witkowski, A. M.; Mather, P. T.; Graf, T.; Shipp, D. A., Dynamic covalent exchange in poly(thioether anhydrides). *Polymer Chemistry* **2020,** *11* (47), 7551-7561.

148.    Amamoto, Y.; Higaki, Y.; Matsuda, Y.; Otsuka, H.; Takahara, A., Programmed thermodynamic formation and structure analysis of star-like nanogels with core cross-linked by thermally exchangeable dynamic covalent bonds. *J. Am. Chem. Soc.* **2007,** *129* (43), 13298-304.

149.    Amamoto, Y.; Kikuchi, M.; Masunaga, H.; Sasaki, S.; Otsuka, H.; Takahara, A., Intelligent Build-Up of Complementarity Reactive Diblock Copolymers via Dynamic Covalent Exchange toward Symmetrical and Miktoarm Star-like Nanogels. *Macromolecules* **2010,** *43* (4), 1785-1791.

150.    Azuma, Y.; Terashima, T.; Sawamoto, M., Precision Synthesis of Imine-Functionalized Reversible Microgel Star Polymers via Dynamic Covalent Cross-Linking of Hydrogen-Bonding Block Copolymer Micelles. *Macromolecules* **2017,** *50* (2), 587-596.

151.    Jackson, A. W.; Fulton, D. A., The formation of core cross-linked star polymers containing cores cross-linked by dynamic covalent imine bonds. *Chem Commun (Camb)* **2010,** *46* (33), 6051-3.

152.    Jackson, A. W.; Fulton, D. A., pH triggered self-assembly of core cross-linked star polymers possessing thermoresponsive cores. *Chem Commun (Camb)* **2011,** *47* (24), 6807-9.

153.    Bapat, A. P.; Roy, D.; Ray, J. G.; Savin, D. A.; Sumerlin, B. S., Dynamic-covalent macromolecular stars with boronic ester linkages. *J. Am. Chem. Soc.* **2011,** *133* (49), 19832-8.

154.    Song, X.; Wen, Y.; Zhu, J. L.; Zhao, F.; Zhang, Z. X.; Li, J., Thermoresponsive Delivery of Paclitaxel by beta-Cyclodextrin-Based Poly(N-isopropylacrylamide) Star Polymer via Inclusion Complexation. *Biomacromolecules* **2016,** *17* (12), 3957-3963.

155.    Wang, G.; Wang, C.; Wang, Z.; Zhang, X., Bolaform superamphiphile based on a dynamic covalent bond and its self-assembly in water. *Langmuir* **2011,** *27* (20), 12375-80.

156.    Cambre, J. N.; Roy, D.; Sumerlin, B. S., Tuning the sugar-response of boronic acid block copolymers. *J. Polym. Sci., Part A: Polym. Chem.* **2012,** *50* (16), 3373-3382.

157.	Perez-Baena, I.; Loinaz, I.; Padro, D.; García, I.; Grande, H. J.; Odriozola, I., Single-chain polyacrylic nanoparticles with multiple Gd(iii) centres as potential MRI contrast agents. *J. Mater. Chem.* **2010,** *20* (33).

158.	Tooley, C. A.; Pazicni, S.; Berda, E. B., Toward a tunable synthetic [FeFe] hydrogenase mimic: single-chain nanoparticles functionalized with a single diiron cluster. *Polymer Chemistry* **2015,** *6* (44), 7646-7651.

159.	Rubio-Cervilla, J.; Gonzalez, E.; Pomposo, J. A., Advances in Single-Chain Nanoparticles for Catalysis Applications. *Nanomaterials (Basel)* **2017,** *7* (10).

160.	Sanchez-Sanchez, A.; Akbari, S.; Etxeberria, A.; Arbe, A.; Gasser, U.; Moreno, A. J.; Colmenero, J.; Pomposo, J. A., "Michael" Nanocarriers Mimicking Transient-Binding Disordered Proteins. *ACS Macro Letters* **2013,** *2* (6), 491-495.

161.	Gillissen, M. A. J.; Voets, I. K.; Meijer, E. W.; Palmans, A. R. A., Single chain polymeric nanoparticles as compartmentalised sensors for metal ions. *Polymer Chemistry* **2012,** *3* (11).

162.	Rothfuss, H.; Knofel, N. D.; Roesky, P. W.; Barner-Kowollik, C., Single-Chain Nanoparticles as Catalytic Nanoreactors. *J. Am. Chem. Soc.* **2018,** *140* (18), 5875-5881.

163.	Kodura, D.; Houck, H. A.; Bloesser, F. R.; Goldmann, A. S.; Du Prez, F. E.; Frisch, H.; Barner-Kowollik, C., Light-fueled dynamic covalent crosslinking of single polymer chains in non-equilibrium states. *Chem Sci* **2020,** *12* (4), 1302-1310.

164.	Bloesser, F. R.; Walden, S. L.; Irshadeen, I. M.; Chambers, L. C.; Barner-Kowollik, C., Chemiluminescent self-reported unfolding of single-chain nanoparticles. *Chem Commun (Camb)* **2021,** *57* (42), 5203-5206.

165.	Wiltshire, J. T.; Qiao, G. G., Recent Advances in Star Polymer Design: Degradability and the Potential for Drug Delivery. *Aust. J. Chem.* **2007,** *60* (10).

166.	Willenbacher, J.; Altintas, O.; Trouillet, V.; Knöfel, N.; Monteiro, M. J.; Roesky, P. W.; Barner-Kowollik, C., Pd-complex driven formation of single-chain nanoparticles. *Polymer Chemistry* **2015,** *6* (24), 4358-4365.

167.	Rothfuss, H.; Knofel, N. D.; Tzvetkova, P.; Michenfelder, N. C.; Baraban, S.; Unterreiner, A. N.; Roesky, P. W.; Barner-Kowollik, C., Phenanthroline-A Versatile Ligand for Advanced Functional Polymeric Materials. *Chemistry* **2018,** *24* (66), 17475-17486.

168.	Altintas, O.; Barner-Kowollik, C., Single-Chain Folding of Synthetic Polymers: A Critical Update. *Macromol. Rapid Commun.* **2016,** *37* (1), 29-46.

169.	Bohlen, J. L.; Kulendran, B.; Rothfuss, H.; Barner-Kowollik, C.; Roesky, P. W., Heterobimetallic Au(i)/Y(iii) single chain nanoparticles as recyclable homogenous catalysts. *Polymer Chemistry* **2021**.

170.	Knofel, N. D.; Rothfuss, H.; Tzvetkova, P.; Kulendran, B.; Barner-Kowollik, C.; Roesky, P. W., Heterobimetallic Eu(iii)/Pt(ii) single-chain nanoparticles: a path to enlighten catalytic reactions. *Chem Sci* **2020,** *11* (38), 10331-10336.

171.	Perez-Baena, I.; Barroso-Bujans, F.; Gasser, U.; Arbe, A.; Moreno, A. J.; Colmenero, J.; Pomposo, J. A., Endowing Single-Chain Polymer Nanoparticles with Enzyme-Mimetic Activity. *ACS Macro Letters* **2013,** *2* (9), 775-779.

172.	Li, S. D.; Huang, L., Pharmacokinetics and biodistribution of nanoparticles. *Mol Pharm* **2008,** *5* (4), 496-504.

173.	Kroger, A. P. P.; Paulusse, J. M. J., Single-chain polymer nanoparticles in controlled drug delivery and targeted imaging. *J Control Release* **2018,** *286*, 326-347.

174.	Basasoro, S.; Gonzalez-Burgos, M.; Moreno, A. J.; Verso, F. L.; Arbe, A.; Colmenero, J.; Pomposo, J. A., A Solvent-Based Strategy for Tuning the Internal Structure of Metallo-Folded Single-Chain Nanoparticles. *Macromol. Rapid Commun.* **2016,** *37* (13), 1060-5.

175.	Skjel, M. K.; Houghton, A. Y.; Kirby, A. E.; Harrison, D. J.; McDonald, R.; Rosenberg, L., Silane-controlled diastereoselectivity in the tris(pentafluorophenyl)borane-catalyzed reduction of alpha-diketones to silyl-protected 1,2-Diols. *Org. Lett.* **2010,** *12* (2), 376-9.

176.	Harth, E.; Van Horn, B.; Lee, V. Y.; Germack, D. S.; Gonzales, C. P.; Miller, R. D.; Hawker, C. J., A facile approach to architecturally defined nanoparticles via intramolecular chain collapse. *J. Am. Chem. Soc.* **2002,** *124* (29), 8653-60.

177.	Watanabe, K.; Tanaka, R.; Takada, K.; Kim, M.-J.; Lee, J.-S.; Tajima, K.; Isono, T.; Satoh, T., Intramolecular olefin metathesis as a robust tool to synthesize single-chain nanoparticles in a size-controlled manner. *Polymer Chemistry* **2016,** *7* (29), 4782-4792.

178.	Galant, O.; Donmez, H. B.; Barner-Kowollik, C.; Diesendruck, C. E., Flow Photochemistry for Single-Chain Polymer Nanoparticle Synthesis. *Angew. Chem.* **2020,** *133* (4), 2070-2074.

179.	Engelke, J.; Tuten, B. T.; Schweins, R.; Komber, H.; Barner, L.; Plüschke, L.; Barner-Kowollik, C.; Lederer, A., An in-depth analysis approach enabling precision single chain nanoparticle design. *Polymer Chemistry* **2020**.

180.	Perez-Baena, I.; Asenjo-Sanz, I.; Arbe, A.; Moreno, A. J.; Lo Verso, F.; Colmenero, J.; Pomposo, J. A., Efficient Route to Compact Single-Chain Nanoparticles: Photoactivated Synthesis via Thiol–Yne Coupling Reaction. *Macromolecules* **2014,** *47* (23), 8270-8280.

181.	Hanlon, A. M.; Martin, I.; Bright, E. R.; Chouinard, J.; Rodriguez, K. J.; Patenotte, G. E.; Berda, E. B., Exploring structural effects in single-chain "folding" mediated by intramolecular thermal Diels–Alder chemistry. *Polymer Chemistry* **2017,** *8* (34), 5120-5128.

182.     Nitsche, T.; Blanksby, S. J.; Blinco, J. P.; Barner-Kowollik, C., Pushing the limits of single chain compaction analysis by observing specific size reductions via high resolution mass spectrometry. *Polymer Chemistry* **2020,** *11* (10), 1696-1701.

183.     Lo Verso, F.; Pomposo, J. A.; Colmenero, J.; Moreno, A. J., Simulation guided design of globular single-chain nanoparticles by tuning the solvent quality. *Soft Matter* **2015,** *11* (7), 1369-75.

184.     Gillespie, D. T., Exact stochastic simulation of coupled chemical reactions. *The Journal of Physical Chemistry* **1977,** *81* (25), 2340-2361.

185.     Trigilio, A. D.; Marien, Y. W.; Van Steenberge, P. H. M.; D'hooge, D. R., Gillespie-Driven kinetic Monte Carlo Algorithms to Model Events for Bulk or Solution (Bio)Chemical Systems Containing Elemental and Distributed Species. *Industrial & Engineering Chemistry Research* **2020,** *59* (41), 18357-18386.

186.     Saldívar-Guerra, E., Numerical Techniques for the Solution of the Molecular Weight Distribution in Polymerization Mechanisms, State of the Art. *Macromolecular Reaction Engineering* **2020,** *14* (4).

187.     Bamford, C. H.; Tompa, H., On the calculation of molecular weight distributions from kinetic schemes. *J. Polym. Sci.* **1953,** *10* (3), 345-350.

188.     Mastan, E.; Zhu, S., Method of moments: A versatile tool for deterministic modeling of polymerization kinetics. *Eur. Polym. J.* **2015,** *68*, 139-160.

189.     Guo, J.-K.; Zhou, Y.-N.; Luo, Z.-H., Kinetic insight into electrochemically mediated ATRP gained through modeling. *AlChE J.* **2015,** *61* (12), 4347-4357.

190.     Zhou, Y.-N.; Luo, Z.-H., State-of-the-Art and Progress in Method of Moments for the Model-Based Reversible-Deactivation Radical Polymerization. *Macromolecular Reaction Engineering* **2016,** *10* (6), 516-534.

191.     Cao, Y.; Gillespie, D. T.; Petzold, L. R., Adaptive explicit-implicit tau-leaping method with automatic tau selection. *J. Chem. Phys.* **2007,** *126* (22), 224101.

192.     Tripathi, A. K.; Sundberg, D. C., A hybrid algorithm for accurate and efficient Monte Carlo simulations of free-radical polymerization reactions. *Macromol. Theory Simul.* **2015,** *24* (1), 52-64.

193.     Zapata-González, I.; Saldívar-Guerra, E.; Ortiz-Cisneros, J., Full Molecular Weight Distribution in RAFT Polymerization. New Mechanistic Insight by Direct Integration of the Equations. *Macromol. Theory Simul.* **2011,** *20* (6), 370-388.

194.     Zapata-González, I.; Saldívar-Guerra, E.; Flores-Tlacuahuac, A.; Vivaldo-Lima, E.; Ortiz-Cisneros, J., Efficient numerical integration of stiff differential equations in polymerisation reaction engineering: Computational aspects and applications. *The Canadian Journal of Chemical Engineering* **2012,** *90* (4), 804-823.

195.     Crowley, T. J.; Choi, K. Y., Discrete Optimal Control of Molecular Weight Distribution in a Batch Free Radical Polymerization Process. *Industrial & Engineering Chemistry Research* **1997,** *36* (9), 3676-3684.

196.     Kumar, S.; Ramkrishna, D., On the solution of population balance equations by discretization—I. A fixed pivot technique. *Chem. Eng. Sci.* **1996,** *51* (8), 1311-1332.

197.     Saliakas, V.; Chatzidoukas, C.; Krallis, A.; Meimaroglou, D.; Kiparissides, C., Dynamic Optimization of Molecular Weight Distribution Using Orthogonal Collocation on Finite Elements and Fixed Pivot Methods: An Experimental and Theoretical Investigation. *Macromolecular Reaction Engineering* **2007,** *1* (1), 119-136.

198.     Wulkow, M., The simulation of molecular weight distributions in polyreaction kinetics by discrete Galerkin methods. *Macromol. Theory Simul.* **1996,** *5* (3), 393-416.

199.     De Rybel, N.; Van Steenberge, P. H. M.; Reyniers, M.-F.; Barner-Kowollik, C.; D'Hooge, D. R.; Marin, G. B., An Update on the Pivotal Role of Kinetic Modeling for the Mechanistic Understanding and Design of Bulk and Solution RAFT Polymerization. *Macromol. Theory Simul.* **2017,** *26* (1).

200.     Ali Parsa, M.; Kozhan, I.; Wulkow, M.; Hutchinson, R. A., Modeling of functional group distribution in copolymerization: A comparison of deterministic and stochastic approaches. *Macromol. Theory Simul.* **2014,** *23* (3), 207-217.

201.     De Rybel, N.; Van Steenberge, P. H. M.; Reyniers, M. F.; D'hooge, D. R.; Marin, G. B., How chain length dependencies interfere with the bulk RAFT polymerization rate and microstructural control. *Chem. Eng. Sci.* **2018,** *177*, 163-179.

202.     Gillespie, D. T., Approximate accelerated stochastic simulation of chemically reacting systems. *The Journal of Chemical Physics* **2001,** *115* (4), 1716-1733.

203.     Brandão, A. L. T.; Soares, J. B. P.; Pinto, J. C.; Alberton, A. L., When Polymer Reaction Engineers Play Dice: Applications of Monte Carlo Models in PRE. *Macromolecular Reaction Engineering* **2015,** *9* (3), 141-185.

204.     Rathinam, M.; Petzold, L. R.; Cao, Y.; Gillespie, D. T., Stiffness in stochastic chemically reacting systems: The implicit tau-leaping method. *The Journal of Chemical Physics* **2003,** *119* (24), 12784-12794.

205.     Chaffey-Millar, H.; Stewart, D.; Chakravarty, M. M. T.; Keller, G.; Barner-Kowollik, C., A Parallelised High Performance Monte Carlo Simulation Approach for Complex Polymerisation Kinetics. *Macromol. Theory Simul.* **2007,** *16* (6), 575-592.

206.    Gao, H.; Oakley, L. H.; Konstantinov, I. A.; Arturo, S. G.; Broadbelt, L. J., Acceleration of Kinetic Monte Carlo Method for the Simulation of Free Radical Copolymerization through Scaling. *Industrial & Engineering Chemistry Research* **2015,** *54* (48), 11975-11985.

207.    Gao, H.; Broadbelt, L. J.; Konstantinov, I. A.; Arturo, S. G., Acceleration of kinetic monte carlo simulations of free radical copolymerization: A hybrid approach with scaling. *AlChE J.* **2017,** *63* (9), 4013-4021.

208.    Van Steenberge, P. H. M.; D'hooge, D. R.; Reyniers, M. F.; Marin, G. B., Improved kinetic Monte Carlo simulation of chemical composition-chain length distributions in polymerization processes. *Chem. Eng. Sci.* **2014,** *110*, 185-199.

209.    Van Steenberge, P. H. M.; D'hooge, D. R.; Wang, Y.; Zhong, M.; Reyniers, M.-F.; Konkolewicz, D.; Matyjaszewski, K.; Marin, G. B., Linear Gradient Quality of ATRP Copolymers. *Macromolecules* **2012,** *45* (21), 8519-8531.

210.    Toloza Porras, C.; D'hooge, D. R.; Van Steenberge, P. H. M.; Reyniers, M.-F.; Marin, G. B., A Theoretical Exploration of the Potential of ICAR ATRP for One- and Two-Pot Synthesis of Well-Defined Diblock Copolymers. *Macromolecular Reaction Engineering* **2013,** *7* (7), 311-326.

211.    De Smit, K.; Marien, Y. W.; Van Geem, K. M.; Van Steenberge, P. H. M.; D'Hooge, D. R., Connecting polymer synthesis and chemical recycling on a chain-by-chain basis: a unified matrix-based kinetic Monte Carlo strategy. *Reaction Chemistry & Engineering* **2020,** *5* (10), 1909-1928.

212.    Wang, L.; Broadbelt, L. J., Explicit Sequence of Styrene/Methyl Methacrylate Gradient Copolymers Synthesized by Forced Gradient Copolymerization with Nitroxide-Mediated Controlled Radical Polymerization. *Macromolecules* **2009,** *42* (20), 7961-7968.

213.    Tabash, R. Y.; Teymour, F. A.; Debling, J. A., Modeling Linear Free Radical Copolymerization by Digital Encoding. *Macromolecules* **2006,** *39* (2), 829-843.

214.    Hernández-Ortiz, J. C.; Van Steenberge, P. H. M.; Reyniers, M.-F.; Marin, G. B.; D'hooge, D. R.; Duchateau, J. N. E.; Remerie, K.; Toloza, C.; Vaz, A. L.; Schreurs, F., Modeling the reaction event history and microstructure of individual macrospecies in postpolymerization modification. *AlChE J.* **2017,** *63* (11), 4944-4961.

215.    Keer, L. D. Designing Individual Linear and Network Polymer Molecules Building
Block by Building Block. Ghent University, Belgium, 2021.

216.    Meimaroglou, D.; Kiparissides, C., A Novel Stochastic Approach for the Prediction of the Exact Topological Characteristics and Rheological Properties of Highly-Branched Polymer Chains. *Macromolecules* **2010,** *43* (13), 5820-5832.

217.    D'hooge, D. R.; Van Steenberge, P. H. M.; Reyniers, M. F.; Marin, G. B., The strength of multi-scale modeling to unveil the complexity of radical polymerization. *Prog. Polym. Sci.* **2016,** *58*, 59-89.

218.    Kryven, I.; Zhao, Y. R.; McAuley, K. B.; Iedema, P., A deterministic model for positional gradients in copolymers. *Chem. Eng. Sci.* **2018,** *177*, 491-500.

219.    Teraoka, I., *Polymer Solutions*. 2002.

220.    Pikulin, A.; Bityurin, N., Spatial resolution in polymerization of sample features at nanoscale. *Physical Review B* **2007,** *75* (19), 195430.

221.    Fritzsche, J., Ueber die festen Kohlenwasserstoffe des Steinkohlentheers. *Journal fr Praktische Chemie* **1867,** *101* (1), 333-343.

222.    Fabbrizzi, L.; Licchelli, M.; Pallavicini, P.; Perotti, A.; Sacchi, D., An Anthracene-Based Fluorescent Sensor for Transition Metal Ions. *Angewandte Chemie International Edition in English* **1994,** *33* (19), 1975-1977.

223.    Chen, M.; Zhao, Y.; Yan, L.; Yang, S.; Zhu, Y.; Murtaza, I.; He, G.; Meng, H.; Huang, W., A Unique Blend of 2-Fluorenyl-2-anthracene and 2-Anthryl-2-anthrance Showing White Emission and High Charge Mobility. *Angew. Chem. Int. Ed. Engl.* **2017,** *56* (3), 722-727.

224.    Haldar, S.; Chakraborty, D.; Roy, B.; Banappanavar, G.; Rinku, K.; Mullangi, D.; Hazra, P.; Kabra, D.; Vaidhyanathan, R., Anthracene-Resorcinol Derived Covalent Organic Framework as Flexible White Light Emitter. *J. Am. Chem. Soc.* **2018,** *140* (41), 13367-13374.

225.    Van Damme, J.; Du Prez, F., Anthracene-containing polymers toward high-end applications. *Prog. Polym. Sci.* **2018**.

226.    Zdobinsky, T.; Maiti, P. S.; Klajn, R., Support curvature and conformational freedom control chemical reactivity of immobilized species. *J. Am. Chem. Soc.* **2014,** *136* (7), 2711-4.

227.    Ihara, T.; Fujii, T.; Mukae, M.; Kitamura, Y.; Jyo, A., Photochemical ligation of DNA conjugates through anthracene cyclodimer formation and its fidelity to the template sequences. *J. Am. Chem. Soc.* **2004,** *126* (29), 8880-1.

228.    Manchester, J.; Bassani, D. M.; Duprey, J. L.; Giordano, L.; Vyle, J. S.; Zhao, Z. Y.; Tucker, J. H., Photocontrolled binding and binding-controlled photochromism within anthracene-modified DNA. *J. Am. Chem. Soc.* **2012,** *134* (26), 10791-4.

229.    Bhola, R.; Payamyar, P.; Murray, D. J.; Kumar, B.; Teator, A. J.; Schmidt, M. U.; Hammer, S. M.; Saha, A.; Sakamoto, J.; Schluter, A. D.; King, B. T., A two-dimensional polymer from the anthracene dimer and triptycene motifs. *J. Am. Chem. Soc.* **2013,** *135* (38), 14134-41.

230.     Telitel, S.; Blasco, E.; Bangert, L. D.; Schacher, F. H.; Goldmann, A. S.; Barner-Kowollik, C., Photo-reversible bonding and cleavage of block copolymers. *Polymer Chemistry* **2017,** *8* (27), 4038-4042.

231.     Biedermann, F.; Ross, I.; Scherman, O. A., Host–guest accelerated photodimerisation of anthracene-labeled macromolecules in water. *Polymer Chemistry* **2014,** *5* (18), 5375-5382.

232.     Claus, T. K.; Telitel, S.; Welle, A.; Bastmeyer, M.; Vogt, A. P.; Delaittre, G.; Barner-Kowollik, C., Light-driven reversible surface functionalization with anthracenes: visible light writing and mild UV erasing. *Chem Commun (Camb)* **2017,** *53* (10), 1599-1602.

233.     Connal, L. A.; Vestberg, R.; Hawker, C. J.; Qiao, G. G., Fabrication of Reversibly Crosslinkable, 3-Dimensionally Conformal Polymeric Microstructures. *Adv. Funct. Mater.* **2008,** *18* (20), 3315-3322.

234.     Froimowicz, P.; Frey, H.; Landfester, K., Towards the generation of self-healing materials by means of a reversible photo-induced approach. *Macromol. Rapid Commun.* **2011,** *32* (5), 468-73.

235.     Frank, P.; Prasher, A.; Tuten, B.; Chao, D.; Berda, E., Characterization of single-chain polymer folding using size exclusion chromatography with multiple modes of detection. *Applied Petrochemical Research* **2014,** *5* (1), 9-17.

236.     Bouas-Laurent, H.; Desvergne, J.-P.; Castellan, A.; Lapouyade, R., Photodimerization of anthracenes in fluid solution: structural aspects. *Chem. Soc. Rev.* **2000,** *29* (1), 43-55.

237.     T. Offenloch, J.; Gernhardt, M.; Blinco, J.; Frisch, H.; Mutlu, H.; Barner-Kowollik, C., Contemporary Photoligation Chemistry – The Visible Light Challenge. *Chemistry - A European Journal* **2018,** *24*.

238.     Oldham, K. B.; Parnis, J. M., Shining light on Beer's law. *ChemTexts* **2017,** *3* (2).

239.     Hippler, M., Photochemical Kinetics: Reaction Orders and Analogies with Molecular Beam Scattering and Cavity Ring-Down Experiments. *J. Chem. Educ.* **2003,** *80* (9), 1074.

240.     Parnis, J. M.; Oldham, K. B., Beyond the Beer–Lambert law: The dependence of absorbance on time in photochemistry. *Journal of Photochemistry and Photobiology A: Chemistry* **2013,** *267*, 6-10.

241.     Gegenhuber, T.; De Keer, L.; Goldmann, A. S.; Van Steenberge, P. H. M.; Mueller, J. O.; Reyniers, M.-F.; Menzel, J. P.; D'hooge, D. R.; Barner-Kowollik, C., Fusing Light-Induced Step-Growth Processes with RAFT Chemistry for Segmented Copolymer Synthesis: A Synergetic Experimental and Kinetic Modeling Study. *Macromolecules* **2017,** *50* (17), 6451-6467.

242.     Petrov, A. K., Main directions in the development of additive technologies for micron-resolution printing. *Inorg. Mater.* **2017,** *53* (12), 1349-1359.

243.     Hansen, M. J.; Velema, W. A.; Lerch, M. M.; Szymanski, W.; Feringa, B. L., Wavelength-selective cleavage of photoprotecting groups: strategies and applications in dynamic systems. *Chem. Soc. Rev.* **2015,** *44* (11), 3358-77.

244.     Olson, J. P.; Kwon, H. B.; Takasaki, K. T.; Chiu, C. Q.; Higley, M. J.; Sabatini, B. L.; Ellis-Davies, G. C., Optically selective two-photon uncaging of glutamate at 900 nm. *J. Am. Chem. Soc.* **2013,** *135* (16), 5954-7.

245.     Okuda, M.; Katayama, K., Photochemical reaction dynamics measured using the near-field heterodyne transient grating method. *J. Phys. Chem. A* **2008,** *112* (20), 4545-9.

246.     Marien, Y. W.; Van Steenberge, P. H. M.; Barner-Kowollik, C.; Reyniers, M.-F.; Marin, G. B.; D'hooge, D. R., Kinetic Monte Carlo Modeling Extracts Information on Chain Initiation and Termination from Complete PLP-SEC Traces. *Macromolecules* **2017,** *50* (4), 1371-1385.

247.     Levine, I. N., *Physical chemistry*. 5th ed. ed.; McGraw-Hill: Boston, 2002.

248.     Logan, S. R., Does a Photochemical Reaction Have a Reaction Order? *J. Chem. Educ.* **1997,** *74* (11), 1303.

249.     Simon, D. A. M. J. D., *Physical Chemistry: A Molecular Approach*. 1 ed.; Univ Science Books: 1997.

250.     del Barrio, J.; Sánchez-Somolinos, C., Light to Shape the Future: From Photolithography to 4D Printing. *Adv. Optical Mater.* **2019,** *7* (16), 1900598-1900598.

251.     Nie, Z.; Kumacheva, E., Patterning surfaces with functional polymers. *Nat Mater.* **2008,** *7* (4), 277-90.

252.     Lin, L.; Kollipara, P. S.; Zheng, Y., Digital manufacturing of advanced materials: Challenges and perspective. *Mater. Today* **2019,** *28*, 49-62.

253.     Tofail, S. A. M.; Koumoulos, E. P.; Bandyopadhyay, A.; Bose, S.; O'Donoghue, L.; Charitidis, C., Additive manufacturing: scientific and technological challenges, market uptake and opportunities. *Mater. Today* **2018,** *21* (1), 22-37.

254.     Jung, K.; Corrigan, N.; Ciftci, M.; Xu, J.; Seo, S. E.; Hawker, C. J.; Boyer, C., Designing with Light: Advanced 2D, 3D, and 4D Materials. *Adv. Mater.* **2020,** *32* (18), e1903850.

255.     Dolinski, N. D.; Page, Z. A.; Callaway, E. B.; Eisenreich, F.; Garcia, R. V.; Chavez, R.; Bothman, D. P.; Hecht, S.; Zok, F. W.; Hawker, C. J., Solution Mask Liquid Lithography (SMaLL) for One-Step, Multimaterial 3D Printing. *Adv. Mater.* **2018,** *30* (31), e1800364.

256.     Matsui, J.; Ochi, Y.; Tamaki, K., Photodimerization of Anthryl Moieties in a Poly(methacrylic acid) Derivative as Reversible Cross-linking Step in Molecular Imprinting. *Chem. Lett.* **2006,** *35* (1), 80-81.

257.     Wojtecki, R. J.; Meador, M. A.; Rowan, S. J., Using the dynamic bond to access macroscopically responsive structurally dynamic polymers. *Nat Mater* **2011,** *10* (1), 14-27.

258.    Krishnakumar, B.; Sanka, R. V. S. P.; Binder, W. H.; Parthasarthy, V.; Rana, S.; Karak, N., Vitrimers: Associative dynamic covalent adaptive networks in thermoset polymers. *Chem. Eng. J.* **2020,** *385*.

259.    Koo, B.; Nofen, E.; Chattopadhyay, A.; Dai, L., Dimeric anthracene-based mechanophore for damage precursor detection in epoxy-based thermoset polymer matrix: Characterization and atomistic modeling. *Comput. Mater. Sci.* **2017,** *133*, 167-174.

260.    Dvornikov, A. S.; Bouas-Laurent, H.; Desvergne, J. P.; Rentzepis, P. M., Ultrafast kinetics of 9-decylanthracene photodimers and their application to 3D optical storage. *J. Mater. Chem.* **1999,** *9* (5), 1081-1084.

261.    Rumer, J. W.; McCulloch, I., Organic photovoltaics: Crosslinking for optimal morphology and stability. *Mater. Today* **2015,** *18* (8), 425-435.

262.    Tomlinson, W. J.; Chandross, E. A.; Fork, R. L.; Pryde, C. A.; Lamola, A. A., Reversible photodimerization: a new type of photochromism. *Appl. Opt.* **1972,** *11* (3), 533-48.

263.    Bergmark, W. R.; Jones, G.; Reinhardt, T. E.; Halpern, A. M., Photoisomerization of bis(9-anthryl)methane and other linked anthracenes. The role of excimers and biradicals in photodimerization. *J. Am. Chem. Soc.* **1978,** *100* (21), 6665-6673.

264.    Kislyak, A.; Frisch, H.; Gernhardt, M.; Van Steenberge, P. H. M.; D'Hooge D, R.; Barner-Kowollik, C., Time-Dependent Differential and Integral Quantum Yields for Wavelength-Dependent [4+4] Photocycloadditions. *Chemistry* **2020,** *26* (2), 478-484.

265.    Cramer, N. B.; Davies, T.; O'Brien, A. K.; Bowman, C. N., Mechanism and Modeling of a Thiol–Ene Photopolymerization. *Macromolecules* **2003,** *36* (12), 4631-4636.

266.    Vana, P.; Davis, T. P.; Barner-Kowollik, C., Kinetic Analysis of Reversible Addition Fragmentation Chain Transfer (RAFT) Polymerizations: Conditions for Inhibition, Retardation, and Optimum Living Polymerization. *Macromol. Theory Simul.* **2002,** *11* (8), 823-835.

267.    Wols, B. A.; Hofman-Caris, C. H. M., Modelling micropollutant degradation in UV/H2O2 systems: Lagrangian versus Eulerian method. *Chem. Eng. J.* **2012,** *210*, 289-297.

268.    Ng, K. H.; Lee, C. H.; Khan, M. R.; Cheng, C. K., Photocatalytic degradation of recalcitrant POME waste by using silver doped titania: Photokinetics and scavenging studies. *Chem. Eng. J.* **2016,** *286*, 282-290.

269.    Marien, Y. W.; Van Steenberge, P. H. M.; Kockler, K. B.; Barner-Kowollik, C.; Reyniers, M.-F.; Marin, G. B.; D'Hooge, D. R., Estimating the photodissociation quantum yield from PLP-SEC peak heights. *Polym. Chem.* **2017,** *8* (20), 3124-3128.

270.    Van Steenberge, P. H. M.; Sedlacek, O.; Hernandez-Ortiz, J. C.; Verbraeken, B.; Reyniers, M. F.; Hoogenboom, R.; D'Hooge D, R., Visualization and design of the functional group distribution during statistical copolymerization. *Nat Commun* **2019,** *10* (1), 3641.

271.    Frisch, H.; Tuten, B. T.; Barner-Kowollik, C., Macromolecular Superstructures: A Future Beyond Single Chain Nanoparticles. *Isr. J. Chem.* **2020,** *60* (1-2), 86-99.

272.    Fierens, S. K.; Telitel, S.; Van Steenberge, P. H. M.; Reyniers, M.-F.; Marin, G. B.; Lutz, J.-F.; D'hooge, D. R., Model-Based Design To Push the Boundaries of Sequence Control. *Macromolecules* **2016,** *49* (24), 9336-9344.

273.    Gody, G.; Zetterlund, P. B.; Perrier, S.; Harrisson, S., The limits of precision monomer placement in chain growth polymerization. *Nat Commun* **2016,** *7*, 10514.

274.    De Keer, L.; Kilic, K. I.; Van Steenberge, P. H. M.; Daelemans, L.; Kodura, D.; Frisch, H.; De Clerck, K.; Reyniers, M. F.; Barner-Kowollik, C.; Dauskardt, R. H.; D'Hooge D, R., Computational prediction of the molecular configuration of three-dimensional network polymers. *Nat Mater* **2021**.

275.    Meier, M. A. R.; Barner-Kowollik, C., A New Class of Materials: Sequence-Defined Macromolecules and Their Emerging Applications. *Adv. Mater.* **2019,** *31* (26), e1806027.

276.    Dobson, C. M., Protein folding and misfolding. *Nature* **2003,** *426* (6968), 884-90.

277.    Wen, W.; Chen, A., Influence of single chain nanoparticle stabilizers on polymerization induced hierarchical self-assembly. *Polymer Chemistry* **2021**.

278.    Altintas, O.; Willenbacher, J.; Wuest, K. N. R.; Oehlenschlaeger, K. K.; Krolla-Sidenstein, P.; Gliemann, H.; Barner-Kowollik, C., A Mild and Efficient Approach to Functional Single-Chain Polymeric Nanoparticles via Photoinduced Diels–Alder Ligation. *Macromolecules* **2013,** *46* (20), 8092-8101.

279.    Hanlon, A. M.; Chen, R.; Rodriguez, K. J.; Willis, C.; Dickinson, J. G.; Cashman, M.; Berda, E. B., Scalable Synthesis of Single-Chain Nanoparticles under Mild Conditions. *Macromolecules* **2017,** *50* (7), 2996-3003.

280.    Scharnagl, C.; Reif, M.; Friedrich, J., Stability of proteins: temperature, pressure and the role of the solvent. *Biochim. Biophys. Acta* **2005,** *1749* (2), 187-213.

281.    Hiltebrandt, K.; Elies, K.; D'Hooge D, R.; Blinco, J. P.; Barner-Kowollik, C., A Light-Activated Reaction Manifold. *J. Am. Chem. Soc.* **2016,** *138* (22), 7048-54.

282.    Poloukhtine, A. A.; Mbua, N. E.; Wolfert, M. A.; Boons, G. J.; Popik, V. V., Selective labeling of living cells by a photo-triggered click reaction. *J. Am. Chem. Soc.* **2009,** *131* (43), 15769-76.

283.    Kislyak, A.; Kodura, D.; Frisch, H.; Feist, F.; Van Steenberge, P. H. M.; Barner-Kowollik, C.; D'Hooge, D. R., A holistic approach for anthracene photochemistry kinetics. *Chem. Eng. J.* **2020,** *402*.

284.    Liu, M.; Wenzel, W.; Frisch, H., Photocycloreversions within single polymer chains. *Polymer Chemistry* **2020,** *11* (41), 6616-6623.

285.    Liu, J. W.; Mackay, M. E.; Duxbury, P. M., Molecular Dynamics Simulation of Intramolecular Cross-Linking of BCB/Styrene Copolymers. *Macromolecules* **2009,** *42* (21), 8534-8542.

286.    Moreno, A. J.; Lo Verso, F.; Sanchez-Sanchez, A.; Arbe, A.; Colmenero, J.; Pomposo, J. A., Advantages of Orthogonal Folding of Single Polymer Chains to Soft Nanoparticles. *Macromolecules* **2013,** *46* (24), 9748-9759.

287.    Moreno, A. J.; Bacova, P.; Lo Verso, F.; Arbe, A.; Colmenero, J.; Pomposo, J. A., Effect of chain stiffness on the structure of single-chain polymer nanoparticles. *J Phys Condens Matter* **2018,** *30* (3), 034001.

288.    Danilov, D.; Barner-Kowollik, C.; Wenzel, W., Modelling of reversible single chain polymer self-assembly: from the polymer towards the protein limit. *Chem Commun (Camb)* **2015,** *51* (27), 6002-5.

289.    Smyth, M. S.; Martin, J. H., x ray crystallography. *Mol Pathol* **2000,** *53* (1), 8-14.

290.    Martin, J. E.; Eichinger, B. E., Dimensions of intramolecularly crosslinked polymers. 1. Theory. *Macromolecules* **1983,** *16* (8), 1345-1350.

291.    Martin, J. E.; Eichinger, B. E., Dimensions of intramolecularly crosslinked polymers. 2. Dilute solution thermodynamic parameters and photon correlation results on the polystyrene/cyclopentane system. *Macromolecules* **1983,** *16* (8), 1350-1358.

292.    Tzounis, P.-N.; Anogiannakis, S. D.; Theodorou, D. N., General Methodology for Estimating the Stiffness of Polymer Chains from Their Chemical Constitution: A Single Unperturbed Chain Monte Carlo Algorithm. *Macromolecules* **2017,** *50* (11), 4575-4587.

293.    D'hooge, D. R.; Van Steenberge, P. H. M.; Derboven, P.; Reyniers, M.-F.; Marin, G. B., Model-based design of the polymer microstructure: bridging the gap between polymer chemistry and engineering. *Polymer Chemistry* **2015,** *6* (40), 7081-7096.

294.    Devlaminck, D. J. G.; Van Steenberge, P. H. M.; De Keer, L.; Reyniers, M.-F.; D'Hooge, D. R., A detailed mechanistic study of bulk MADIX of styrene and its chain extension. *Polymer Chemistry* **2017,** *8* (45), 6948-6963.

295.    Fierens, S. K.; D'hooge, D. R.; Van Steenberge, P. H. M.; Reyniers, M.-F.; Marin, G. B., MAMA-SG1 initiated nitroxide mediated polymerization of styrene: From Arrhenius parameters to model-based design. *Chem. Eng. J.* **2015,** *278*, 407-420.

296.    Van Steenberge, P. H. M.; Verbraeken, B.; Reyniers, M.-F.; Hoogenboom, R.; D'hooge, D. R., Model-Based Visualization and Understanding of Monomer Sequence Formation in Gradient Copoly(2-oxazoline)s On the basis of 2-Methyl-2-oxazoline and 2-Phenyl-2-oxazoline. *Macromolecules* **2015,** *48* (21), 7765-7773.

297.    Lemos, T.; Melo, P. A.; Pinto, J. C., Stochastic Modeling of Polymer Microstructure From Residence Time Distribution. *Macromolecular Reaction Engineering* **2015,** *9* (3), 259-270.

298.    Arraez, F. J.; Van Steenberge, P. H. M.; D'hooge, D. R., Conformational Distributions near and on the Substrate during Surface-Initiated Living Polymerization: A Lattice-Based Kinetic Monte Carlo Approach. *Macromolecules* **2020,** *53* (12), 4630-4648.

299.    Arraez, F. J.; Steenberge, P.; D'Hooge D. R., The Competition of Termination and Shielding to Evaluate the Success of Surface-Initiated Reversible Deactivation Radical Polymerization. *Polymers (Basel)* **2020,** *12* (6).

300.    Gernhardt, M. Multi-material microstructures with novel stimuli-responsive properties. Queensland University of Technology, 2021.

301.    Erdmann, A.; Rumler, M.; Onanuga, T., Simulation flow and model verification for laser direct-write lithography. *Journal of Micro/Nanolithography, MEMS, and MOEMS* **2017,** *16* (03), 1.

302.    Blasco, E.; Wegener, M.; Barner-Kowollik, C., Photochemically Driven Polymeric Network Formation: Synthesis and Applications. *Adv. Mater.* **2017,** *29* (15).

303.    Photonic professional (GT). Nanoscribe GmbH: Germany, 2015.

304.    Decker, C., Kinetic study of light-induced polymerization by real-time UV and IR spectroscopy. *J. Polym. Sci., Part A: Polym. Chem.* **1992,** *30* (5), 913-928.

305.    Kenning, N. S.; Ficek, B. A.; Hoppe, C. C.; Scranton, A. B., Spatial and temporal evolution of the photoinitiation rate for thick polymer systems illuminated by polychromatic light: selection of efficient photoinitiators for LED or mercury lamps. *Polym. Int.* **2008,** *57* (10), 1134-1140.

306.    Schwalm, R., *UV Coatings*. 2007.

307.    Jockusch, S.; Turro, N. J., Radical Addition Rate Constants to Acrylates and Oxygen:  α-Hydroxy and α-Amino Radicals Produced by Photolysis of Photoinitiators. *J. Am. Chem. Soc.* **1999,** *121* (16), 3921-3925.

308.    Kockler, K. B.; Haehnel, A. P.; Fleischhaker, F.; Schneider-Baumann, M.; Misske, A. M.; Barner-Kowollik, C., No Apparent Correlation of $k_p$ with Steric Hindrance for Branched Acrylates. *Macromol. Chem. Phys.* **2015,** *216* (14), 1573-1582.

309.     Asua, J. M.; Beuermann, S.; Buback, M.; Castignolles, P.; Charleux, B.; Gilbert, R. G.; Hutchinson, R. A.; Leiza, J. R.; Nikitin, A. N.; Vairon, J. P.; Van Herk, A. M., Critically evaluated rate coefficients for free-radical polymerization, 5: Propagation rate coefficient for butyl acrylate. *Macromol. Chem. Phys.* **2004,** *205* (16), 2151-2160.

310.     Johnston-Hall, G.; Monteiro, M. J., Bimolecular radical termination: New perspectives and insights. *J. Polym. Sci., Part A: Polym. Chem.* **2008,** *46* (10), 3155-3173.

311.     Barth, J.; Buback, M.; Hesse, P.; Sergeeva, T., Termination and Transfer Kinetics of Butyl Acrylate Radical Polymerization Studied via SP-PLP-EPR. *Macromolecules* **2010,** *43* (9), 4023-4031.

312.     Andrzejewska, E.; Bogacki, M. B.; Andrzejewski, M.; Janaszczyk, M., Termination mechanism during the photo-induced radical cross-linking polymerization in the presence and absence of oxygen. *PCCP* **2003,** *5* (12), 2635.

313.     Matyjaszewski, K.; Davis, T. P., *Handbook of Radical Polymerization*. 2002.

314.     Vir, A. B.; Marien, Y. W.; Van Steenberge, P. H. M.; Barner-Kowollik, C.; Reyniers, M.-F.; Marin, G. B.; D'Hooge, D. R., From n-butyl acrylate Arrhenius parameters for backbiting and tertiary propagation to β-scission via stepwise pulsed laser polymerization. *Polymer Chemistry* **2019,** *10* (30), 4116-4125.

315.     Maeder, S.; Gilbert, R. G., Measurement of Transfer Constant for Butyl Acrylate Free-Radical Polymerization. *Macromolecules* **1998,** *31* (14), 4410-4418.

316.     Mueller, J. B.; Fischer, J.; Mange, Y. J.; Nann, T.; Wegener, M., In-situ local temperature measurement during three-dimensional direct laser writing. *Appl. Phys. Lett.* **2013,** *103* (12).

317.     Kalayci, K.; Frisch, H.; Truong, V. X.; Barner-Kowollik, C., Green light triggered [2+2] cycloaddition of halochromic styrylquinoxaline-controlling photoreactivity by pH. *Nat Commun* **2020,** *11* (1), 4193.

318.     Kalayci, K.; Frisch, H.; Barner-Kowollik, C.; Truong, V. X., Wavelength-Dependent Stiffening of Hydrogel Matrices via Redshifted [2+2] Photocycloadditions. *Adv. Funct. Mater.* **2020,** *30* (15).

319.     Claus, T. K.; Zhang, J.; Martin, L.; Hartlieb, M.; Mutlu, H.; Perrier, S.; Delaittre, G.; Barner-Kowollik, C., Stepwise Light-Induced Dual Compaction of Single-Chain Nanoparticles. *Macromol. Rapid Commun.* **2017,** *38* (16).

# APPENDIX A: SUPPORTING INFORMATION FOR CHAPTER 2

This supporting information accompanying **Chapter 2** has been published as Kislyak, A.; Frisch, H.; Gernhardt, M.; Van Steenberge, P. H. M.; D'Hooge D, R.; Barner-Kowollik, C., Time-Dependent Differential and Integral Quantum Yields for Wavelength-Dependent [4+4] Photocycloadditions. *Chemistry* **2020,** *26* (2), 478-484.

## A.1 Derivation related to photoreaction rate law

### A.1.1 Derivation of $\mathcal{J}_a(c_A)$ (eq 2-4 in the main text)

The number of excited species formed in a singlet excited state is equal to the amount of photons absorbed,[1] thus, in order to obtain an expression for the rate of excited species formation, we need to derive the equation in terms of moles of photons absorbed per second. Based on expressions provided in the book by Levine I. N.[1] as well as work of Marien Y. W. et al.,[2] one can derive the required expression.

First, the number of photons generated per pulse (reaching the sample holder) $n_{\gamma\,pp}$ can be determined by division of energy per pulse emitted by the laser at a certain wavelength λ by the energy of a single photon at the said wavelength as is seen in **eq A-1** with

$$n_{\gamma\,pp}(\lambda) = \frac{E_{pp}}{E_\lambda}$$

eq A-1

Further, in order to obtain the actual number of photons reaching the solution one has to account for the fraction of light being absorbed, reflected or otherwise by multiplication with an experimentally determined glass transmittance value, $T_\lambda$. Next, in order to translate the number of photons reaching the solution per pulse to moles of photons per second it is necessary to multiply our expression by the number of pulses per second, *f*, as well as dividing it by the Avogadro number, $N_A$. In addition, the expression was divided by the sample volume, V, in order to obtain moles of photons reaching the solution per second per unit of volume. Finally, with accordance to the Beer-Lambert law[1] the factor $(1 - 10^{-\varepsilon c_A L})$ is introduced, so that one can determine the amount of moles of photons absorbed per unit time per unit volume, **eq 2-4** (in the main text).

$$\mathcal{J}_a(c_A) = \frac{E_{pp}T_\lambda f}{E_\lambda N_A V}(1 - 10^{-\varepsilon c_A L})$$

## A.1.2 Derivation of photoreaction rate law for anthracene dimerization

In this section **eq 2-5** shown in the main text is derived. The mass balance for anthracene species **A** in the reaction volume can be written as **eq A-2**, based on the reaction scheme in **Scheme 2-1b** in the main text. Hereby, we assume perfect mixing in the sample and consider a constant volume and temperature.

$$\frac{dc_A}{dt} = k_{-1}c_{^1A} + k_3 c_{^1A} c_A - k_2 c_{^1A} c_A - \mathcal{J}_a \qquad \text{eq A-2}$$

By analogy, the continuity equation for anthracene monomer in the singlet excited state can be written as:

$$\frac{dc_{^1A}}{dt} = -k_{-1}c_{^1A} - k_3 c_{^1A} c_A - k_2 c_{^1A} c_A + \mathcal{J}_a \qquad \text{eq A-3}$$

Here we make a quasi-steady-state assumption for the calculation of the concentration of the $^1A$ species $\left(\frac{dc_{^1A}}{dt} \text{ formally equal to } 0\right)$, which under rearrangement yields **eq A-4**. If **eq A-4** is substituted in **eq A-2**, we arrive to **eq A-5**. Finally, simplification of **eq A-5** leads to **eq 2-5** in the main text.

$$c_{^1A} = \frac{\mathcal{J}_a}{(k_3 + k_2)c_A + k_{-1}} \qquad \text{eq A-4}$$

$$\frac{dc_A}{dt} = \frac{(k_{-1} + k_3 c_A - k_2 c_A)\mathcal{J}_a}{(k_3 + k_2)c_A + k_{-1}} - \mathcal{J}_a \qquad \text{eq A-5}$$

## A.2 Synthesis
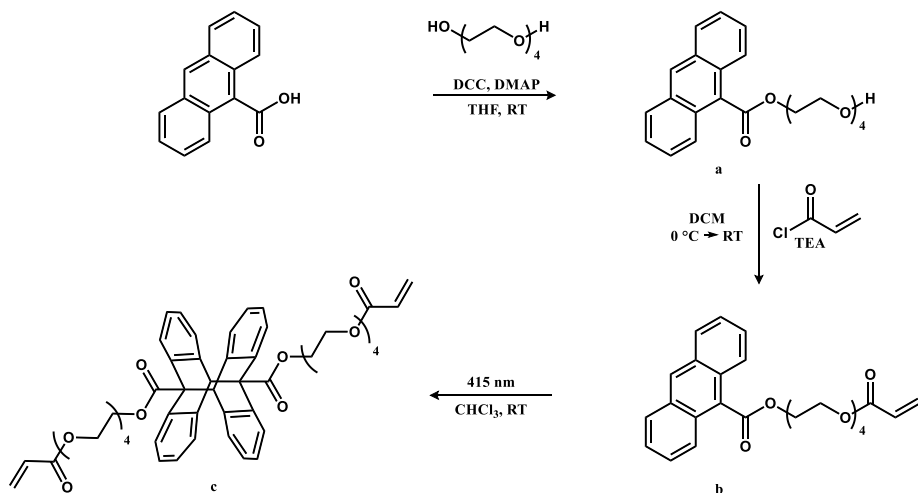


Scheme A-1 Synthesis of the anthracene dimer c.

### A.2.1 Synthesis of 2-(2-(2-(2-hydroxyethoxy)ethoxy)ethoxy)ethyl anthracene-9-carboxylate (a)
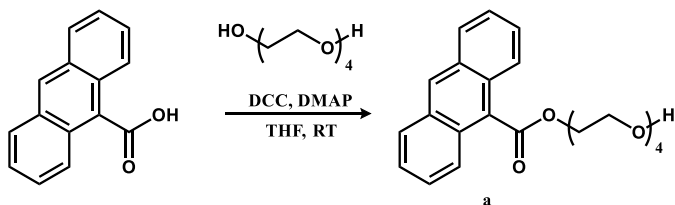


Scheme A-2 Synthesis of a.

2.50 g (11.25 mmol, 1.00 eq.) of 9-anthracenecarboxylic acid, 19.4 mL (112.49 mmol, 10.0 eq.) of tetraethylene glycol and 0.14 g (1.13 mmol, 0.10 eq.) of DMAP were dissolved in 70 mL of THF in a dry flask under argon. 2.79 g (13.5 mmol, 1.20 eq.) of DCC were dissolved in 7 mL of THF and added to the flask over the course of 30 min using a syringe pump. In order to increase conversion, another 4.19 g (16.9 mmol, 1.5 eq.) of DCC was added after 24 h. After 72 h in total, the reaction solution was diluted with DCM, filtered to remove dicyclohexylurea (DCU) and washed with saturated sodium bicarbonate solution, water and brine. The organic

phase was dried with sodium sulphate and the solvent was evaporated. The raw product was purified in several steps: It was dissolved in acetone, before cooling the solution and filtering it in order to remove remaining DCU. Afterwards, it was purified using column chromatography, starting in 1:1 cyclohexane : ethyl acetate, then switching to 10% v/v methanol in ethyl acetate. The product was obtained in a yield of 41% (1.85g, 4.64 mmol).

**¹H NMR** (600 MHz, DMSO, δ): 8.79 (s, 1H, Ar H), 8.17 (d, $J$ = 8.7 Hz, 2H, Ar H), 8.06 (d, $J$ = 8.7 Hz, 2H, Ar H), 7.63 (m, 2H, Ar H), 7.59 (m, 2H, Ar H), 4.73 (t, 2H, $J$ = 4.7 Hz, PEG H), 4.55 (t, 2H, $J$ = 5.4 Hz, PEG -OH), 3.84 (t, 2H, $J$ = 4.7 Hz, PEG H), 3.64-3.35 (m, 12 H, PEG H) ppm.
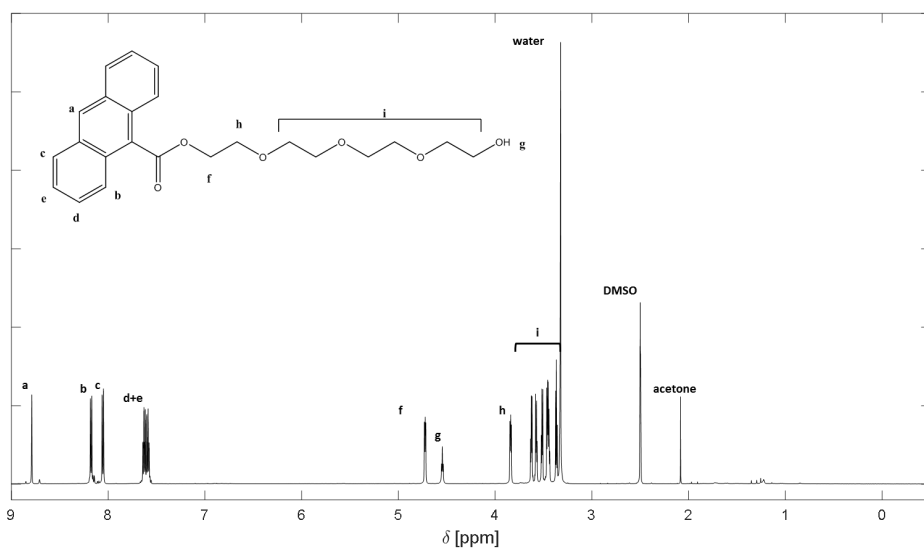


**Fig A-1 ¹HNMR-spectrum of** a **(600 MHz, DMSO-d6).**

## A.2.2 Synthesis of anthracene monomer 13-oxo-3,6,9,12-tetraoxapentadec-14-en-1-yl anthracene-9-carboxylate (b)
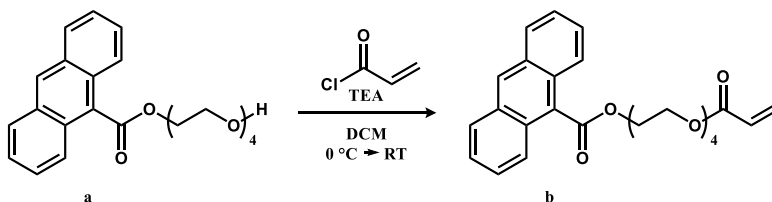


**Scheme A-3 Synthesis of b.**

1.75 g (4.39 mmol, 1.00 eq.) of **a** and 0.74 mL (5.27 mmol, 1.20 eq.) of triethylamine (TEA) were dissolved in 10.0 mL DCM in a dry flask under argon. 0.43 mL (5.27 mmol, 1.20 eq.) of acryloyl chloride were dissolved in 2.50 mL of DCM. The solution was added to the reaction flask using a syringe pump over the course of 30 min while the reaction flask was cooled in an ice bath. The reaction was allowed to reach room temperature and continued to be stirred overnight.

The reaction mixture was washed three times each with 5% HCl, saturated sodium bicarbonate solution and water. The organic phase was dried with sodium sulphate and the solvent was evaporated. The product was obtained in a yield of 85% (1.69 g, 3.73 mmol).

**¹H NMR** (600 MHz, CDCl₃, δ): 8.53 (s, 1H, Ar H), 8.13 (d, $J$ = 8.7 Hz, 2H, Ar H), 8.01 (d, $J$ = 8.7 Hz, 2H, Ar H), 7.54 (m, 2H, Ar H), 7.48 (m, 2H, Ar H), 6.43-6.37 (m, 1 H, -CO-CH-CH-C*H*H), 6.16-6.09 (m, 1 H, -CO-CH-C*H*-CHH), 5.82-5.78 (m, 1 H, -CO-CH-CH-CH*H*), 4.78 (t, 2H, $J$ = 4.8 Hz, PEG H), 4.27 (t, 2H, $J$ = 4.5 Hz, PEG H), 3.94 (t, 2H, $J$ = 4.8 Hz, PEG H), 3.76-3.56 (m, 12 H, PEG H) ppm.
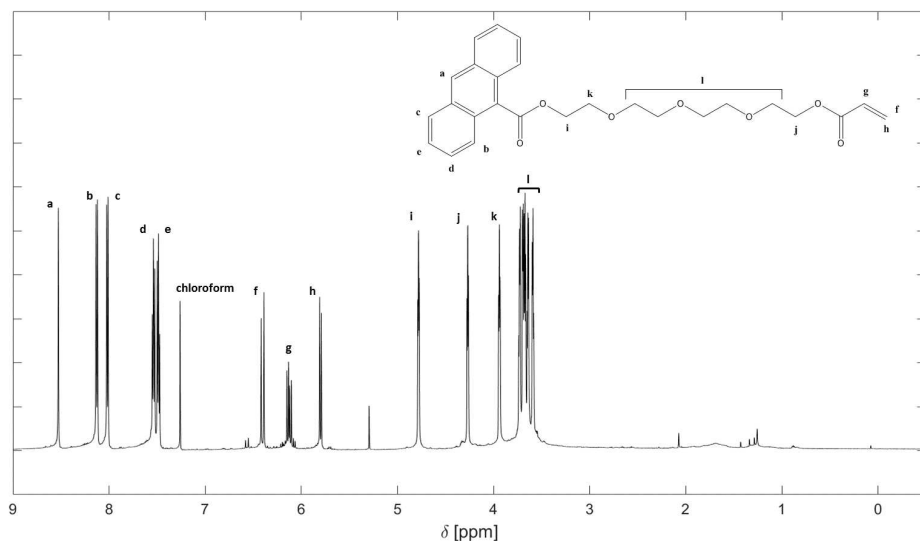


**Fig A-2 ¹HNMR-spectrum of b (600 MHz, CDCl₃).**

## A.2.3 Synthesis of anthracene dimer 13-oxo-3,6,9,12-tetraoxapentadec-14-en-1-yl anthracene-9-carboxylate dimer (c)
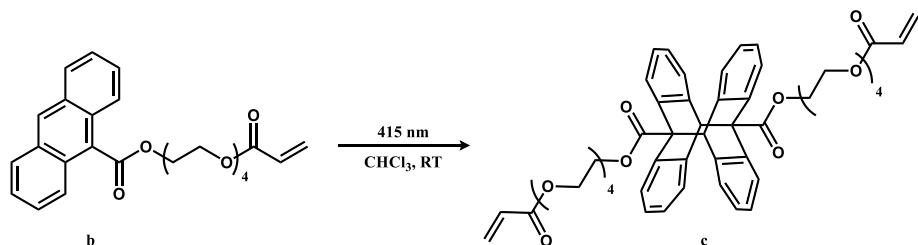


**Scheme A-4 Synthesis of c.**

A solution of **b** in chloroform with a concentration of 12 mg/mL was prepared. It was degassed by bubbling argon through it for 10 min. The reaction vial was irradiated with a 10 W 415 nm LED. Full conversion after 16 h reaction time was verified using $^1$H-NMR.

**$^1$H NMR** (600 MHz, CDCl$_3$, δ): 6.97 (d, $J$ = 7.2 Hz, 4H, Ar H), 6.81 (m, 8H, Ar H), 6.72 (d, $J$ = 7.2 Hz, Ar H), 6.43-6.38 (m, 2H, -CO-CH-CH-C*H*H), 6.16-6.10 (m, 2H, -CO-CH-C*H*-CHH), 5.83-5.79 (m, 2H, -CO-CH-CH-CH*H*), 5.72 (s, 1H), 4.56 (t, 2H, $J$ = 4.8 Hz, PEG H), 4.27 (m, 2H, $J$ = 4.8 Hz, PEG H), 3.71 (m, 2H, $J$ = 4.8 Hz, PEG H), 3.66 (m, 2H, $J$ = 4.8 Hz, PEG H), 3.57-3.52 (m, 8 H, PEG H) ppm.
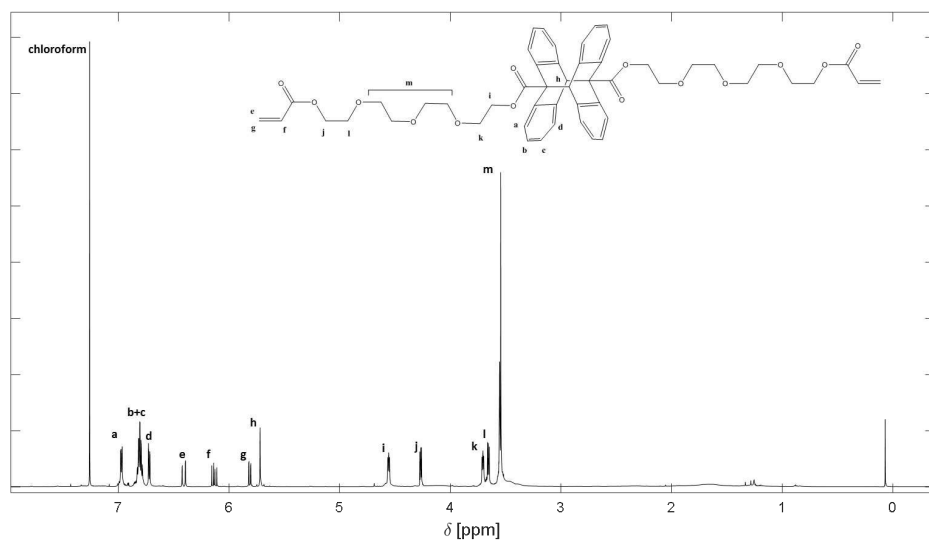
**Fig A-3 $^1$HNMR-spectrum of c (600 MHz, CDCl$_3$).**

## A.3 Experimental procedures

### A.3.1 UV-VIS

Obtaining 100% pure anthracene monomer **A** and its dimer **A₂** separately is an experimental challenge. Thus, the following procedure was used in order to obtain extinction coefficients of pure compounds. First, ^{1}H-NMRs of mostly anthracene and mostly anthracene dimer samples (>90%) were taken to determine the percentage of each of the compounds in the samples. Subsequently, UV-VIS spectra of the samples were taken in a chloroform solution for three separate stock solutions for each of the compounds. Furthermore, due to high absorbance of the anthracene monomer **A,** each stock solution was measured three times as well. The data averaged over measurements of three stock solutions and equations below were applied in order to determine pure molar attenuation coefficients.

$$\varepsilon_A = \frac{Abs_1 - \varepsilon_D [D]_1}{[A]_1} \qquad\qquad\qquad \text{eq A-6}$$

$$\varepsilon_D = \frac{Abs_2 - Abs_1 \frac{[A]_2}{[A]_1}}{[D]_2 - [D]_1 \frac{[A]_2}{[A]_1}} \qquad\qquad\qquad \text{eq A-7}$$

With $Abs_1$ representing average absorbance values for solution 1 (99.41% anthracene dimer and 0.59% anthracene monomer), $Abs_2$– average absorbance values for solution 2 (98.89% anthracene monomer and 1.11% anthracene dimer),$[A]_1$ – concentration of anthracene monomer in solution 1 in mol L⁻¹, $[A]_2$ – concentration of anthracene monomer in solution 2 in mol L⁻¹, $[D]_1$ – concentration of anthracene dimer in solution 1, mol L⁻¹, $[D]_2$ – concentration of anthracene dimer in solution 2, mol L⁻¹, $\varepsilon_D$ – molar attenuation coefficient of anthracene dimer, $L\,mol^{-1}\,cm^{-1}$ $\varepsilon_A$ – molar attenuation coefficient of anthracene monomer, $L\,mol^{-1}\,cm^{-1}$.

## A.3.2 Laser experimental procedure

Samples for the laser experiments were prepared by two procedures, which yielded similar results. The first procedure involved preparation of the solution of anthracene in dichloromethane, sealing off the solution in the laser vial and subsequent degassing of the solution for 10 min in nitrogen flow. An alternative procedure involved several freeze-pump-thaw cycles of dichloromethane prior to the placement of the solvent into the glovebox. Anthracene monomer, **A**, was dried and placed into the glovebox, where the solution was made under the nitrogen atmosphere. In both cases solution was sealed in 0.7 mL glass laser vials.

Experiments were conducted on a tunable 20Hz Opolette laser at 375 nm unless specified otherwise. The laser experimental set up is depicted in **Fig A-4**. The glass transmittance measured before each set of experiments with accordance to procedures described in Ref [3], which involved using 5 laser vial bottoms obtained from laser vials cut about 3.6mm from the bottom, placing the vial bottoms in sample holder 5 in place of the sample and measuring the resulting energies per pulse with and without the vial bottom in place.[3] From the resulting values glass transmittance, $T_\lambda$, can be readily calculated as $\frac{E_{pp\,with\,vial\,in\,place}}{E_{pp\,with\,out\,vial\,in\,place}}$.



1. Laser
2. Lenses
3. Shutter
4. Prism
5. Sample holder
6. Sample
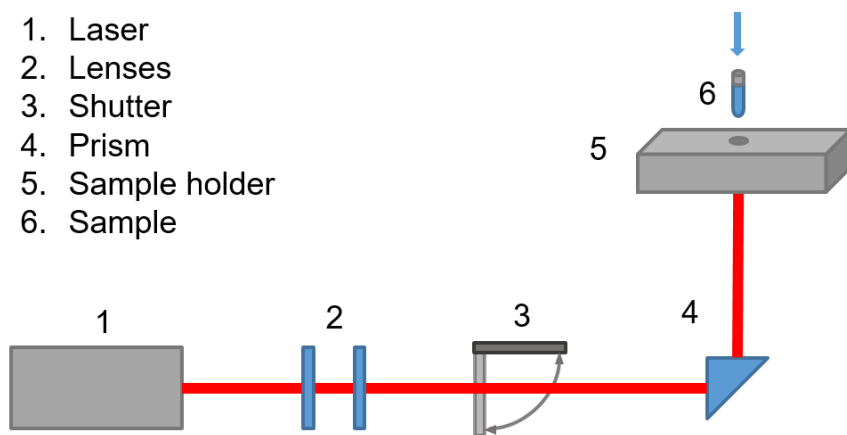
**Fig A-4 Laser experiment set up.**

## A.4 Supporting results

### A.4.1 Error analysis for Fig 2-2

Error bars present in **Fig 2-2** are the result of error propagation based on the uncertainties in the equipment used. Error of the scale used was $\pm 0.01$ mg, error of 100-1000 µL blue Eppendorf pipette both systematic and random was accounted for and dependent on the volume used (data available from the Eppendorf manual),[4] NMR error was taken as a residual error of the fit and, finally, further 3% error was added on top of the calculated error to estimate for an uncertainty related to the laser use.

### A.4.2 Conversion and fraction of light absorbed vs wavelength
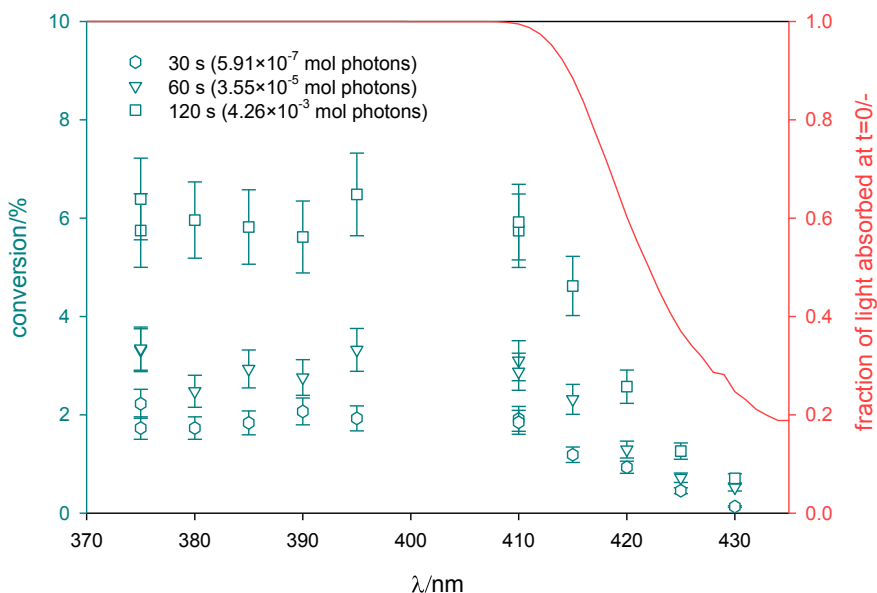


**Fig A-5 Conversion of anthracene (1) in DCM after irradiation at 30, 60 and 120 s at different wavelengths as in Fig 2-2 in the main text. All of the samples were irradiated at a photon rate of $1.97 \times 10^{-8}$ mol s$^{-1}$. In comparison to Fig 2-2 in the main text, here on the second axis the fraction of light absorbed at the initial irradiation for the concentration, calculated in accordance to Beer-Lambert's law,[1] $(1 - 10^{-\varepsilon c_A L})$, and volume of samples used can be seen for the ease of comparison. The major reduction in conversion at wavelengths beyond 410 nm is associated with decrease of the fraction of light absorbed.**

## A.4.3 Experimental data

Table A-1 Data for experiments performed at 375 nm and 2 mg per sample. Data used for construction of Fig 2-2, 2-3 and 2-4.

| Wavelength $\lambda$, nm | Initial mass of anthracene monomer 1 per sample m, mg | Sample volume V, $\mu$L | Energy per pulse measured by the energy meter $E_{pp}$, $\mu$J pulse$^{-1}$ | Glass transmittance $T_1$ | Irradiation time t, s | Moles of photons reaching the solution until that time $n_\gamma$, mol | Monomer amount at time t $n_A$, mol | Apparent rate coefficient (eq 2-12) $k_{app}$, s$^{-1}$ | Standard error of $k_{app}$ from the fitting, s$^{-1}$ | $R^2$ of the fit |
|---|---|---|---|---|---|---|---|---|---|---|
| 375 | 1.98 | 100 | 397 | 0.758 | 0 | - | 4.35E-06 | 3.56E-04 | 2.91E-06 | 1.00 |
| | | | | | 30 | 5.57E-07 | 4.26E-06 | | | |
| | | | | | 60 | 1.14E-06 | 4.18E-06 | | | |
| | | | | | 120 | 2.28E-06 | 4.00E-06 | | | |
| 375 | 1.98 | 100 | 401 | 0.802 | 0 | - | 4.34E-06 | 4.15E-04* | 1.76E-05 | 0.996 |
| | | | | | 30 | 6.07E-07 | 4.23E-06 | | | |
| | | | | | 60 | 1.19E-06 | 4.11E-06 | | | |
| | | | | | 120 | 2.37E-06 | 3.93E-06 | | | |
| | | | | | 300 | 6.13E-06 | 3.37E-06 | | | |
| | | | | | 600 | 1.20E-05 | 2.65E-06 | | | |
| | | | | | 900 | 1.82E-05 | 1.99E-06 | | | |
| | | | | | 1800 | 3.66E-05 | 8.38E-07 | | | |
| | | | | | 3600 | 7.32E-05 | 1.78E-07 | | | |
| | | | | | 1800 | 3.68E-05 | 6.86E-07 | | | |
| | | | | | 10800 | 2.20E-04 | 3.11E-08 | | | |
| 375 | 1.99 | 250 | 402 | 0.821 | 0 | - | 4.35E-06 | 2.45E-04 | 1.40E-05 | 0.994 |
| | | | | | 30 | 6.27E-07 | 4.27E-06 | | | |
| | | | | | 60 | 1.24E-06 | 4.20E-06 | | | |
| | | | | | 120 | 2.47E-06 | 4.10E-06 | | | |
| 375 | 1.99 | 250 | 399 | 0.758 | 0 | - | 4.36E-06 | 2.67E-04 | 1.89E-05 | 0.990 |
| | | | | | 30 | 5.70E-07 | 4.26E-06 | | | |
| | | | | | 60 | 1.14E-06 | 4.21E-06 | | | |
| | | | | | 120 | 2.27E-06 | 4.08E-06 | | | |
| 375 | 1.98 | 250 | 401 | 0.802 | 0 | - | 4.35E-06 | - | - | - |
| | | | | | 300 | 5.99E-06 | 3.80E-06 | | | |
| | | | | | 600 | 1.20E-05 | 3.11E-06 | | | |

| 375 | 1.99 | 500 | 396 | 0.800 | 900 | 1.81E-05 | 2.57E-06 | 1.43E-04 | 4.46E-06 | 0.998 |
| | | | | | 1800 | 3.60E-05 | 1.42E-06 | | | |
| | | | | | 3600 | 7.48E-05 | 6.02E-07 | | | |
| | | | | | 7200 | 1.44E-04 | 6.20E-08 | | | |
| | | | | | 10800 | 2.17E-04 | 1.35E-08 | | | |
| 375 | 1.99 | 500 | 401 | 0.758 | 0 | - | 4.36E-06 | 1.64E-04 | 1.49E-05 | 0.984 |
| | | | | | 30 | 5.97E-07 | 4.31E-06 | | | |
| | | | | | 60 | 1.18E-06 | 4.28E-06 | | | |
| | | | | | 120 | 2.40E-06 | 4.21E-06 | | | |
| 375 | 1.99 | 250 | 304 | 0.778 | 0 | - | 4.35E-06 | 1.57E-04 | 1.23E-05 | 0.988 |
| | | | | | 40 | 5.90E-07 | 4.29E-06 | | | |
| | | | | | 80 | 1.18E-06 | 4.22E-06 | | | |
| | | | | | 160 | 2.39E-06 | 4.13E-06 | | | |
| 375 | 1.99 | 250 | 197 | 0.778 | 0 | - | 4.35E-06 | 1.19E-04 | 8.26E-06 | 0.990 |
| | | | | | 60 | 5.84E-07 | 4.27E-06 | | | |
| | | | | | 120 | 1.15E-06 | 4.24E-06 | | | |
| | | | | | 240 | 2.29E-06 | 4.10E-06 | | | |

* $k_{app}$ determination is based on first 4 points

**Table A-2 Data for experiments performed at 375 nm and 4 mg per sample. Data used for construction of Fig 2-3.**

| Wavelength λ, nm | Initial mass of anthracene monomer 1 per sample m, mg | Sample volume V, µL | Energy per pulse measured by the energy meter $E_{pp}$, µJ pulse$^{-1}$ | Glass transmittance $T_\lambda$ | Irradiation time t, s | Moles of photons reaching the solution until that time $n_\gamma$, mol | Monomer amount at time t $n_A$, mol | Apparent rate coefficient (eq 2-12) $k_{app}$, s$^{-1}$ | Standard error of $k_{app}$ from the fitting, s$^{-1}$ | R² of the fit |
|---|---|---|---|---|---|---|---|---|---|---|
| 375 | 3.97 | 100 | 397 | 0.800 | 0 | 8.69E-06 | 3.99E-08 | 2.74E-04 | 1.02E-06 | 1.00 |
|  |  |  |  |  | 60 | 8.40E-06 | 1.83E-07 |  |  |  |
|  |  |  |  |  | 120 | 8.13E-06 | 3.18E-07 |  |  |  |
|  |  |  |  |  | 240 | 7.61E-07 | 5.76E-07 |  |  |  |
| 375 | 3.97 | 100 | 397 | 0.758 | 0 | 8.72E-06 | 2.84E-08 | 2.02E-04 | 1.56E-05 | 0.988 |
|  |  |  |  |  | 60 | 8.44E-06 | 1.72E-07 |  |  |  |
|  |  |  |  |  | 120 | 8.25E-06 | 2.68E-07 |  |  |  |
|  |  |  |  |  | 240 | 7.90E-06 | 4.40E-07 |  |  |  |
| 375 | 3.97 | 200 | 403 | 0.803 | 0 | 8.69E-06 | 3.99E-08 | 1.81E-04 | 7.57E-06 | 0.997 |
|  |  |  |  |  | 60 | 8.48E-06 | 1.47E-07 |  |  |  |
|  |  |  |  |  | 120 | 8.28E-06 | 2.44E-07 |  |  |  |
|  |  |  |  |  | 240 | 7.96E-06 | 4.04E-07 |  |  |  |
| 375 | 3.97 | 200 | 401 | 0.758 | 0 | 8.71E-06 | 2.83E-08 | 1.61E-04 | 7.68E-06 | 0.995 |
|  |  |  |  |  | 60 | 8.50E-06 | 1.32E-07 |  |  |  |
|  |  |  |  |  | 120 | 8.35E-06 | 2.08E-07 |  |  |  |
|  |  |  |  |  | 240 | 8.05E-06 | 3.56E-07 |  |  |  |
| 375 | 3.97 | 500 | 397 | 0.803 | 0 | 8.69E-06 | 4.00E-08 | 1.04E-04 | 9.34E-06 | 0.984 |
|  |  |  |  |  | 60 | 8.58E-06 | 9.74E-08 |  |  |  |
|  |  |  |  |  | 120 | 8.52E-06 | 1.26E-07 |  |  |  |
|  |  |  |  |  | 240 | 8.27E-06 | 2.54E-07 |  |  |  |
| 375 | 3.97 | 500 | 397 | 0.758 | 0 | 8.72E-06 | 2.84E-08 | 1.18E-04 | 5.32E-06 | 0.996 |
|  |  |  |  |  | 60 | 8.57E-06 | 1.04E-07 |  |  |  |
|  |  |  |  |  | 120 | 8.45E-06 | 1.61E-07 |  |  |  |
|  |  |  |  |  | 240 | 8.23E-06 | 2.71E-07 |  |  |  |

Table A-3 Data for experiments performed at 375 nm and 6 or 8 mg per sample. Data used for construction of Fig 2-3.

| Wavelength $\lambda$, nm | Initial ass of anthracene monomer per sample m, mg | Sample volume V, $\mu$L | Energy per pulse measured by the energy meter $E_{pp}$, $\mu$J pulse$^{-1}$ | Glass transmittance $T_\lambda$ | Irradiation time t, s | Moles of photons reaching the solution until that time $n_\gamma$, mol | Monomer amount at time t $n_A$, mol | Apparent rate coefficient $k_{app}$, s$^{-1}$ (eq 2-12) | Standard error of $k_{app}$ from the fitting, s$^{-1}$ | $R^2$ of the fit |
|---|---|---|---|---|---|---|---|---|---|---|
| 375 | 5.94 | 100 | 399 | 0.800 | 0 | 1.30E-05 | 5.98E-08 | 1.77E-04 | 5.70E-06 | 0.998 |
| | | | | | 120 | 1.24E-05 | 3.56E-07 | | | |
| | | | | | 240 | 1.19E-05 | 6.31E-07 | | | |
| | | | | | 480 | 1.10E-05 | 1.08E-06 | | | |
| 375 | 5.95 | 150 | 404 | 0.778 | 0 | 1.30E-05 | 5.99E-08 | 1.27E-04 | 4.84E-06 | 0.997 |
| | | | | | 120 | 1.26E-05 | 2.93E-07 | | | |
| | | | | | 240 | 1.22E-05 | 4.77E-07 | | | |
| | | | | | 480 | 1.15E-05 | 8.18E-07 | | | |
| 375 | 5.95 | 300 | 406 | 0.800 | 0 | 1.30E-05 | 5.99E-08 | 1.92E-04 | 4.29E-06 | 0.999 |
| | | | | | 120 | 1.24E-05 | 3.90E-07 | | | |
| | | | | | 240 | 1.19E-05 | 6.46E-07 | | | |
| | | | | | 480 | 1.08E-05 | 1.17E-06 | | | |
| 375 | 5.95 | 300 | 401 | 0.821 | 0 | 1.30E-05 | 5.99E-08 | 1.16E-04 | 8.03E-06 | 0.990 |
| | | | | | 120 | 1.26E-05 | 2.98E-07 | | | |
| | | | | | 240 | 1.22E-05 | 4.64E-07 | | | |
| | | | | | 480 | 1.16E-05 | 7.57E-07 | | | |
| 375 | 7.93 | 400 | 401 | 0.800 | 0 | 1.74E-05 | 7.98E-08 | 8.05E-05 | 2.27E-06 | 0.998 |
| | | | | | 240 | 1.68E-05 | 3.84E-07 | | | |
| | | | | | 480 | 1.60E-05 | 7.51E-07 | | | |
| | | | | | 960 | 1.49E-05 | 1.31E-06 | | | |

**Table A-4 Data for experiments performed at various wavelengths for Fig 2-2.**

| Wavelength $\lambda$, nm | Initial mass of anthracene monomer 1 per sample m, mg | Sample volume V, $\mu$L | Energy per pulse measured by the energy meter $E_{pp}$, $\mu$J pulse$^{-1}$ | Glass transmittance $T_\lambda$ | Irradiation time t, s | Moles of photons reaching the solution until that time $n_\gamma$, mol | Monomer amount at time t $n_A$, mol | Apparent rate coefficient $k_{app}$, s$^{-1}$ (eq 2-12) | Standard error of $k_{app}$ from the fitting, s$^{-1}$ | $R^2$ of the fit |
|---|---|---|---|---|---|---|---|---|---|---|
| 380 | 1.98 | 250 | 406 | 0.766 | 0 | - | 4.36E-06 | 2.51E-04 | 2.25E-05 | 0.984 |
|  |  |  |  |  | 30 | 5.92E-07 | 4.28E-06 |  |  |  |
|  |  |  |  |  | 60 | 1.18E-06 | 4.25E-06 |  |  |  |
|  |  |  |  |  | 120 | 2.38E-06 | 4.10E-06 |  |  |  |
| 385 | 1.98 | 250 | 385 | 0.783 | 0 | - | 4.36E-06 | 2.45E-04 | 1.19E-05 | 0.995 |
|  |  |  |  |  | 30 | 5.85E-07 | 4.28E-06 |  |  |  |
|  |  |  |  |  | 60 | 1.16E-06 | 4.23E-06 |  |  |  |
|  |  |  |  |  | 120 | 2.33E-06 | 4.11E-06 |  |  |  |
| 390 | 1.98 | 250 | 379 | 0.799 | 0 | - | 4.36E-06 | 2.32E-04 | 2.25E-05 | 0.981 |
|  |  |  |  |  | 30 | 5.92E-07 | 4.27E-06 |  |  |  |
|  |  |  |  |  | 60 | 1.19E-06 | 4.24E-06 |  |  |  |
|  |  |  |  |  | 120 | 2.36E-06 | 4.11E-06 |  |  |  |
| 395 | 1.98 | 250 | 384 | 0.778 | 0 | - | 4.36E-06 | 2.76E-04* | 8.65E-06 | 0.998 |
|  |  |  |  |  | 30 | 5.94E-07 | 4.28E-06 |  |  |  |
|  |  |  |  |  | 60 | 1.18E-06 | 4.21E-06 |  |  |  |
|  |  |  |  |  | 120 | 2.36E-06 | 4.08E-06 |  |  |  |
|  |  |  |  |  | 300 | 5.91E-06 | 3.69E-06 |  |  |  |
| 410 | 1.98 | 250 | 352 | 0.824 | 0 | - | 4.36E-06 | 2.41E-04* | 1.43E-05 | 0.993 |
|  |  |  |  |  | 30 | 5.97E-07 | 4.28E-06 |  |  |  |
|  |  |  |  |  | 60 | 1.19E-06 | 4.22E-06 |  |  |  |
|  |  |  |  |  | 120 | 2.38E-06 | 4.11E-06 |  |  |  |
|  |  |  |  |  | 300 | 5.97E-06 | 3.70E-06 |  |  |  |
|  |  |  |  |  | 600 | 1.20E-05 | 3.20E-06 |  |  |  |
| 410 | 1.98 | 250 | 355 | 0.801 | 0 | - | 4.36E-06 | 2.49E-04* | 1.34E-05 | 0.994 |
|  |  |  |  |  | 30 | 5.82E-07 | 4.28E-06 |  |  |  |
|  |  |  |  |  | 60 | 1.16E-06 | 4.23E-06 |  |  |  |
|  |  |  |  |  | 120 | 2.31E-06 | 4.10E-06 |  |  |  |

| | | | | | Time | | | kapp* | | |
|---|---|---|---|---|---|---|---|---|---|---|
| 415 | 1.98 | 250 | 359 | 0.797 | 600 | 1.18E-05 | 3.22E-06 | 1.97E-04 | 9.76E-07 | 1.00 |
| | | | | | 1200 | 2.34E-05 | 2.45E-06 | | | |
| | | | | | 1800 | 3.47E-05 | 1.98E-06 | | | |
| | | | | | 2400 | 4.78E-05 | 1.52E-06 | | | |
| | | | | | 0 | - | 4.36E-06 | | | |
| | | | | | 30 | 5.98E-07 | 4.31E-06 | | | |
| | | | | | 60 | 1.19E-06 | 4.26E-06 | | | |
| | | | | | 120 | 2.37E-06 | 4.16E-06 | | | |
| 420 | 1.98 | 250 | 352 | 0.803 | 0 | - | 4.36E-06 | 1.05E-04 | 9.42E-06 | 0.984 |
| | | | | | 30 | 6.06E-07 | 4.32E-06 | | | |
| | | | | | 60 | 1.18E-06 | 4.30E-06 | | | |
| | | | | | 120 | 2.36E-06 | 4.25E-06 | | | |
| 425 | 1.98 | 250 | 344 | 0.802 | 0 | - | 4.36E-06 | 5.15E-05 | 4.62E-06 | 0.984 |
| | | | | | 30 | 5.88E-07 | 4.34E-06 | | | |
| | | | | | 60 | 1.18E-06 | 4.33E-06 | | | |
| | | | | | 120 | 2.36E-06 | 4.30E-06 | | | |
| 430 | 1.98 | 250 | 349 | 0.797 | 0 | - | 4.36E-06 | 3.10E-05 | 6.36E-06 | 0.922 |
| | | | | | 30 | 6.07E-07 | 4.35E-06 | | | |
| | | | | | 60 | 1.19E-06 | 4.34E-06 | | | |
| | | | | | 120 | 2.37E-06 | 4.33E-06 | | | |

* $k_{app}$ determination is based on first 4 points

## A.4.4 From $k_{app}$ towards the individual rate coefficients

**Fig A-6** shows plot of the experimental data from **Fig 2-3** the main text divided by $\mathcal{J}_a$ (red hollow points) as well as a resulting fit function. The fitting was performed using a dynamic fit function of SigmaPlot and **eq 2-14** of the main text. Note that we opted for a pragmatic description based on only the initial anthracene concentration (one variable $c_{A0}$), leading to an elegant formula despite the recording of the experimental data in **Fig 2-3** in the main text based on two variables: the initial mass amount and the volume of the system.

$r_1 = \frac{k_2}{k_{-1}} = 5.41 \pm 0.48 \, L \, mol^{-1}$

$r_2 = \frac{k_2 + k_3}{k_{-1}} = 44.2 \pm 8.1 \, L \, mol^{-1}$

$R^2 = 0.963$
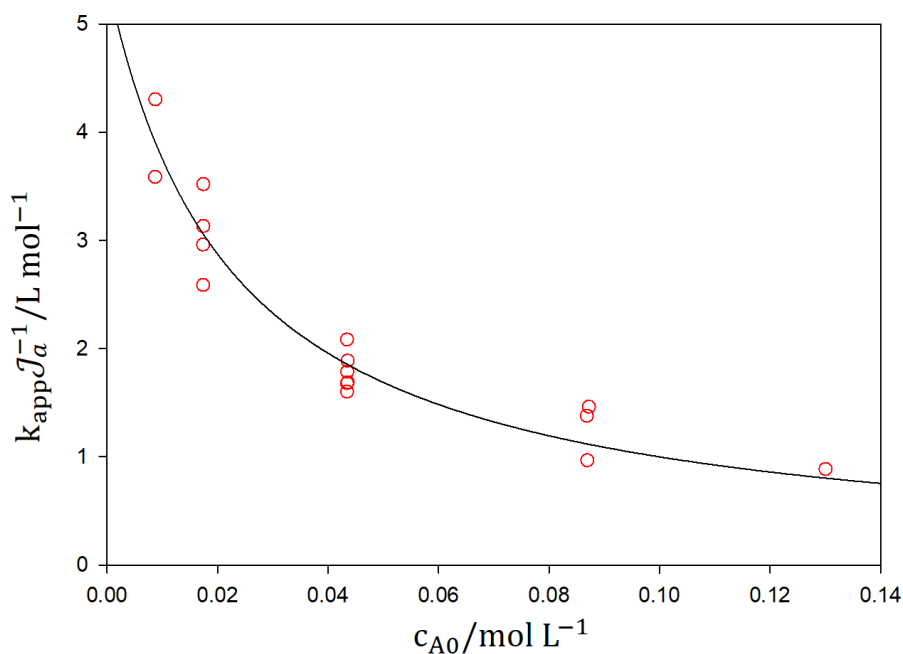


**Fig A-6 Adjustment of parameters in eq 2-14 for the experimental data from Fig 2-3.**
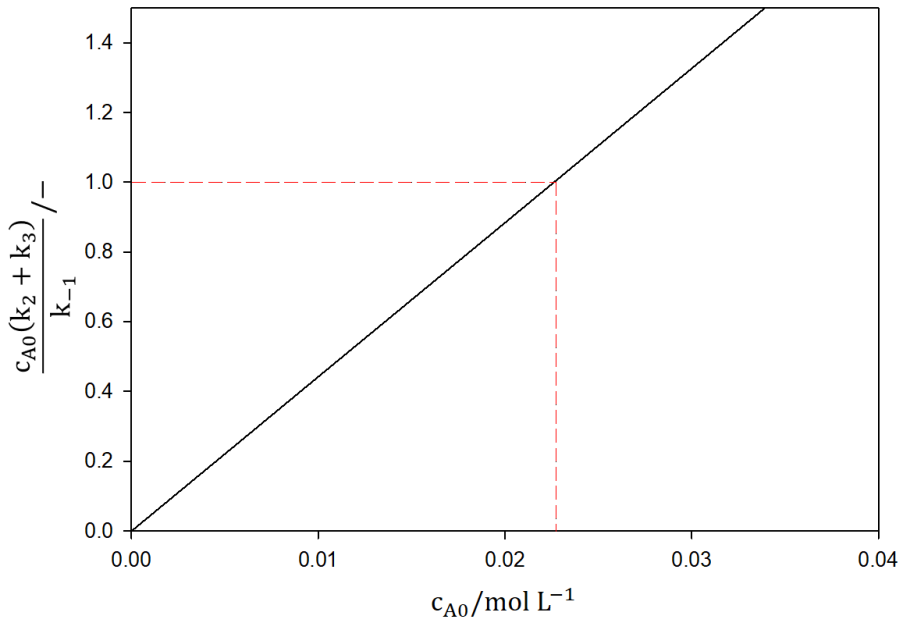
**Fig A-7** $\frac{k_2+k_3}{k_{-1}} c_{A0}$ vs $c_{A0}$. The figure shows critical value of $c_{A0}$ for the rate coefficients ratio, i.e. when $\frac{k_2+k_3}{k_{-1}} c_{A0} = 1$, to be 0.0226 mol L$^{-1}$; parameters as specified in the main text.

## A.4.5 Variation of energy per pulse
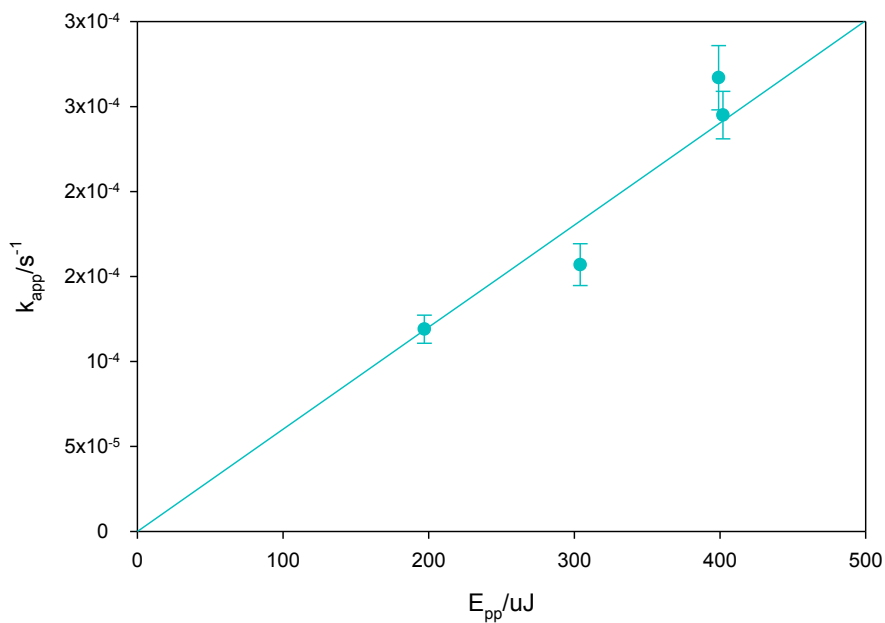


**Fig A-8 Change in $k_{app}$ values versus change in energy per pulse irradiated by the laser beam. Samples with $c_{A0}$ of 0.0174mol $L^{-1}$ and volume of 0.25mL were irradiated with 375 nm wavelength at 20 Hz. Line plotted is $k_{app}$ prediction preformed with the use of eq 2-10.**

## A.4.6 Variation of wavelength
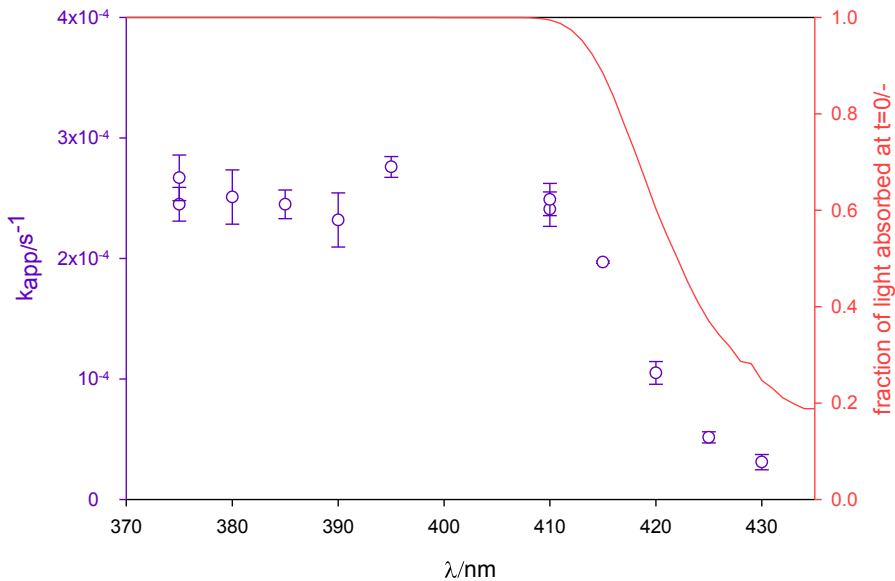


**Fig A-9 Variation in $k_{app}$ with the change of irradiation wavelength (purple). In red an overlay graph show the fraction of light absorbed for a given initial conditions used to experimentally determine the $k_{app}$. For experimental conditions used please refer to the Tables A-1 and A-4 above.**

## A.4.7 Model validation

The prediction calculations were performed using Excel. Calculation of monomer and concentration present as well as the apparent rate coefficient at a specified time step were performed using **eq 2-2**. Calculation of the integral and differential quantum yields were achieved the following way:

$$\Phi_{int} = \frac{n_{A_2 t_i} - n_{A_2 0}}{I_{a \, t_{i-1}}(t_i - t_{i-1}) + n_{\gamma \, abs}}$$  eq A-8

$$\Phi_{diff} = \frac{n_{A_2 t_i} - n_{A_2 t_{i-1}}}{I_{a \, t_{i-1}}(t_i - t_{i-1})}$$  eq A-9

With the $\Phi_{int}$ being integral quantum yield, $\Phi_{diff}$ - differential quantum yield, $n_{A_2}$ - moles of dimer at time $t_i$ or 0, mol, $t$ - time, s, $n_{\gamma \, abs}$ - moles of photons cumulatively absorbed by time $t_{i-1}$, mol, $I_a$ - moles of photons absorbed per unit time at time $t_{i-1}$, $mol \ s^{-1}$. $I_{a \, t_{i-1}}$ is defined by

$$I_{a \, t_{i-1}} = \frac{E_{pp} T \lambda f}{E_\lambda N_A} (1 - 10^{-\varepsilon c_A L})$$  eq A-10

where $c_A$ is concentration of anthracene monomer at time $t_{i-1}$ in mol L$^{-1}$. It is thus assumed, that time step is sufficiently small to be able to treat the rate of photon absorption, $I_a$, as constant for the duration of the said time step.

**Table A-5 Relative changes in k$_{app}$ during step wise updates in long time predictions.**

| Data set | Max $k_{app}$ change per step, % | Average $k_{app}$ change per step, % | $k_{app}$ change between first and last point, % |
|---|---|---|---|
| Prediction 1 (a-b from **Fig 2-5**) | 0.08% | 0.03% | 82% |
| Prediction 2 (c-d from **Fig 2-5**) | 0.03% | 0.02% | 58% |
| Prediction 3 (e-f from **Fig 2-5**) | 0.02% | 0.02% | 74% |
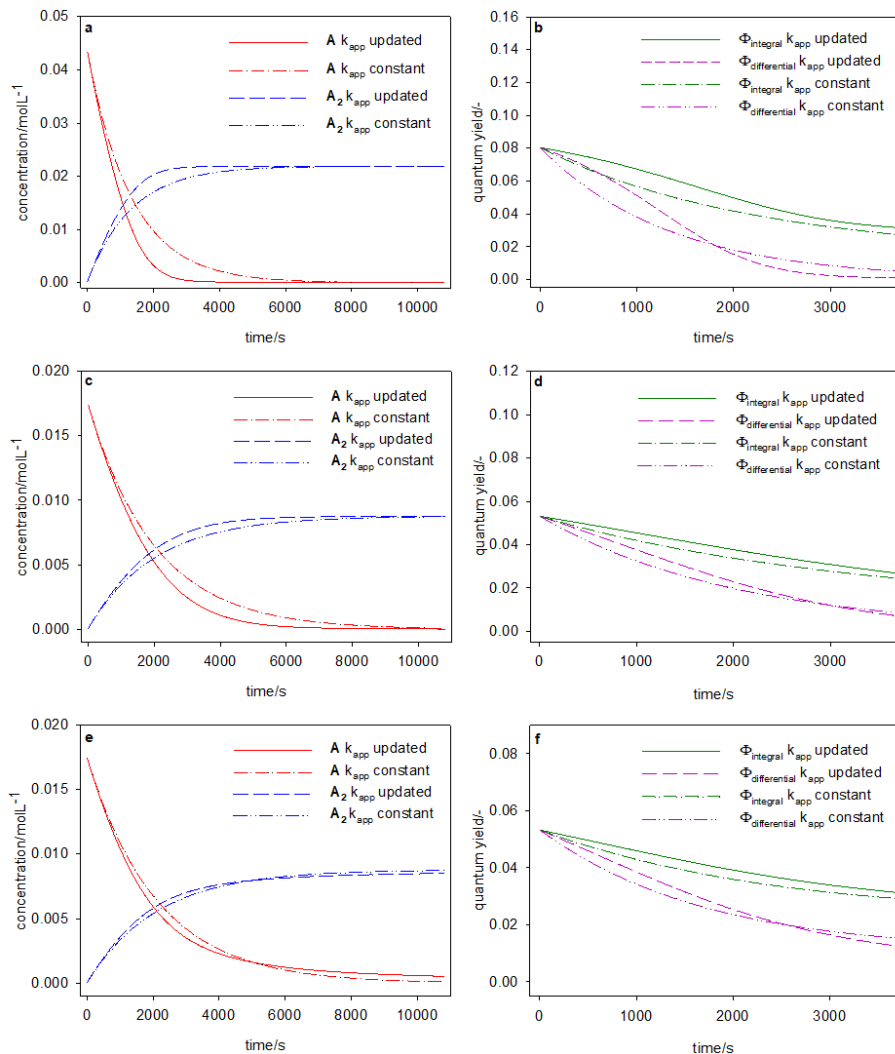
**Fig A-10 Simulations shown in Fig 2-5 overlaid with the predictions made by omitting the change in $k_{app}$ over time but rather assuming a constant value determined at the initial conditions of the given experiment, i.e. using $k_{app}$ ($c_{A0}$) determined at $t_0$.**

# APPENDIX B: SUPPORTING INFORMATION FOR CHAPTER 3

his supporting information accompanying **Chapter 3** has been published as Kislyak, A.; Kodura, D.; Frisch, H.; Feist, F.; Van Steenberge, P. H. M.; Barner-Kowollik, C.; D'Hooge, D. R., A holistic approach for anthracene photochemistry kinetics. *Chem. Eng. J.* **2020,** *402*.

## B.1 Synthesis procedure

In this section the synthesis procedure as depicted in **Fig B-1** for the **A** species used in this work is described. The synthesis was performed in two steps. In the first step 6-hydroxyhexyl anthracene-9-carboxylate was synthesised (Subsection B.1.1; **Fig B-2**), which was then used in the second step for the synthesis of the final product, 6-acetoxyhexyl anthracene-9-carboxylate (Subsection B.1.2; **Fig B-5**).
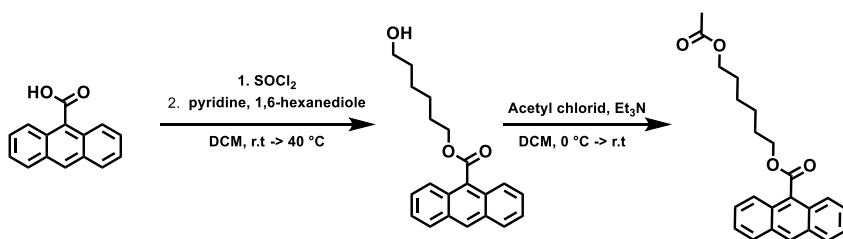


**Fig B-1 Synthetic scheme of the synthesis of A in Fig 3-1.**

### B.1.1 6-hydroxyhexyl anthracene-9-carboxylate
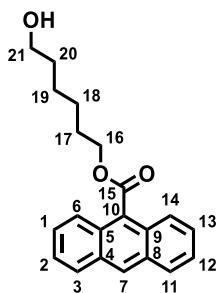
**Fig B-2 6-hydroxyhexyl anthracene-9-carboxylate.**

6-hydroxyhexyl anthracene-9-carboxylate was synthesized according to a literature procedure.[5]

**Isolated yield**: 1.10 g (3.51 mmol, 71%).

**$^1$H NMR** (600 MHz, DMSO-$d_6$) δ ($^1$H) = 8.77 (s, 1H, CH-7), 8.17 (dd, $J$ = 8.3, 1.2 Hz, 2H, CH-6,14), 8.02 – 7.93 (m, 2H, CH-3,11), 7.63 (ddd, $J$ = 8.7, 6.5, 1.3 Hz, 2H, CH-2,12), 7.58 (ddd, $J$ = 7.9, 6.5, 1.2 Hz, 2H, CH-1,13), 4.57 (t, $J$ = 6.6 Hz, 2H, CH$_2$-16), 4.36 (t, $J$ = 5.2 Hz, 1H, OH), 3.39 (td, $J$ = 6.4, 5.1 Hz, 2H, CH$_2$-21), 1.83 – 1.76 (m, 2H, CH$_2$-17), 1.47 – 1.23 (m, 6H, CH$_2$-18,19,20).

**$^{13}$C NMR** (151 MHz, DMSO-$d_6$) δ ($^{13}$C) = 168.78 (C-15), 136.11 (C-10), 130.45(C-4,8), 129.07 (C-7), 128.69 (C-6,14), 127.93 (C-5,9), 127.39 (C-2,12), 125.79 (C-1,13), 124.48 (C-3,11), 65.62 (C-16), 60.59 (C-21), 32.42 (C-20), 28.19 (C-17), 25.41 (C-19), 25.11 (C-18).

**LC-ESI-HRMS (m/z)** Calculated for [C$_{21}$H$_{22}$O$_3$H]$^+$ :323.1642 measured: 323.1651.

Calculated for [C$_{21}$H$_{22}$O$_3$NH$_4$]$^+$ : 340.1907 measured: 340.1917.

Calculated for [C$_{21}$H$_{22}$O$_3$Na]$^+$ : 345.1461 measured: 345.1469.

Fig B-3 ¹H-NMR spectrum of 6-hydroxyhexyl anthracene-9-carboxylate in dimethylsulfoxide-d₆.
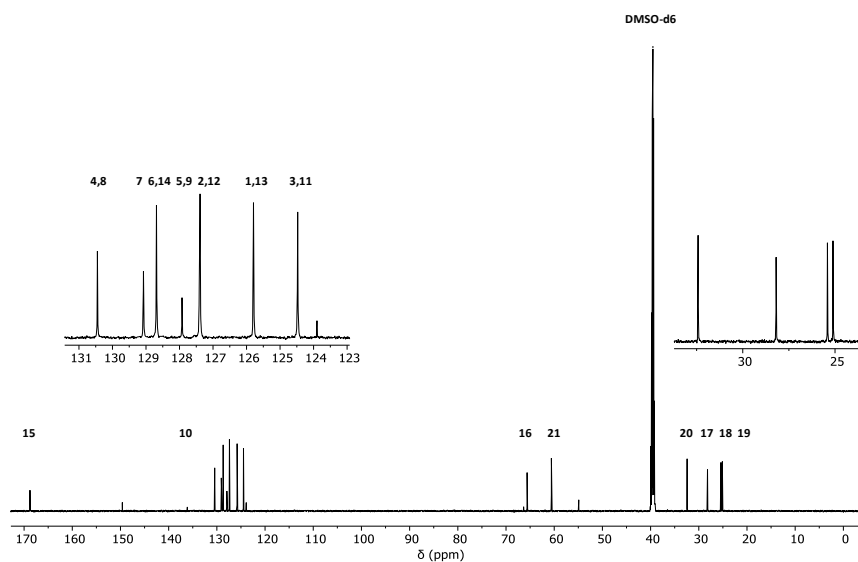


Fig B-4 ¹³C-NMR spectrum of 6-hydroxyhexyl anthracene-9-carboxylate in dimethylsulfoxide-d6.

## B.1.2 6-acetoxyhexyl anthracene-9-carboxylate
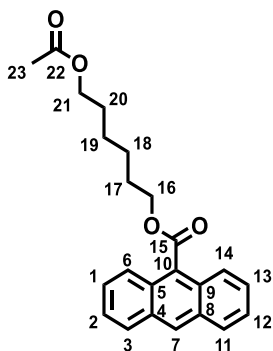


Fig B-5 6-acetoxyhexyl anthracene-9-carboxylate.

6-hydroxyhexyl anthracene-9-carboxylate (500 mg, 1.55 mmol, 1.0 eq.) and triethylamine (1.27 mL, 941.6 mg, 9.31 mmol, 6.0 eq.) were dissolved in dry DCM (10 mL) and cooled with an ice bath. Acetylchloride (0.56 mL,

608.6 mg, 7.75 mmol, 5.0 eq.) was diluted with dry DCM (5 mL) and added dropwise using a syringe pump over a period of 1 h. After the addition, the ice bath was removed and the mixture stirred overnight, followed by extraction with saturated ammonium chloride solution (30 mL), water (50 mL) and brine (50 mL). The organic layer was dried over $Mg_2SO_4$ and the solvent removed under reduced pressure. The pure product was obtained after flash column chromatography (100% DCM, $R_f$: 0.45).

**Isolated yield**: 0.520 g (1.42 mmol, 91%).

**LC-ESI-HRMS (m/z)** Calculated for $[C_{23}H_{24}O_4H]^+$ : 365.1747 measured: 365.1749.

Calculated for $[C_{23}H_{24}O_4Na]^+$ : 387.1567 measured: 387.1568.

**$^1$H-NMR** (600 MHz, DMSO-$d_6$) δ ($^1$H) = 8.76 (s, 1H, CH-7), 8.16 (d, J = 8.4 Hz, 2H, CH-6,14), 7.97 (d, J = 8.7 Hz, 2H, CH-3,11), 7.62 – 7.55 (m, 4H, CH-1,2,12,13), 4.56 (t, J = 6.6 Hz, 2H, CH$_2$-16), 3.96 (t, J = 6.5 Hz, 2H, CH$_2$-21), 1.96 (s, 3H, CH$_3$-23), 1.82– 1.72 (m, 2H, CH$_2$-17), 1.58 – 1.51 (m, 2H, CH$_2$-21), 1.44 – 1.30 (m, 4H, CH$_2$-18,19).

**$^{13}$C-NMR** (151 MHz, DMSO-$d_6$) δ ($^{13}$C) = 170.35 (C-15), 168.75 (C-22), 130.44 (C-10), 129.06 (C-4,8), 128.66 (C-7), 127.90 (C-6,14), 127.42 (C-5,9), 127.39 (C-3,11), 125.76 (C-2,12), 124.47 (C-1,13), 65.53 (C-16), 63.68 (C-21), 28.00 (C-17), 27.96 (C-20), 25.17 (C-18), 24.99 (C-19), 20.66 (C-23).

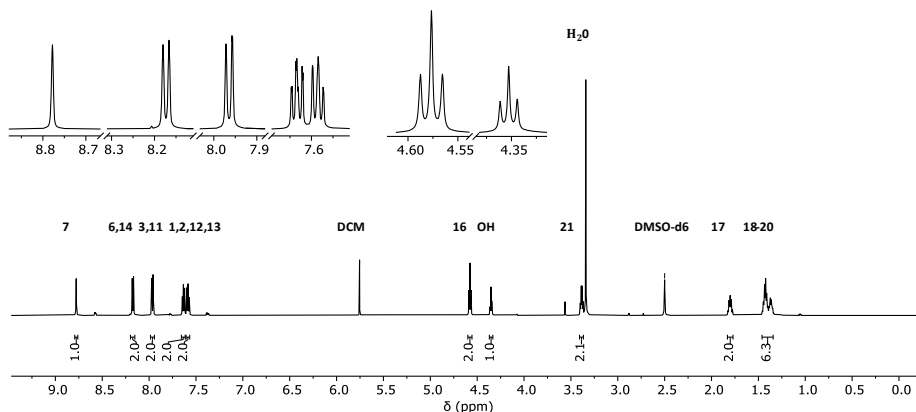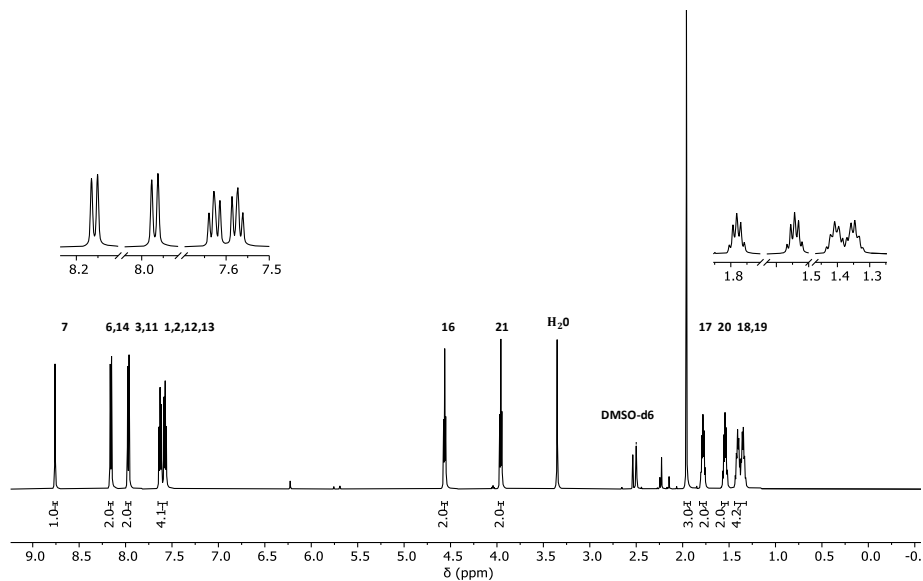Fig B-6 $^1$H-NMR spectrum of 6-acetoxyhexyl anthracene-9-carboxylate in dimethylsulfoxide-d$_6$.
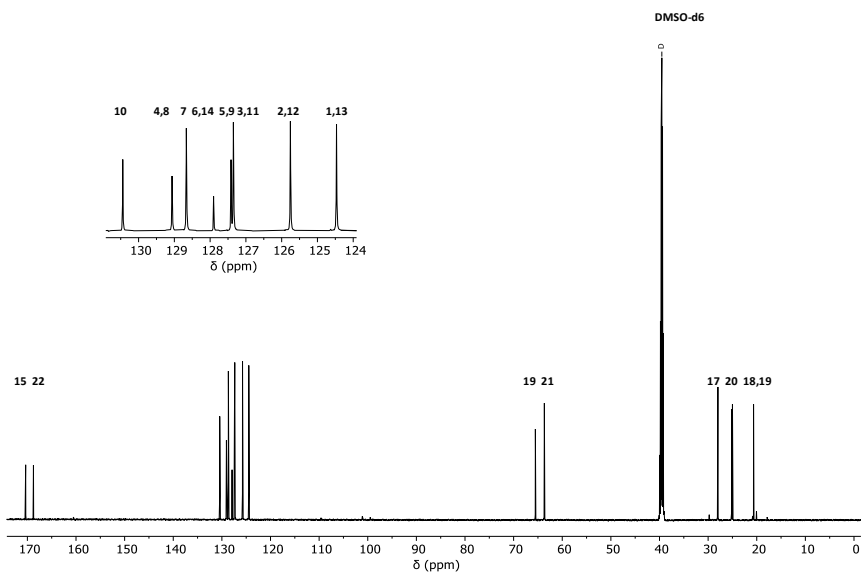


Fig B-7 $^{13}$C-NMR spectrum of 6-acetoxyhexyl anthracene-9-carboxylate in dimethylsulfoxide-d$_6$.
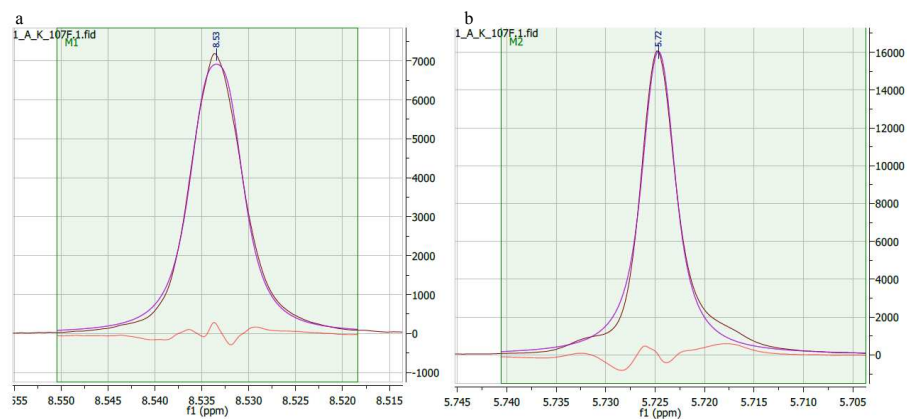
**Fig B-8 An example of NMR analysis. Mathematical fit was used for the calculation of the area under the peaks in the NMR. a: peak for tracking A presence; b: peak for tracking $A_2$ presence.**

## B.2 Derivations

### B.2.1 Derivation of the photo-kinetics for exclusive dimerization (Case 1 in the main text)

The derivation of the photokinetics for the exclusive dimerization has already been treated in detail in the previous work,[6] hence; in here only the main steps will be highlighted.

The mass balance for the **A** species (no volume effect) is:

$$\frac{dc_A}{dt} = k_{-1}c_{1A} + k_3 c_{1A}c_A - k_2 c_{1A}c_A - \mathcal{J}_A(c_A) \qquad \text{eq B-1}$$

in which

$$\mathcal{J}_A(c_A) = \frac{E_{pp}T_\lambda f}{E_\lambda N_{AV}}(1 - 10^{-\varepsilon_A c_A l}) \qquad \text{eq 3-10}$$

Similarly the mass balance for **A** in a singlet excited state is:

$$\frac{dc_{1A}}{dt} = -k_{-1}c_{1A} - k_3 c_{1A}c_A - k_2 c_{1A}c_A + \mathcal{J}_A(c_A) \qquad \text{eq B-2}$$

Applying the steady state approximation (QSSA) for the determination of the concentration of **A** in singlet exited state it follows:

$$c_{1A} = \frac{\mathcal{J}_A(c_A)}{(k_3+k_2)c_A+k_{-1}} \qquad \text{eq B-3}$$

Substituting this back into the mass balance for **A** species gives:

$$\frac{dc_A}{dt} = -2\left[\frac{k_2 \mathcal{J}_A(c_A)}{(k_2+k_3)c_A+k_{-1}}\right]c_A \qquad \text{eq B-4}$$

The integration of the above equation denoting the term in the brackets as $k_{+app}$ leads to Eq. (6) of the main text.

## B.2.2 Derivation of the photo-kinetics for exclusive dimer cleavage (Case 2 in the main text)

The mass balance for the dimer species (no volume effect) is:

$$\frac{dc_{A_2}}{dt} = -\mathcal{J}_{A_2}(c_{A_2}) + k_{-4}c_{1A_2}$$

eq B-5

in which

$$\mathcal{J}_{A_2}(c_{A_2}) = \frac{E_{pp}T\lambda f}{E_\lambda N_A V}\left(1 - 10^{-\varepsilon_{A_2}c_{A_2}l}\right)$$

eq 3-10

Similarly the mass balance for dimer in a singlet excited state is:

$$\frac{dc_{1A_2}}{dt} = \mathcal{J}_{A_2}(c_{A_2}) - (k_5 + k_{-4})c_{1A_2}$$

eq B-6

Applying the QSSA for the determination of the concentration of dimer in singlet exited state

$$\frac{dc_{1A_2}}{dt} = 0$$

eq B-7

one obtains:

$$c_{1A_2} = \frac{\mathcal{J}_{A_2}(c_{A_2})}{k_5 + k_{-4}}$$

eq B-8

Substituting this back into the mass balance for dimer species it follows that:

$$\frac{dc_{A_2}}{dt} = -\mathcal{J}_{A_2}(c_{A_2}) + k_{-4}\frac{\mathcal{J}_{A_2}(c_{A_2})}{k_5 + k_{-4}}$$

eq B-9

After rewriting one obtains the photoreaction law in the main text (**eq 3-9**).

For the integration of **eq 3-9** in the main text one can write:

$$\frac{1}{\frac{E_{pp}T\lambda f}{E_\lambda N_A V}(1 - 10^{-\varepsilon_{A_2}c_{A_2}l})}dc_{A_2} = -\frac{k_5}{k_5 + k_{-4}}\ dt$$

eq B-10

$$\int_{c_{A_2 0}}^{c_{A_2}}\frac{10^{\varepsilon_{A_2}c_{A_2}l}}{1 - 10^{\varepsilon_{A_2}c_{A_2}l}}dc_{A_2} = \frac{k_5}{k_5 + k_{-4}}\frac{E_{pp}T\lambda f}{E_\lambda N_A V}\int_{t_0}^{t}1\ dt$$

eq B-11

In order to integrate **eq B-11**, the left side will be considered initially. Integration by parts was used in the following way:

$$u = 1 - 10^{\varepsilon_{A_2} c_{A_2} l}$$ 

eq B-12

Therefore

$$\frac{du}{dc_{A_2}} = -\varepsilon_{A_2} l \ln 10 \times 10^{\varepsilon_{A_2} c_{A_2} l}$$ 

eq B-13

Substitution of **eq B-12** & **eq B-13** leads to:

$$\int_{u_0}^{u} \frac{1-u}{u} \frac{du}{-\varepsilon_{A_2} l \ln 10 \times (1-u)} = \frac{k_5}{k_5 + k_{-4}} \frac{E_{pp} T_\lambda f}{E_\lambda N_A V} \int_{t_0}^{t} 1 \, dt$$ 

eq B-14

Integration of **eq B-14** and substitution of **eq B-12** leads to **eq B-15**, with further rearrangement leads to **eq 3-14** of the main text.

$$\frac{-1}{\varepsilon_{A_2} l \ln 10} \left[ \ln\left(1 - 10^{\varepsilon_{A_2} c_{A_2} l}\right) \right]_{c_{A_2}(0)}^{c_{A_2}(t)} = \left[ \frac{k_5}{k_5 + k_{-4}} \frac{E_{pp} T_\lambda f}{E_\lambda N_A V} t \right]_{t_0}^{t}$$ 

eq B-15

Furthermore, if we were to look at the two limiting situations discussed in the main text we can give the following extra details. The first one is with $\varepsilon_{A_2} c_{A_2} l$ so large that $\mathcal{J}_{A2}$ appears independent of $c_{A_2}$. The integration gives:

$$c_{A_2} = c_{A_2 0} - \frac{k_5}{k_5 + k_{-4}} \left( \frac{E_{pp} T_\lambda f}{E_\lambda N_A V} \right) (t - t_0)$$ 

eq B-16

For the second situation with $\varepsilon_{A_2} c_{A_2} l$ small so that $\mathcal{J}_{A2} \propto c_{A_2}$ it holds that:

$$c_{A_2} = c_{A_2 0} \exp - \frac{k_5}{k_5 + k_{-4}} \left( \frac{E_{pp} T_\lambda f}{E_\lambda N_A V} \right) 2.303 \varepsilon l (t - t_0)$$ 

eq B-17

### B.2.3 Derivation of the photo-kinetics for competitive dimerization and dimer cleavage (Case 3 in the main text)

In order to derive the photo-kinetics of the competitive case the first mass balance for monomer will be first derived (again no volume effect)

$$\frac{dc_A}{dt} = k_{-1}c_{1A} - \mathcal{J}_A + (k_3 - k_2)c_{1A}c_A + 2k_5 c_{1A_2} \qquad \text{eq B-18}$$

The mass balance for anthracene monomer in singlet excited state can also be written as:

$$\frac{dc_{1A}}{dt} = -k_{-1}c_{1A} + \mathcal{J}_A - (k_3 + k_2)c_{1A}c_A \qquad \text{eq B-19}$$

Similarly the mass balance for anthracene dimer in the singlet excited state can be written in the following way:

$$\frac{dc_{1A_2}}{dt} = \mathcal{J}_{A_2} - (k_5 + k_{-4})c_{1A_2} \qquad \text{eq B-20}$$

Here we apply the QSSA for the determination of the concentration of the intermediate species.

$$\frac{dc_{1A}}{dt} = 0 \qquad \text{thus} \qquad c_{1A} = \frac{\mathcal{J}_A}{k_{-1} + (k_3 + k_2)c_A} \qquad \text{eq B-21}$$

$$\frac{dc_{1A_2}}{dt} = 0 \qquad \text{thus} \qquad c_{1A_2} = \frac{\mathcal{J}_{A_2}}{k_5 + k_{-4}} \dots \qquad \text{eq B-22}$$

Substitution of **eq B-21** and **eq B-22** into **eq B-18** results in **eq 3-20** in the main text.

Integration of **eq 3-20** of the main text with temporarily constant apparent parameters leads to

$$\left[ -\frac{\ln(2k_{-app} - 2k_{+app}c_A)}{2k_{+app}} \right]_t^{t+\Delta t} = [t]_t^{t+\Delta t} \qquad \text{eq B-23}$$

$$-\frac{\ln(2k_{-app} - 2k_{+app}c_{A,t+\Delta t})}{2k_{+app}} + \frac{\ln(2k_{-app} - 2k_{+app}c_{A,t})}{2k_{+app}} = \Delta t \qquad \text{eq B-24}$$

Rearrangement of **eq B-24** for $c_{A,t+\Delta t}$ can finally lead to **eq 3-24** of the main text.

## B.2.4 Derivation of equation for equilibrium concentration in Case 3 in the main text

In order to derive the equation for determination of equilibrium (**eq 3-26** in the main text), first **eq 3-21** in the main text needs to be considered, representing the case of competitive **A** dimerization and **A₂** cleavage. At equilibrium photostationary state is reached there is no net change in concentration of either **A** or **A₂** observed, thus $\frac{dc_A}{dt} = 0$ and:

$$0 = -2\,k_{+app}(c_{A,eq}, c_{A2,eq})c_{A,eq} + 2k_{-app}(c_{A,eq}, c_{A2,eq}) \qquad \text{eq B-25}$$

Rearrangement of the equation above leads to **eq B-26**, which with further substitution of **eq 3-16**, **3-17**, **3-19** and **3-20** of the main text leads to **eq B-27**:

$$k_{+app}(c_{A,eq}, c_{A2,eq})c_{A,eq} = k_{-app}(c_{A,eq}, c_{A2,eq}) \qquad \text{eq B-26}$$

$$\frac{\frac{k_2}{k_{-1}}c_{A,eq}}{\left(\frac{k_2}{k_{-1}}+\frac{k_3}{k_{-1}}\right)c_{A,eq}+1}\frac{E_{pp}T_\lambda f}{E_\lambda N_A V}\frac{\varepsilon_A c_{A,eq}}{\varepsilon_A c_{A,eq}+\varepsilon_{A_2}c_{A2,eq}}\left(1-10^{-(\varepsilon_A c_{A,eq}+\varepsilon_{A_2}c_{A2,eq})L}\right) = \qquad \text{eq B-27}$$

$$= \frac{1}{1+\frac{k_{-4}}{k_5}}\frac{E_{pp}T_\lambda f}{E_\lambda N_A V}\frac{\varepsilon_{A_2}c_{A2,eq}}{\varepsilon_A c_{A,eq}+\varepsilon_{A_2}c_{A2,eq}}\left(1-10^{-(\varepsilon_A c_{A,eq}+\varepsilon_{A_2}c_{A2,eq})L}\right)$$

**eq B-27** can in turn be simplified to:

$$\frac{\frac{k_2}{k_{-1}}c_{A,eq}}{\left(\frac{k_2}{k_{-1}}+\frac{k_3}{k_{-1}}\right)c_{A,eq}+1}\frac{\varepsilon_A c_{A,eq}}{\varepsilon_A c_{A,eq}+\varepsilon_{A_2}c_{A2,eq}} = \frac{1}{1+\frac{k_{-4}}{k_5}}\frac{\varepsilon_{A_2}c_{A2,eq}}{\varepsilon_A c_{A,eq}+\varepsilon_{A_2}c_{A2,eq}} \qquad \text{eq B-28}$$

**eq B-28** ultimately becomes **eq 3-26** of the main text with the help of $g_A$ and $g_{A_2}$ that are auxiliary functions as defined by **eq 3-27 & 3-28** in the main text.

# B.3 Supporting experimental and modelling results

## B.3.1 Initial conditions and main experimental data

Table B-1 Data from the small time experiments performed for monomer dimerization at 260 - 320 nm. Data used in Fig 3-5 in the main text.

| Wavelength λ, nm | Glass transmittance $T_A$ | Average energy per pulse hitting the bottom of the vial $E_{pp}$, µJ pulse$^{-1}$ | Mass of the sample m, mg | Sample volume V, µL | $c_{A0}$, mol L$^{-1}$ | $c_{A20}$, mol L$^{-1}$ | Irradiation time, s | Amount of A at time t $n_A$, mol | Amount of $A_2$ at time t $n_{A2}$, mol | Apparent rate coefficient $k_{+app}(c_{A0})$, s$^{-1}$ | $R^2$ | $k_{+app}(c_{A0})J_A^{-1}(c_{A0})$, L mol$^{-1}$ | $J_A(c_{A0})$, mol γ L$^{-1}$ s$^{-1}$ |
|---|---|---|---|---|---|---|---|---|---|---|---|---|---|
| 260 | 0.74 | 577 | 1.59 | 250 | 0.0174 | 0 | 0 | 4.36E-06 | 0.00E+00 | 1.14E-04 | 0.998 | 1.53 | 7.46E-05 |
| | | | | | | | 30 | 4.32E-06 | 1.73E-08 | | | | |
| | | | | | | | 60 | 4.30E-06 | 3.05E-08 | | | | |
| | | | | | | | 120 | 4.24E-06 | 5.96E-08 | | | | |
| 280 | 0.73 | 537 | 1.59 | 250 | 0.0174 | 0 | 0 | 4.36E-06 | 0.00E+00 | 1.58E-04 | 0.997 | 2.14 | 7.36E-05 |
| | | | | | | | 30 | 4.31E-06 | 2.15E-08 | | | | |
| | | | | | | | 60 | 4.27E-06 | 4.46E-08 | | | | |
| | | | | | | | 120 | 4.20E-06 | 8.07E-08 | | | | |
| 300 | 0.74 | 501 | 1.59 | 250 | 0.0174 | 0 | 0 | 4.36E-06 | 0.00E+00 | 1.36E-04 | 0.999 | 1.83 | 4.42E-05 |
| | | | | | | | 30 | 4.32E-06 | 1.78E-08 | | | | |
| | | | | | | | 60 | 4.28E-06 | 3.66E-08 | | | | |
| | | | | | | | 120 | 4.22E-06 | 6.95E-08 | | | | |
| 320 | 0.72 | 486 | 1.59 | 250 | 0.0174 | 0 | 0 | 4.36E-06 | 0.00E+00 | 1.85E-04 | 0.999 | 2.48 | 7.44E-05 |
| | | | | | | | 30 | 4.31E-06 | 2.51E-08 | | | | |
| | | | | | | | 60 | 4.26E-06 | 4.83E-08 | | | | |
| | | | | | | | 120 | 4.17E-06 | 9.46E-08 | | | | |
| 280 | 0.73 | 544 | 1.59 | 100 | 0.0436 | 0 | 0 | 4.36E-06 | 0.00E+00 | 2.91E-04 | 0.993 | 1.56 | 1.86E-04 |
| | | | | | | | 30 | 4.26E-06 | 5.02E-08 | | | | |
| | | | | | | | 60 | 4.19E-06 | 8.13E-08 | | | | |
| | | | | | | | 120 | 4.06E-06 | 1.50E-07 | | | | |
| 280 | 0.73 | 528 | 1.59 | 400 | 0.0109 | 0 | 0 | 4.36E-06 | 0.00E+00 | 1.32E-04 | 0.995 | 2.92 | 4.52E-05 |
| | | | | | | | 30 | 4.32E-06 | 1.88E-08 | | | | |
| | | | | | | | 60 | 4.28E-06 | 3.85E-08 | | | | |
| | | | | | | | 120 | 4.22E-06 | 6.81E-08 | | | | |
| 280 | 0.73 | 511 | 1.59 | 500 | 0.0087 | 0 | 0 | 4.36E-06 | 0.00E+00 | 1.11E-04 | 0.992 | 3.17 | 3.50E-05 |

**Table B-2 Data from the small time experiments performed on monomer dimerization at 375 and 260 nm. Data used in Fig 3-5 in the main text.**

| Wavelength λ, nm | Glass transmittance $T_1$ | Average energy per pulse hitting the bottom of the vial $E_{pp}$, µJ pulse⁻¹ | Mass of the sample m, mg | Sample volume V, µL | $c_{A0}$, mol L⁻¹ | $c_{A20}$, mol L⁻¹ | Irradiation time, s | Amount of A at time t $n_A$, mol | Amount of $A_2$ at time t $n_{A2}$, mol | Apparent rate coefficient $k_{+app}(c_{A0})$, s⁻¹ | $R^2$ | $k_{+app}(c_{A0})J_A^{-1}(c_{A0})$, L mol⁻¹ | $J_A(c_{A0})$, mol Y L⁻¹ s⁻¹ |
|---|---|---|---|---|---|---|---|---|---|---|---|---|---|
| 375 | 0.76 | 398 | 1.59 | 250 | 0.0174 | 0 | 0 | 4.36E-06 | 0.00E+00 | 2.22E-04 | 0.997 | 2.95 | 7.53E-05 |
|  |  |  |  |  |  |  | 30 | 4.29E-06 | 3.46E-08 |  |  |  |  |
|  |  |  |  |  |  |  | 60 | 4.24E-06 | 5.87E-08 |  |  |  |  |
|  |  |  |  |  |  |  | 120 | 4.13E-06 | 1.15E-07 |  |  |  |  |
| 375 | 0.76 | 394 | 1.59 | 100 | 0.0436 | 0 | 0 | 4.36E-06 | 0.00E+00 | 4.09E-04 | 1.00 | 2.20 | 1.86E-04 |
|  |  |  |  |  |  |  | 30 | 4.25E-06 | 5.28E-08 |  |  |  |  |
|  |  |  |  |  |  |  | 60 | 4.15E-06 | 1.04E-07 |  |  |  |  |
|  |  |  |  |  |  |  | 120 | 3.95E-06 | 2.04E-07 |  |  |  |  |
| 375 | 0.76 | 395 | 1.59 | 400 | 0.0109 | 0 | 0 | 4.36E-06 | 0.00E+00 | 3.23E-04 | 0.796 | 6.90 | 4.67E-05 |
|  |  |  |  |  |  |  | 30 | 4.13E-06 | 1.19E-07 |  |  |  |  |
|  |  |  |  |  |  |  | 60 | 4.08E-06 | 1.40E-07 |  |  |  |  |
|  |  |  |  |  |  |  | 120 | 4.00E-06 | 1.81E-07 |  |  |  |  |
| 260 | 0.73 | 522 | 1.59 | 100 | 0.0436 | 0 | 0 | 4.36E-06 | 0.00E+00 | 2.18E-04 | 0.996 | 1.22 | 1.79E-04 |
|  |  |  |  |  |  |  | 30 | 4.29E-06 | 3.31E-08 |  |  |  |  |
|  |  |  |  |  |  |  | 60 | 4.25E-06 | 5.41E-08 |  |  |  |  |
|  |  |  |  |  |  |  | 120 | 4.13E-06 | 1.13E-07 |  |  |  |  |
| 260 | 0.73 | 497 | 1.59 | 200 | 0.0220 | 0 | 0 | 4.39E-06 | 0.00E+00 | 1.37E-04 | 0.997 | 1.61 | 8.52E-05 |
|  |  |  |  |  |  |  | 30 | 4.35E-06 | 2.10E-08 |  |  |  |  |
|  |  |  |  |  |  |  | 60 | 4.32E-06 | 3.49E-08 |  |  |  |  |
|  |  |  |  |  |  |  | 120 | 4.25E-06 | 7.22E-08 |  |  |  |  |
| 260 | 0.73 | 527 | 1.59 | 300 | 0.0146 | 0 | 0 | 4.37E-06 | 0.00E+00 | 9.31E-05 | 0.979 | 1.54 | 6.01E-05 |
|  |  |  |  |  |  |  | 30 | 4.33E-06 | 1.76E-08 |  |  |  |  |
|  |  |  |  |  |  |  | 60 | 4.31E-06 | 3.03E-08 |  |  |  |  |
|  |  |  |  |  |  |  | 120 | 4.27E-06 | 4.94E-08 |  |  |  |  |
| 260 | 0.73 | 514 | 1.59 | 400 | 0.0109 | 0 | 0 | 4.35E-06 | 0.00E+00 |  | 0.968 | 1.72 | 4.40E-05 |

Additional values:

| Irradiation time, s | $n_A$, mol | $n_{A2}$, mol |
|---|---|---|
| 30 | 4.32E-06 | 1.73E-08 |
| 60 | 4.29E-06 | 3.37E-08 |
| 120 | 4.24E-06 | 5.78E-08 |

Table B-3 Data from the small time experiments performed on dimer cleavage between 260 and 330 nm. Data used in Fig 3-5 in the main text; also mentioned are the ratios $k_2/k_{-1}$, $k_3/k_{-1}$, $k_3/k_{-4}$ as determined based on the small time experiments in dimerization.

Additional values (top box):

| Irradiation time, s | $n_{A_2}$, mol | Amount of $A_2$ | ... |
|---|---|---|---|
| 30 | 1.56E-08 | 4.32E-06 | 7.59E-05 |
| 60 | 2.57E-08 | 4.30E-06 | |
| 120 | 4.05E-08 | 4.27E-06 | |

| Wavelength λ, nm | Glass transmittance $T_\lambda$ | Average energy per pulse hitting the bottom of the vial $E_{pp}$, μJ pulse$^{-1}$ | Mass of the sample m, mg | Sample volume V, μL | $c_{A0}$, mol L$^{-1}$ | $c_{A20}$, mol L$^{-1}$ | Irradiation time, s | Amount of A at time t $n_A$, mol | Amount of $A_2$ at time t $n_{A_2}$, mol | $k_2/k_{-1}$ used, L mol$^{-1}$ | $k_3/k_{-1}$ used, L mol$^{-1}$ | $k_3/k_{-4}$ | $k_{-app} f_{A_2}^{-1}$ | $k_{-app}(c_{A0}, c_{A20})$, mol L$^{-1}$ s$^{-1}$ | $R^2$ |
|---|---|---|---|---|---|---|---|---|---|---|---|---|---|---|---|
| 260 | 566 | 0.74 | 2 | 250 | 3.52E-5 | 0.0110 | 0 | 8.80E-09 | 2.74E-06 | 1.9 | 10.5 | 4.9E-02 | 4.67E-02 | 3.29E-06 | 0.99 |
| | | | | | | | 15 | 2.94E-08 | 2.73E-06 | | | | | | |
| | | | | | | | 30 | 5.61E-08 | 2.72E-06 | | | | | | |
| | | | | | | | 60 | 8.70E-08 | 2.70E-06 | | | | | | |
| 270 | 550 | 0.75 | 2 | 250 | 3.52E-5 | 0.0110 | 0 | 8.80E-09 | 2.74E-06 | 3.5 | 26.1 | 0.35 | 2.59E-01 | 1.91E-05 | 1.00 |
| | | | | | | | 15 | 1.51E-07 | 2.67E-06 | | | | | | |
| | | | | | | | 30 | 2.77E-07 | 2.61E-06 | | | | | | |
| | | | | | | | 60 | 5.02E-07 | 2.49E-06 | | | | | | |
| 280 | 543 | 0.73 | 2 | 250 | 3.52E-5 | 0.0110 | 0 | 8.80E-09 | 2.74E-06 | 4.4 | 34.6 | 0.60 | 3.75E-01 | 2.77E-05 | 1.00 |
| | | | | | | | 15 | 2.32E-07 | 2.63E-06 | | | | | | |
| | | | | | | | 30 | 4.14E-07 | 2.54E-06 | | | | | | |
| | | | | | | | 60 | 7.33E-07 | 2.38E-06 | | | | | | |
| 290 | 522 | 0.73 | 2 | 250 | 3.52E-5 | 0.0110 | 0 | 8.80E-09 | 2.74E-06 | 4.8 | 39.3 | 0.53 | 3.46E-01 | 2.56E-05 | 1.00 |
| | | | | | | | 15 | 1.92E-07 | 2.65E-06 | | | | | | |
| | | | | | | | 30 | 3.54E-07 | 2.57E-06 | | | | | | |
| | | | | | | | 60 | 6.72E-07 | 2.41E-06 | | | | | | |
| 300 | 503 | 0.74 | 2 | 250 | 3.52E-5 | 0.0110 | 0 | 8.80E-09 | 2.74E-06 | 5.1 | 41.9 | 0.13 | 1.15E-01 | 8.44E-06 | 0.94 |
| | | | | | | | 15 | 9.43E-08 | 2.70E-06 | | | | | | |
| | | | | | | | 30 | 1.51E-07 | 2.67E-06 | | | | | | |
| | | | | | | | 60 | 2.18E-07 | 2.64E-06 | | | | | | |
| 310 | 498 | 0.72 | 2 | 250 | 3.52E-5 | 0.0110 | 0 | 8.80E-09 | 2.74E-06 | 5.2 | 43.3 | 0.13 | 1.15E-01 | 8.13E-06 | 0.94 |
| | | | | | | | 15 | 8.17E-08 | 2.70E-06 | | | | | | |
| | | | | | | | 30 | 1.35E-07 | 2.68E-06 | | | | | | |
| | | | | | | | 60 | 1.82E-07 | 2.65E-06 | | | | | | |
| 320 | 484 | 0.72 | 2 | 250 | 3.52E-5 | 0.0110 | 0 | 8.80E-09 | 2.74E-06 | 5.3 | 44.1 | 0.14 | 1.23E-01 | 7.99E-06 | 0.98 |
| | | | | | | | 15 | 7.54E-08 | 2.71E-06 | | | | | | |
| | | | | | | | 30 | 1.12E-07 | 2.69E-06 | | | | | | |
| | | | | | | | 60 | 1.67E-07 | 2.66E-06 | | | | | | |
| 330 | 468 | 0.72 | 2 | 250 | 3.52E-5 | 0.0110 | 0 | 8.80E-09 | 2.74E-06 | 5.4 | 44.5 | 0.15 | 1.30E-01 | 8.17E-06 | 0.93 |
| | | | | | | | 15 | 7.52E-08 | 2.71E-06 | | | | | | |
| | | | | | | | 30 | 1.16E-07 | 2.69E-06 | | | | | | |
| | | | | | | | 60 | 1.45E-07 | 2.67E-06 | | | | | | |

Table B-4 Data from the long-time irradiation experiment performed on dimer cleavage at 280nm. Data used in Fig 3-7 in the main text.

| Wavelength $\lambda$, nm | Glass transmittance T | Average energy per pulse hitting the bottom of the vial $E_{pp}$, $\mu J$ pulse$^{-1}$ | Mass of the sample m, mg | Sample volume V, $\mu L$ | $c_{A0}$, mol L$^{-1}$ | $c_{A20}$, mol L$^{-1}$ | Irradiation time, s | Amount of A at time t $n_A$, mol | Amount of $A_2$ at time t $n_{A2}$, mol | $k_2/k_{-1}$ used, L mol$^{-1}$ | $k_3/k_{-1}$ used, L mol$^{-1}$ | $k_5/k_{-4}$ used | $R^2$ |
|---|---|---|---|---|---|---|---|---|---|---|---|---|---|
| 280 | 0.73 | 541 | 2 | 250 | 0 | 0.0110 | 0 | 0.00E+00 | 2.74E-06 | 4.4 | 34.6 | 0.6 | 0.87 |
| | | | | | | | 15 | 2.21E-07 | 2.63E-06 | | | | |
| | | | | | | | 30 | 3.92E-07 | 2.55E-06 | | | | |
| | | | | | | | 60 | 7.13E-07 | 2.39E-06 | | | | |
| | | | | | | | 120 | 1.22E-06 | 2.14E-06 | | | | |
| | | | | | | | 300 | 2.06E-06 | 1.71E-06 | | | | |
| | | | | | | | 600 | 2.77E-06 | 1.36E-06 | | | | |
| | | | | | | | 900 | 2.77E-06 | 1.36E-06 | | | | |
| | | | | | | | 1800 | 3.89E-06 | 7.97E-07 | | | | |
| | | | | | | | 3600 | 4.15E-06 | 6.69E-07 | | | | |
| | | | | | | | 5400 | 4.25E-06 | 6.18E-07 | | | | |

## B.3.2 Fraction of light absorbed during small time A dimerization experiments

**Table B-5 Data on fraction of light absorbed by A and $A_2$ during small time A dimerization experiments at different wavelengths and same initial concentration.**

| Wavelength $\lambda$, nm | Time, s | Concentration of A, mol $L^{-1}$ | Fraction of light absorbed by A | Concentration of $A_2$, mol $L^{-1}$ | Fraction of light absorbed by $A_2$ |
|---|---|---|---|---|---|
| 260 | 0 | 1.74E-02 | 1.00 | 0.00E-04 | 0.00 |
|  | 30 | 1.73E-02 | 1.00 | 6.93E-05 | 0.00 |
|  | 60 | 1.72E-02 | 1.00 | 1.22E-04 | 0.00 |
|  | 120 | 1.69E-02 | 1.00 | 2.38E-04 | 0.00 |
| 280 | 0 | 1.74E-02 | 1.00 | 0.00E-04 | 0.00 |
|  | 30 | 1.73E-02 | 0.99 | 8.61E-05 | 0.01 |
|  | 60 | 1.71E-02 | 0.99 | 1.78E-04 | 0.01 |
|  | 120 | 1.68E-02 | 0.98 | 3.23E-04 | 0.02 |
| 300 | 0 | 1.74E-02 | 1.00 | 0.00E-04 | 0.00 |
|  | 30 | 1.73E-02 | 1.00 | 7.10E-05 | 0.00 |
|  | 60 | 1.71E-02 | 1.00 | 1.46E-04 | 0.00 |
|  | 120 | 1.69E-02 | 0.99 | 2.78E-04 | 0.01 |
| 320 | 0 | 1.74E-02 | 1.00 | 0.00E-04 | 0.00 |
|  | 30 | 1.72E-02 | 1.00 | 1.01E-04 | 0.00 |
|  | 60 | 1.70E-02 | 1.00 | 1.93E-04 | 0.00 |
|  | 120 | 1.67E-02 | 1.00 | 3.79E-04 | 0.00 |
| 375 | 0 | 1.74E-02 | 1.00 | 0.00E-04 | 0.00 |
|  | 30 | 1.71E-02 | 1.00 | 3.46E-08 | 0.00 |
|  | 60 | 1.70E-02 | 1.00 | 5.87E-08 | 0.00 |
|  | 120 | 1.65E-02 | 1.00 | 1.15E-07 | 0.00 |

**Table B-6 Data on fraction of light absorbed by A and $A_2$ during small time A dimerization experiments at different initial concentration and same wavelengths.**

| Wavelength $\lambda$, nm | $c_{A0}$, mol $L^{-1}$ | Time, s | Concentration of A, mol $L^{-1}$ | Fraction of light absorbed by A | Concentration of $A_2$, mol $L^{-1}$ | Fraction of light absorbed by $A_2$ |
|---|---|---|---|---|---|---|
| **280** | 4.36E-02 | 0 | 4.36E-02 | 1.00 | 0.00E+00 | 0.00 |
| | | 30 | 4.26E-02 | 0.99 | 5.02E-08 | 0.01 |
| | | 60 | 4.19E-02 | 0.98 | 8.13E-08 | 0.02 |
| | | 120 | 4.06E-02 | 0.96 | 1.50E-07 | 0.04 |
| **280** | 1.09E-02 | 0 | 1.09E-02 | 1.00 | 0.00E+00 | 0.00 |
| | | 30 | 1.08E-02 | 0.99 | 1.88E-08 | 0.01 |
| | | 60 | 1.07E-02 | 0.99 | 3.85E-08 | 0.01 |
| | | 120 | 1.06E-02 | 0.98 | 6.81E-08 | 0.02 |
| **280** | 8.72E-03 | 0 | 8.72E-03 | 1.00 | 0.00E+00 | 0.00 |
| | | 30 | 8.65E-03 | 0.99 | 1.73E-08 | 0.01 |
| | | 60 | 8.58E-03 | 0.99 | 3.37E-08 | 0.01 |
| | | 120 | 8.49E-03 | 0.98 | 5.78E-08 | 0.02 |

**Table B-7 Data on fraction of light absorbed by A and $A_2$ during small time A dimerization experiments at different initial concentration and same wavelengths.**

| Wavelength $\lambda$, nm | $c_{A0}$, mol L$^{-1}$ | Time, s | Concentration of A, mol L$^{-1}$ | Fraction of light absorbed by A | Concentration of $A_2$, mol L$^{-1}$ | Fraction of light absorbed by $A_2$ |
|---|---|---|---|---|---|---|
| 260 | 4.36E-02 | 0 | 4.36E-02 | 1.00 | 0.00E+00 | 0.00 |
| | | 30 | 4.29E-02 | 1.00 | 3.31E-04 | 0.00 |
| | | 60 | 4.25E-02 | 1.00 | 5.41E-04 | 0.00 |
| | | 120 | 4.13E-02 | 1.00 | 1.13E-03 | 0.00 |
| 260 | 2.20E-02 | 0 | 2.20E-02 | 1.00 | 0.00E+00 | 0.00 |
| | | 30 | 2.17E-02 | 1.00 | 1.05E-04 | 0.00 |
| | | 60 | 2.16E-02 | 1.00 | 1.74E-04 | 0.00 |
| | | 120 | 2.12E-02 | 1.00 | 3.61E-04 | 0.00 |
| 260 | 1.46E-02 | 0 | 1.46E-02 | 1.00 | 0.00E+00 | 0.00 |
| | | 30 | 1.44E-02 | 1.00 | 5.87E-05 | 0.00 |
| | | 60 | 1.44E-02 | 1.00 | 1.01E-04 | 0.00 |
| | | 120 | 1.42E-02 | 1.00 | 1.65E-04 | 0.00 |
| 260 | 1.09E-02 | 0 | 1.09E-02 | 1.00 | 0.00E+00 | 0.00 |
| | | 30 | 1.08E-02 | 1.00 | 3.89E-05 | 0.00 |
| | | 60 | 1.07E-02 | 1.00 | 6.41E-05 | 0.00 |
| | | 120 | 1.07E-02 | 1.00 | 1.01E-04 | 0.00 |

## B.3.3 Data for determination of the initial forward apparent rate coefficient for monomer dimerization at 260, 280 and 375 nm
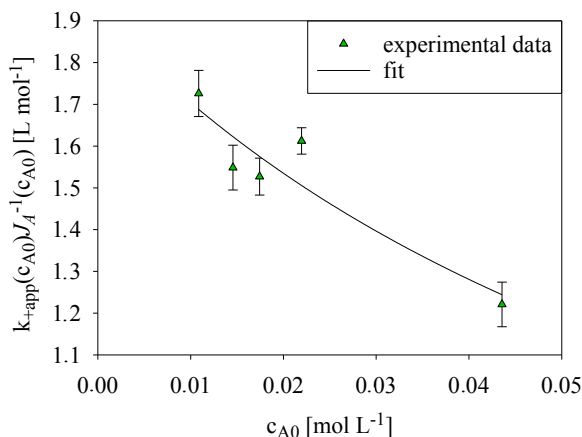


**Fig B-9 Results of the parameter tuning of eq 3-6 to the experimental data at 260 nm from Table B-1 and B- 2. The tuning was performed with the help of the curve fit function of SigmaPlot and resulted in the $\frac{k_2}{k_{-1}} = 1.92\ L\ mol^{-1}$ and $\frac{k_2+k_3}{k_{-1}} = 12.4\ L\ mol^{-1}$ (or $\frac{k_3}{k_{-1}} = 10.5\ L\ mol^{-1}$) with $R^2 = 0.85$. The corresponding comparison of simulated and experimental data at low times to determine the individual data points thus the k+app values are given in Fig B-12.**
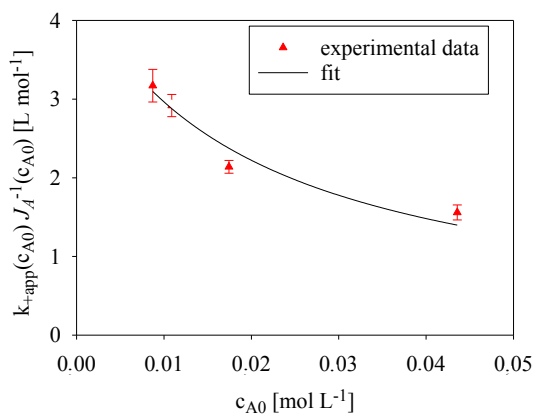


**Fig B-10 Results for the parameter tuning using eq 3-6 in the main text to the experimental data at 280 nm from Table B-1. The tuning was performed with the help of the curve fit function of SigmaPlot and resulted in the $\frac{k_2}{k_{-1}} = 4.45\ L\ mol^{-1}$ and $\frac{k_2+k_3}{k_{-1}} = 50.1\ L\ mol^{-1}$ (or $k_3/k_{-1} = 45.7\ L\ mol^{-1}$) with $R^2 = 0.9$. The corresponding comparison of simulated and experimental data at low times to determine the individual data points thus the k+app values are given in Fig B-13.**
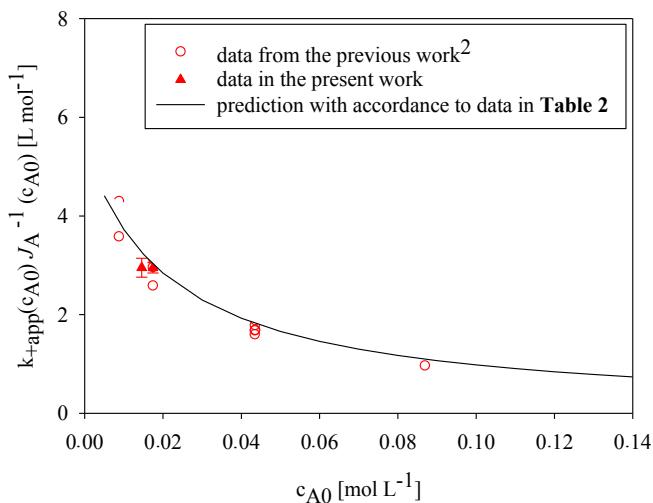
Fig B-11 Comparison of data from previous work[6] of $k_{+app}(c_{A0})J_A^{-1}(c_{A0})$ vs $c_{A0}$ vs data as determined in the present work. This figure is used as a basis for an assumption of the same $k_2/k_{-1}$ and $k_3/k_{-1}$ for the anthracene used in the current paper as well as the one in the previous contribution.[6] The chemical difference lies in the nature of the R group: see Fig B-11. However, the apparent reactivities can be seen as the same. The corresponding comparison of simulated and experimental data at low times to determine the individual data points thus the k+app values are given in Fig B-14. Also shown is the corresponding line based on the numbers given in Table 3-2 in the main text for this wavelength.
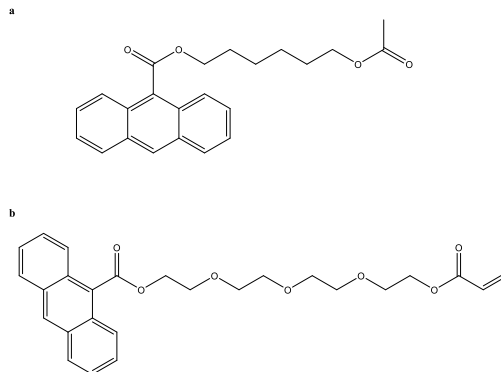


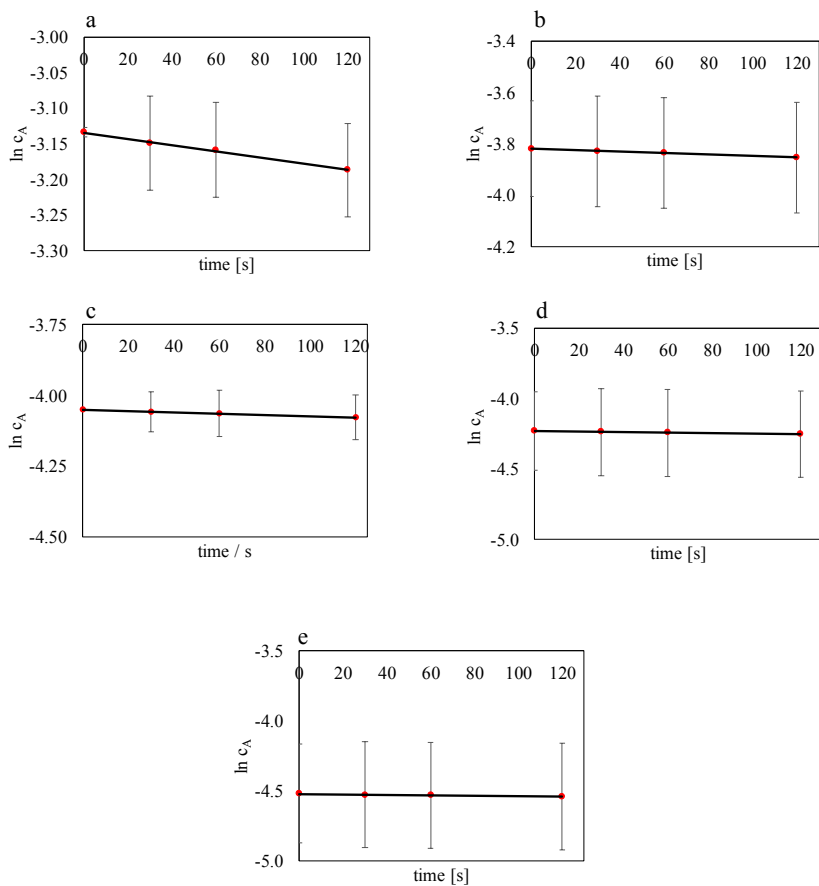Fig B-12 Structure of anthracene used: a: present work; b: previous work.[6]

**Fig B-13 Fits of the short time experimental data for A dimerization at 260 nm. a: $c_{A0}$ = 4.36 × $10^{-2}$ mol $L^{-1}$; b: $c_{A0}$ = 2.20 × $10^{-2}$ mol $L^{-1}$; c: $c_{A0}$ = 1.74× $10^{-2}$ mol $L^{-1}$; d: cA0 = 1.46× $10^{-2}$ mol $L^{-1}$; e $c_{A0}$ = 1.09 × $10^{-3}$ mol $L^{-1}$. More detailed data on the experimental conditions can be found it Table B-2.**

**Fig B-14** Fits of the short time experimental data for A dimerization at 280 nm. a: $c_{A0} = 4.36 \times 10^{-2}$ mol L$^{-1}$; b: $c_{A0} = 1.74 \times 10^{-2}$ mol L$^{-1}$; c: $c_{A0} = 1.09 \times 10^{-2}$ mol L$^{-1}$; d: $c_{A0} = 8.72 \times 10^{-3}$ mol L$^{-1}$. More detailed data on the experimental conditions can be found it Table B-1.
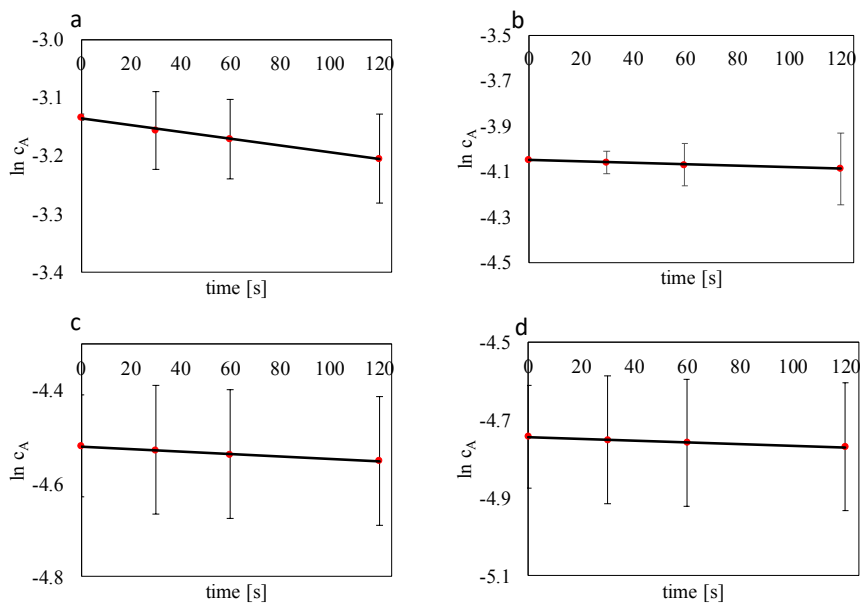


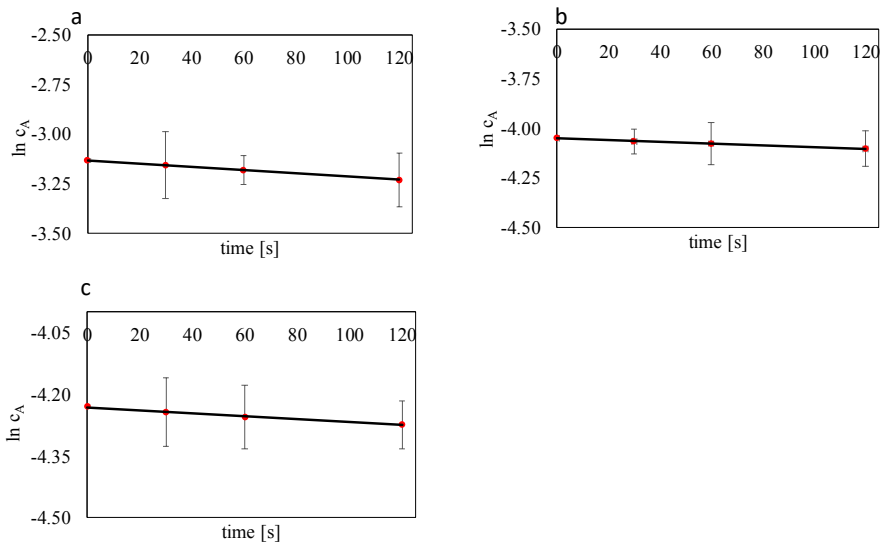**Fig B-15** Fits of the short time experimental data for A dimerization at 375 nm. $c_{A0} = 4.36 \times 10^{-2}$ mol L$^{-1}$; b: $c_{A0} = 1.74 \times 10^{-2}$ mol L$^{-1}$; c: $c_{A0} = 1.45 \times 10^{-2}$ mol L$^{-1}$. More detailed data on the experimental conditions can be found it Table B-1 & B-2.

## S3.5 Fraction of light absorbed during small time $A_2$ cleavage experiments

**Table B-8 Data on fraction of light absorbed by A and $A_2$ during small time $A_2$ cleavage experiments.**

| Wavelength $\lambda$, nm | Time, s | Concentration of A, mol L$^{-1}$ | Fraction of light absorbed by A | Concentration of $A_2$, mol L$^{-1}$ | Fraction of light absorbed by $A_2$ |
|---|---|---|---|---|---|
| 260 | 0 | 3.52E-05 | 0.05 | 1.10E-02 | 0.95 |
| | 15 | 1.18E-04 | 0.15 | 1.09E-02 | 0.85 |
| | 30 | 2.24E-04 | 0.25 | 1.09E-02 | 0.75 |
| | 60 | 3.48E-04 | 0.35 | 1.08E-02 | 0.65 |
| 270 | 0 | 3.52E-05 | 0.00 | 1.10E-02 | 1.00 |
| | 15 | 6.03E-04 | 0.08 | 1.07E-02 | 0.92 |
| | 30 | 1.11E-03 | 0.14 | 1.04E-02 | 0.86 |
| | 60 | 2.01E-03 | 0.23 | 9.97E-03 | 0.77 |
| 280 | 0 | 3.52E-05 | 0.00 | 1.10E-02 | 1.00 |
| | 15 | 9.30E-04 | 0.07 | 1.05E-02 | 0.93 |
| | 30 | 1.66E-03 | 0.11 | 1.01E-02 | 0.89 |
| | 60 | 2.93E-03 | 0.20 | 9.51E-03 | 0.80 |
| 290 | 0 | 3.52E-05 | 0.00 | 1.10E-02 | 1.00 |
| | 15 | 7.69E-04 | 0.08 | 1.06E-02 | 0.92 |
| | 30 | 1.42E-03 | 0.14 | 1.03E-02 | 0.86 |
| | 60 | 2.69E-03 | 0.25 | 9.63E-03 | 0.75 |
| 300 | 0 | 3.52E-05 | 0.01 | 1.10E-02 | 0.99 |
| | 15 | 3.77E-04 | 0.10 | 1.08E-02 | 0.90 |
| | 30 | 6.03E-04 | 0.15 | 1.07E-02 | 0.85 |
| | 60 | 8.72E-04 | 0.20 | 1.05E-02 | 0.80 |
| 310 | 0 | 3.52E-05 | 0.03 | 1.10E-02 | 0.95 |
| | 15 | 3.27E-04 | 0.21 | 1.08E-02 | 0.78 |
| | 30 | 5.38E-04 | 0.30 | 1.07E-02 | 0.69 |
| | 60 | 7.28E-04 | 0.38 | 1.06E-02 | 0.62 |
| 320 | 0 | 3.52E-05 | 0.05 | 1.10E-02 | 0.88 |
| | 15 | 3.02E-04 | 0.31 | 1.08E-02 | 0.66 |
| | 30 | 4.47E-04 | 0.41 | 1.08E-02 | 0.58 |
| | 60 | 6.69E-04 | 0.51 | 1.06E-02 | 0.48 |
| 330 | 0 | 3.52E-05 | 0.07 | 1.10E-02 | 0.84 |
| | 15 | 3.01E-04 | 0.43 | 1.08E-02 | 0.56 |
| | 30 | 4.64E-04 | 0.54 | 1.07E-02 | 0.45 |
| | 60 | 5.80E-04 | 0.60 | 1.07E-02 | 0.40 |

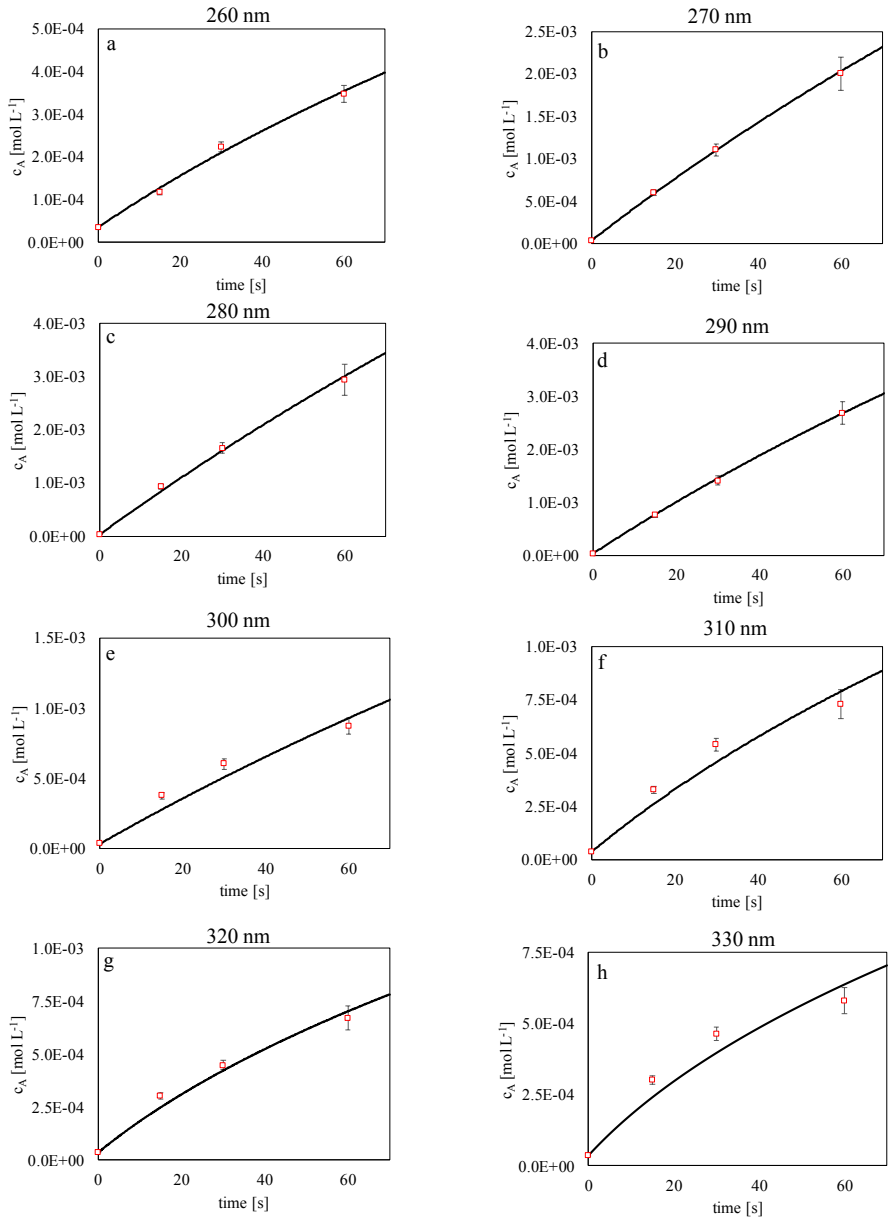## B.3.5 Data for determination of the reverse apparent rate coefficient



**Fig B-16 Visualisation of the fit for short time dimer cleavage experiments from Table B-3 and B-7.**
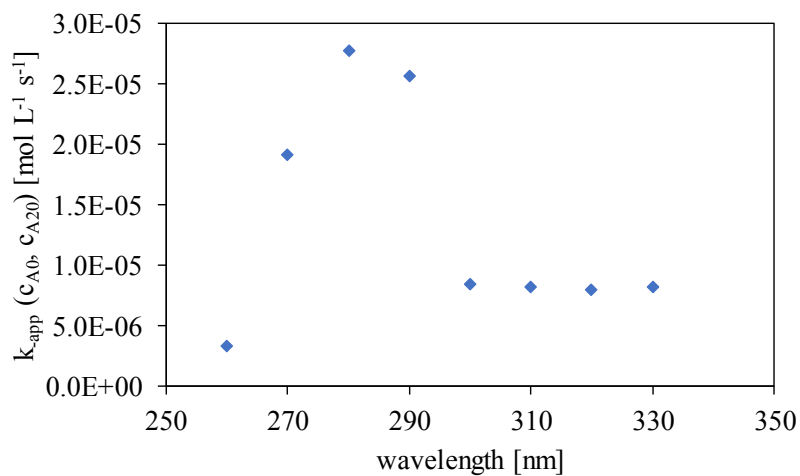
**Fig B-17 k$_{app}$ (c$_{A0}$, c$_{A20}$) at different wavelength at initial conditions in the short time A$_2$ cleavage experiment. c$_{A20}$=1.10×10$^{-2}$ mol L$^{-1}$ and c$_{A0}$=3.52×10$^{-5}$ mol L$^{-1}$ For more experimental conditions please refer to Table B-3. Plot with fitting line is shown in Fig B-17, also knowing that zero data point at 375 nm.**

**B.3.6 $k_2/k_{-1}$, $k_3/k_{-1}$ and $k_5/k_{-4}$ change with wavelength: experimental data and parameter tuning: lines at bottom of Table 3-2 in the main text**
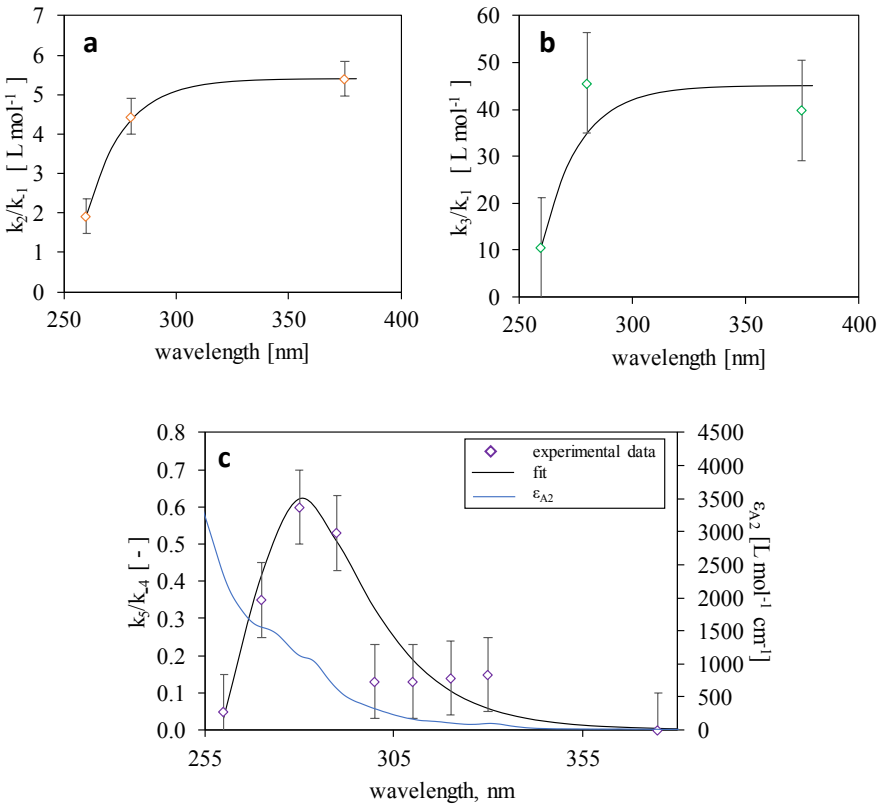


**Fig B-18 Summary of ratio of rate coefficients as used to construct the formulas as stated in Table 3-2 of the main text. a: $k_2/k_{-1}$ at different wavelengths; b: $k_3/k_{-1}$ at different wavelengths; k. $_4/k_5$ at different wavelengths. For the former two a straightforward description based on exponential functions can be used. For the latter a more complex formula is needed. In the present work it is decided to use a physically relevant equation to capture the overall trend and knowing the absence of dimer cleavage at very high wavelength, as can be deduced from the extra added data on attenuation. 0.1 error bars are included for scale.**

# B.3.7 Sensitivity analysis: effect of change in $k_2/k_{-1}$ and $k_3/k_{-1}$ on the determination of $k_5/k_{-4}$

Table B-9 Data showing the limited effect of change in $k_2/k_{-1}$ and $k_3/k_{-1}$ on the determination of $k_5/k_{-4}$, the experimental conditions are set to be the same as in Table B-3 (short time experiments for dimer cleavage).

| Wavelength λ, nm | Assume $k_2/k_{-1}$ and $k_3/k_{-1}$ to be constant and equal to the values at 375 nm from Table B-2 in the main text | | | | Simulating variation in $k_{-1}$ with change in λ from 330 to 260 nm | | | | Simulating variation in $k_2$ with change in λ from 330 to 260 nm | | | | Simulating variation in $k_3$ with change in λ from 330 to 260 nm | | | |
|---|---|---|---|---|---|---|---|---|---|---|---|---|---|---|---|---|
| | Input | | Output | | Input | | Output | | Input | | Output | | Input | | Output | |
| | $k_2/k_{-1}$, L mol$^{-1}$ | $k_3/k_{-1}$, L mol$^{-1}$ | $k_5/k_{-4}$ | $R^2$ | $k_2/k_{-1}$, L mol$^{-1}$ | $k_3/k_{-1}$, L mol$^{-1}$ | $k_5/k_{-4}$ | $R^2$ | $k_2/k_{-1}$, L mol$^{-1}$ | $k_3/k_{-1}$, L mol$^{-1}$ | $k_5/k_{-4}$ | $R^2$ | $k_2/k_{-1}$, L mol$^{-1}$ | $k_3/k_{-1}$, L mol$^{-1}$ | $k_5/k_{-4}$ | $R^2$ |
| 330 | 5.4 | 38.8 | **0.15** | 0.93 | 5.4 | 38.8 | **0.15** | 0.93 | 5.4 | 38.8 | **0.15** | 0.93 | 5.4 | 38.8 | **0.15** | 0.93 |
| 320 | 5.4 | 38.8 | **0.14** | 0.98 | 4.9 | 34.9 | **0.14** | 0.98 | 5.0 | 38.8 | **0.14** | 0.98 | 5.4 | 50.0 | **0.14** | 0.98 |
| 310 | 5.4 | 38.8 | **0.13** | 0.94 | 4.3 | 31.0 | **0.13** | 0.94 | 4.5 | 38.8 | **0.13** | 0.94 | 5.4 | 60.0 | **0.13** | 0.94 |
| 300 | 5.4 | 38.8 | **0.13** | 0.94 | 3.8 | 27.2 | **0.13** | 0.94 | 4.1 | 38.8 | **0.13** | 0.94 | 5.4 | 75.0 | **0.13** | 0.94 |
| 290 | 5.4 | 38.8 | **0.53** | 1.00 | 3.3 | 23.3 | **0.53** | 1.00 | 3.7 | 38.8 | **0.53** | 1.00 | 5.4 | 95.0 | **0.53** | 1.00 |
| 280 | 5.4 | 38.8 | **0.60** | 1.00 | 2.7 | 19.4 | **0.59** | 1.00 | 3.2 | 38.8 | **0.59** | 1.00 | 5.4 | 115 | **0.60** | 1.00 |
| 270 | 5.4 | 38.8 | **0.35** | 1.00 | 2.7 | 15.5 | **0.35** | 1.00 | 2.8 | 38.8 | **0.35** | 1.00 | 5.4 | 135 | **0.35** | 1.00 |
| 260 | 5.4 | 38.8 | **4.9E-02** | 0.99 | 1.6 | 11.6 | **4.9E-02** | 0.99 | 2.3 | 38.8 | **4.9E-02** | 0.99 | 5.4 | 170 | **4.9E-02** | 0.99 |

## B.3.8 Supplementary plot for Fig 3-8 aii.
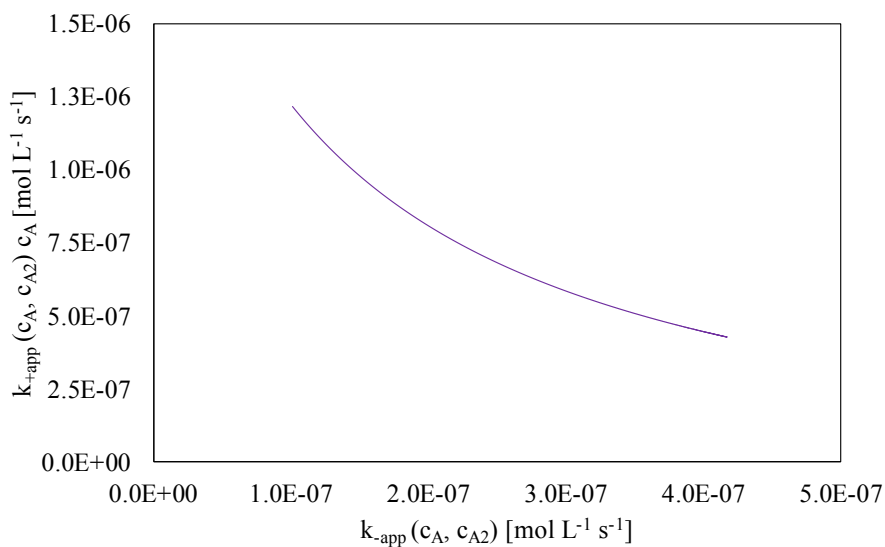


**Fig B-19 Plot of $k_{+app}$ ($c_A$,$c_{A2}$) $c_A$ against $k_{-app}$ ($c_A$,$c_{A2}$) for the Fig 3-8a in the main text. As time progresses, the concentration of A decreases while the concentration of $A_2$ increases leasing to a decrease in $k_{+app}$ ($c_A$,$c_{A2}$) $c_A$ and an increase in $k_{-app}$ ($c_A$,$c_{A2}$) until eventually photostationary state is reached with $k_{+app}$ ($c_A$,$c_{A2}$) $c_A$ being equal to $k_{-app}$ ($c_A$,$c_{A2}$).**

# B.4 Extra sensitivity parameters beyond the examples in Fig 3-8 and considering general kinetic parameters

In this section, an extra sensitivity analysis is considered for general kinetic parameters. Since individual rate coefficients are not required for the use of **eq 3-24** and **3-25** ratios are used for convenience. In order to perform the analysis the following ratios are changed $k_2/k_{-1}$, $k_3/k_{-1}$ and $k_{-4}/k_5$. Each ratio was changed in turn while keeping the other two constant apart from the case where change in $k_{-1}$ was mimicked, in that case both $k_2/k_{-1}$ and $k_3/k_{-1}$ where both changed proportionally. In **Fig B-20** one can see the result of the sensitivity analysis accomplished by starting from pure monomer **A**. Overall with changes in each of the individual rate coefficients has led to the expected changes in the equilibrium concentrations.

First, if we look at **Fig B-20 a** we will be able to see that decrease in $k_3/k_{-1}$, i.e. increase in $k_3$, which corresponds to concentration quenching and thus not leading to formation of dimer, leads to equilibrium point shifting towards producing more dimer as expected. **Fig B-20 b** in turn shows, that increase in $k_{-1}$ and, therefore a decrease in lifetime of **A** in the singlet excited state, leads to reduction in time available for the for the $^1$**A** species to react, consequently leading to less dimer being formed. **Fig B-20 c** corresponds to effect of change in $k_2$, responsible for dimerization reaction itself. An increase in $k_2$ thus leads to shift equilibrium towards producing more dimer. Finally, **Fig B-20 d** looks at the combined effect of $k_5/k_{-4}$ on the equilibrium. The parameter $k_{-4}$ corresponds to the de-excitation of $^1$**A$_2$**, while $k_5$ is responsible for the dimer dissociation reaction, therefore a decrease in $k_5/k_{-4}$, i.e. increase in $k_{-4}$ and/or decrease in $k_5$, results in lower rates of dimer dissociation and, hence, a shift in equilibrium towards having more dimer.

Furthermore in **Fig B-21** one shows that if one selects three cases of the same overall amount of "A" groups one always ends with the correct equilibrium setting, highlighting the overall consistency of the developed platform. This is thus further supporting results in the second situation in **Fig 3-8** in the main text.
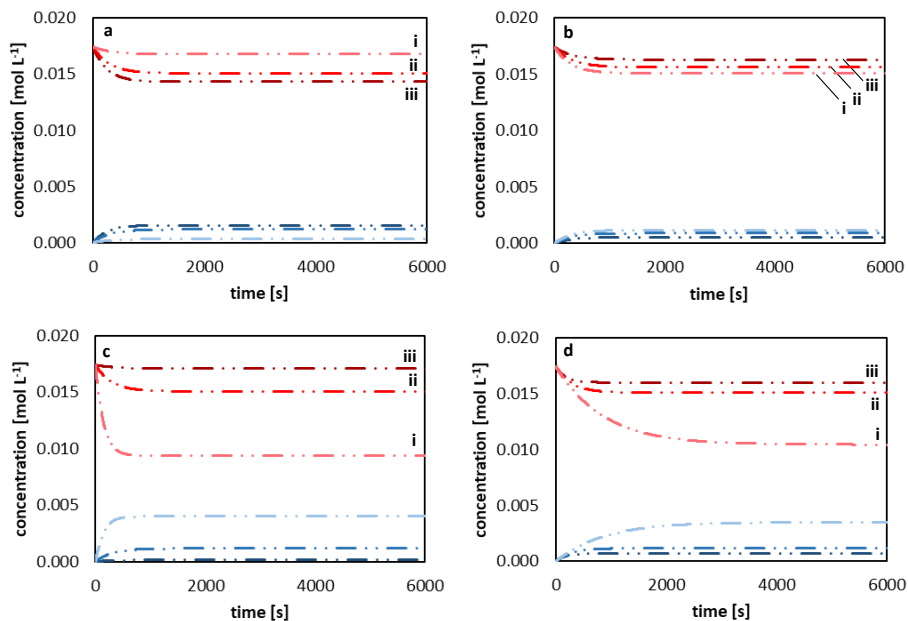
**Fig B-20 Sensitivity analysis performed on eq 3-24 and 3-25. Red lines represent anthracene monomer and blue lines anthracene dimer. The following conditions were used to predict reaction conversion: $c_{A0}$=0.0174 mol L$^{-1}$, $c_{A2}$=0 mol L$^{-1}$, 20Hz, 538 µJ pulse$^{-1}$, 280nm;**

**a: $k_2/k_{-1}$ = 5.41 $L\ mol^{-1}$, $k_5/k_{-4}$ = 1,**
*i.*  $k_3/k_{-1}$ = 387.9 $L\ mol^{-1}$,
*ii.*  $k_3/k_{-1}$ = 38.79 $L\ mol^{-1}$,
*iii.*  $k_3/k_{-1}$ = 3.879 $L\ mol^{-1}$;
**b: $k_5/k_{-4}$ =1,**
*i.*  $k_2/k_{-1}$ = 5.41 $L\ mol^{-1}$, $k_3/k_{-1}$ = 38.79 $L\ mol^{-1}$,
*ii.*  $k_2/k_{-1}$ = 3.25 $L\ mol^{-1}$, $k_3/k_{-1}$ = 23.27 $L\ mol^{-1}$,
*iii.*  $k_2/k_{-1}$ = 1.62 $L\ mol^{-1}$, $k_3/k_{-1}$ = 11.64 $L\ mol^{-1}$;
**c: $k_3/k_{-1}$ = 38.79 $L\ mol^{-1}$, $k_5/k_{-4}$ = 1,**
*i.*  $k_2/k_{-1}$ = 54.10 $L\ mol^{-1}$,
*ii.*  $k_2/k_{-1}$ = 5.41 $L\ mol^{-1}$,
*iii.*  $k_2/k_{-1}$ = 0.541 $L\ mol^{-1}$;
**d: $k_3/k_{-1}$ = 38.79 $L\ mol^{-1}$, $k_2/k_{-1}$ = 5.41 $L\ mol^{-1}$,**
*i.*  $k_5/k_{-4}$ = 0.1,
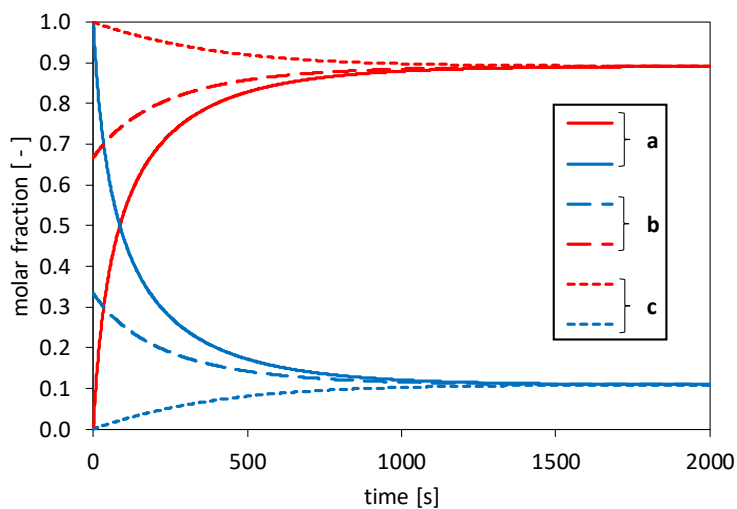*ii.*  $k_5/k_{-4}$ = 1,
*iii.*  $k_5/k_{-4}$ = 10.

**Fig B-21 An illustration of the ability to use eq 3-24 and 3-25 from any point of initial concentration combinations obeying the same overall amount of A moieties (same $c_{A,tot,}$). Parameters were arbitrarily set to $k_2/k_{-1}$ = 5 $L\ mol^{-1}$, $k_3/k_{-1}$ = 35 $L\ mol^{-1}$, $k_5/k_{-4}$ = 1, molar attenuation coefficients were also arbitrarily set to $\varepsilon_A = 600\ L\ mol^{-1}\ cm^{-1}$ and $\varepsilon_{A2} = 300\ L\ mol^{-1}\ cm^{-1}$. A same equilibrium point is always reached regardless of the initial ratio of monomer to dimer. a: $c_{AO} = 10^{-10}\ mol\ L^{-1}$ and $c_{A20} = 5 \times 10^{-3}\ mol\ L^{-1}$; b: $c_{A0} = 5 \times 10^{-3}\ mol\ L^{-1}$ and $c_{A20} = 2.5 \times 10^{-3}\ mol\ L^{-1}$; c: $c_{A0} = 10^{-2}\ mol\ L^{-1}$ and $c_{A20} = 5 \times 10^{-10}\ mol\ L^{-1}$.**

# APPENDIX C: SUPPORTING INFORMATION FOR CHAPTER

# 4

## C.1 Kinetics of anthracene exclusive dimerization in solution

In this section, the kinetic expression for anthracene dimerization reaction, where anthracenes are freely reacting in solution, i.e. not attached to the polymer chain (**Fig 4-2 a** of the main text), is briefly described. The model for such a case has been previously derived in Ref [6]. Therefore, here are only the main points stated. The simplified reaction scheme for anthracene dimerization can be seen in the figure below.
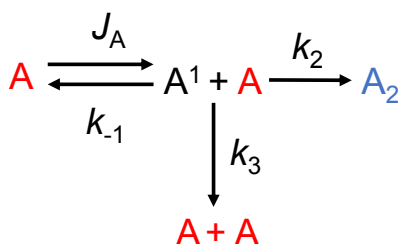


**Fig C-1 Simplified reaction scheme of Anthracene dimerization free in solution.[6-7] $k_{-1}$ and $k_3$ are the de-excitation rate coefficients and $k_2$ rate coefficient for $A_2$ formation.**

Following the reaction scheme in **Fig C-1**, the rate expression for A species, assuming a steady-state (QSSA) for $^1A$ species can be written and rearranged as:

$$\frac{dc_{A,t}}{dt} = -2k_{+app}(c_{A,t})\, c_{A,t} \qquad\qquad \text{eq C-1}$$

where

$$k_{+app}(c_{A,t}) = \frac{\frac{k_2}{k_{-1}}\mathcal{J}_{A,t}(c_{A,t})}{\left(\frac{k_2}{k_{-1}}+\frac{k_3}{k_{-1}}\right)c_{A,t}+1} \qquad\qquad \text{eq C-2}$$

$$\mathcal{J}_{A,t}(c_{A,t}) = \frac{E_{pp}T_\lambda f}{E_\lambda N_A V_{sample}}(1 - 10^{-\varepsilon_A c_{A,t} L}) \qquad\qquad \text{eq C-3}$$

Here $\mathcal{J}_{A,t}$ represents a molar volumetric rate of photon absorption in mol L$^{-1}$ s$^{-1}$. $k_{-1}$, $k_2$, and $k_3$ rate coefficients are defined as per **Fig C-1**. In **eq C-3**, $E_{pp}$ is energy per pulse of the laser beam per pulse in J pulse$^{-1}$, $T_\lambda$ - the transmittance of the vial bottom, f - the frequency of the laser beam, in pulse s$^{-1}$, $E_\lambda$ - the energy of one photon

at wavelength, λ, in J, $V_{sample}$ - the sample solution volume in L, $\varepsilon_A$ - the A molar attenuation coefficient L mol$^{-1}$ cm$^{-1}$, and, finally, L is the height of the solution (i.e. light path) in cm.

Model for photodimerization reaction of free anthracenes in solution (**eq C-1 – C-3**) will now be used as a basis for developing the model for photodimerization reaction of anthracenes attached to polymer chains. **Sections C.2 and C.3** gradually adapt the model above to the SCNP environment.

## C.2 Derivation to describe folding of infinitely flexible identical linear, thus ideal chains

The first step in the model construction for anthracene photo dimerization in the SCNP environment is an attachment of anthracenes to infinitely flexible identical ideal chains (**Fig 4-3 a-b**). This condition requires some adjustments to the model, which will be discussed below.

All anthracenes are now divided into groups according to their attachment to a polymer chain, assuming no inter-chain reaction and that anthracenes are only able to react with other anthracenes attached to the same polymer chain, i.e. creating numerous small defined reaction volumes (**Fig 4-2 b-c**). To understand the folding behaviour within these volumes, the volumetric rate of light absorbed by the SCNP needs to be known at any reaction time $t$ ($J_{A\,SCNP,\,t}$). This requires *a priori* knowledge regarding the utilized molar concentration of polymer chains in the solution, $c_{ch,\,sol,0}$ [mol L$_{sample}^{-1}$], as defined in **Fig 4-2 c**. Since identical molecules/SCNPs are considered, $J_{A\,SCNP,\,t}$ can be derived from the overall value for the solution ($J_{A\,sol,\,t}$) considering homogenization:

$$\mathcal{J}_{A,SCNP\,t}\left(c_{A,\,sol,\,t}\right) = \frac{\mathcal{J}_{A\,sol,t}\left(c_{A,\,sol,\,t}\right)}{c_{ch,\,sol,0}\,N_A V_{SCNP,H,0}} \qquad \text{eq C-4}$$

in which $N_A$ is the Avogadro number, $V_{SCNP,\,H,0}$ the initial single-molecule hydrodynamic volume. The denominator in this equation represents the SCNP amount, which is equivalent to $\left(\frac{c_{A,\,sol,0}}{c_{A,\,SCNP,0}}\right)$ with $c_{A,\,SCNP,0}$ [mol L$_{SCNP}^{-1}$] the initial molar concentration of **A** moieties within the initial hydrodynamic volume (**Fig 4-2 c**).

$J_{A,sol,\,t}$ in **eq C-4** depends on $c_{A,sol,t}$, which is the (pseudo-)homogeneous molar concentration of **A** in the solution [mol L$^{-1}_{sample}$], as shown in **Fig 4-2 a**. Formally we can wipe out the presence of chains for **A** movement, as they are assumed highly flexible to claim in the limit freely floating **A** moieties. For exclusive dimerization, $J_{A,sol,\,t}$ is using the Beer-Lambert law without the interference of **A₂** light absorption and is defined similarly to **eq C-3** in **Section C.1** as:[6]

$$\mathcal{J}_{A,sol,t}\left(c_{A,\,sol,\,t}\right) = \frac{E_{pp}T_\lambda f}{E_\lambda N_A V_{sample}}\left(1 - 10^{-\varepsilon_A c_{A,\,sol,t}L}\right) \qquad \text{eq C-5}$$

in which $E_{pp}$ is energy per pulse of the laser beam per pulse, $T_\lambda$ the transmittance at the vial bottom, $f$ the frequency of the laser beam, $E_\lambda$ the energy of one photon at λ, $V_{sample}$ the solution volume, $\varepsilon_A$ the **A** molar

attenuation coefficient, and $L$ the height of the solution. The overall equation for $\mathcal{J}_{A,SCNP\,t}(c_{A,\,sol,\,t})$ can be seen at the bottom of **Fig 4-2**.

A second kinetic characteristic required to understand the ideal folding behaviour is the time variation of $c_{A,}$ $_{SCNP,t}$, $\left(\frac{dc_{A,SCNP,t}}{dt}\right)$, which is affected by $J_{A,\,SCNP,t}$ (**eq C-4**) and defines the progress of the intramolecular reaction in an SCNP. As **A** moieties are assumed to be freely moving in $V_{SCNP,H}$ (**Fig 4-2 d**), we can describe the dimerization kinetics using photoreaction rate laws as derived in our previous work (**Section C.1**),[6] considering only **A** solution species (**Fig 4-2 c**), but properly adapting the reaction focus from the solution to one molecule/SCNP:

$$\frac{dc_{A,SCNP,t}}{dt} = -2k_{+app,ideal}(c_{A,\,sol,t}, c_{A\,SCNP,t})\,c_{A,SNCP,t} \qquad \text{eq C-6}$$

In **eq C-6**, $k_{+app,\,ideal}$ is an apparent rate coefficient for dimerization linked to the individual reactions in **eq C-7**, highlighting the fundamental nature of the theoretical approach from a chemistry point of view:

$$k_{+app,ideal}(c_{A,\,sol,t}, c_{A\,SCNP,t}) = \frac{\frac{k_2}{k_{-1}}\mathcal{J}_{A,SCNP,t}(c_{A,\,sol,\,t})}{\left(\frac{k_2}{k_{-1}}+\frac{k_3}{k_{-1}}\right)c_{A,SCNP,t}+1} \qquad \text{eq C-7}$$

with $k_2/k_{-1}$ and $k_3/k_{-1}$ ratios of rate coefficients that can be determined from low time experiments considering various $c_{A,sol,0}$ values ideally in the absence of chains.[6]

A stepwise integration of **eq C-6** is required as $k_{+app,ideal}$ is $t$ dependent.[6] Only for a small time step, $\Delta t$, we can consider $k_{+app,ideal}$ constant so that the variation of the moles of **A** moieties in a highly flexible polymer chain ($n_{A,SCNP}$) always assuming in the first instance $V_{SCNP,H,0}$ can be calculated from:

$$n_{A,SCNP,\,t+\Delta t} = n_{A,SCNP,\,t}e^{-2k_{+app,ideal}(c_{A,\,sol,t}, c_{A\,SCNP,t})\Delta t} \qquad \text{eq C-8}$$

However, as anthracenes react and form crosslinks, the polymer chain contracts (**Fig 4-3 b**), reducing the volume occupied by the chain, leading to decreasing $V_{SCNP,H}$ with increasing $t$, as shown in **Fig 4-3 b**. Therefore, $V_{SCNP,H,\,t}$ needs to be updated per $\Delta t$. This time variation for $V_{SCNP,H,\,t}$ can be calculated from the experimentally accessible SCNP hydrodynamic radius $R_{SCNP,\,H,\,t}$:

$$V_{SCNP,H,t} = \frac{4}{3}\pi(R_{SCNP,H,t})^3 \qquad \text{eq C-9}$$

with $R_{SCNP,\,H,\,t}$ being the hydrodynamic radius. A lowered $V_{SCNP,H,\,t}$ goes hand in hand with a higher $c_{A,\,SCNP,\,t}$ and a lower $k_{+app,\,ideal}(c_{A,\,sol,\,t}, c_{A,\,SCNP,\,t})$. To calculate the $t$ variation of the radius of gyration, $R_{SCNP,\,g}$, Martin *et al.*[8] proposed the Zimm and Stockmayer contraction factor $g$.[9-10] Contraction factor is defined as a ratio of the mean square radius of gyration of a branched-chain to a linear one, which here we apply to hydrodynamic radius:

$$R_{SNCP,H,t} = R_{SNCP,H,t=0}\sqrt{g_t} = R_{SNCP,H,t=0}\sqrt{1 - \beta\rho_t^{\alpha}}$$

eq C-10

with $\alpha$ and $\beta$ parameters with literature values of 0.5 and 0.7,[9] and $\rho_t$ the crosslinking density in mole crosslinks

(thus $A_2$ moieties) at $t$ on a monomer unit basis.[9] This density can be correlated with the $A$ conversion at $t$ ($X_{A,t}$)

and thus the folding kinetics:

$$\rho_t = \frac{X_{A,t}\, n_{A,SNCP,nc=0}\, N_A}{2N_{ch,\ l}}$$

eq C-11

with $n_{A,\ SCNP,\ nc=0}$ the mole of $A$ species for all chains without crosslinks (thus no $A_2$ present) and $N_{ch,\ l}$ the

number of monomer units in the chain both reactive, *i.e.* containing $A$ moieties, and not. Factor 2 is included

to reflect that 2 $A$ moieties create one link.

## C.3 Derivation to describe folding of identical chains with given flexibility: confinement corrections added to the model in C.2

The second step in the model for anthracene photo dimerization in the SCNP environment is a transition from infinitely flexible identical ideal chains to a more realistic scenario by application of additional considerations regarding the flexibility of the chain and other possible structural features of the chain (as is illustrated in **Fig 4-3 c-d**).

As per previous **Section C.2**, **A** moieties in **Fig 4-3 a** have been considered to be freely moving in $V_{SCNP,H}$. At the start no **A** dimerization reactions have taken place yet and as a result, the **A** moieties should indeed be able to move rather freely. However, if initial dimerization reactions have taken place, as shown in **Fig 4-3 c**, further dimerization could be hindered due to the decreased mobility of **A** moieties as well as possible unfavourable spatial arrangements, although, volume contraction has brought them closer to each other (**Fig 4-3 c**). Additionally, the **A** conversion is limited as one requires two **A** molecules for one dimerization and, thus, if there is an odd number of **A** molecules incorporated in a chain it is impossible for the remaining **A** moiety to react intramolecularly (**Fig 4-3 c**).

To capture these mobility limitations $k_{+app,ideal}(c_{A,sol,t}, c_{A,SCNP,t})$ from **eq C-7**, which is an essential input for the main **eq C-6**, needs to be adjusted with a confinement factor $z$ with the previous highly flexible case retrieved if $z = 1$ (**eq C-13**). Thus $k_{+app,ideal}(c_{A,sol,t}, c_{A,SCNP,t})$ becomes $k_{+app}(c_{A,sol,t}, c_{A,SCNP,t})$ in **eq C-6** (see **Fig 4-3 c**). In the present chapter, we propose a basic power law $t$ dependent driven equation:

$$z_t = 1 - \left(\frac{X_{A,t}}{X_{A,lim}}\right)^w$$

eq C-12

$$k_{+app}(c_{A,sol,t}, c_{A,SCNP,t}) = k_{+app,ideal}(c_{A,sol,t}, c_{A,SCNP,t}) z_t$$

eq C-13

in which $X_{A,lim}$ is the limiting **A** conversion that follows from $\frac{2N_{A2,lim}}{N_{A,SNCP,nc=0}}$ with $N_{A,SCNP,nc=0}$ the number of **A** available in a polymer chain with no crosslinks, and $N_{A2,lim}$ the maximum number of **A₂** that can be formed given by $\left\lfloor \frac{N_{A,SNCP,nc=0}}{2} \right\rfloor$, with the L type brackets denoting the floor function, *i.e.* the nearest integer value lower or equal to the value of $N_{A,SCNP}/2$.

Furthermore, in **eq C-12**, $w$ is a system-dependent fitting parameter that depends on the structural characteristics of the chain, as illustrated in **Fig 4-3 d**. The stiffness of the polymer backbone and the spacer length for **A** units codetermine flexibility. These chemical characteristics could vary significantly implying a different $w$ value per polymer/**A** system considered. In the long term, $w$ data can be made even more fundamental by correlating them with polymer physics parameters such as the stiffness ratio $C_\infty$.[11]

## C.4 Summary of interaction experimental and modelling work

The summary of the protocol proposed in the current thesis is shown in **Fig C-2** below. Step 1 of the current protocol determines the $\alpha$ and $\beta$ constants in the expression for the contraction factor expression (**eq C-10**). Step 2 enables the determination of the $w$ parameter for the efficiency function using **eq C-6**, **eq C-12**-**eq C-13**. Step 3 validates the model and establishes confidence boundaries.

The summary of all equations used in this model is provided in an interactive format in **Fig C-3** below. In the first step $c_{A,sol,t}$, $c_{A,SCNP,t}$ and $V_{SCNP,H,t}$ are calculated using initial number of moles of A available ($n_{A,SCNP,t}$ where t=0). Next, in step two the calculated values of concentrations and SCNP volume are used to determine $J_{A,SCNP,t}$, which is turn is used to calculate $k_{+app}$ value in step 3. Correction factor, $z_t$ is also calculated. Finally, the new number of moles of A after time step $\Delta t$, $n_{A,SCNP,t+\Delta t}$, is determined. $t + \Delta t$ becomes t and the sequence is repeated with the new $n_{A,SCNP,t}$ value. The result of using the protocol from **Fig C-2** and **Fig C-3** can be seen in **Fig 4-4** of the main text.
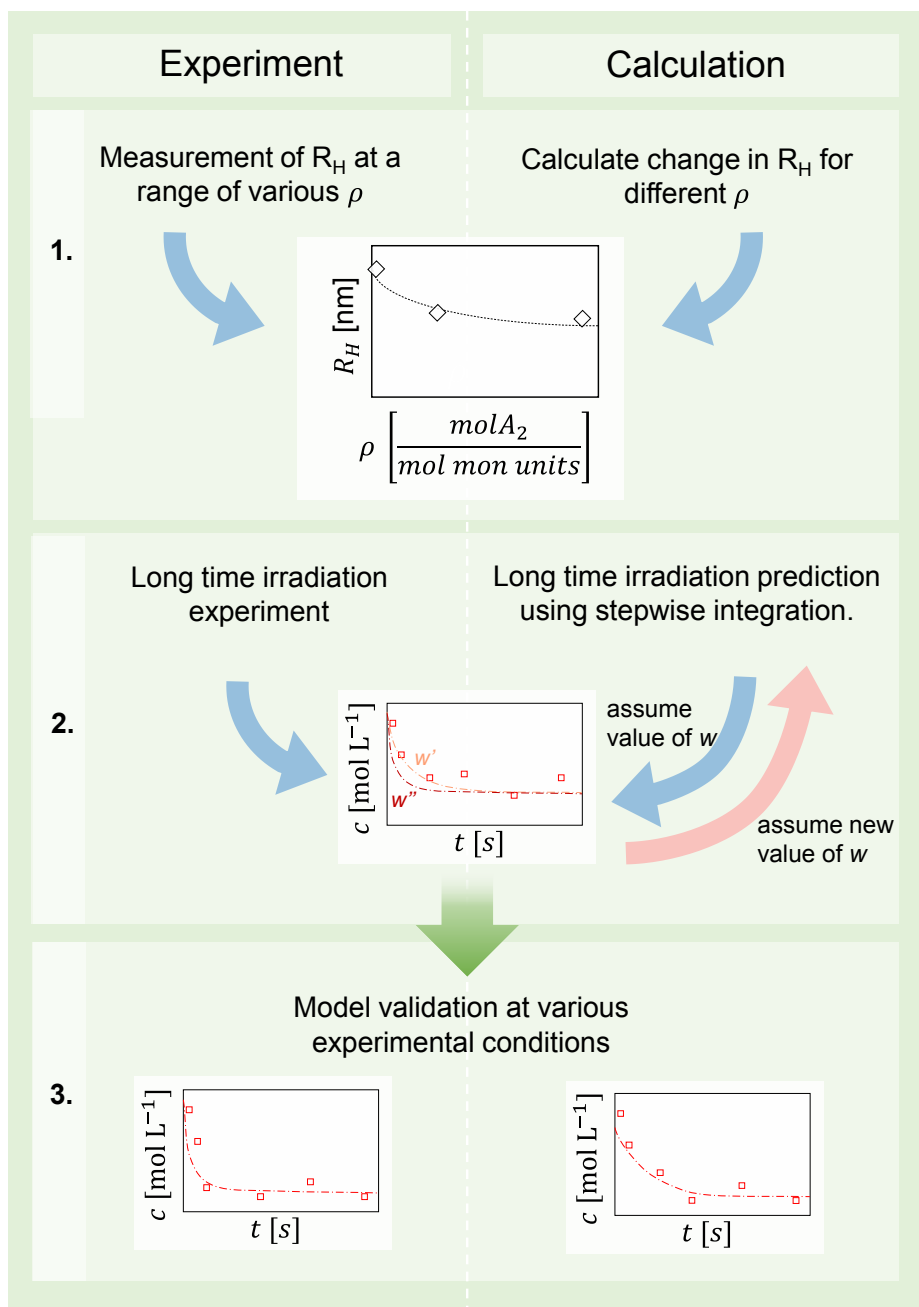
**Fig C-2 Schematic diagram of the protocol proposed in this chapter to determine the model parameters.**

## Summary of the main model steps

### 1. Calculation/update of $V_{SCNP,t}$ , $c_{A,SCNP,t}$ and $c_{A,sol,t}$

$$\rho_t = \frac{X n_{A,ncp,nc=0} N_A}{2 N_{ch} l}$$

$$g_t = 1 - \beta \rho_t^{\alpha}$$

$$V_{SCNP,t} = \frac{4}{3} \pi (R_{SCNP,nc=0} \sqrt{g_t})^3$$

$$c_{A,SCNP,t} = \frac{n_{A,SCNP,t}}{V_{H,t}}$$

$$c_{A,sol,t} = c_{A,SCNP,t} c_{ch,sol} N_A V_{SCNP,t}$$

### 2. Calculation/update of $\mathcal{J}_{A,SCNP,t}(c_{A,sol,t}, c_{A,SCNP,t})$

$$\mathcal{J}_{A,sol,t}(c_{A,sol,t}) = \frac{E_{pp} T_\lambda f}{E_\lambda N_A V_{sample}} (1 - 10^{-\varepsilon c_{A,sol,t} L})$$

$$\mathcal{J}_{A,SCNP,t}(c_{A,sol,t}, c_{A,SCNP,t}) = \mathcal{J}_{A,sol,t}(c_{A,sol,t}) \times \left( \frac{1}{c_{ch,sol} N_A V_{HSCNP,t}} \right)$$

### 3. Calculation/update of $z$ and $k_{+app}(c_{A,sol,t}, c_{A,SCNP,t})$

$$z_t = 1 - \left( \frac{X_t}{X_{lim}} \right)^w$$

$$k_{+app}(c_{A,sol,t}, c_{A,SCNP,t}) = \frac{\frac{k_2}{k_{-1}} \mathcal{J}_{A,SCNP,t}(c_{A,sol,t}, c_{A,SCNP,t})}{\left( \frac{k_2}{k_{-1}} + \frac{k_3}{k_{-1}} \right) c_{A,SCNP,t} + 1} z_t$$

### 4. Calculation of $n_{A,SCNP,t+\Delta t}$

$$n_{A,SCNP,t+\Delta t} = n_{A,SCNP,t} e^{-2k_{+app}(c_{A,sol,t}, c_{A,SCNP,t}) \Delta t}$$

Next iteration: $n_{A,SCNP,t+\Delta t} \rightarrow n_{A,SCNP,t}$

**Fig C-3 Summary of the main steps to calculate the folding kinetics for a single molecule nanoparticle due to dimerization.**
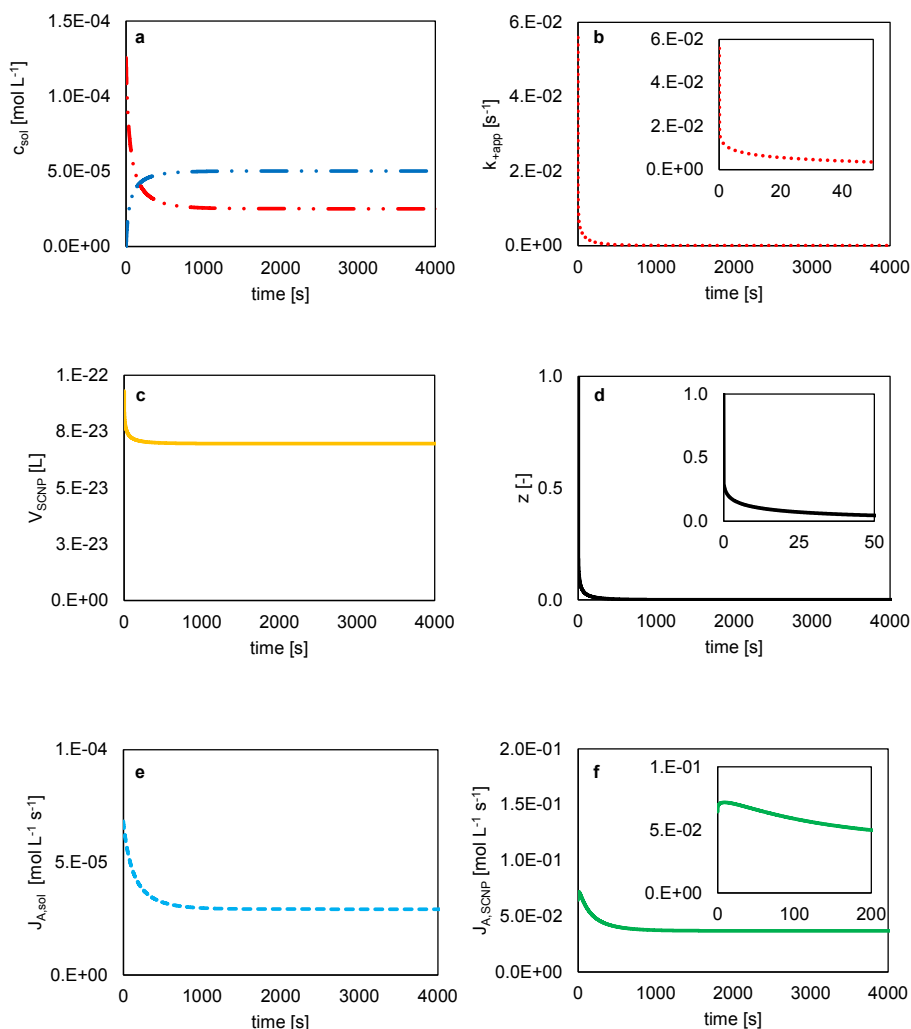
**Fig C-4 Results of the sample model prediction for chain folding. Modelled conditions $c_{ch,\,sol}$ = 1.89×10⁻⁵ mol L⁻¹, the ratio of non-functional monomer to A on the chain 16:1, 6.65 A per chain on average, sample irradiated with 375 nm at 392 uJ pulse⁻¹. a: change in pseudo homogenous concentrations of A (red) and $A_2$ (blue) with time; b: change in apparent rate coefficient with time; c: change in SCNP volume with time; d: change in efficiency factor, z, with time; e: change in $J_{A,\,sol,\,t}$ ($c_{A,\,sol,\,t}$); f: change in $J_{A,\,SCNP,\,t}$ ($c_{A,\,SCNP,\,t}$, $c_{A,\,sol,\,t}$) vs time. For the prediction, w is taken to be 0.065.**

## C.5 Comparison with the existing simplified method

Our method is related to the work of Liu et al. on the intramolecular coupling of benzocyclobutenes attached

to a single polymeric backbone, in which the bimolecular crosslinking reaction rate displayed second-order

kinetics in the number of benzocyclobutenes $(x(t) = \frac{x(0)}{1+k \cdot x(0) \cdot t}$, where $x$ refers to unreacted benzocyclobutenes). Additionally, to predict (potentially incomplete) crosslinking progress, they generalized this model solution by including a parameter x∞ (similar to our proposed z-function: $x(t) = \frac{x(0)}{B+k \cdot x(0) \cdot t} + x_\infty$) which allowed predicting a plateau value in the number of unreacted crosslinkers, e.g. representing steric hindrance.[12] In contrast, in this chapter we do not hardcode any solution, instead, we separate the chemical kinetics from the steric hindrance on a model description level, followed by numerical solution integration. Hence, the present chapter goes way beyond previous work in which crosslinker conversion profiles have been formally fitted.

## C.6 Details of the *k*MC model

In this section, some clarifications and additional data are presented regarding the "Macromolecular reverse engineering to unravel the folding of individual chains" section in the main text.

### C.6.1 RAFT polymerization

The current kinetic model for RAFT polymerization builds on our previous *k*MC contributions,[13-18] that enable the design and optimization of living polymerization, as well as reversible-deactivation radical polymerization (RDRP) processes, which in turn stems from the pioneering stochastic simulation algorithm developed by Gillespie.[19] In this stochastic model, the reaction events, as well as the time between these events, are selected randomly according to their reaction probabilities calculated from the so-called MC reaction rates expressed in $s^{-1}$ and the number of reactive molecules involved in each reaction event:

$$\tau = \frac{1}{a_0} \ln \left( \frac{1}{r_1} \right) = \frac{1}{\sum a_{j,k}} \ln \left( \frac{1}{r_1} \right) \qquad \text{eq C-14}$$

$$\sum_{j=1}^{\mu} a_{j,k} \geq r_2 a_0 \qquad \text{eq C-15}$$

Here $a_0$ stands for the total MC reaction rate, which is calculated from the sum of the individual Monte Carlo reaction rates following from the so-called MC reaction channels ($a_0 = \sum a_{j,k}$). Furthermore, $r_1$ and $r_2$ are uniformly distributed random numbers in the interval (0,1], and μ is the smallest integer that satisfies **eq C-15**. The rate coefficients used in the *k*MC model are summarized in **Table C-1** below. **Fig C-5** and **Fig C-6** show some additional data from the RAFT polymerization modelling results presented in **Fig 4-5**. The additional data presented in **Fig C-5** includes fractional comonomer conversion at different times, end-group functionality, polymer dispersity, and number-average chain length at different conversions. **Fig C-6 e** includes the explicit

visualisation of 400 polymer chain samples. The chain length distribution and distribution of the monomers are also presented in **Fig C-6 a-b**.

**Table C-1 Mechanism and kinetic parameters used in the kMC model for the RAFT copolymerization of MMA (M₁) and A containing monomer (modelled as BMA) (M₂) at 343 K.**

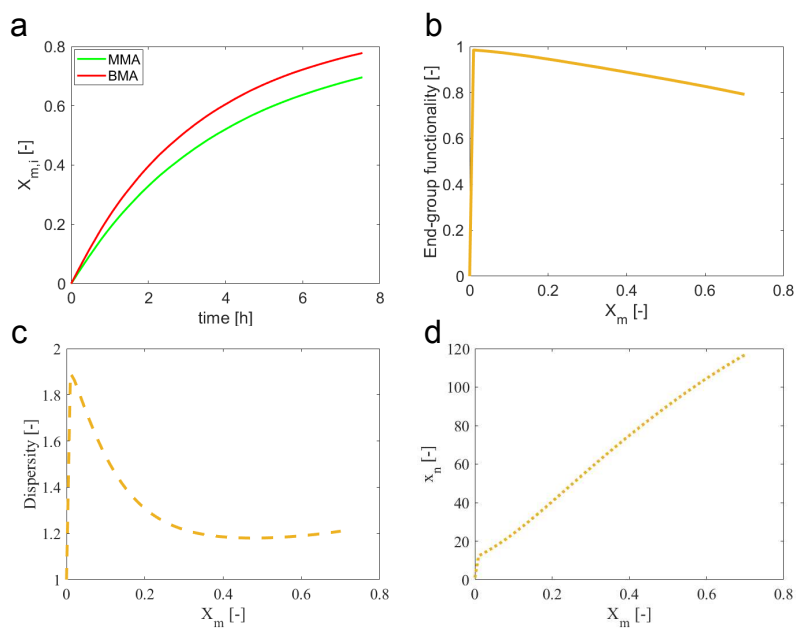| Reaction | Equation | $k$ (dm$^3$ mol$^{-1}$ s$^{-1}$) | Ref |
|---|---|---|---|
| Bimolecular dissociation | $I_2 \xrightarrow{f,\,k_{dis}} 2I^*$ | $4.35\times10^{-5}$ | 20-21 |
| Chain initiation | $I^* + M_1 \xrightarrow{k_{pI}} R^*_{1,M_1}$ | $3.6\times10^3$ | 20-21 |
| | $I^* + M_2 \xrightarrow{k_{pI}} R^*_{1,M_2}$ | $3.6\times10^3$ | |
| | $R^*_0 + M_1 \xrightarrow{k_{pR_0}} R^*_{1,M_1}$ | $3.6\times10^3$ | |
| | $R^*_0 + M_2 \xrightarrow{k_{pR_0}} R^*_{1,M_2}$ | $3.6\times10^3$ | |
| Propagation | $R^*_{i,M_1} + M_1 \xrightarrow{k_{p_{11}}} R^*_{i+1,M_1}$ | $1.0\times10^3$ | 20 |
| | $R^*_{i,M_1} + M_2 \xrightarrow{k_{p_{12}}} R^*_{i+1,M_2}$ | $k_{p_{12}} = k_{p_{11}}/r_1\,;\ r_1 = 0.79$ | 22 |
| | $R^*_{i,M_2} + M_2 \xrightarrow{k_{p_{22}}} R^*_{i+1,M_2}$ | $1.2\times10^3$ | 20-21 |
| | $R^*_{i,M_2} + M_1 \xrightarrow{k_{p_{21}}} R^*_{i+1,M_1}$ | $k_{p_{21}} = k_{p_{22}}/r_2\,;\ r_2 = 1.27$ | 22 |
| RAFT exchange | $R^*_{i,M_1} + R_0X \underset{}{\overset{k_{tr,0}}{\rightleftarrows}} R_{i,M_1}X + R^*_0$ | $k_{tr,0} = C_{tr,0} \times k_{p_{11}}$ | |
| | $R^*_{i,M_2} + R_0X \underset{}{\overset{k_{tr,0}}{\rightleftarrows}} R_{i,M_2}X + R^*_0$ | $k_{tr,0} = C_{tr,0} \times k_{p_{22}}$   $C_{tr,0} = 20$ | 23 |
| | $I^* + R_0X \underset{}{\overset{k_{tr,0}}{\rightleftarrows}} IX + R^*_0$ | $k_{tr,0} = C_{tr,0} \times k_{pI}$ | |
| RAFT main equilibrium | $R^*_{i,M_1} + R_{j,M_1}X \underset{}{\overset{k_{tr}}{\rightleftarrows}} R_{i,M_1}X + R^*_{j,M_1}$ | $k_{tr} = C_{tr} \times k_{p_{11}}$ | |
| | $R^*_{i,2} + R_{j,M_2}X \underset{}{\overset{k_{tr}}{\rightleftarrows}} R_{i,M_2}X + R^*_{j,M_2}$ | $k_{tr} = C_{tr} \times k_{p_{22}}$ | |
| | $R^*_{i,M_1} + R_{j,M_2}X \underset{}{\overset{k_{tr}}{\rightleftarrows}} R_{i,M_1}X + R^*_{j,M_2}$ | $k_{tr} = C_{tr} \times k_{p_{12}}$   $C_{tr} = 76$ | 23 |
| | $R^*_{i,M_1} + IX \underset{}{\overset{k_{tr}}{\rightleftarrows}} R_{i,M_1}X + I^*$ | $k_{tr} = C_{tr} \times k_{p_{11}}$ | |
| | $R^*_{i,M_2} + IX \underset{}{\overset{k_{tr}}{\rightleftarrows}} R_{i,M_2}X + I^*$ | $k_{tr} = C_{tr} \times k_{p_{22}}$ | |
| Termination by recombination | $R^*_0 + R^*_0 \xrightarrow{k_{tc,00}} P_0$ | $1.0\times10^7$ | |
| | $R^*_{i,M_1} + R^*_0 \xrightarrow{k_{tc,0}} P_i$ | $1.0\times10^7$ | |
| | $R^*_{i,M_2} + R^*_0 \xrightarrow{k_{tc,0}} P_i$ | $7.5\times10^6$ | 20-21 |
| | $R^*_{i,M_1} + R^*_{j,M_1} \xrightarrow{k^{i,j}_{tc,11}} P_{i+j}$ | $1.0\times10^7$ | |
| | $R^*_{i,M_2} + R^*_{j,M_2} \xrightarrow{k^{i,j}_{tc,22}} P_{i+j}$ | $5.5\times10^6$ | |
| | $R^*_{i,M_1} + R^*_{j,M_2} \xrightarrow{k^{i,j}_{tc,12}} P_{i+j}$ | $7.5\times10^6$ | |
| Termination by disproportionation | $R^*_0 + R^*_0 \xrightarrow{k_{td,00}} P_0 + P_0$ | $9.2\times10^7$ | |
| | $R^*_{i,M_1} + R^*_0 \xrightarrow{k_{td,0}} P_i + P_0$ | $9.2\times10^7$ | |
| | $R^*_{i,M_2} + R^*_0 \xrightarrow{k_{td,0}} P_i + P_0$ | $6.7\times10^7$ | 20-21 |
| | $R^*_{i,M_1} + R^*_{j,M_1} \xrightarrow{k^{i,j}_{td,11}} P_i + P_j$ | $9.2\times10^7$ | |
| | $R^*_{i,M_2} + R^*_{j,M_2} \xrightarrow{k^{i,j}_{td,22}} P_i + P_j$ | $4.9\times10^7$ | |
| | $R^*_{i,M_1} + R^*_{j,M_2} \xrightarrow{k^{i,j}_{td,12}} P_i + P_j$ | $6.7\times10^7$ | |

**Fig C-5 a: fractional comonomer conversion versus time; b: end-group functionality vs conversion; c: dispersity vs conversion; d: number-average chain length vs conversion.**
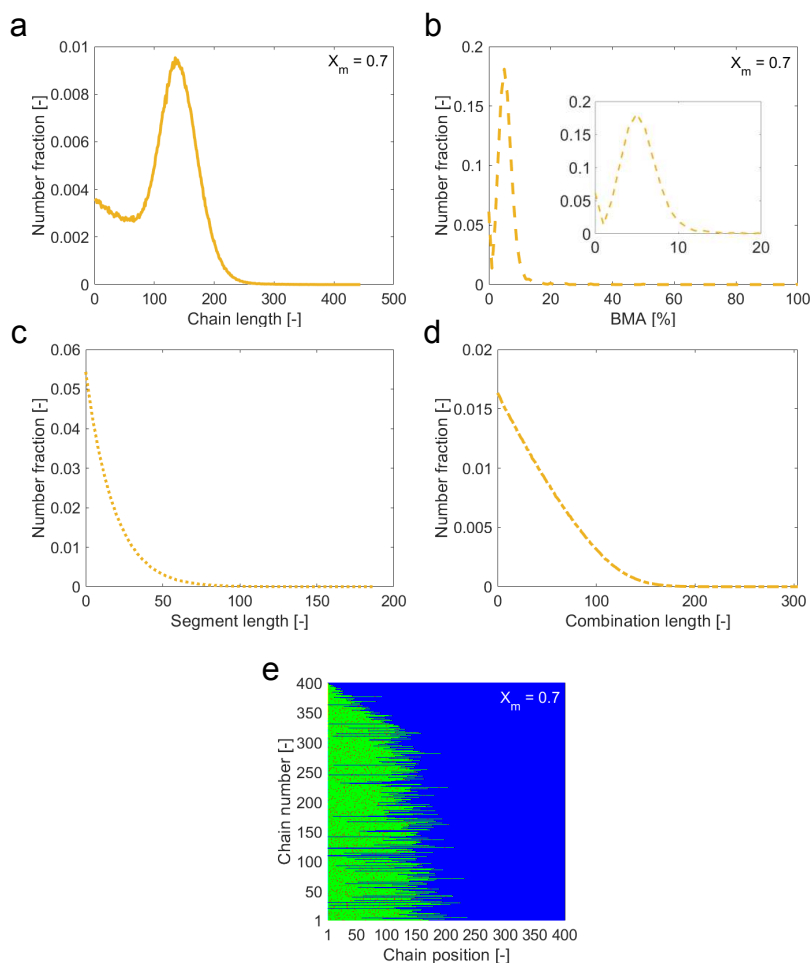
**Fig C-6 Example of the results of the kMC code modelling RAFT polymerization under the conditions specified in Section C.6.1 a: number chain length distribution; b: chemical composition distribution; c: segment length distribution between two anthracene units per polymer chain; d: all possible combinations of length distributions between two anthracene units per polymer chain; e: 400 samples polymer chains as the end of the polymerization, green corresponds to MMA monomer, while red stands for the anthracene containing monomer.**

## C.6.2 Folding of SCNP

As mentioned in the "Macromolecular reverse engineering to unravel the folding of individual chains" section

of the main text, **eq 4-2** is used to calculate the fundamental dimerization apparent rate coefficient ($k_{+app,A-A}$)

for each possible pair on the chain. The variation of $k_{+app,A-A}$ with time is shown in **Fig C-7** where the time-

average apparent rate coefficient is calculated. As expected, **Fig C-7** is consistent with the apparent rate

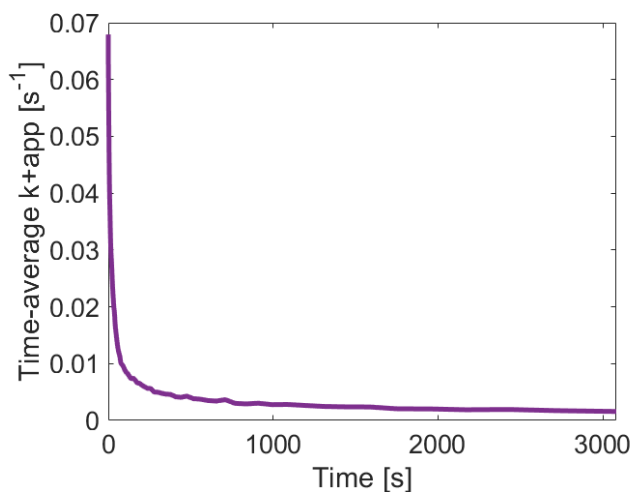coefficient vs time curve in **Fig C-4 b**.

**Fig C-7 An example of the resultant time-average apparent rate coefficient versus time for kMC folding.**

The folding of SCNP can proceed through multiple sequences as illustrated in **Fig C-8** below, which is accounted for by the model presented in this chapter. As a result, at the end of the simulation, it is possible to restore the sequence of crosslinking events and visualise the polymer chain contraction process in a 3D space (see **Fig C-9**).
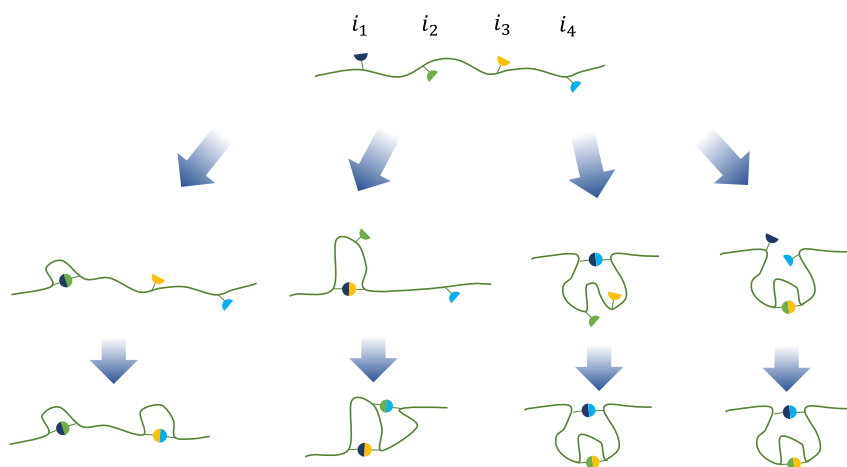


**Fig C-8 Examples illustrating some of the various folding scenarios upon irradiation for one chain capable of two clicks.**
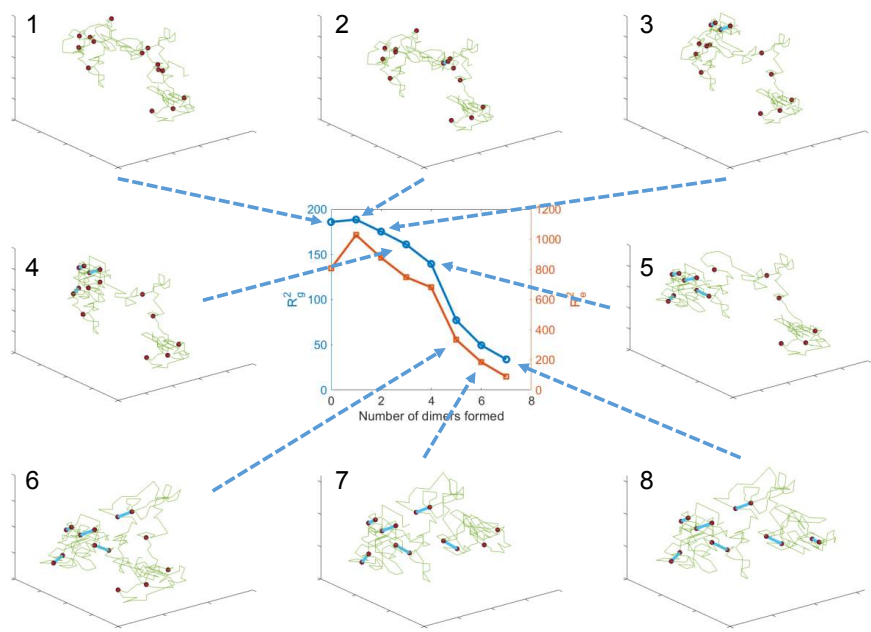
**Fig C-9 Changes in a mean square radius of gyration (red line) and a mean square end-to-end distance (blue line) vs a number of clicks. A sample of 3D conformations is presented for each of the points.**
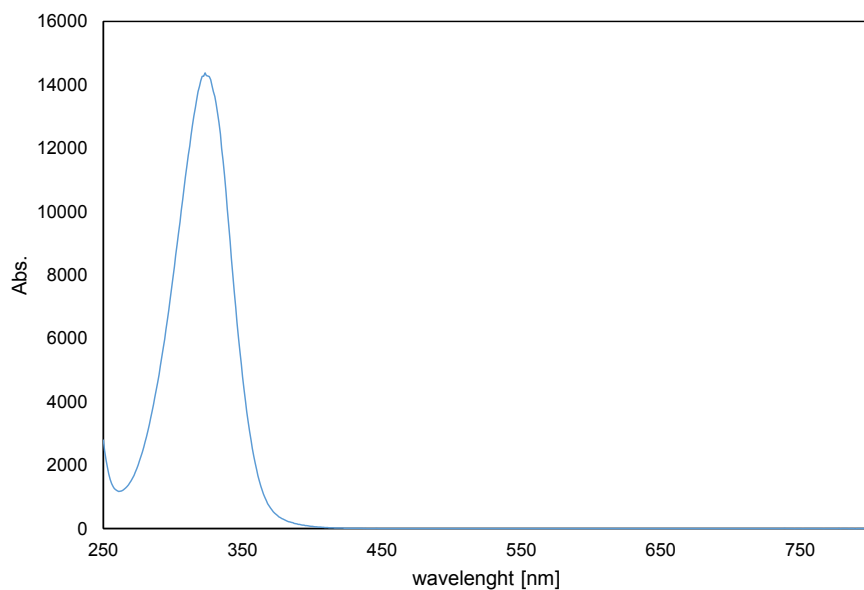
# APPENDIX D: SUPPORTING INFORMATION FOR CHAPTER 5



**Fig D-1 UV-VIS spectrum of IRG369 at $2.02 \times 10^{-4}$ mol L$^{-1}$ in propylene carbonate.**

# APPENDIX E: STATEMENT OF CONTRIBUTION OF CO-AUTHORS FOR THESIS BY PUBLISHED PAPER

## E.1 Statement of contribution for Chapter 2

**QUT** Division of Research and Innovation

**GRADUATE RESEARCH CENTRE**     hdr@qut.edu.au     +61 (0) 7 3138 7200

### Statement of Contribution of Co-Authors for Thesis by Published Paper

**The following is the suggested format for the required declaration provided at the start of any thesis chapter which includes a co-authored publication.**

The authors listed below have certified that:

1. they meet the criteria for authorship and that they have participated in the conception, execution, or interpretation, of at least that part of the publication in their field of expertise;
2. they take public responsibility for their part of the publication, except for the responsible author who accepts overall responsibility for the publication;
3. there are no other authors of the publication according to these criteria;
4. potential conflicts of interest have been disclosed to (a) granting bodies, (b) the editor or publisher of journals or other publications, and (c) the head of the responsible academic unit, and
5. they agree to the use of the publication in the student's thesis and its publication on the QUT's ePrints site consistent with any limitations set by publisher requirements.

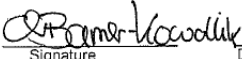In the case of this chapter: Chapter 2.

**Please state the publication title and date of publication or status:**

Kislyak, A.; Frisch, H.; Gernhardt, M.; Van Steenberge, P. H. M.; D'Hooge D, R.; Barner-Kowollik, C., Time-Dependent Differential and Integral Quantum Yields for Wavelength-Dependent [4+4] Photocycloadditions. *Chemistry* **2020**, *26* (2), 478-484.
Published: 2019/09/07

| Contributor | Statement of contribution* |
|---|---|
| Kislyak. A. | Manuscript writing, conduction of experiments, data analysis, experimental design, model design |
| Frisch, H. | Conceptualization, supervision, manuscript writing, aided experimental design, data analysis |
| Gernhardt, M. | Synthesis, writing of the synthesis section of the manuscript |
| Van Steenberge, P. H. M. | Conceptualization, supervision, manuscript writing, data analysis, model design |
| D'Hooge D, R. | Conceptualization, supervision, manuscript writing, data analysis, model design |
| Barner-Kowollik, C. | Conceptualization, supervision, manuscript writing, data analysis |

**Principal Supervisor Confirmation**

I have sighted email or other correspondence from all Co-authors confirming their certifying authorship.
(If the Co-authors are not able to sign the form please forward their email or other correspondence confirming the
certifying authorship to the GRC).

Chr. Barner-Kowollik   &Barner-Kowollik   13/7/21
Name                        Signature                    Date

## E.2 Statement of contribution for Chapter 3



**QUT** Division of Research and Innovation

**GRADUATE RESEARCH CENTRE**   hdr@qut.edu.au   +61 (0) 7 3138 7200

### Statement of Contribution of Co-Authors for Thesis by Published Paper

The following is the suggested format for the required declaration provided at the start of any thesis chapter which includes a co-authored publication.

The authors listed below have certified that:

1. they meet the criteria for authorship and that they have participated in the conception, execution, or interpretation, of at least that part of the publication in their field of expertise;
2. they take public responsibility for their part of the publication, except for the responsible author who accepts overall responsibility for the publication;
3. there are no other authors of the publication according to these criteria;
4. potential conflicts of interest have been disclosed to (a) granting bodies, (b) the editor or publisher of journals or other publications, and (c) the head of the responsible academic unit, and
5. they agree to the use of the publication in the student's thesis and its publication on the QUT's ePrints site consistent with any limitations set by publisher requirements.

In the case of this chapter: Chapter 3.

**Please state the publication title and date of publication or status:**

Kislyak, A.; Kodura, D.; Frisch, H.; Feist, F.; Van Steenberge, P. H. M.; Barner-Kowollik, C.; D'Hooge, D. R., A holistic approach for anthracene photochemistry kinetics. *Chem. Eng. J.* **2020**, *402*.
A holistic approach for anthracene photochemistry kinetics
Published: 2020/07/13

| Contributor | Statement of contribution* |
|---|---|
| Kislyak. A. | Manuscript writing, conduction of experiments, data analysis, experimental design, model design |
| Kodura, D. | Synthesis, writing of the synthesis section of the manuscript |
| Frisch, H. | Conceptualization, supervision, manuscript writing, aided experimental design, data analysis |
| Feist, F. | Purification experiments |
| Van Steenberge, P. H. M. | Conceptualization, supervision, manuscript writing, data analysis, model design |
| Barner-Kowollik, C. | Conceptualization, supervision, manuscript writing, data analysis |

| | |
|---|---|
| D'Hooge D, R. | Conceptualization, supervision, manuscript writing, data analysis, model design |

**Principal Supervisor Confirmation**

I have sighted email or other correspondence from all Co-authors confirming their certifying authorship.
(If the Co-authors are not able to sign the form please forward their email or other correspondence confirming the
certifying authorship to the GRC).

Chr. Barner-Kowollik     13/7/21

Name          Signature          Date

Graduate Research Centre, Level 4, 88 Musk Ave, Kelvin Grove Qld 4059        Page 1 of 1
Current @ 20/02/2020        CRICOS No. 00213J

A-76

# REFERENCES

1.    Levine, I. N., *Physical chemistry*. 5th ed. ed.; McGraw-Hill: Boston, 2002.
2.    Marien, Y. W.; Van Steenberge, P. H. M.; Barner-Kowollik, C.; Reyniers, M.-F.; Marin, G. B.; D'hooge, D. R., Kinetic Monte Carlo Modeling Extracts Information on Chain Initiation and Termination from Complete PLP-SEC Traces. *Macromolecules* **2017,** *50* (4), 1371-1385.
3.    Menzel, J. P.; Noble, B. B.; Lauer, A.; Coote, M. L.; Blinco, J. P.; Barner-Kowollik, C., Wavelength Dependence of Light-Induced Cycloadditions. *J. Am. Chem. Soc.* **2017,** *139* (44), 15812-15820.
4.    Eppendorf Research plus. Operating manual. Eppendorf AG: Germany, 2019.
5.    Frisch, H.; Kodura, D.; Bloesser, F. R.; Michalek, L.; Barner-Kowollik, C., Wavelength-Selective Folding of Single Polymer Chains with Different Colors of Visible Light. *Macromol. Rapid Commun.* **2020,** *41* (1), e1900414.
6.    Kislyak, A.; Frisch, H.; Gernhardt, M.; Van Steenberge, P. H. M.; D'Hooge D, R.; Barner-Kowollik, C., Time-Dependent Differential and Integral Quantum Yields for Wavelength-Dependent [4+4] Photocycloadditions. *Chemistry* **2020,** *26* (2), 478-484.
7.    Bouas-Laurent, H.; Desvergne, J.-P.; Castellan, A.; Lapouyade, R., Photodimerization of anthracenes in fluid solutions: (part 2) mechanistic aspects of the photocycloaddition and of the photochemical and thermal cleavage. *Chem. Soc. Rev.* **2001,** *30* (4), 248-263.
8.    Zimm, B. H.; Stockmayer, W. H., The Dimensions of Chain Molecules Containing Branches and Rings. *The Journal of Chemical Physics* **1949,** *17* (12), 1301-1314.
9.    Martin, J. E.; Eichinger, B. E., Dimensions of intramolecularly crosslinked polymers. 1. Theory. *Macromolecules* **1983,** *16* (8), 1345-1350.
10.    Martin, J. E.; Eichinger, B. E., Dimensions of intramolecularly crosslinked polymers. 2. Dilute solution thermodynamic parameters and photon correlation results on the polystyrene/cyclopentane system. *Macromolecules* **1983,** *16* (8), 1350-1358.
11.    Tzounis, P.-N.; Anogiannakis, S. D.; Theodorou, D. N., General Methodology for Estimating the Stiffness of Polymer Chains from Their Chemical Constitution: A Single Unperturbed Chain Monte Carlo Algorithm. *Macromolecules* **2017,** *50* (11), 4575-4587.
12.    Liu, J. W.; Mackay, M. E.; Duxbury, P. M., Molecular Dynamics Simulation of Intramolecular Cross-Linking of BCB/Styrene Copolymers. *Macromolecules* **2009,** *42* (21), 8534-8542.
13.    D'hooge, D. R.; Van Steenberge, P. H. M.; Derboven, P.; Reyniers, M.-F.; Marin, G. B., Model-based design of the polymer microstructure: bridging the gap between polymer chemistry and engineering. *Polymer Chemistry* **2015,** *6* (40), 7081-7096.
14.    Devlaminck, D. J. G.; Van Steenberge, P. H. M.; De Keer, L.; Reyniers, M.-F.; D'Hooge, D. R., A detailed mechanistic study of bulk MADIX of styrene and its chain extension. *Polymer Chemistry* **2017,** *8* (45), 6948-6963.
15.    D'Hooge, D.; Van Steenberge, P.; Reyniers, M.-F.; Marin, G., Fed-Batch Control and Visualization of Monomer Sequences of Individual ICAR ATRP Gradient Copolymer Chains. *Polymers* **2014,** *6* (4), 1074-1095.
16.    Van Steenberge, P. H. M.; D'hooge, D. R.; Reyniers, M. F.; Marin, G. B., Improved kinetic Monte Carlo simulation of chemical composition-chain length distributions in polymerization processes. *Chem. Eng. Sci.* **2014,** *110*, 185-199.
17.    Van Steenberge, P. H. M.; D'hooge, D. R.; Wang, Y.; Zhong, M.; Reyniers, M.-F.; Konkolewicz, D.; Matyjaszewski, K.; Marin, G. B., Linear Gradient Quality of ATRP Copolymers. *Macromolecules* **2012,** *45* (21), 8519-8531.
18.    Arraez, F. J.; Xu, X.; Van Steenberge, P. H. M.; Jerca, V.-V.; Hoogenboom, R.; D'hooge, D. R., Macropropagation Rate Coefficients and Branching Levels in Cationic Ring-Opening Polymerization of 2-Ethyl-2-oxazoline through Prediction of Size Exclusion Chromatography Data. *Macromolecules* **2019,** *52* (11), 4067-4078.
19.    Gillespie, D. T., Exact stochastic simulation of coupled chemical reactions. *The Journal of Physical Chemistry* **1977,** *81* (25), 2340-2361.
20.    Nikitin, A. N.; Grady, M. C.; Kalfas, G. A.; Hutchinson, R. A., Investigation of Catalytic Chain Transfer Copolymerization of Methacrylates. *Macromolecular Reaction Engineering* **2008,** *2* (5), 422-435.
21.    Van Steenberge, P. H. M.; Hutchinson, R. A., Design of 2-hydroxyethyl methacrylate-functional macromonomer dispersants by semi-batch cobalt chain transfer polymerization. *AIChE J.* **2019,** *65* (11).
22.    Manders, B. G.; Smulders, W.; Aerdts, A. M.; van Herk, A. M., Determination of Reactivity Ratios for the System Methyl Methacrylate–n-Butyl Methacrylate. *Macromolecules* **1997,** *30* (2), 322-323.

23.     Derboven, P.; Van Steenberge, P. H. M.; Reyniers, M. F.; Barner-Kowollik, C.; D'hooge, D. R.; Marin, G. B., A novel method for the measurement of degenerative chain transfer coefficients: proof of concept and experimental validation. *Polymer Chemistry* **2016,** *7* (19), 3334-3349.